Spectromicroscopic characterisation of the formation of complex interfaces

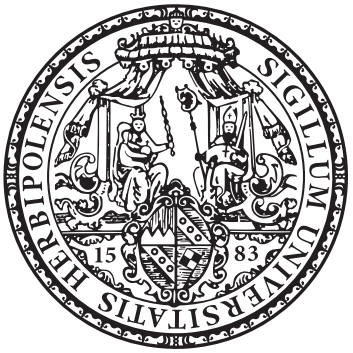

Dissertation zur Erlangung des naturwissenschaftlichen Doktorgrades der Julius–Maximilians Universität Würzburg

vorgelegt von
Florian C. Maier
aus Nürnberg

Berlin, Würzburg 2010

Eingereicht am: 29. Oktober 2010
bei der Fakultät für Physik und Astronomie

1. Gutachter – Prof. Dr. Eberhard Umbach
2. Gutachter – Priv.-Doz. Dr. Jörg Schäfer
der Dissertation.

1. Prüfer – Prof. Dr. Eberhard Umbach
2. Prüfer – Priv.-Doz. Dr. Jörg Schäfer
3. Prüfer – Priv.-Doz. Dr. Reinhold F. Fink
im Promotionskolloquium.

Tag des Promotionskolloquiums: 09. Dezember 2010
Doktorurkunde ausgehändigt am ...

Contents

Summary

Spectromicroscopic characterisation of the formation of complex interfaces

Within the framework of this thesis the mechanisms of growth and reorganisation were investigated that are the basis for the fabrication of high quality thin films and interfaces. The majority of the measurements was performed with the recently developed low energy electron spectromicroscope SMART [1], the first double–aberration corrected instrument of its kind [2]. Comprehensive methods (LEEM/PEEM, µ–LEED, µ–XPS) integrated in this system were utilised to study in–situ and in real time the formation processes on surfaces and to determine the morphology, local structure and local chemical composition of the resulting thin film. Complementarily, a commercial AFM [3] was used ex–situ to get a direct measure of the morphology and the absolute height of surface objects. XPEEM and µ–XPS measurements were made possible by attaching SMART to a high flux density beamline of the soft–X–ray source BESSY–II [4] which included the development of proper alignment strategies.
Depending on the application, stacked homogeneous layers or the controlled formation of semiconductor nanostructures are desired. Such quantum structures may offer new properties as, e.g., the trapping of carriers for enhanced emission or even show size dependent quantum effects.
Two quite different model systems were chosen to study details of the growth and reorganisation process of thin films and to demonstrate the power of the aberration corrected spectromicroscope at the same time. Here the measurements benefit especially from the enhanced transmission of the microscope and also from its improved resolution.

PTCDA/Ag(111) – Growth and structure of the first two layers

Although PTCDA/Ag(111) is one of the most intensely studied model systems for the growth of organic semiconductor thin films, it still offers new insights into a complex growth behaviour. Hence the presented studies enlighten the temperature dependant influence of morphological features as small as monatomic Ag steps on

the **growth process** of the first two layers.
At sufficiently low temperatures of the substrate, single steps act as diffusion barriers for the migrating PTCDA molecules in the first layer. This barrier is reduced as soon as the Ag is covered by PTCDA, which allows interdiffusion between adjacent Ag terraces. Nevertheless domain boundaries in the first PTCDA–layers persist as boundaries for crystallite growth in the second layer. This leads to different growth regimes in the second layer.
The first and the common second layer grow differently in respect to the expanding domains. Whereas the first layer islands are more compact, the more dendritic development of the second layer indicates a reduced interaction strength between 2^{nd} and 1^{st} layer.
These findings are explained by two effects: First, the reduced substrate – layer interaction in case of second layer molecules allows enhanced diffusion, which is also observed across former barriers. Second, the structural difference between neighbouring domains in the first layer prevents the overgrowth by single coherent 2^{nd} layer domains.

The second part of the PTCDA study reveals a **variety of phases** that appears if only two layers are deposited. Besides the six known, rotational domains of the interface system PTCDA/Ag(111) [5], a further manifold of structures was discovered, which was not reported before. Besides a surprising striped image contrast, the second layer also grows in an elongated way along the so–called 'ripples'. The latter show a rather large period of 40 nm and were found in a temperature range between 210 and 280 K. Additionally the µ–LEED pattern of such a domain shows a new super–superstructure as well.
This phase is explained by a structural model that introduces a rotated, more relaxed domain in the second layer that does not exist in the first layer. Its structural parameters are similar to those of the bulk unitcells of PTCDA.
This approach for the stacking is confirmed by the observation of two different rotational domains that grow on top of one single 'substrate' domain in the first layer. The orientations of the ripple phases fit as well to the predictions of the model. The growth direction along the ripples corresponds to the short diagonal of the super–structure unit cell with diamond–like shape.
The alternating contrast in the second layer is explained by an oscillation of the inter layer distance but also a periodic change in, e.g., the electron density, that might lead to a variation of the work function, could be its origin.

CdSe/ZnSe – Inverse structuring by sublimation of an α–Te cap

Besides the direct organic growth by deposition of PTCDA layers on a Ag(111) surface, the formation of CdSe quantum dots from strained epi–layers was investi-

gated. In this case the structures do not form during deposition but rather during sublimation of the so–called "ignition cap".
These were pilot experiments with a spectromicroscope at CdSe/ZnSe heterostructures. Hence not only the process of QD formation itself was of interest but also the portability of the preparation and the prevention of contaminations during on–air transport were evaluated. It turned out that the α–Se cap is well suited for protection against contaminations. And the last step of the QD preparation, the sublimation of the α–Te cap, needs a sufficiently high change in temperature.

Subsequently the cap, the desorption process and the final surface with the quantum structures were investigated in detail. The cap was deposited in the MBE as an amorphous Te layer but was found to contain many different structures. Holes, cracks, and micro–crystallites within a α–Te matrix were identified. Holes penetrate deep into the cap leaving only 2 ML of Te that covers the underlying CdSe.
The following annealing of the sample lead to desorption of the cap which was investigated in real–time. Thus the structures that were found in the cap could be correlated with the newly formed features as, e.g., the quantum dots on the bare CdSe surface. It turned out that QDs form only outside the areas with holes in the cap. They prefer to form in the neighbourhood of the Te µ–crystallites. Hence it is concluded that the presence of tellurium plays a major role in the formation process of the CdSe/ZnSe quantum dots. Different explanations as the impact of Te as a surfactant, an enhanced mobility of adatoms or as stressor nuclei are discussed.
The spectromicroscopic characterisation of the released CdSe surface with QDs on top revealed the crystallographic directions and hence allowed for their correlation with the cap features. Further, an increased Cd signal of the film was found at the positions of the former holes. Several possibilities as segregation or surface termination are reviewed, that might explain this slight Cd variation.
Therewith, a first important step to a detailed understanding of the complex reorganisation process in coating systems could be achieved.

Zusammenfassung

Spektromikroskopische Charakterisierung der Bildung komplexer Grenzflächen

In Rahmen dieser Arbeit wurden der Schicht– und Grenzflächenpräparation zu Grunde liegende Wachstums– und Reorganisationsmechanismen in–situ untersucht. Für die Messungen stand mit SMART die noch recht jungen Methode der niederenergetischen Elektronen–Spektromikroskopie zur Verfügung.
SMART [1, 2], das erste doppelt aberrationskorrigierte Spektromikroskop, erlaubt nicht nur Messungen unter UHV–Bedingungen sondern auch in Echtzeit, wobei zwischen einer Reihe von Methoden (LEEM/PEEM, µ–LEED, µ–XPS) kurzfristig und in–situ gewählt werden kann. Flankiert wurden die Messungen durch ein kommerzielles AFM [3]. Erst die Installation von SMART an einem Strahlrohr von BESSY–II [4] mit hoher Flussdichte im Bereich der weichen Röntgenstrahlung ermöglichte die XPEEM– und µ–XPS–Messungen.
Je nach Anwendung sind nicht nur gestapelte, möglichst homogene Schichten gewünscht sondern auch die kontrollierte Bildung von Halbleiternanostrukturen. Diese Quantenstrukturen ergeben mitunter neue Eigenschaften, wie zum Beispiel die Fähigkeit, Ladungsträger zu lokalisieren, was zur Effizienzsteigerung von LEDs und LASERn führt, oder zeigen sogar schon bei Raumtemperatur Quanteneffekte, wenn die Strukturen ausreichend klein sind.
Anhand von zwei unterschiedlichen Modellsystemen wurden zum Einen Wachstums– und Reorganisationsprozesse dünner Schichten im Bereich einiger Monolagen untersucht und zum Anderen die Möglichkeiten, die das aberrationskorrigierte Spektromikroskop bietet, demonstriert. Dabei wurde besonders von der gesteigerten Transmission des Mikroskops, aber auch von der verbesserten Auflösung durch die Aberrationskorrektur profitiert.

PTCDA/Ag(111) – Wachstum und Struktur der ersten beiden Lagen

Das inzwischen ausgiebig untersuchte Modellsystem PTCDA/Ag(111) ist nach wie vor für Überraschungen gut. So konnte bei den hier vorgestellten Untersuchungen der Einfluss der Morphologie auf den **Wachstumsprozess** der ersten beiden Lagen

– bis hinunter zu monoatomaren Ag–Stufen – detailliert beobachtet werden.
Es stellte sich heraus, dass bei ausreichender Kühlung des Substrats monoatomare Ag–Stufen als T–abhängige Diffusionsbarrieren für die PTCDA–Moleküle in der ersten Lage fungieren. Hingegen ist die Diffusion von Molekülen der zweiten Lage über Domänengrenzen in der ersten Lage hinweg leicht möglich, wenngleich PTCDA–Domänengrenzen der ersten ML auch für Kristallite in der zweiten Lage begrenzend sind. Dies führt zu unterschiedlichen Wachstumsregimes in der zweiten Lage. Das unterschiedliche Domänenwachstumsverhalten – eher kompakt für die erste und stärker dendritisch für die zweite Lage – ist ein Hinweis darauf, dass die Wechselwirkungsstärke zwischen zweiter und erster Lage im Vergleich zum Wachstum der ersten Lage auf der blanken Ag(111) Oberfläche reduziert ist.
Dieses Verhalten lässt sich durch zwei Effekte erklären: Einerseits erlaubt die zu erwartende, reduzierte Substrat–Adsorbat–Wechselwirkung der Moleküle in der zweiten, im Vergleich zur ersten Monolage erhöhte Diffusion, die auch über ehemalige Diffusionsbarrieren hinweg beobachtet wird. Andererseits verhindert der strukturelle Unterschied benachbarter Domänen in der ersten Lage, dass diese Domänengrenzen von einer einzelnen zusammenhängenden Domäne in der zweiten Lage überwachsen wird.

Ein zweiter Teilaspekt beleuchtet die **Vielfalt der Strukturen** der Stapelkristallite und Domänen in der zweiten Lage. Es fanden sich neben den sechs bekannten Rotationsdomänen [5], die PTCDA auf Ag(111) bildet, in der Stapelung weitere Varianten. Diese zeigen nicht nur einen ungewöhnlichen, linear variierenden Kontrast sondern auch anisotropes Wachstum, bevorzugt entlang der sogenannten 'Ripple'. Letztere haben eine vergleichsweise große Periode von etwa 40 nm und treten in einem Temperaturbereich zwischen 210 und 280 K auf.
Ergänzend zeigt das µ–LEED Beugungsbild eine neue, kristallographische Über–Überstruktur[1]. Die Abmessungen der Einheitszelle der Moleküle in der zweiten Lage ähneln denen der ersten Lage, sind aber gegenüber diesen um etwa 75° gedreht.
Zudem wurden in DF(Dunkelfeld)–LEEM zwei unterschiedliche Rotationsdomänen auf einer einzelnen Substratdomäne (erste Lage) beobachtet. Dies zeigt direkt, dass die Domäne der ersten Monolage nicht zwingend die Orientierung aufwachsender Domänen bestimmt.
Zur Erklärung dieser Beobachtungen wird ein Strukturmodell vorgeschlagen, das aus zwei unterschiedlichen, gestapelten PTCDA–Domänen besteht. Die obere gleicht zwar den bekannten PTCDA/Ag(111) Rotationsdomänen, ihre Abmessungen liegen aber näher an der Einheitszelle von Volumen–PTCDA Kristalliten als die der ersten Lage.
Derart verspannt wachsen diese Domänen bevorzugt entlang der „Ripples“und damit entlang der kurzen Diagonalen der vorgeschlagenen Über[2]struktur auf. Die von

[1] Über–Überstruktur wird der Übersichtlichkeit halber im Folgenden mit Über[2]struktur abgekürzt.

diesem Modell vorhergesagten Orientierungen wurden ebenfalls in den aufgespürten Ripple–Strukturen gefunden.
Der linienförmige Kontrast in der zweiten Lage lässt sich durch eine Oszillation des Lagenabstandes erklären. Allerdings könnte auch eine periodische Variation der Elektronendichte zu einer Änderung der Austrittsarbeit und somit zu dem beobachteten Kontrast führen.

CdSe/ZnSe – Rückwirkende Strukturbildung durch Sublimation einer α–Te Deckschicht

Neben der Untersuchung des Lagenwachstums von PTCDA/Ag(111) wurde in weiteren Experimenten die Bildung von CdSe–Quantenpunkten (QD) aus verspannten CdSe/ZnSe(001) Schichten untersucht, die sich bei Sublimation der Te–Schicht reorganisieren. Bei diesen Pilotexperimenten mit einem Spektromikroskop an CdSe/ZnSe Heterostruturen waren neben dem Bildungsprozess der Quantenstrukturen selbst sowohl die Portabilität der Präparationsmethode als auch der kontaminationsfreie Transport von der MBE zum SMART von Interesse. Dabei empfahl sich die α–Se Deckschicht als verlässlicher Schutz vor Verunreinigungen. Der letzte Schritt bei der Präparation der Quantenstrukturen, die in–situ Sublimation der mikromorphen Te Deckschicht, erfordert ausreichend hohe Heizraten.
Schrittweise wurden detailliert die Deckschicht, der Desorptionsprozess und die resultierende Oberfläche mit den Quantenstrukturen untersucht. Die als α–Te abgeschiedene Kappe weist eine Vielzahl von Strukturen auf, die als Löcher, Risse und Mikrokristallite in einer α–Te Matrix identifiziert wurden. Die Löcher (und Risse) dringen tief in die Kappe ein und nur ein 2 ML dünner Te Film bedeckt den Boden aus CdSe.
Die Probe wurde nun geheizt; damit wurde die Kappe entfernt und der Desorptionsprozess konnte beobachtet werden. Dadurch konnten die Positionen der Strukturen in der Kappe mit den zurückbleibenden bzw. neu entstehenden Strukturen, wie den Quantenpunkten korreliert werden. Es stellte sich heraus, dass die QDs nur außerhalb der Bereiche entstehen, an denen die Kappe vorher Löcher hatte. Zudem findet man sie hauptsächlich in der Nachbarschaft der Mikrokristallite. Daraus wird gefolgert, dass die Präsenz von Tellur bei der Bildung der Quantenpunkte eine wichtige Rolle spielt. Verschiedene Möglichkeiten wie zum Beispiel die Wirkung als „Surfactant“, Erhöhung der Diffusion und spannungsinduzierte Nukleation werden diskutiert.
Die Charakterisierung der entspannten CdSe Oberfläche mit den QDs fördert einerseits die Orientierung der Strukturen in Bezug auf die kristallographischen Richtungen des Substrats zutage und zeigt andererseits ein erhöhtes Cd–Signal unter den Löchern. Letzteres mag durch Cd–Segregation zustande kommen oder

auch durch Oberflächenrekonstruktionen, die Cd–terminiert sind. Damit ist ein erster, wichtiger Schritt zur detaillierten Aufklärung des Reorganisationsprozesses des komplexen Schichtsystems bei der Bildung von selbstorganisierten Quantenpunkten gelungen.

1 Introduction

Research activities are nowadays driven either by bare curiosity and fascination or the demand for improvements and devices with new functionalities. Organic semi–conductor thin films are already implemented into quite some consumer products, especially as self shining displays. Recently, also self–assembled nano–structures start to be integrated into devices as, e.g., LASERs and solar cells [6, 7]. Most of these electronic devices base on stacks of several different semi–conductor thin films. Depending on their desired functionality these components have specific demands on structure, composition, quality and homogeneity of each film by itself and the interaction among them. The challenge is to design and fabricate such stacks, which requires a detailed, basic knowledge of all material properties, and the formation processes itself.
To improve devices it is not just necessary to know and tailor the properties but also to control the process parameters for reproducible results. Therefore it is important to know which constraints limit the quality and homogeneity of the films and how they can be overcome.

Numerous researches on, e.g., electronic, magnetic, and optical properties of various materials are already published [8–10]. While the investigation of bulk properties has already a long tradition, in the last decades the focus is drawn to interfaces and thin films. Hence the mechanisms and strengths of interaction between substrate and deposit were investigated in detail [5, 11–13]. It is found, for example, that not only the substrate determines the structure of the deposit but vice versa the substrate can be reorganised at the interface by the first layer of the adsorbate [14, 15] as

well. Besides the direct growth studies on multilayer systems [16, 17], various methods for the inverse fabrication of self–assembled quantum structures from strained epi–layers were discussed [18–20]. The interface misfit strain is widely agreed to drive relaxation processes in crystalline systems [19, 21–23]. Hence the strength of interaction and the misfit at the interface, two quantities that determine the relaxation, are addressed in many studies. Therefore just monolayers or thin films are typically investigated.

For this work the focus was put to the border zone between interface and thin film. Systems that have layer thicknesses between single layers and bulk–like multi–layers. There the substrate influences still the thin film, possibly indirectly.
Many questions arise concerning this intermediate zone. How far reaches the influence of the substrate into the deposit? What indicates a reduction of this interaction?
To what extent does the morphology of the substrate determine the growth of the adlayers? What does it depend on? Is the formation of layers or nano–structures directly driven by the interaction with the substrate or does it need a kind of lubricant or "ignition–cap"? What induces, or vice versa inhibits, the relaxation or rather the (re)organisation? Which material properties, as, e.g., structure or composition, actually cause the local "mismatch"?

To answer at least some of these questions, two different approaches shall be made: First the straight forward deposition is chosen where the organic molecule PTCDA will be grown well defined on a Ag(111) surface. In the second part the reorganisation procedure will be reversed – a full stack of several epitactically grown (strained) thin films will be annealed to remove the cap layer which is intended to induce the formation of quantum structures. These processes are to be observed directly in–situ and in real–time. Of major interest is the morphological, structural or chemical inhomogeneity of the surface and its influence on the (re)organisation process during growth and annealing respectively.

The morphology of static surfaces and the size and distribution of features is commonly investigated by microscopic techniques as AFM, STM or TEM. Dynamic processes are studied typically by integrative methods as LEED [24], RHEED or XRD. Crystalline order is investigated by diffraction techniques that are typically less sensitive to chemical composition. Hence x–ray spectroscopic techniques are used to determine the chemical composition (XPS) or the electronic structure (NEXAFS). Photoluminescence (PL) is used not only to characterise the optical properties but also the size distribution of, e.g., QDs.
With the double–aberration corrected spectromicroscope SMART a powerful multi–method tool is available. It is well suited for in–situ and real–time studies of heterogeneously structured and composed surfaces. The combination of different

methods together with the benefits from aberration correction allows the comprehensive characterisation of complex surfaces without removing the sample from the well–defined conditions of the UHV environment.

2

Experimental Methodology

This chapter introduces the fundamentals of the combined electron probe techniques as microscopy, spectroscopy and diffraction within the spectromicroscope with aberration–correction for enhanced resolution and transmission (SMART) – in its latest state of assembly – as well as the complementarily used atomic force microscopy (AFM). Besides the high–flux–density soft x–ray source BESSY–II[1] is briefly introduced.

2.1 Spectro–microscope SMART

Techniques, that image directly, record the momentary state of all displayed areas of an object at the same time. This allows real–time observation on a time scale of a few ten milliseconds. Slow electrons are used in case of SMART to study the properties of the sample surface. In principle three different sources are available to reflect or emit electrons from the surface as are a collimated, magnifiable electron beam, a Hg–short–arc–lamp and the soft–X–ray–source as is BESSY II.

[1] BESSY–II: Berliner Elektronen Speicherring Gesellschaft für Synchrotronstrahlung mbH II

2.1.1 Instrumental setup of the microscope

Electron optical system

Electrons, originating from the surface, are accelerated into the microscope and projected by the electron optical system onto a two dimensional detector (see figure 2.1).

Objective. An immersion field is applied between the grounded front electrode of the magnetic objective lens and the specimen. The specimen is at negative potential (−15 kV, gap 2-3 mm). Hence all electrons emitted into half-sphere are collected by the instrument. This kind of objective is known as immersion or cathode lens [25]. It is the dominant source of aberrations.

Optical elements and alignment. Electromagnetic and –static lenses (yellow jokes and blue outlines, respectively, in fig. 2.1) allow to zoom and to switch operation modes (2.2) with fixed geometry. This is possible by varying the excitation (current or voltage) which changes the focal length of the lenses. That is in contrast to typical light optical devices (e.g. camera, microscope), where the refractive elements are of rigid material.
Deflectors enable the user to run the optical axis accurately through the centre of the imaging elements and to operate the system with minimised aberrations in a well aligned state. Furthermore multi–poles of both types, i.e. electrostatic and –magnetic, enable the correction of stigmatism and higher order deformation of intermediate planes. Appropriate alignment ensures for all modes of operation high resolution and is crucial for fast (within seconds) switching between them. A brief introduction to the alignment of lenses using pairs of dipoles is given in [17].

Aberration correction. A special device in the SMART improves the resolution below 5 nm and, for this work even more useful, enhances the transmission by up to two orders of magnitude.
The electrostatic tetrode mirror is the first corrector in a low energy electron microscope, that compensates simultaneously for both, chromatic and spherical aberrations. As a consequence of this aberration correction, one can use a larger acceptance angle as well as a wider energy band of the imaged electrons. Therefore one gets better lateral resolution together with enlarged transmission. The mirror works in combination with the highly corrected, magnetic beam splitter that guides electrons from the objective to the mirror and the returning electrons into the transfer optics towards the detector without introducing aberrations up to the sixth

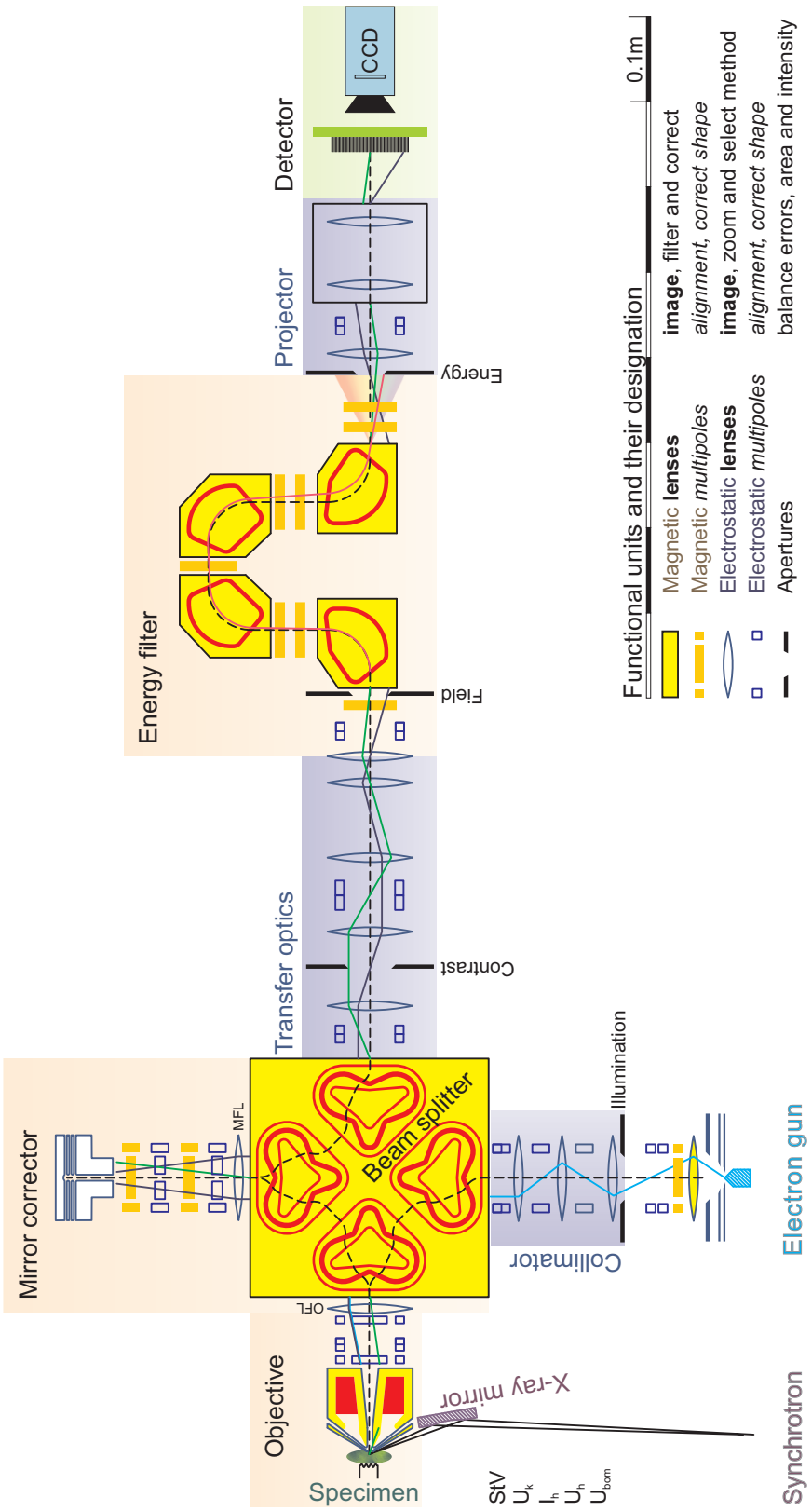

Figure 2.1: Colour online. Schematic of SMART, the **S**pectro-**M**icroscope with **A**berration correction, enhancing **R**esolution and **T**ransmission. Electrons follow the optical axis (dashed line) from left to right leaving the specimen imaged on the detector. They pass the highly magnifying objective, source of aberrations, are corrected by the electrostatic tetrode mirror and filtered by the omega–shaped energy filter. Transfer optics and projector allow to change the magnification and to switch between real, reciprocal and dispersive plane.

order. Due to its four–fold symmetry it furthermore allows to attach an e–gun to the microscope. Both elements were described in detail and invented for the SMART by Preikszas et. al. [26, 27].
The second special module is the (omega–shaped) imaging energy analyser. The dispersion of its four magnetic dipoles allows to reduce the transmitted energy band to 0.1 eV resulting in a resolving power of 150 000 with respect to the electron pass energy of the microscope. This reduces the influence of the remaining chromatic aberrations and allows for highly monochromatic image acquisition.

Sources

Different kinds of intense illumination sources with high brilliance may be used such as UV-lamp, Laser, synchrotron or an electron-gun. The choice depends on the physical properties one is interested in to study. The microscope optics restricts the choice only to methods that provide electrons, either emitted (e.g. by photons (PEEM), thermally, Auger processes, SEEM etc.)[2] or reflected (LEEM, MEM, SPLEEM)[3].
The present version of SMART is equipped with a Hg–short–arc lamp, the soft X–ray synchrotron radiation source BESSY II(see section 2.3) and a well collimated e–gun. It is intended to use low energy electrons in the range between -2 eV to several hundred eV with respect to the vacuum level. Negative values represent electrons reflected (mirror electron microscopy (MEM)) at the surface potential that cannot overcome the potential barrier of the specimen.

2.1.2 Modes of operation

Finally, the setup as described above allows three different modes of operation, namely microscopy, spectroscopy and diffraction (see also Schmidt et. al [28]). They are selected just by imaging the corresponding planes directly onto the screen. These planes are at the intersection of the optical axis (see figure 2.1) with exemplarily given electron rays. They are in case of microscopy the green line (e.g., field aperture) and for diffraction the blue solid line (e.g., contrast aperture). In Spectroscopy mode the dispersive plane is imaged which contains the energy slit. Figure 2.2 illustrates these modes in the case of illumination by photon.
In the microscopy mode a real space image of the surface is projected. Diffraction

[2] Photo Emitted Electron Microscopy, Secondary electron emission mass spectroscopy (see chp. A)
[3] Low Energy Electron Microscopy, Mirror Electron Microscopy, Spin Polarised LEEM

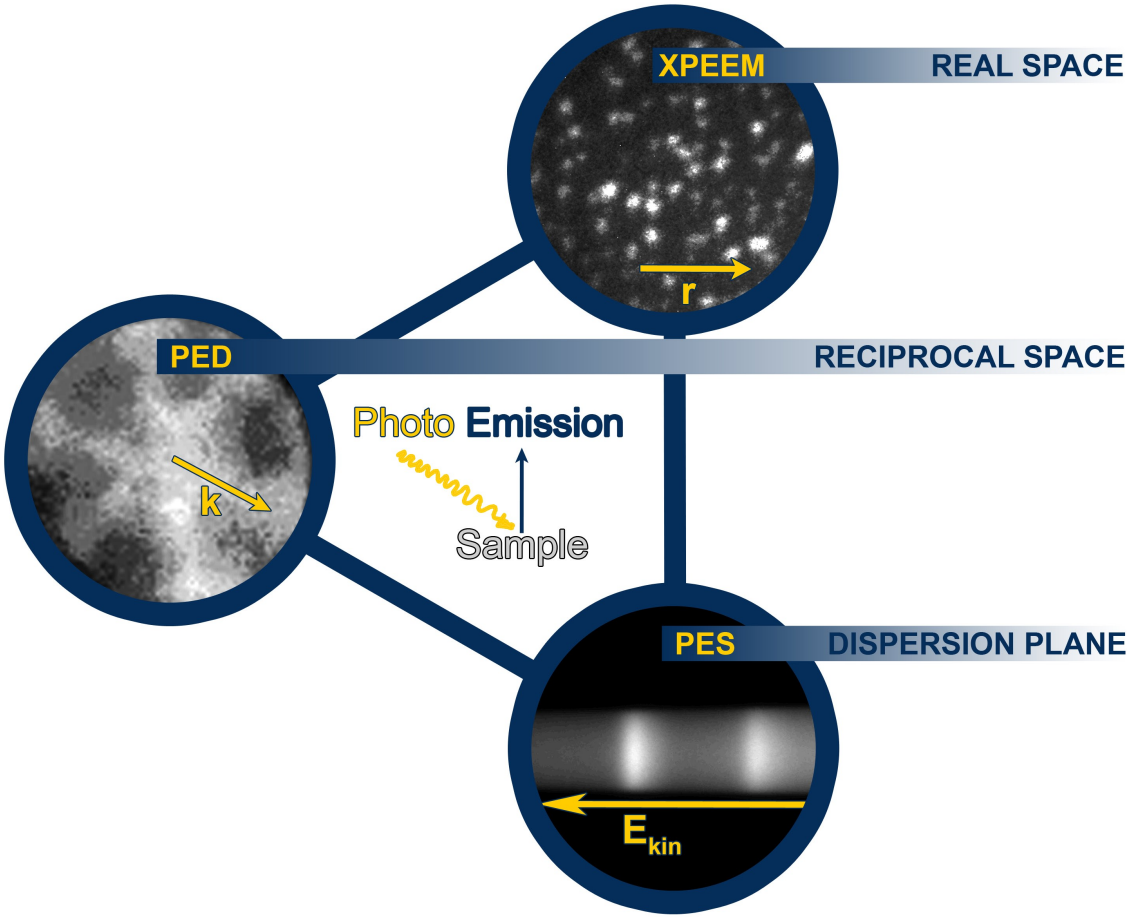

Figure 2.2: Colour online. Three operation modes are applicable by the SMART: The instrument allows to image the real space plane (microscopy), the reciprocal space plane (diffraction) or the dispersion plane (spectroscopy). In either mode apertures – i.e. field, contrast, and energy – in the other planes allow to optimize the gathered information.

Table 2.1: Use of Apertures (for positions see fig. 2.1) in the three modes of operation. Apertures that are used are indicated by *X*. The three applicable methods are, i.e., electron imaging – microscopy (PEEM/LEEM), diffraction (μ–PED/LEED), and dispersion – spectroscopy (μ–XPS/EELS).

Method	**Contrast aperture**	**Field aperture**	**Energy slit**
Microscopy	X	-	(X)
Diffraction	-	X	(X)
Spectroscopy	X	X	-

pattern from selected areas are formed in the back focal plane of the objective. Consequently just imaging of this reciprocal space plane is necessary to gain structural information. By imaging the dispersion plane of the omega–shaped energy filter spectroscopy from µm–sized areas can be performed.
Within each of these planes one aperture is available. They are used to enhance the quality of the measurements. Their use is summarised in table 2.1. For example in imaging mode (microscopy) the contrast aperture is used to select the angular acceptance and therefore choose the structures of interest. Additionally with the energy slit the image can be balanced between intensity and energy resolution. The desired energy is chosen adjusting the sample potential.
Details are given in the following paragraphs where the addressable physical properties are introduced.

2.2 Principles of applicable methods

The following sections are meant to give a brief introduction to the basic principles that underly the three different modes of operation mentioned in the previous chapter 2.1.2 and how they are used interactively.

2.2.1 Electron Diffraction

Operating SMART to gain diffraction patterns

In a microscope, the back focal plane (BFP) of the objective lens contains the angular distribution of electrons starting at the surface. In an image of this plane the so–called contrast aperture (CA)[4] is located. This plane might be also referred to as Fourier–plane, since the angular distribution of a periodic structure equals its Fourier–transformation in case of collimated illumination. Therefore the BFP contains the LEED pattern.
Hence the transfer optics allows to project the Fourier–plane, in other words the reciprocal space, of reflected or emitted electrons on the detector.
The use of a field aperture allows to select the area of interest (AoI), i.e. to limit the area where the detected pattern stems from. A special LEED–mode (DPEA050) transfers the intermediate specimen image from the exit of the beam splitter into the plane of the CA, which is therefore used as field aperture (FA). Thus the pattern from µm–sized, selectable (single–)domains can be measured leading to the so–called µ–LEED. The diameter of the selected area depends on the magnification M of the image in the plane of the contrast aperture of size S_{CA}. In case of SMART

[4]It is named according to its contrast enhancing property in LEEM instruments

$M = 18.5$ and S_{CA} can be selected out of a set of apertures within the range from 10 to 100 µm. For the present measurements the diameter of the CA was typically

$$\varnothing = \frac{S_{CA}}{M} \approx \frac{70\,\mu m}{18.5} = 3.8\,\mu m \tag{2.1}$$

In case of LEED the energy slit basically discriminates disturbing intensity from the secondary, inelastically scattered electrons. This is especially important if operated at very low kinetic energies of only a few eV.

Low energy electron diffraction

The geometric structure of surfaces may be investigated by low energy electron diffraction (LEED). This is a very common technique invented already in 1927 by Davison and Germer [29] and hence widely discussed [30–32]. A good introduction to spot–profile analysis LEED (SPALEED) using high k–space resolution for the analysis of spot profiles is given by Horn von Hoegen [33].
SMART uses a well collimated electron beam with selectable diameter for µ–LEED and tunable intensity. The de–Broglie wave length of electrons with energy E_{kin} between 2 and 200 eV ranges from 9 to 0.9 Å. These dimensions are in the order of magnitude of atomic distances and dimensions of superstructure lattices. Since electrons interact strongly with the surface, the inelastic mean free path (IMFP) (see fig. 2.3) is typically rather short. Consequently the electrons are elastically backscattered basically at the two dimensional surface structure of the topmost layers. Tuning the kinetic energy one can also access the vertical periodicity within the limits of penetration depth.
The diffraction spots give insight into the periodicity of the surface lattices that cannot (yet) be resolved in the microscopy mode, for example the periodicity of the crystal structures (typically some 2.5 Å) or even larger superstructures of e.g. PTCDA/Ag(111) with unit cell dimensions of $1.4 \times 0.9\,nm^2$. It also gives a hint on the quality of the surface and surface roughness.
It allows to correlate structures and their extension found in real space, as islands or domains, to crystallographic directions. Superstructures may be related to the substrate, e.g., as commensurate as found for PTCDA/Ag(111) by Glöckler et al. [5, 16]. If the superstructure unit cell breaks the symmetry of the substrate domains, mirror and rotational domains may be identified.
The behaviour of spots as a function of E_{kin} allows to typify structures in terms of tilt towards the chosen surface normal, as facets (step bunches) or regularly stepped, vicinal surfaces.
A more detailed analysis in terms of IV–LEED would also allow to determine the atomic arrangement within the surface unit cell [34].
µ–LEED proves to be very useful if superstructure phases with large unit cells are

unlikely, i.e. unstable or unfavourable. In this case the large real–space periodicity leads to plenty narrow spots in reciprocal–space. Since they all share the same total available intensity, they can easily be overlooked in standard LEED.

Photoelectron diffraction

Although it was not used within this work photo–electron diffraction (PED)[35] is to be mentioned as well together with the related photo–electron angular distribution (PEAD). Both PED at the crystal lattice and band–structure measurements called PEAD were already demonstrated with similar instruments, e.g., by Schmidt et al. [28] using the spectroscopic photo–emission and LEEM (SPELEEM) instrument at ELETTRA[5].
PED and PEAD effects in general have an influence on the photoelectron spectroscopy (PES) intensity. This happens if a pronounced pattern is not completely transferred through the contrast aperture.

For the present photoelectron measurements the influence of PED on XPS–intensity was neglected since the surface of the QD sample is not well ordered (α–Te) as seen in the diffuse background (BG) from LEED measurements. Furthermore the electron wavelength of the photoelectrons would have to match the surface lattice dimensions well to form pronounced patterns. And last such features were not seen. An influence of PEAD is neglected since the band–structures of ZnSe, determined by Markowski or Madelung [36, 37], and of CdSe [38] show only a low variation in k–space for the weakly bound (around 10 eV) Cd 4d and Zn 3d lines. The use of these lines just to distinguish between the two elements rather than to quantify their appearance justifies this behaviour since the energy separation is still larger than the overlap of their band structures.

2.2.2 Electron Spectroscopy

Spectroscopy mode of SMART

In spectroscopy mode SMART is capable to gain electron spectra from µm–sized, pre–selected areas of the sample surface. For the selection of the AoI, in the imaging mode a proper field aperture (fig. 2.1) is inserted and the sample is placed as desired. A contrast aperture is chosen according to the needs of energy resolution, since it acts as the entrance slit of the analyser. Returned to the spectroscopy mode the

[5]ELETTRA is the multidisciplinary Synchrotron Light Laboratory in Trieste, Italy

projector in figure 2.1 images the dispersive plane of the omega shaped energy filter (without energy aperture inserted) onto the detector. Stigmators in the filter allow to spread the intensity perpendicular to the direction of dispersion (energy axis) to reduce the flux density if necessary and therefore enhance the dynamic range of the detector system by several orders of magnitude.
The section of the dispersive plane imaged, the so–called energy window, was about 13 eV wide (maximum of 30 eV[39] is possible) having enough overlap to create continuous long–range photoelectron spectra (PES) together with Auger–electron spectra (AES). With the planned properly decoupled and well stabilised voltage supplies of e–gun and sample, electron energy loss spectroscopy (EELS) can be preformed as well.

The µ–PES contains spectroscopic information averaged across a selected, µm–sized area. In principle, diameters of less than 10 nm would be possible using the magnification by the transfer optics [39]. This allows to determine selectively the chemical composition (binding energy as elemental finger print) and the chemical environment of the atoms within a compound (shift of binding energies compared to references). If intensity measurements are reliable, quantitative analysis of the chemical composition is possible as well.

Photoelectron spectroscopy (PES)

Several textbooks (e.g., [40], [41]) discuss the AES (excitation followed by radiationless decay) and PES (ionisation) processes in detail. For the latter a good summary is given in [42]. In case of PES, where the occupied electronic states are probed, the basic idea, that was explained by Einstein in 1906, is the photon induced emission of bound electrons from the orbitals of atoms or molecules.

The transition probability $w_{i\to f}$ from the initial $\langle\psi_i|$ into the final state $\langle\psi_f|$ of such a process can be approximated by time dependant first order perturbation theory by Fermis golden rule [42]

$$w_{o\to f} \propto |\langle\psi_f|\hat{H}_S|\psi_i\rangle|^2\delta(E_f - E_i - h\nu) \tag{2.2}$$

where E_i and E_f are the energies of the electron system before and after emission of an electron. $\hat{H}_S$ is the perturbation operator that represents the electromagnetic waves of the incident photon. The delta–function describes the conservation of energy. With the relations[6]

$$E_f = E_f(N-1) + E_{kin} \tag{2.3}$$
$$E_i - E_f(N-1) = -(E_{bin} + \phi) \tag{2.4}$$

[6]The sign of binding energy and work function is due to the positive definition of both energies.

where N equals the number of electrons of an atom or molecule and ϕ is the work function that results from the binding energy measured with respect to the Fermi level E_F, a correlation between E_{bin} and E_{kin} is given. From equations 2.3 with 2.2 directly follows the photoelectric effect

$$h\nu = E_f - E_i = E_{kin} + E_{bin} + \phi \tag{2.5}$$

This allows with known photon energy $h\nu$ and tabulated [43] core level binding energies E_{bin} to identify the elemental species via the measurement of the kinetic energy E_{kin}. It is emphasised that not only different elements can be distinguished but also different elemental species in terms of chemical environment.
Together with the matrix element in equation 2.2 being correlated to the cross section for this process, a quantitative analysis of the elemental distribution is possible as well (see next section) using the intensity of the PES–signal.

The surface sensitivity of the method is due to the low IMFP of electrons within a solid. The so called universal curve, shown in figure 2.3, illustrates the attenuation of the electrons within the first few monolayers (ML) as a function of E_{kin}. It is noted that, in contrast to the "universal curve", the IMFP for energies lower than about 30 eV is in the order of only a few layers for molecules, for which vibronic excitations play an important role, as, e.g., PTCDA (see also [17]).

Determination of stoichiometry from XPS data

The PES–intensity $I(x, y)$ from a selected area, that is assumed to be homogeneous and atomically flat, is given [42, 44, 45] by the relation:

$$I(x, y) = I_0(x, y) \cdot \sigma_Z(N, h\nu) L_Z(\gamma) \cdot c_Z(\overrightarrow{r}) \cdot T(E_{kin}) \cdot D(x, y). \tag{2.6}$$

In this equation I_0 is the illumination, σ_Z and L_Z are the cross section and the angular asymmetry parameter of element Z for photoemission from level N. T is the electron transmission of the microscope and $D(x, y)$ describes the detection efficiency of micro channel plate and camera setup. c_Z accounts for the accumulated signal of the distribution of element Z within the sampled layers (see below eq. 2.9). The asymmetry parameter L_Z as a function of angle γ [41] between source and analyser (analyser oriented along the surface normal) is given by

$$L(\gamma) = 1 + \frac{1}{2}\beta_N \left(\frac{3}{2} sin^2\gamma - 1\right) \tag{2.7}$$

β_N as well as the cross section σ_Z are found in tables by, e.g., Yeh et al. [46]. Furthermore Jablonski et al. [47] found a reduction of β_N within solids by elastic scattering right for normal emission that leads to

$$\beta^* = (0.781 - 0.005\,14\,\mathrm{Z} + 0.000\,031\,\mathrm{Z}^2)\beta_N. \tag{2.8}$$

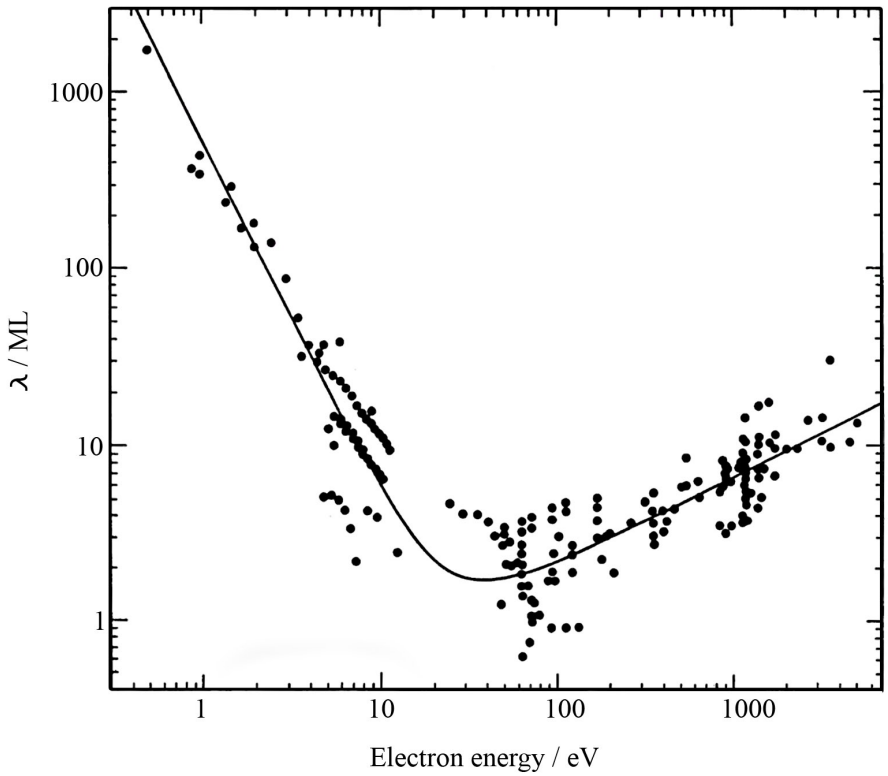

Figure 2.3: Universal curve for the IMFP of electrons in a solid [41]

With these equations and the tabulated values one can in principle determine the stoichiometry of the sampled areas.

The asymmetry parameter is necessary since in the SMART experiment, unlike in typical spectrometers, the geometry is not arranged in the so–called "magic angle" [41, 45] of 54.73° but the x–rays impinge onto the surface under an angle of about 70° with respect to the surface normal.
However it is close enough that under the conditions of the present experiments the intensity is overestimated by less than 5 %. Furthermore the higher the angular acceptance (up to about 60°) of the microscope, the lower is the influence of this estimate, and intensity ratios are used for the calculations which reduce again the deviation. Therefore this effect was neglected for the calculations.

Determination of the layer thickness from XPS

To determine the thickness of layers one has to model the concentration of the element of interest within the layer. In case of the investigated QD system this was done by calculating the elemental distribution factor c_Z in equation 2.6 using a model of alternating layers of material Z covered by Z_0 (if applicable, e.g., in case of the CdSe(100) compound) as follows

$$c_Z = \sum_{n=0}^{N} e^{-\frac{n+1}{\lambda_{Z_0}}} \cdot e^{-\frac{n}{\lambda_Z}}. \tag{2.9}$$

In equation 2.9 the IMFPs λ are meant in layers and are hence unitless. For homogeneous material (e.g. Te–cap) equation 2.9 simplifies just by skipping the factor for element Z_0. In this equation N is the total thickness in layers of the homogeneous film and λ the energy dependant, combined IMFP of electrons λ_e and attenuation length of photons in solids λ_{ph}

$$\lambda = \left(\frac{1}{\lambda_e} + \frac{1}{\lambda_{ph}} \right)^{-1}. \tag{2.10}$$

In general λ_{ph} is much larger than λ_e and can be neglected. With the help of this model one can calculate the number N of layers if it succeeds to determine or eliminate the product of detection efficiency $D(\overrightarrow{r})$ and I_0[7] from equation 2.6.

It was accomplished by making use of lateral surface inhomogeneities (i.e., α–Te–cap versus hole), different photon energies, and distinction of chemical species

[7] For correction of inhomogeneities in the detection sensitivity see B.1

(α–Se/(Cd,Zn)Se). E.g., in case of the α–Te film the intensity ratios of the Te–signal recorded at two different photon energies were compared at different sample positions, i.e., hole and cap. In good approximation, cap areas are infinitely thick and thus provide a flux measurement.
The intensities of the peaks were measured using the peak fitting tool fityk [48]. Due to the low S/N–ratio of the XPEEM–spectra from selected areas as small as 50 nm × 10 nm typically a linear BG was subtracted. All peaks were fitted with strict constraints deduced from doublet separation (literature), multiplicity (orbital) and instrumental broadening.

2.2.3 Microscopy

There are two different ways to gain images from microscopic structures. The first is direct imaging, the second scanning. Direct imaging is well known from light microscopes and applied to electron microscopy, e.g., by the SMART or other LEEM/PEEM systems for surface studies or by TEM for studies of thin bulk–like samples. In contrast scanning probe techniques, as AFM (section 2.4), STM or scanning electron microsopy (SEM) recover images from a two dimensional array of serially detected image points.
Both principles were used for the present work to study nanoscopic structures on semiconductor and single crystalline metal surfaces. Their major characteristics will be introduced briefly in this chapter. The main focus of this work lies surely on the imaging technique of low energy electron spectro–microscopy.

Operating SMART as microscope

This is the most relevant mode of operation of the SMART. As expected, in this case the projection optics transfers the image plane onto the multi–channel–plate (MCP). Contrast aperture and energy slit may be set according to the needs of contrast enhancement and resolution balanced to sufficient transmission for acceptable acquisition times.
With the contrast aperture it is possible to select an area in k–space to limit the acceptance angles that can contribute to image formation. Above the diffraction limit this helps to reduce the remaining spherical aberrations.
The energy slit selects an energy window between 0.1 eV up to 30 eV (no slit) in the dispersive plane of the omega–filter (fig. 2.1). Usually the 0.5 eV and 1 eV energy slits were used for the LEEM and PEEM experiments, thus reducing the chromatic aberration. The influence and power of the two apertures on the image contrast is discussed in detail below.

Contrast

It is obvious that only samples with a lateral variation of a physical property are of interest for microscopic studies since this gives a detectable contrast. The main objective from a microscopic point of view is therefore to perfectly reproduce the available contrast in the image. A **quantitative measure** of the contrast is given by the definition of the MTF[8]. According to Engel[9] the contrast is given by

$$MTF = \frac{I_{\vec{r}_i} - I_{\vec{r}_j}}{I_{\vec{r}_i} + I_{\vec{r}_j}} \tag{2.11}$$

where $I_{\vec{r}}$ is the signal [49] intensity from adjacent structures i and j. The maximum detectable contrast is hence a difference in intensity of 100 % between two adjacent image points.
Typically the contrast is much lower due to, e.g., low resolution, high background, or low variations of material properties. To transfer the available contrast as good as possible it is necessary to understand the underlying contrast mechanisms that are introduced in the following paragraphs.

Contrast mechanisms with low energetic electrons

As mentioned earlier in the case of electron irradiation it is distinguished between different classes of electron microscopy depending on electron properties as spin (spin polarized LEEM (SPLEEM)) and energy (MEM: reflection at the surface potential; LEEM: penetration into the surface). The following focusses on the latter two as they are used within this work.

Mirror electron microscopy MEM. In MEM basically all incident electrons are reflected at the potential barrier of the surface, since their kinetic energy is too small to overcome the vacuum level of the specimen. Therefore MEM is sensitive to the morphology and the lateral variations of the work function at the transition to LEEM. Advantages of this method are a high image intensity and that the electrons do not interact with the surface atoms which prevents beam damage. Furthermore no crystalline structure of the specimen is required.

[8] The modulation transfer function (MTF) strictly spoken describes the contrast as a function of the spatial frequency [49].
[9] Wilfried Engel, SMART Archiv — `BenoetigtePhotonenflussdichte.doc`

Structural contrast in BF–LEEM. LEEM bases on LEED. With the help of well collimated electron illumination contrast related even to small structural differences can be achieved just using the central (00)–beam of the LEED–pattern (bright field (BF) mode). Different structures cause different k–dependant reflectivity. This is demonstrated in our publication by Schmidt et al. [2] for the herringbone surface reconstruction of the Au(111) surface shown in figure 2.4. The linear contrast is due to a structural change from hcp to fcc lattice of the Au surface reconstruction. Besides the lateral variation in surface structures we also observed interference contrast from different thin films. Interference of the electron wave reflected at the surface of the thin film with the one reflected at the substrate – thin film interface may cause different grey scales for different layer thicknesses [17]. This is attributed to the (partial) destructive or constructive interference of the two waves which depends on the electron energy and is called interference or quantum interference contrast QIC.

Phase, step or step–phase contrast. Maybe less intuitive is the mechanism underlying the phase, step or step–phase called contrast [50, 51]. In principle steps allow the electron wave reflected by the top terrace to interfere with its part reflected by the lower one. This leads to a spread, oscillating intensity distribution perpendicular to the step edge. It is often referred to as "Fresnel diffraction" [2, 50]. Figure 2.5 illustrates the results of Fresnel interference pattern calculations by Altman et al. [51, 52] at a monatomic step of hight a_0. The distances in (a) are not to scale. Cross sections (b) and (c), calculated for the under–focus[10] condition, show an intensity variation across the step with electron wave phase shifts ϕ of $\pi/2$ and π, respectively. Note the large periodicity of the oscillation close to the step compared to the step hight. The influence of instrumental effects due to an energy spread of the source (d), a lateral extension of the source (e) and an estimated typical lens aberration (f) is shown for the in phase condition $\phi = \pi$ (again under–focus).
Two points shall be made: First the pattern is asymmetric for $\phi = (2n + 1)\pi/2$. This allows to distinguish between upper and lower side of the step, provided that the pattern can be resolved. Second, aberration correction lends itself to provide sufficient resolution for the observation of this Fresnel pattern, at least for the most dominant features. These bright fringes next to the dark steps are well visible in fig. 2.4 (a).
If the pattern itself cannot be resolved, still the lack of intensity at the position of the step results in the dark line commonly seen in LEEM images.

[10] Excitation and hence focal length of the objective are below the best focus, called "in–focus" condition.

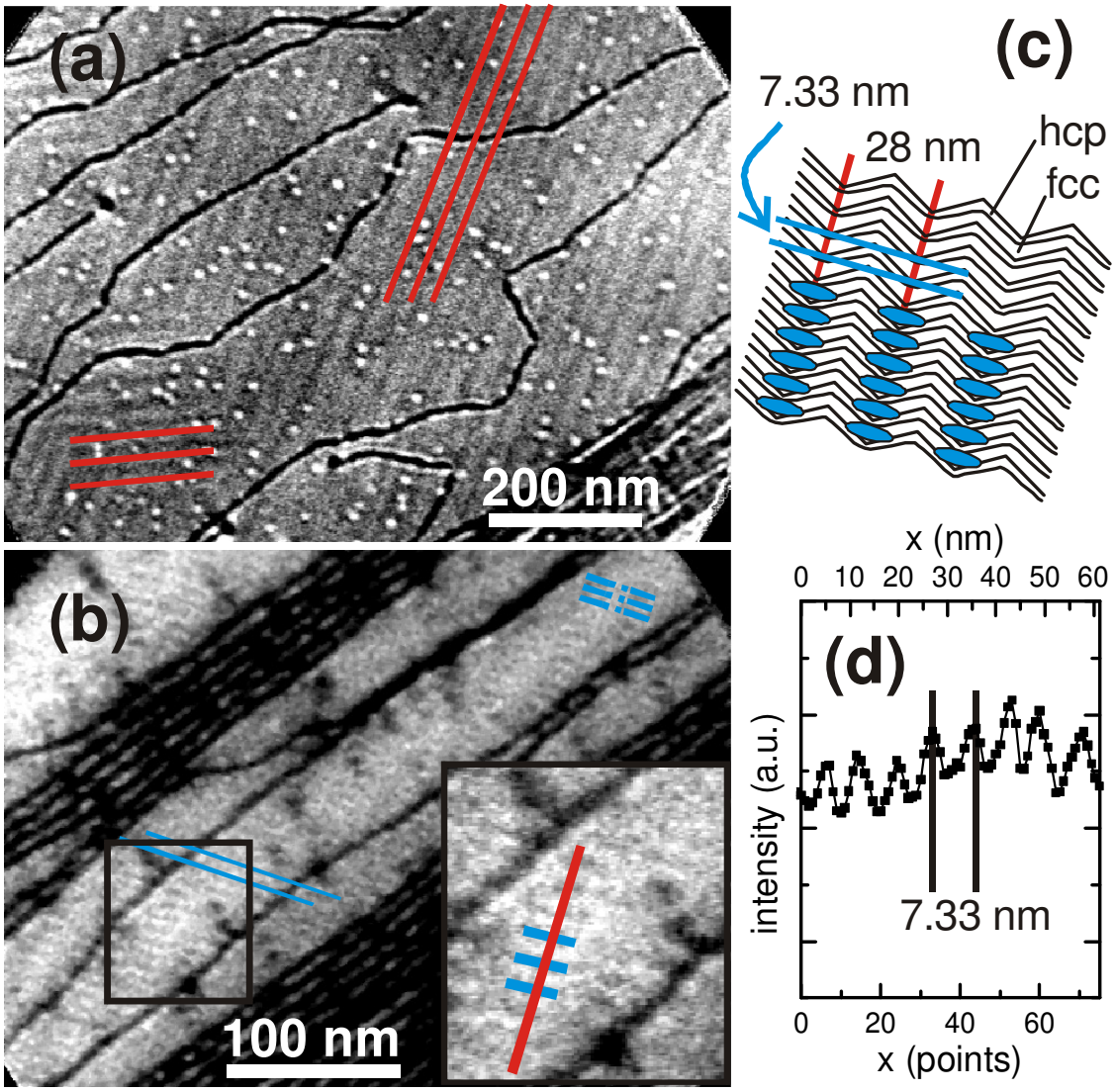

Figure 2.4: Colour online. Au(111) herringbone structure in LEEM: a) and b) are taken at $E_0 = 16\,\text{eV}$ and $15.3\,\text{eV}$, $t = 5\,\text{sec}$ and $0.6\,\text{sec}$, respectively, and at different magnification. A model for the contrast is given in c). d) displays a cross-section along the red line in the inset of b).

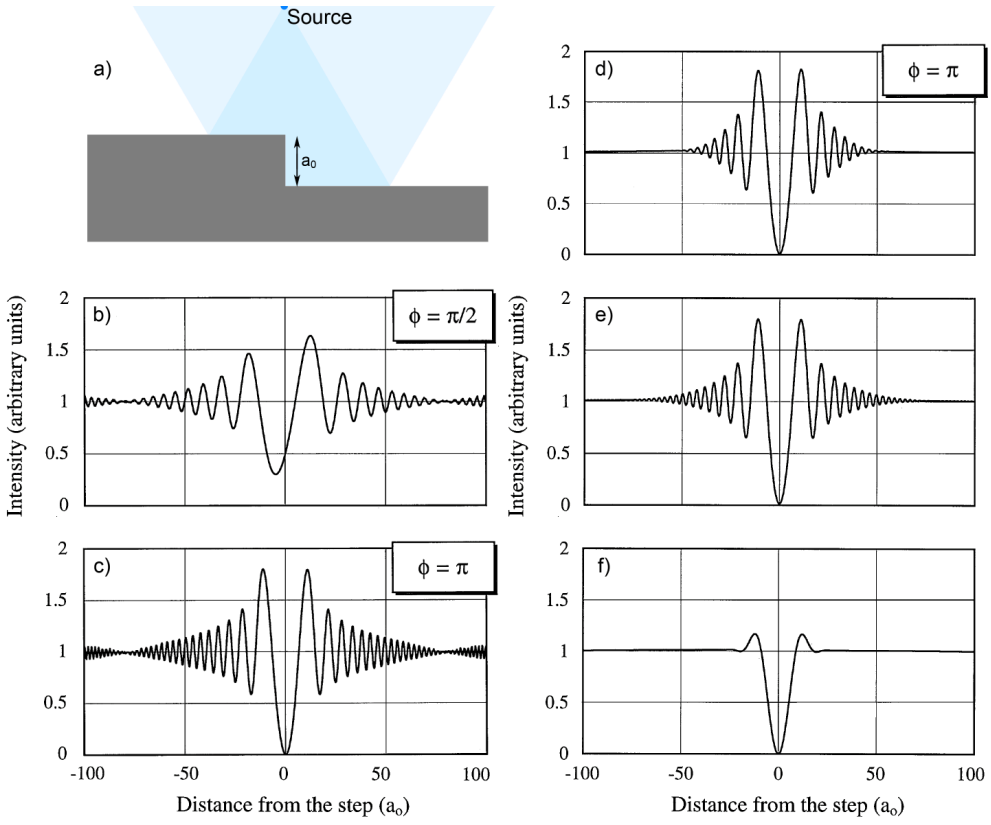

Figure 2.5: Colour online. LEEM step contrast. The model is shown in a) where a_0 is the hight of a monatomic step. For the diagrams the source was $1000\,a_0$ in front of the surface, the image plane $40\,a_0$ away from it. b) and c) show the step contrast calculated in underfocus for an ideal setup with indicated electron wave phase shift ϕ. Instrumental effects due to d) 0.5 eV source energy spread, e) $100\,a_0$ 20 fold source extension and f)an approximated lens aberration are shown. Adopted from Altman et. al. [51, 52]

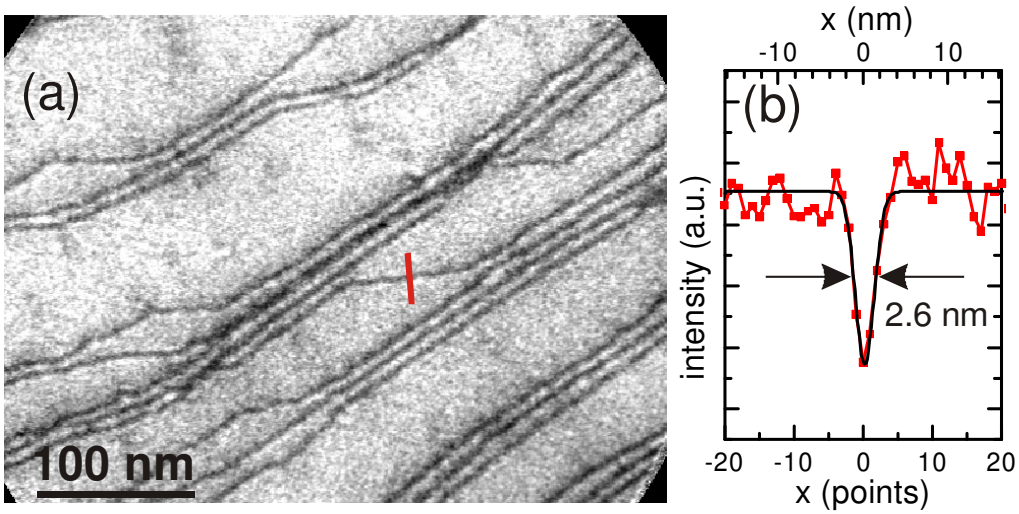

Figure 2.6: Colour online. Lateral resolution in LEEM. (a) shows atomic steps on a Au(111) surface, $E_0 = 15\,\text{eV}$, FoV: 415 nm x 307 nm, acquisition time $t = 1\,\text{sec}$. The Gaussian fit of the cross section through a step (red line in (a)) reveals a lateral resolution of 2.6 nm [2].

Presently best resolution in LEEM. The phase–contrast is commonly used to align the microscope prior to e.g. growth experiments on single crystalline surfaces. Furthermore with its help we were able to demonstrate the resolution record for LEEM–systems at a monatomic step of a Au(111) surface that is shown in figure 2.6. The full width at half maximum (FWHM) of the Gaussian fit to the red marked line–scan across a single step was found to be 2.6 nm. The best values, that were given so far were above 4 nm using a less strict criterion.
Special effort was taken to properly calibrate the length scale of the image. It was done using an intrinsic scale, namely the dimensions of the herringbone reconstruction of the Au(111) surface presented in figure 2.4, that was measured carefully in earlier STM studies to a very high accuracy.

Dark field imaging – structural contrast. Differences in the Bragg condition lead to differences in LEED. Therefore the selection of diffraction spots for imaging, that are specific for (super)structures, generates an image where only the corresponding structures appear bright and signal from other structures is suppressed.
It is simply done by cutting away the intensity, especially of the intense (00)–reflex, using the contrast aperture (fig. 2.1) which is located in an image of the BFP[11]. Thus a contrast is generated between domains with structural differences e.g. rotational

[11]The BFP is the plane one focal length behind (along the optical axis) the corresponding lens, which is usually the objective.

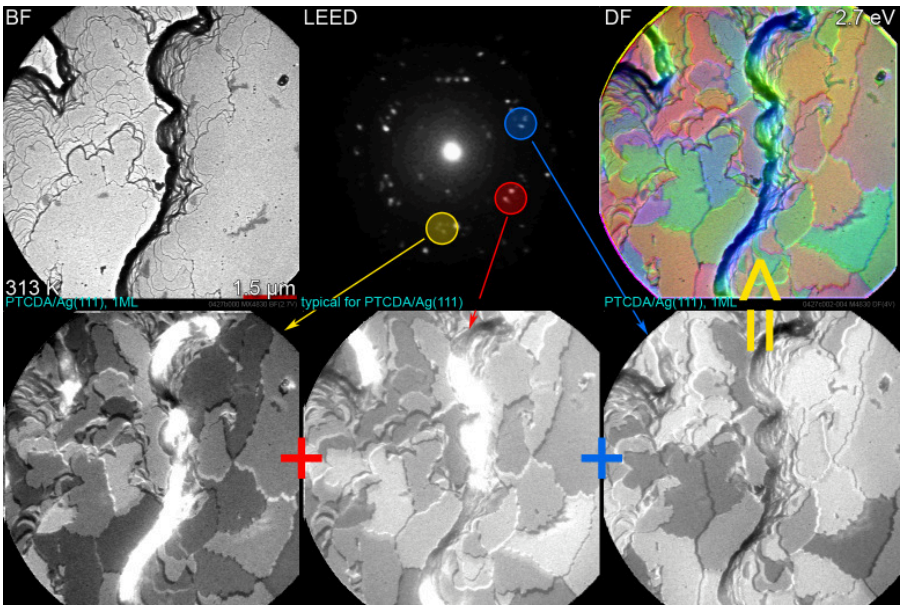

Figure 2.7: Colour online. LEEM DF imaging of 1 ML PTCDA/Ag(111) to distinguish rotational domains ($FoV \approx 6\,\mu m$). Top left is the BF image followed by a typical LEED. For the colour–coded DF image on the right the three bottom row images were put into the RGB–channels resulting in six colours corresponding to the six rotational domains of the thin film. The circles in the LEED pattern show schematically the spots that are selected by the contrast aperture for imaging.

domains, facets, crystal orientation. This mode is known as DF–mode, since the (00)–beam is typically blocked.

In figure 2.7 a series of images is plotted to clarify the difference between BF and DF and how even in case of "incomplete" DF different rotational domains can be identified. The top–left image in the figure shows the BF–image. Only step–phase contrast of steps and step bunches is visible, since the intensity in the (00)–beam is not different for any of the six possible rotational domains [5]. Although the diffraction spots of the single PTCDA herringbone structures were too narrow to be selected separately, it was possible to generate the three following different grey–scale images. For each of them the selection in the LEED–pattern was slightly different which results in the different intensities in the image. For the colour–coded, last image each of the three DF–images was placed in a separate RGB channel. In the resulting contrast each colour corresponds to one of the possible rotational domains. This procedure works well for flat surface areas without steps or step–bunches.

Contrast mechanisms in PEEM

Photo–emission electron microscopy (PEEM) is another important, among several ways to retrieve electrons from the sample surface, as the above introduced LEEM or, e.g., also the thermionic emission electron microscopy (TEEM).
PEEM is closely related to the AES based PEEM methods, as for example NEXAFS–PEEM [53] or x–ray magnetic circular dichroism (XMCD)/x–ray magnetic linear dichroism (XMLD)–PEEM [9], where the x–rays are tuned to excite electrons from a core level into an unoccupied state. In case of electron microscopy only the radiation free decay channels can be probed.
In our group Marchetto [17] and Groh [32] used NEXAFS–PEEM to determine the orientation of PTCDA– and 1,4,5,8–naphthalene–tetracarboxylic acid dianhydride (NTCDA)–molecules in the wetting layer in contrast to 3D–crystallites. The imaging of magnetic domains for example is extensively used at the neighbour beamline at BESSY–II by Kronast et al. using a commercial PEEM instrument.
The use of x–rays in general offers the advantage of an element or even chemical species specific probe. PEEM bases on the photo–ionization process. Typically one distinguishes between ultraviolet PEEM (UV–PEEM) and XPEEM where the UV indicates the ultra–violet and X the X–ray regime of the photon energies used for the studies. In the following their contrast mechanisms shall be introduced.

UV–PEEM. For the ultraviolet (UV) experiments a well focused, highly intense, high pressure Hg–short arc lamp from Oriel was used. Accordingly these studies are called Hg–PEEM. This source typically allows to emit electrons from the surface areas if the effective work function ϕ is below about 4.9 eV. This value is close to typical work functions of many materials (some are given in table 4.1) and especially for those used within this study, such as $\phi(Au(111)) = 5.3\,\text{eV}$, $\phi(Ag(111)) = 4.7\,\text{eV}$ [40] and $\phi(CdSe(100)) = 5.2\,\text{eV}$ [54].

Hence this method addresses the electrons in the valence band of the materials. Such Hg–PEEM allows to study local work function differences. They may be due to structural effects (e.g., step bunches, facets, and surface reconstructions) adsorbates that increase or reduce ϕ – as PTCDA does on Ag(111) or Au(111), respectively – or the field emission features with very small radii.

The low energy of probing radiation and the fact that the electrons pass only once the objective lens make UV–PEEM well suited for alignment issues, since the impact on the structures is very low and the path of electrons is comparatively simple. Furthermore this technique does not require extra energy filtering

because the energy window of the emitted electrons is very narrow – quasi band–pass filtered by the upper limit of the photon energy of 4.9 eV and ϕ as a lower limit.

XPEEM. The contrast in XPEEM is mainly based on the core photoemission lines, as in XPS. The contrast aperture reduces mainly the spherical aberrations (and also chromatic) as long as PED does not play a major role. As for the present XPEEM results no oscillations in the PED–pattern were observed PED effects are neglected. The lines are typically well separated, and thus a moderate energy slit of 1 eV was used to allow for high intensity and reasonably short (typically around 5 sec) acquisition times.

The XPEEM contrast between two adjacent areas i and j can be calculated using the definition of the MTF (eq. 2.11) and the total XPS–intensity (eq. 2.6), that results from the composition within these resolved and probed areas

$$MTF \propto I_0 T D \cdot \left(\sum_{Z_i} \sigma_{Z_i} L_Z c_{Z_i} - \sum_{Z_j} \sigma_Z L_{Z_j} c_{Z_j} \right) \tag{2.12}$$

I_0, T and D are the intensity of irradiation, the transmission of the instrument and the detection efficiency. Their product is equal for both areas i and j after proper flat field (FF)–correction (see cp. B.1) at the selected energy E_{kin}. σ_{Z_i} is the cross section for the photo ionisation process of element Z_i at the position i. L_Z is the asymmetry parameter[12] of the addressed line and c_{Z_i} is the signal contribution of element Z in the probed volume at position i.
Therefore the contrast depends on the difference between the composition ($\sum_Z$), the contribution of the elements to the signal ($\sigma \cdot L$), and the concentration and distribution (c) of elements in area i compared to the adjacent area j.

Typically photoemission lines are chosen, that are far enough separated that $\sum_Z$ vanishes because only one single line contributes to the signal. Further L is neglected as discussed earlier. Hence equation 2.12 simplifies and results with eq. 2.11 in

$$MTF = \frac{I_0 T D \cdot (\sigma_i c_i - \sigma_j L_j c_Z)}{I_0 T D \cdot (\sigma_i c_i + \sigma_j L_j c_Z)}. \tag{2.13}$$

Therefore the higher the total signal, the lower the detectable contrast. Vice versa a high minimal intensity requires a high dynamic range of the detector to visualise intensity differences.
Best contrast may usually be achieved if the two areas have a completely different composition, e.g., the holes in the α–Te cap (fig. 4.12) or the two different Se–species, i.e. α–Se and (Cd,Zn)Se (fig. 4.11). In this case the selection of element specific

[12] It is defined in equation 2.7.

E_{bin} with a $h\nu$ leading to high cross section $\sigma \cdot L$ is sufficient. The choice of E_{kin} is important for the contrast as well as for the definition of the proper surface sensitivity for thin film structures.
Also if the total amount of one element is very rare across the whole surface, this would lead to good contrast in XPEEM if it is locally accumulated. This is in contrast to normal XPS where the total signal would be rather low.
In many cases however the two areas do not differ much in composition. Therefore a careful choice of the energies as well as a good model of the stacking are required for the analysis.

To find the proper focus during alignment even a low contrast reversal (e.g., fig. 4.24) helps. Focussing is crucial and not considered in equations 2.11 to 2.12. It leads to intermixing of the two summands from adjacent areas. In some cases a trick to get close to the desired focus may be helpful B.1.1.
Since the BG in XPS stems from inelastic scattering of photoelectrons in the material its intensity is proportional to the intensity of the photoemission lines as well. Therefore one can even find contrast from differently composed areas at an energy where no line is present. The most prominent case is the imaging using the very intense secondary onset of the spectrum.

2.3 Synchrotron radiation source

The core level photoemission experiments were performed with soft x–rays delivered by the BESSY–II synchrotron radiation source. The brand new µ–focus, high flux–density beamline UE49PGMc at the SMART endstation was used.

2.3.1 BESSY II – Soft X–ray source UE49PGMc

The source (left hand side of figure 2.8) is an APPLE 2 type undulator with 49 mm lateral periodicity of the 64 magnet pairs. Within an energy range between 100 and 1500 eV it delivers average fluxes of 10^{13} to 10^{10} photons/s at ring currents from $I_{ring} = 150$ to 300 mA with $\delta E = 375$ to 8 meV energy spread. A longitudinal shift of the upper magnets relative to the lower allows to tune from linearly to circularly polarised light. For the present measurements only linearly horizontally polarised radiation was used.

Beamline UE49PGMc (fig. 2.8) has a plane grating monochromator (PGM) which was operated in the constant fixed focus (cff) mode. With a setting of *cff*=2.25 the photon energy spread was below 0.5 eV. This mode keeps especially the exit slit at a fixed position for all energies. Therefore the microscope position and the

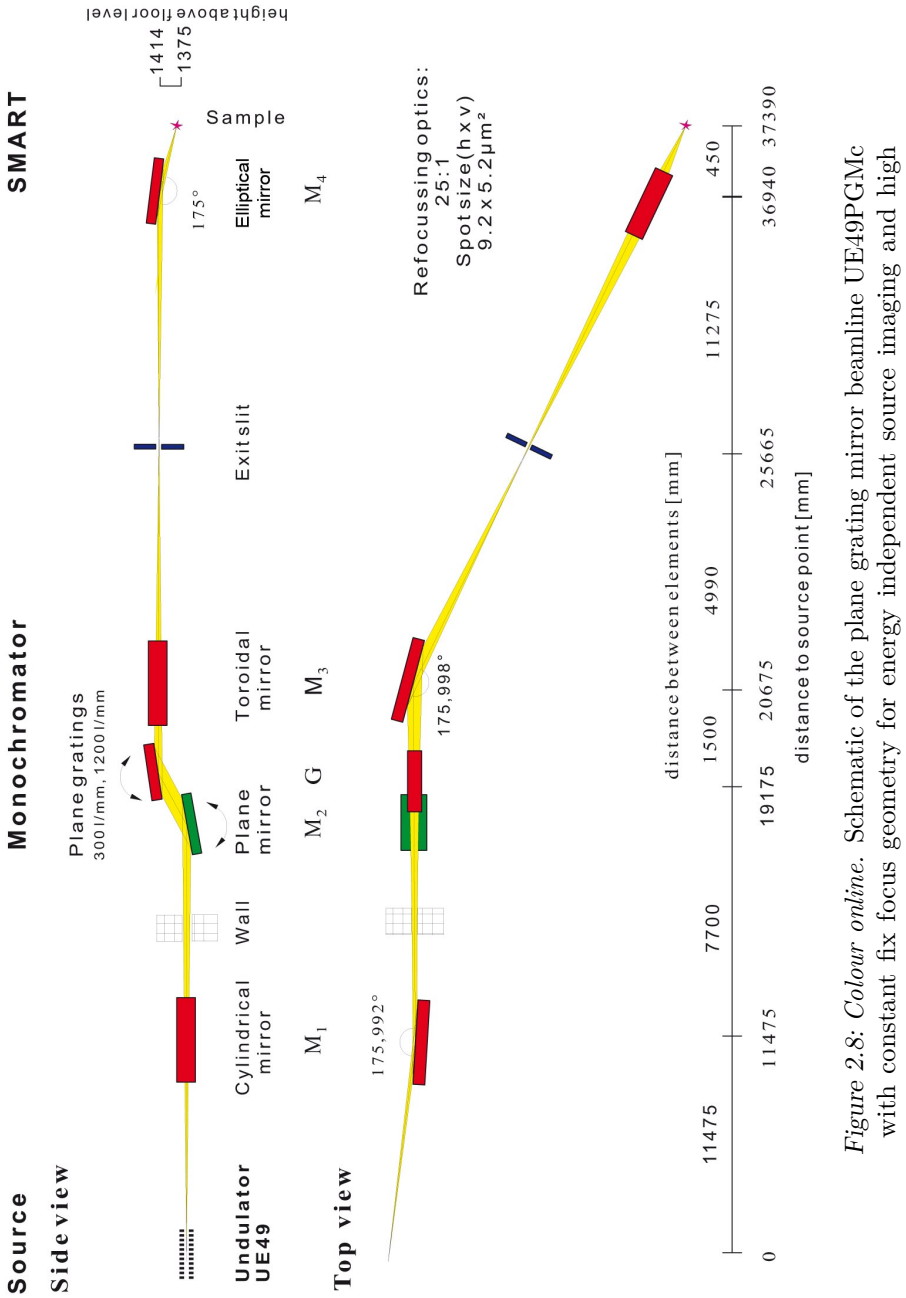

Figure 2.8: Colour online. Schematic of the plane grating mirror beamline UE49PGMc with constant fix focus geometry for energy independent source imaging and high flux–density. Depicted from [4].

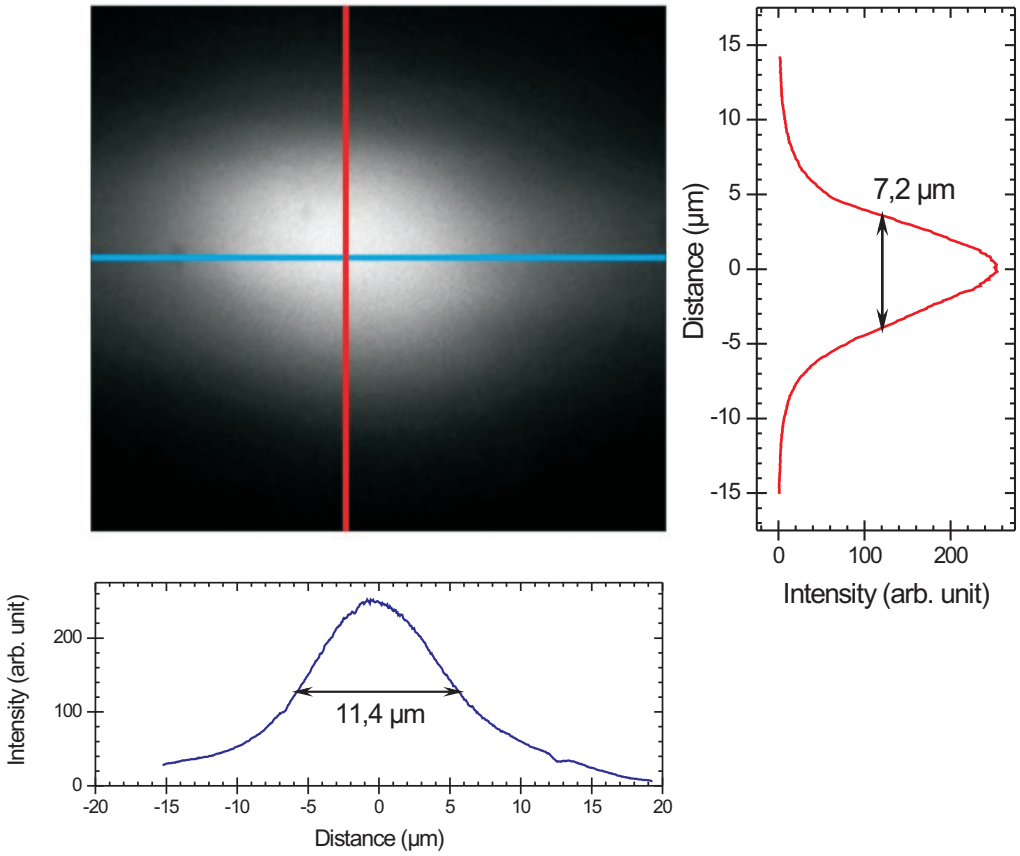

Figure 2.9: Colour online. Image of the optimised focus of the exit slit of the UE49PGMc beamline. Bottom and left profiles show the FWHM of the horizontal and vertical beam profile respectively.

refocussing mirror can be kept constant even during photon energy scans, since the radiation spot on the sample is a demagnified image of the beamline exit slit.

2.3.2 High flux–density by demagnified beam

The very high flux–densities necessary for nano–spectroscopy are achieved at beamline UE49PGMc by using an undulator, only few optical elements in the beam path and demagnification of the source resulting in a spot size of about 11 x 7 µm^2 on the probed area (fig. 2.9). For the last step the beam is focussed onto the sample by an elliptical mirror ($M4$ in fig. 2.8) mounted directly onto the SMART–frame to increase beam stability. Already the rough alignment was carefully done using synchrotron radiation from the zero–order diffraction, where radiation also in the visible range passes along the beam path. This enables an accurate positioning of the

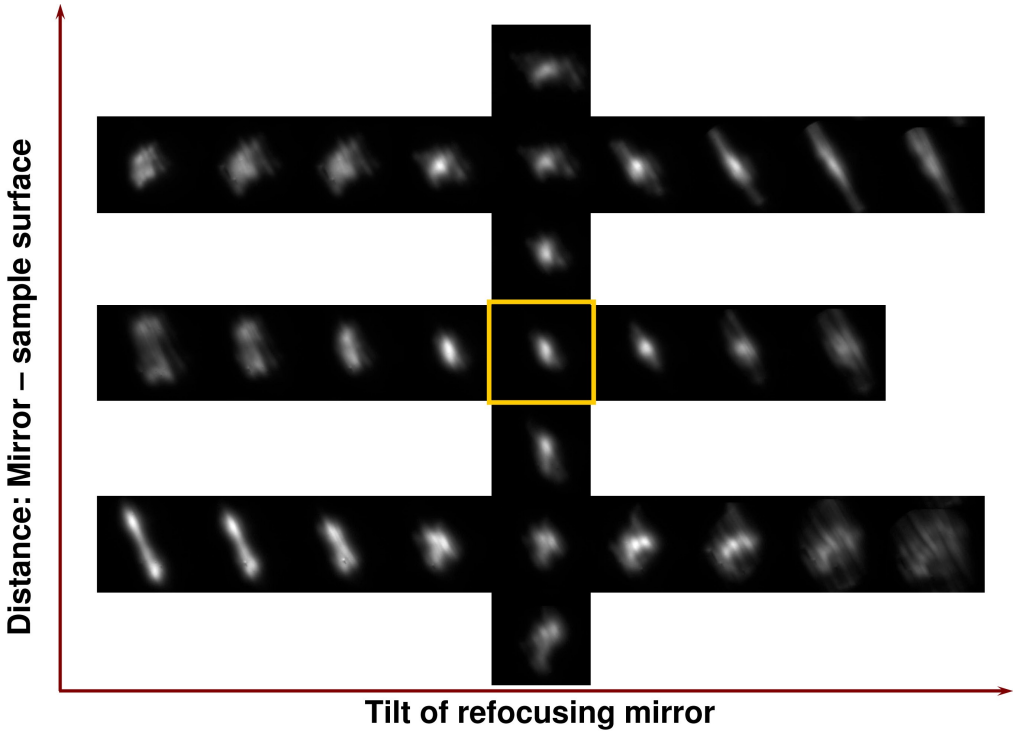

Figure 2.10: Colour online. Image series illustrating the high end alignment strategy for the X-ray refocussing mirror to find the best focus (centre).

beam within a few hundred µm, which is sufficient for the following high precision alignment. To focus and position the beam with micrometre accuracy, a test sample was used in life (25 fps[13]) operation of the microscope. By recording a series of images (fig. 2.10) the best focus condition was found.

2.3.3 Ultrahigh flux–density in 3D-space

While a high flux–density of the photons is required in the x–y–plane of the sample, it may cause problems if the pulse duration is too short (the volume too small), because there are hints that space charge reduces the lateral resolution (trajectory displacement) and maybe as well the energy resolution (Boersch–effect) in XPEEM and µ–XPS, respectively.
First with identical settings and sample we observed a better resolution in LEEM than in secondary electron PEEM although the total recorded intensities were comparable. Typical acquisition times in life–mode are about 40 ms.
Secondly, the energy resolution of SMART stays with 180 meV [17] behind the expectations of better than 100 meV.

[13]fps – frames per second.

In comparison, pulse durations at BESSY–II are typically below 30 ps. Normally 320 pulses are repeated within 800.5515 ns [55] – hence only about 1 % of the time photons arrive at the sample. But the intensity of the e–gun used for LEEM is continuous.
The time structure of the photon source is currently suspected to limit the resolution of the instrument in XPEEM and μ–XPS. Experiments to increase the pulse duration are scheduled for future beam times.

2.4 Atomic Force Microscopy

In contrast to directly imaging low energy electrons, the image in an AFM [57] is reconstructed by scanning a tiny tip across the sample surface while recording the Pauli repulsion for each pixel. The principle is shown in figure 2.11a. Ideally the tip consists of a single atom.
The tip at the very end of an oscillating cantilever (non contact or tapping mode) interacts with the atoms of the surface. The interaction strength influences the resonance frequency of the oscillator. A feed back loop, driven by the LASER–signal on a four sector diode, forces the cantilever into its adequate resonance. Thus the actual frequency shift is detected. The instrument also allows further operation modes, as, e.g., contact mode or uses other interactions, e.g., magnetic (with matched tip).
AFM measurements presented in this work were carried out on air using a diMultiMode V instrument by Veeco (see figure 2.11b,c) in tapping mode [56]. The maximum resolution was on the order of some 10 nm.

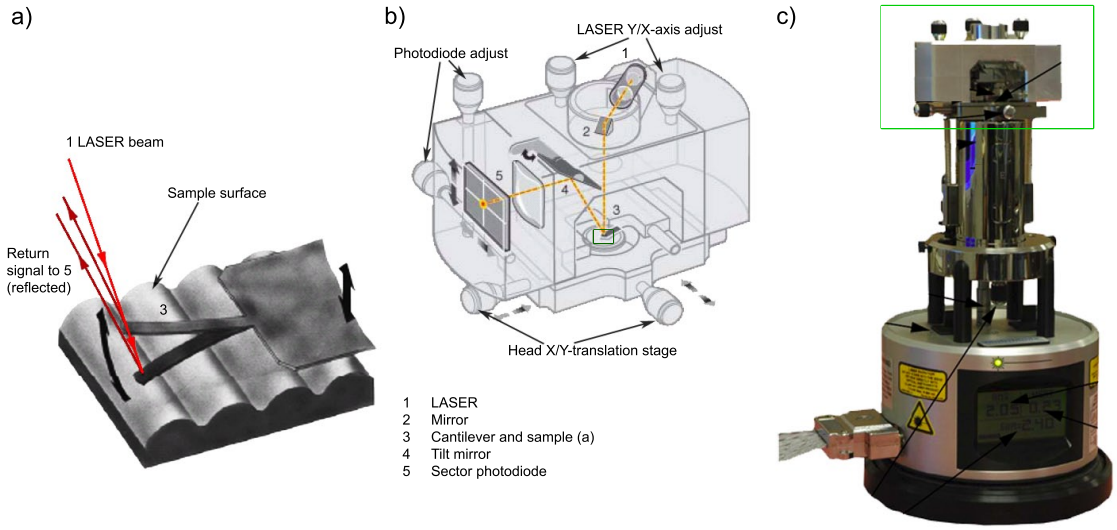

Figure 2.11: Colour online. Illustration of the diMultiMode V from Veeco. It was used as an Atomic Force Microscope AFM in tapping mode (a). This mode is contact free. The topography is detected by the frequency phase shift of the oscillating cantilever when approached to the surface. A schematic of the head is presented in (b) while (c) shows the whole instrument [56].

3

Low T growth of PTCDA/Ag(111)

In recent years the interest in organic thin films has increased since devices were developed that take advantage of the low cost of organic materials and make use of their properties. For example small organic molecules are used for a variety of electronic devices [58]. PTCDA, a well studied model system, is used, e.g., as hole–conductor in a tunable organic light emitting diode (OLED) [59] or acts as an exciton–diffusion barrier in organic photovoltaics (OPV) [60]. In these cases the electronic properties are of major interest and they are coupled to the geometric structure of the molecules and their arrangement at the interfaces. As another application one may think of organic (photo–)catalysts which hence raises the question of the surface structure and its morphology.
A large variety of investigations was performed on the flat, aromatic PTCDA molecules on different substrates [61] and in various thicknesses. Studies of the 3D structure of bulky PTCDA [62, 63] are reported, and the growth processes and the molecular orientation of thin films and multi–layer systems was investigated [12, 17, 64, 65]. The very first ML is studied concerning its geometrical [5, 11, 13, 66] and electronic [67] structure. Even the modification of the substrate surface during the growth of the 1^{st} layer was demonstrated [14, 15].

In this work specific questions are addressed to get a deeper insight and understanding of the manifold influences on the growth behaviour of organic–inorganic interfaces. This knowledge is essential if the homogeneity of the thin films was to be controlled. For this purpose the combined LEEM/LEED was applied to the growth of organics. This allows to study surface sensitive and in real–time the dynamics of the growth process and to characterise in–situ and laterally resolved the structure of the growing

layers [68].
In this way the influence of the substrate surface and of monatomic steps on the growth dynamics of the first and 2^{nd} layer was investigated, the different structural domains of the 2^{nd} layer were studied in detail and hence its greater complexity in terms of (uniaxial) growth modes, new phases and polymorphism was discovered. The 2^{nd} layer might be regarded as the "missing link" between the strongly substrate driven 1^{st} layer and the fully relaxed bulk system.

3.1 Introduction to PTCDA on Ag(111)

The two components, the planar, rectangular organic molecule PTCDA and the hexagonal Ag(111)–surface are well known and hence their basic properties are already described in various works, e.g., [12, 16, 61]. The crystallographic dimensions are summarised in table 3.1 and schematically shown in figure 3.1. The superstructure matrix of the commensurate 1^{st} layer of PTCDA on the Ag(111) surface, as derived by Glöckler et al. [5], is given as

$$\begin{pmatrix} b_1 \\ b_2 \end{pmatrix} = \begin{pmatrix} 6 & 1 \\ -3 & 5 \end{pmatrix} \begin{pmatrix} a_1 \\ a_2 \end{pmatrix} \tag{3.1}$$

The molecules arrange on this substrate flat lying [17] in a herring–bone structure [5]. For the bulk crystal two stacking polymorphs are known to date as α and β [63] phase.

3.1.1 Ag(111) specimen preparation

A Ag(111) single crystal with a miss–cut angle of less than 0.2° from the ideal orientation is used for the growth study. After mechanical and chemical polishing the specimen was cleaned in vacuum by repeated cycles of Argon ion sputtering at 600 eV and subsequent annealing at 750 K (heating rate about 20 K min^{-1}). Several sputtering/annealing cycles were performed prior to each deposition of PTCDA in order to recover a clean surface. This resulted in a clean (checked by XPS) and rather smooth surface. Its morphology (analysed in LEEM) consists of an alternating sequence of µm–wide, smooth areas (with few single atomic steps) and of rough areas with high step density and step bunches (>5 step bunches/µm^2). It was carefully verified that neither the high electric field at the sample nor the intense UV illumination effected the sample or the organic overlayer. Thus, neither radiation damage nor field effect influenced the present findings.

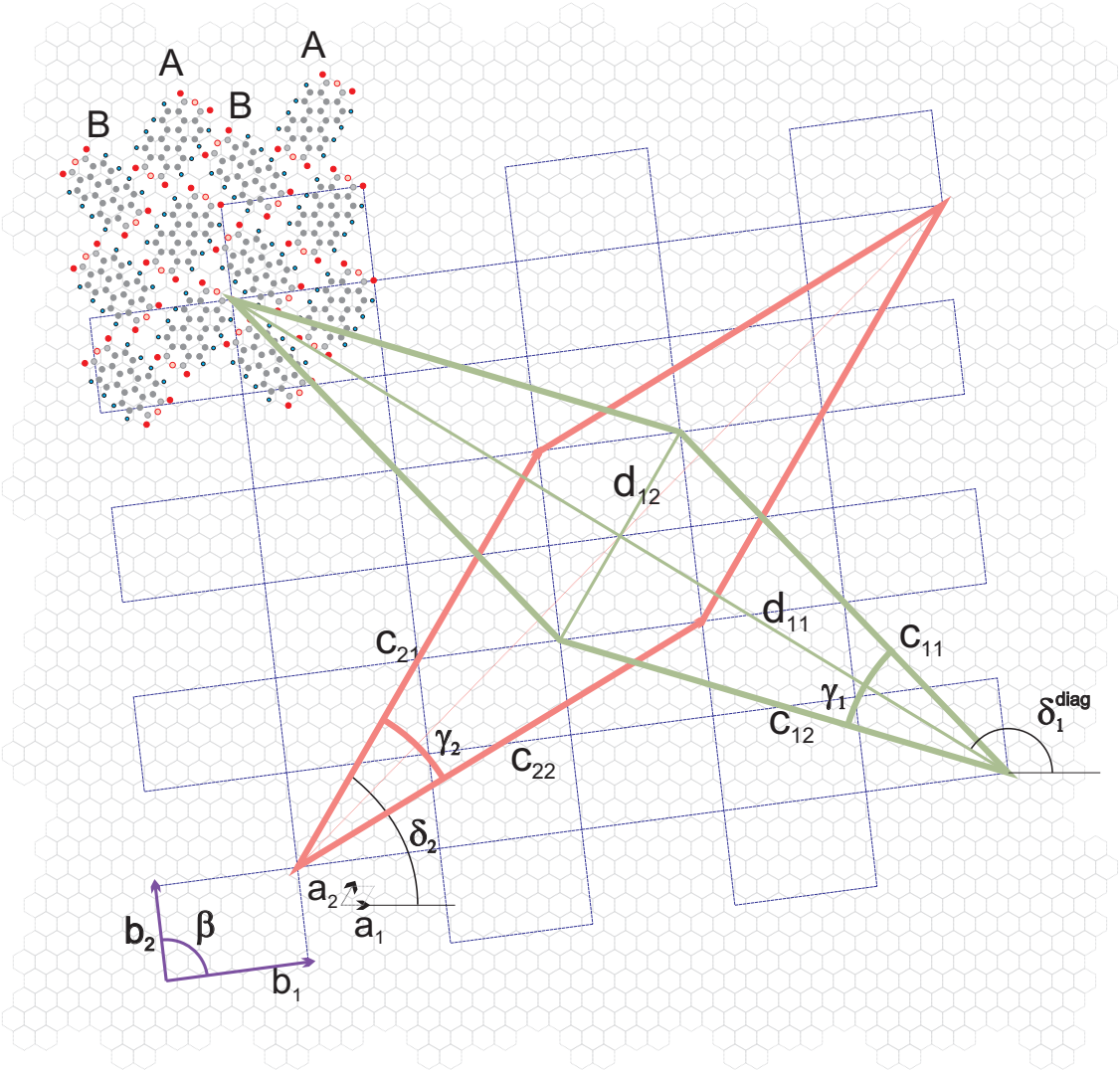

Figure 3.1: Schematic of the PTCDA super– and *super*^{2}structures on Ag(111) in real space. Grey hexagons correspond to the Ag(111) surface with lattice base vectors a_1 and a_2. The blue, nearly rectangular structure is the known PTCDA/Ag(111) herring–bone reconstruction [5]. Rose and green lines mark the two unit cells of possible ripple–phase structures that are discussed in detail in section 3.4. Their base vectors are c_{i1} and c_{i2}.

Table 3.1: Summary of the known parameters concerning the structure of PTCDA as bulk material and on Ag(111) surface. For comparison some data for PTCDA/Au(111) are given as well. The vectors that are parallel to the Ag(111)–plane, or rather the (102)–plane, are sketched in fig. 3.1. d is the interlayer distance, that is derived from geometrical transformation of the data of the bulk unit cell.

Substrate	**Modification Polymorph**	**Monoclinic bulk unit cell**				**in–(102)–plane unit cell**			
						b_1	b_2		
		a [nm]	**b** [nm]	**c** [nm]	β [°]	[010] [nm]	[$\bar{2}$01] [nm]	**d** [nm]	β [°]
Ag(111)	crystal [61, 69]	0.289			60	0.289		0.236	60
PTCDA	molecule [5]					1.42	0.92		
Bulk	α [62, 64]	0.374	1.196	1.734	98.8	1.991	1.196	0.322	90
Bulk	β [63, 70]	0.387	1.930	1.077	83.5	1.930	1.245	0.325	90
Ag(111)	α [58, 62]	0.372	1.196	1.734	98.8			0.322	
Ag(111)	β [63]	0.378(01)	1.930(03)	1.077(02)	83.6(1)	1.930	1.245	0.325	
Ag(111)	1^{st} layer [11, 66, 71, 72]					1.896	1.261	0.286	89
Au(111)	1^{st} layer [11]							0.327	

3.1.2 PTCDA growth conditions

For the in situ preparation of PTCDA films a Knudsen cell type evaporator was installed pointing towards the sample under a grazing incidence angle of 20° with respect to the sample surface. The organic material was cleaned before deposition by cycles of in–vacuum resublimation and was permanently kept at a stand–by temperature of 453 K. The deposition rate was ∼0.1 ML/min at 633 K in all experiments. This evaporator temperature is much lower than the 720 K used for an STM–study by Kraft et al. [67]. The rate was optimised for the recording speed available at the time of the experiments. A nominal coverage of one monolayer (1 ML) is defined as the deposited amount required to complete the first PTCDA layer on the Ag(111) surface at elevated temperature. At substrate temperatures below 350 K during deposition, desorption can be neglected. The specimen was radiation heated from its back side by a heated filament. The temperature was measured with a W–Re 26 %/5 % thermocouple with an absolute accuracy of about 10 K at 400 K and a relative accuracy of 1 K. During deposition the substrate temperature was kept constant within 1 K. The base pressure of the microscopy chamber was better than 3×10^{-10} mbar.

3.2 PTCDA growth mode transition

The growth of PTCDA/Ag(111) was studied extensively by many groups in the past [5, 13, 64, 73]. Previous studies by Kilian [72] and Marchetto et al. [17] showed a growth mode transition. At elevated T above room temperature (RT) the growth behaviour changed from quasi–layer–by–layer or Vollmer–Weber (VW) growth at 320 K via an unstable situation at 355 K — 3^{rd} layer decays when deposition is stopped — to Stranski–Krastanov (SK) growth mode. The latter is typically referred to in literature for the PTCDA/Ag(111) system.

3.2.1 PTCDA growth below RT

In the following the results from a study are presented where the sample was cooled by liquid $N_2(lq)$ down to 270 and 210 K (to provide thermal stability, the sample is usually kept well above RT). To keep T and position stable, first specimen and manipulator were cooled as low as possible (∼ 130 K). Then the cooling was detached to decouple vibrations. The sample was then back–heated (without change in T and thermal drift) with PID–control[1] making use of the heat sink provided by the cold manipulator setup. Thus, it was possible to measure for about 45 min. A

[1] Proportional–Integral–Differential (PID)

typical nominal growth rate was about 0.1 ML/min.
Unlike in the study of Marchetto who used Hg–PEEM, for the present measurements the growth was observed using LEEM in the BF–mode at 1.4 eV. Therefore the contrast in the images is different. Nevertheless it is possible to clearly distinguish between the layers using the interference contrast introduced in section 2.2.3.
Figure 3.2 shows two image series recorded during deposition at 210 K and 270 K. Every 3 sec an image with an acquisition time of 1 sec was recorded. On the left an overview is presented with a FoV≈ 6 µm at a nominal coverage of 0.96 ML. Monatomic steps and step bunches appear as dark lines due to diffraction (as, e.g., the large, central vertical step bunch). At 210 K this coverage leads to the coexistence of several open layers where as even the Ag(111) substrate is still visible. The simultaneous presence of substrate and several layers is very uncommon for PTCDA and in contrast to the behaviour that is seen at 270 K (lower part of the figure). In the latter case the 1^{st} layer first closes completely before the 2^{nd} layer starts to grow. Note that the yet uncovered Ag(111) (marked by 0) is not only more than 5 µm apart from the 2^{nd} layer–nucleus of PTCDA but they are also separated by a large step bunch. This distance is large compared to typical terrace sizes. In this case a terrace is meant as the area limited by step bunches, since those act as diffusion barriers [12].
The series of AoI on the right are depicted from the growth movies. Each image represents the state at increasing nominal coverage. The images on the top right have a lower contrast due to a change in focus and are therefore more fuzzy. Note the different coverage scales for the two series.
While in the 210 K series three different layers started although the 1^{st} layer was not yet completed — Ag(111) is still visible — at 270 K the expected layer–wise growth is observed up to even higher coverages. Moreover, in the low temperature case more condensation nuclei are seen although the clean Ag(111) surface had a lower monatomic step–density or rather higher quality (not shown).
Having a close look at the first series one can clearly see the 2^{nd} and 3^{rd} layer grow on the top–left 1^{st} layer–island marked with 1 (and later 3 as well) although the Ag–substrate is still visible. This can also be seen at the island right of the label 2.

3.2.2 Growth mode transitions

Monte Carlo simulations by Krause et al. [16, 74] already give a hint on this low temperature growth behaviour of the very first layers. Also Kilian et al. [72] report on open layer growth at low temperatures, studied by SPALEED. But to my knowledge this is the first direct observation, especially of a quasi–VW growth mode in a material system that typically shows a wetting of the substrate.
In figure 3.3 the results of the LEEM ($T < 300$ K) and PEEM ($T > 300$ K) [17]

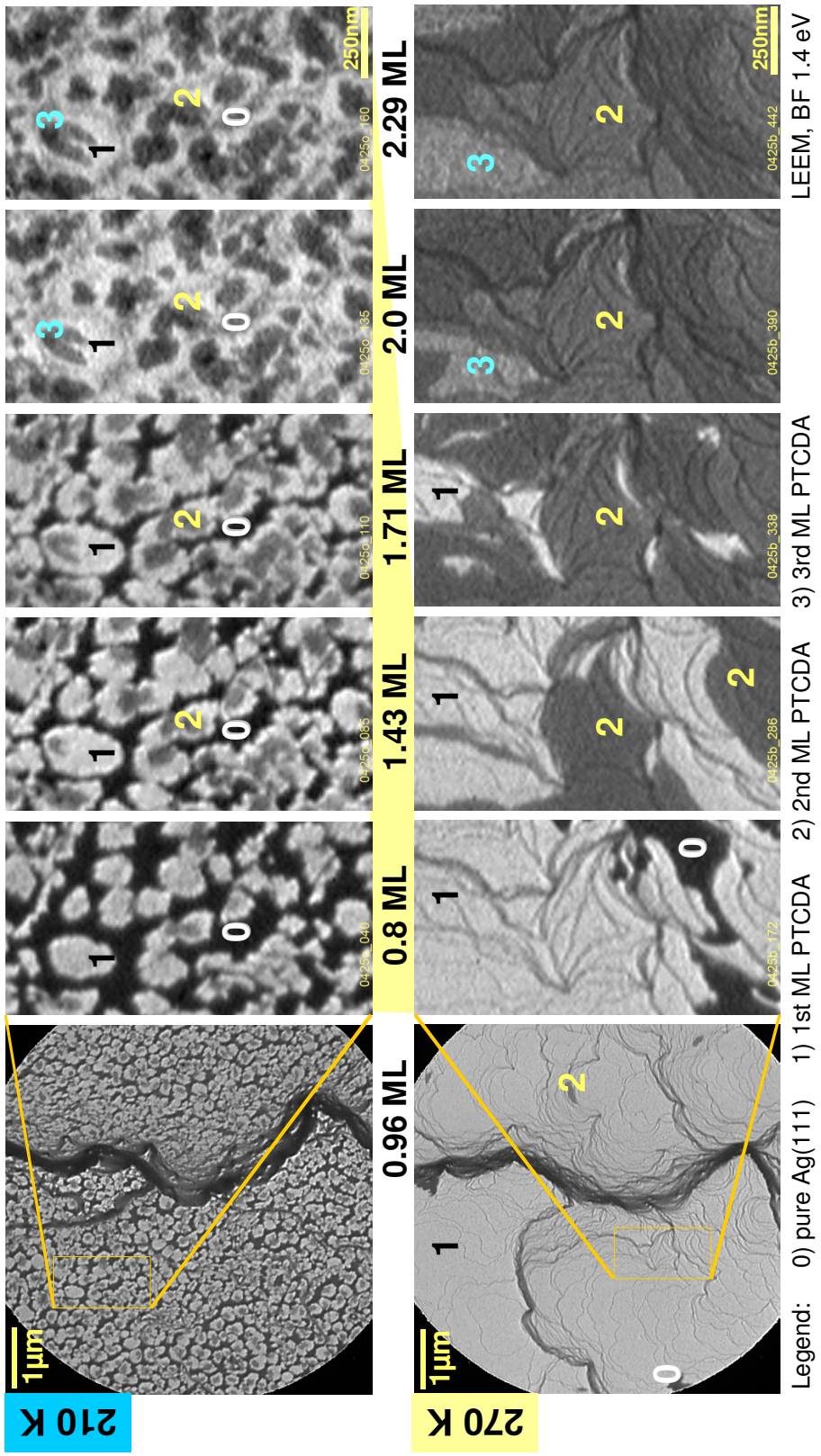

Figure 3.2: LEEM BF series at 1.4 eV show the PTCDA growth behaviour below RT at 210 and 270 K on a clean Ag(111) surface. Note the nominal coverage of the 210 K series ranges only up to 1.43 ML although the 3^{rd} layer already started. This can be seen very well at the terrace marked with 1 and 3. In contrast at 270 K the first two layers nearly fully close before the next one starts.

investigations are summarised. The nominal coverage is denoted below each image. Note the different lateral scales in the images. The contrast in LEEM compared to PEEM images is different simply due to the different sources. Simple layer schemes are given to illustrate the growth mode transition from quasi–VW(210 K) via a layer–by–layer kind of growth(270 K), called Frank–van der Merwe (FvM) growth, around 320 K to clear SK growth mode at 400 K with its intermediate mode of an unstable 3^{rd} layer around 355 K.
This demonstrates very well the complexity of surface processes that often can only hardly be accessed by integrative methods. More details are given in the following section 3.3 .

A rearrangement of the morphology of the PTCDA–film was observed during a heat ramp of $0.2\,\mathrm{K\,s^{-1}}$ from 243 K up to 445 K. The rough PTCDA layer grown at 210 K flattens and especially the 1^{st} layer remainders (figure 3.4) are nearly completely covered by additional material around 300 K. Note that the 1^{st} layer can easily be identified since in LEEM–BF at 1.4 eV it is a lot brighter than all other layers and the Ag(111) substrate as well.
The situation is quite heterogeneous in the following and not fully understood. However, it seems that at about 417 K the closed 2^{nd} layer starts to desorb and only about 33 % of the layer vanish within 180 s equivalent to 6 K. Another 6 K nothing happens before a contrast change in the 2^{nd} layer takes place during the following 4 K. Then suddenly, within only 0.4 K(two images or 12 s), the remaining 67 % of material from the presumable 2^{nd} layer vanishes and leaves the 1^{st} layer contrast behind which shows very slight contrast variations only (BF–image in fig. 3.4). Mainly domain boundaries are visible. This scenery remains for temperatures up to at least 480 K. The molecules are still intact, as an STM study [67] shows after annealing up to 550 K. The DF–image in fig. 3.4 shows the rotational domains and their boundaries. These domain boundaries are identical with the boundaries of the previously observed cells that had different desorption enthalpy.
The question on the origin of the difference of these 2^{nd} layer phases arises. At this point one can only speculate if they are arranged in the herringbone structure as well or if the low T growth enables also less favourable domains as, e.g., a brick–wall structure similar to the one observed for PTCDA/Ag(110) by Seidel et al. [24]. At least the remaining 1^{st} layer shows in DF the typical rotational domains of PTCDA (see fig. 3.4). Has the more stable of the two 2^{nd} layer a compressed–phase — which was observed for NTCDA/Ag(111) [75] — or is it kind of double layer arrangement? For a better understanding additional DF records of the 2^{nd} layer should give more insight. Additionally, UV–PEEM or IV–LEEM would allow to quantify the layer thicknesses leading to deeper insight into the rearrangement process during annealing. LEED might contribute to the exploration of the 2^{nd} layer–phases and allow to

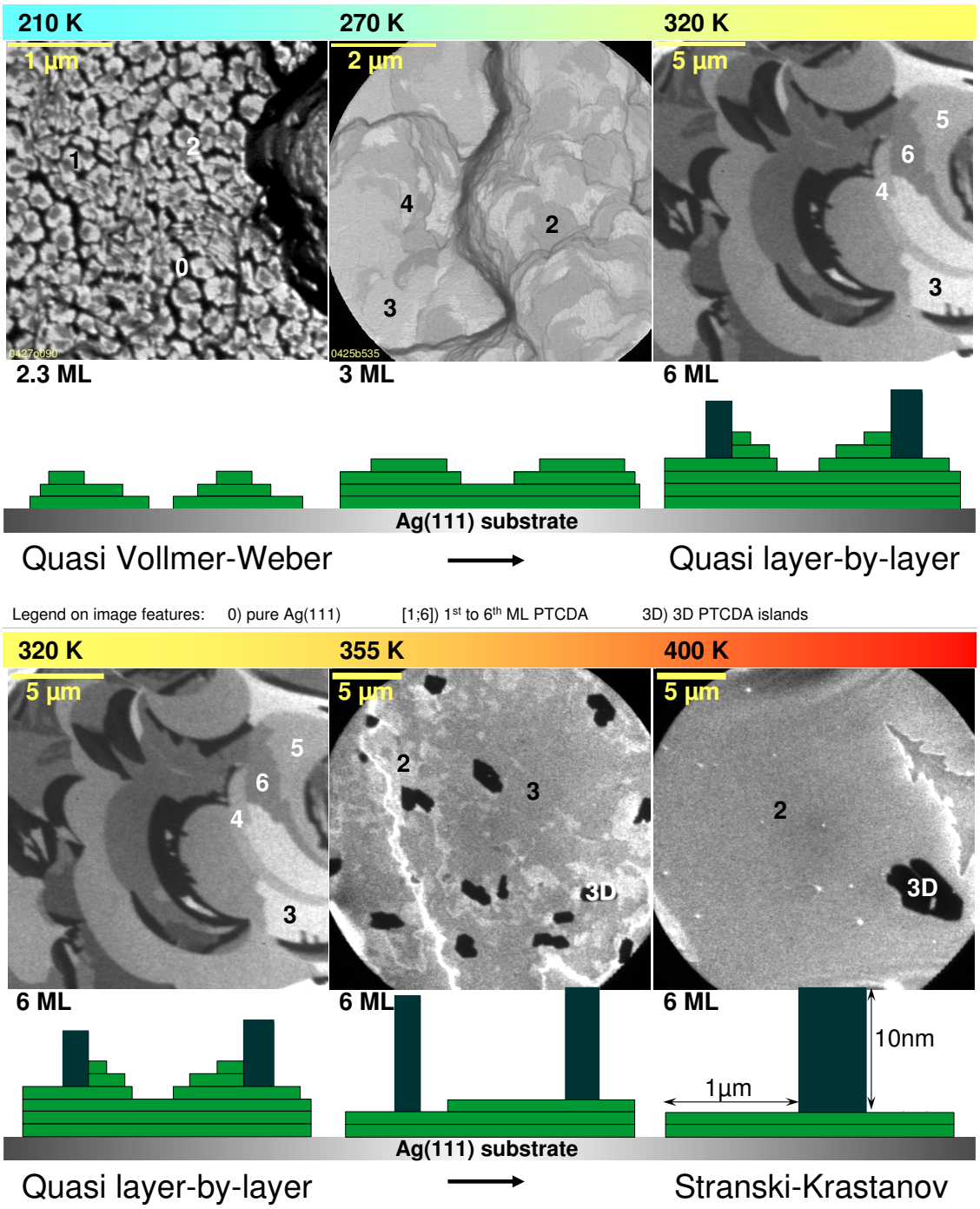

Figure 3.3: Overview of the temperature dependant growth of the first 2 to 6 layers of PTCDA(green) on Ag(111). Below RT, PTCDA starts in quasi–VW mode, switches to FvM around RT and transforms into SK at elevated temperatures [17]. Note the difference in lateral scales. The 320 K image is shown twice for better comparison. Nominal coverage is denoted below the images.

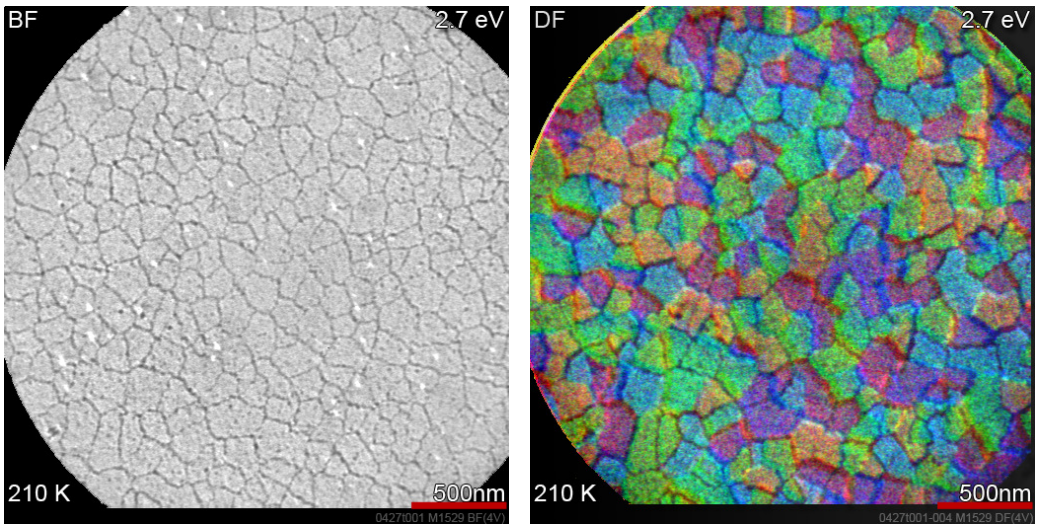

Figure 3.4: BF(left) and RGB composed DF image with superimposed BF image. The images show rotational domains of PTCDA, colour–coded by DF–imaging, in the remaining ML after desorption of the multilayer film. Dark lines result from BF imaging indicating domain boundaries and steps. The deposition temperature was 210 K while the records were taken at 445 K.

correlate them with, e.g., the ripple (see section 3.4) or similar phases. Unfortunately such data are not available and hence these highly interesting questions cannot be answered within this work.

3.3 Growth behaviour of the 1^{st} and 2^{nd} layer

The following investigation on the growth behaviour of the 1^{st} and 2^{nd} layer was carried out at 313 K. LEEM in BF–mode at 1.4 eV accompanied by DF–LEEM were used to study the influence of morphology, as monatomic steps and domain boundaries, as well as the terrace respectively domain size on the growth process. Snapshots from the image series recorded during the growth of the first two layers are presented in figure 3.5. These layers grow in a layer–by–layer fashion followed by a 2D–like multi–layer growth that is typical for this system [12, 76, 77]. Making use of temporal and lateral resolution and the capability to identify different structures separately for the different layers has enabled to enlighten the influence of the morphology and structures on the growth of single rotational domains. An astonishing difference in the growth behaviour between these first two layers was found, and an explanation is proposed.

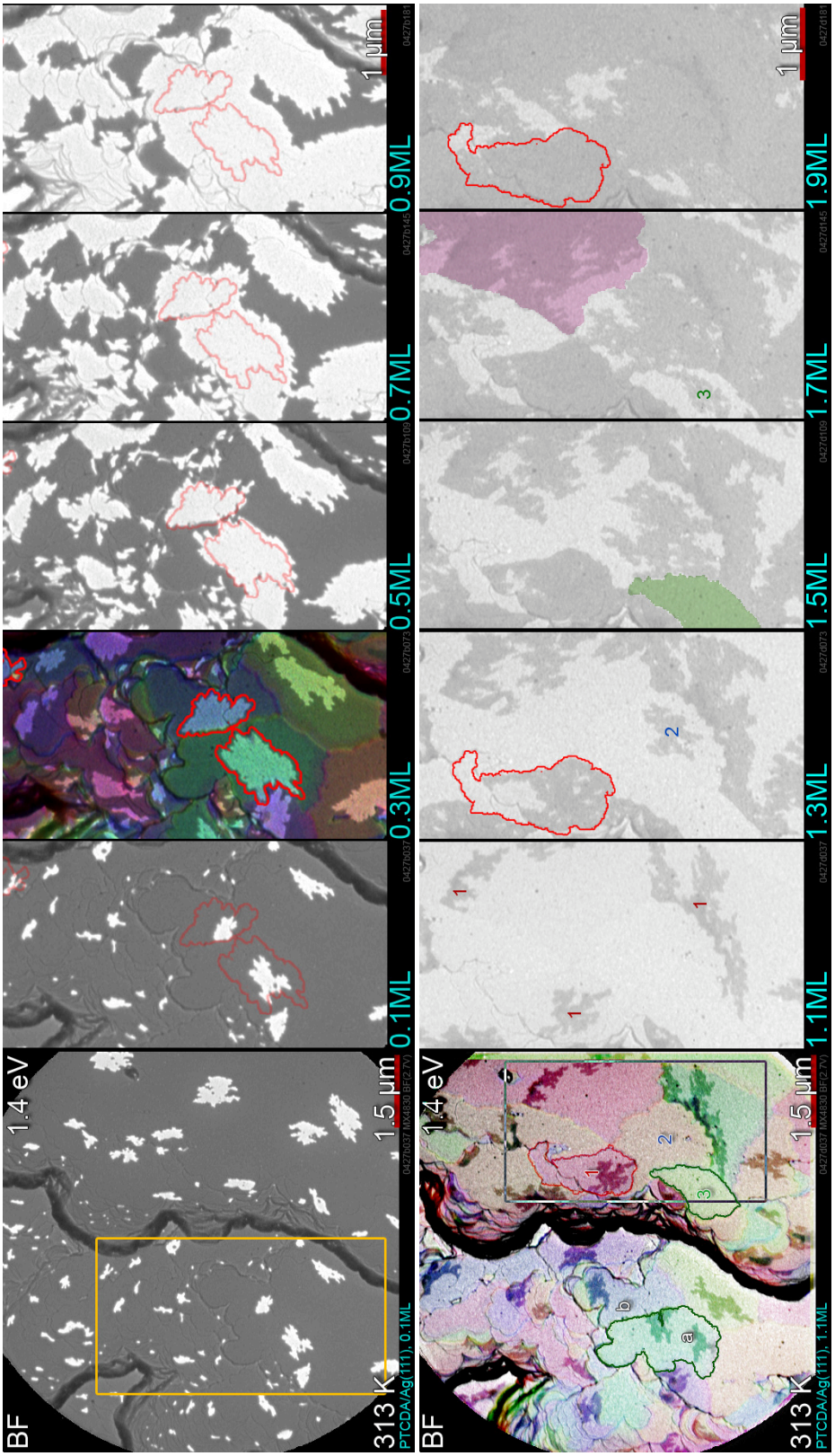

Figure 3.5: Snapshots from a BF image series acquired during growth of the 1^{st} layer (top) and 2^{nd} layer (bottom) of PTCDA/Ag(111) at 313 K. Coverage is 0.1 ML in the first image and increases by 0.2 ML for each of the follwoing. The 1^{st} layer DF–image from fig. 3.6 is superposed to the 3^{rd} and 7^{th} image, with 0.3 and 1.1 ML, respectively, to emphasise the crystallite boundaries in the 1^{st} layer. Contours of domains *a*, 1 and 3 are exemplarily derived from the same 1^{st} layer DF–image.

3.3.1 Substrate morphology determines 1^{st} layer growth

A BF–series of the growth from 0.1 to 0.9 ML is shown in the top row of figure 3.5. The grey scale of the images is kept constant for both rows. Superimposed to the 0.3 ML image is the DF–image shown in figure 3.6. In the first image of the series an overview over the full FoV is given showing PTCDA–domains (white) at $\theta = 0.1$ ML on the dark Ag(111) surface. Black lines indicate step bunches and even monatomic steps that separate adjacent Ag(111) terraces.

Rotational domains in the 1^{st} layer

Different rotational domains are differently coloured in the DF–images of fig. 3.6. The first row shows the rotational domains in the monolayer; below the situation in the 2^{nd} layer is shown — it will be discussed later. The colour code in both series is different.
Two DF–images are presented that are generated from two different sets of diffraction spot groups to ensure correct domain identification. As expected six colours according to the six rotational domains, as found by Glöckler et al. [5], can be seen in each image. Further colours and shadings at the domain boundaries as well as at step bunches are due to misalignment and have to be disregarded. The top, grey–scale BF–image (left) shows the clean Ag(111) surface for comparison. Step bunches and faint monatomic steps are seen as dark lines. On the right a huge about $3 \times 6\,\mu m^2$ single Ag(111) terrace is visible.
In general the rotational domains on adjacent Ag–terraces have different orientation (a and b in example). But there are also identical rotational domains on adjacent terraces. For example the large yellowish domain (below a and b, touching from the left the vertical step–bunch) is grown on top of two different Ag(111) terraces. In contrary the huge single Ag–terrace on the left is, besides others, divided into several different domains (e.g., 1, 2 & 3).

Terrace–resolved nucleation and growth

In the detail image representing a coverage θ of 0.1 ML in figure 3.5 at an initial stage of the ML growth, clearly PTCDA domains of different areas are seen. In agreement with Marchetto et al. [12], their size depends on the area of the underlying terrace. The present results stem from average terrace areas as small[2] as $0.026\,\mu m^2$ up to $2\,\mu m^2$.
Furthermore it was found that the **nucleation starts** in general at defect sites such as (monatomic) step edges or tiny dirt remainders on a terrace. More than

[2] $100\,px^2$— this is the lower limit to operate with a reasonable S/N–ratio.

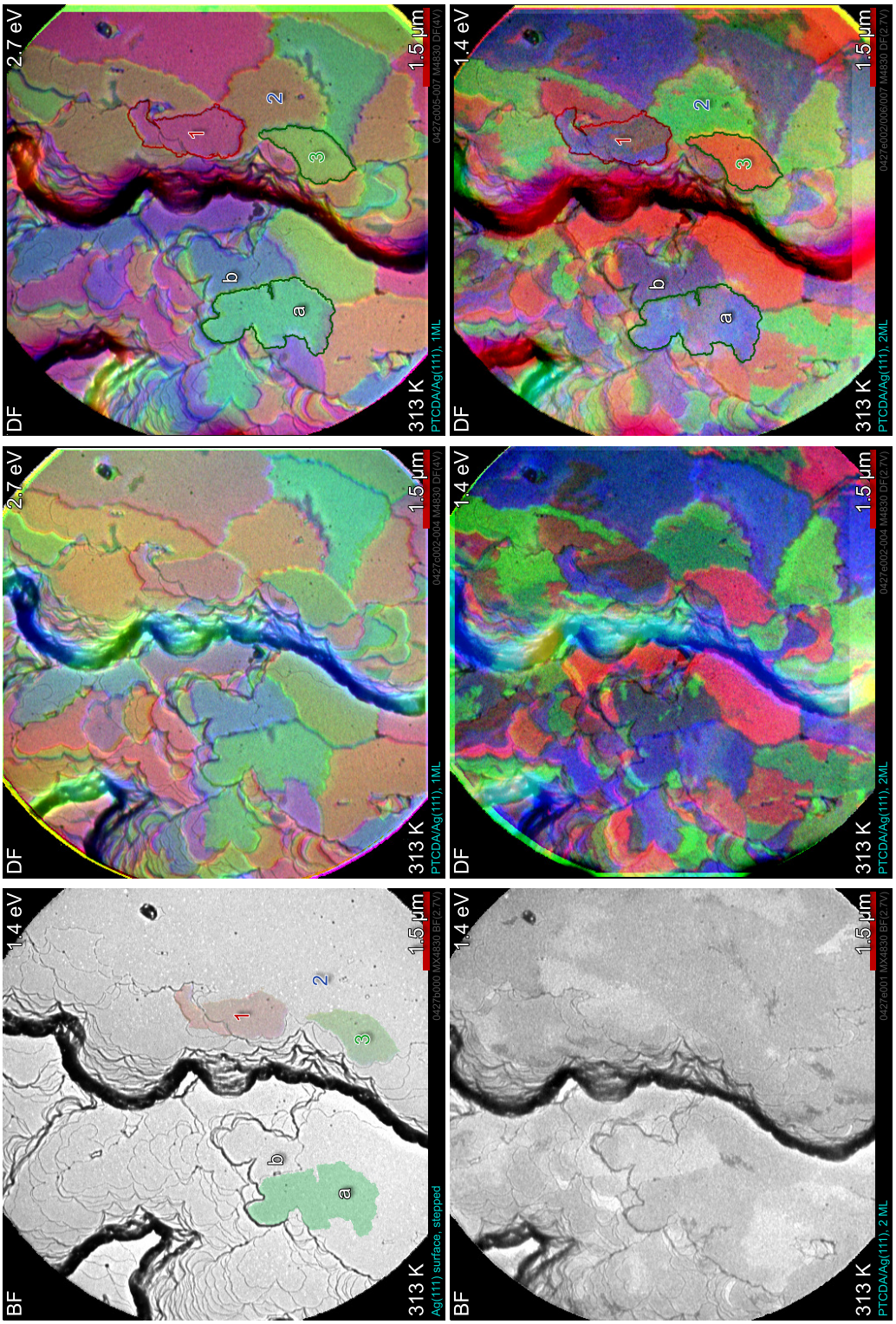

Figure 3.6: LEEM BF(grey–scale) and DF(coloured)–images at 1.4 and 2.7 eV (top–DF). The top left image shows the clean, stepped Ag(111) surface before deposition. It appears similar to the 1^{st} layer–BF–image(not shown). Besides that, the top row shows the rotational domain in the 1^{st} layer while in the second row the 2^{nd} layer is presented. Labels indicate domains already shown in figure 3.5. Adjacent DF–images show the same contrast. They differ only in the LEED–spot group they are recovered from — the pairs of images were generated from symmetric spot groups on the opposite side of the (00)–spot.

one nucleus on a single terrace was found for average diameters larger than about $\varnothing \approx 1\,\mu m$, only — for example on the huge terrace on the right and on the large terrace on which a grows.

The development of the coverage in time for selected terraces of different area is plotted in figure 3.7. Both, the image series and the plot indicate that all domains start at the same time within 0.1 ML nominal coverage. No delayed nuclei are found. Independent of the terrace area A, their local coverage θ by overgrowing domains is always identical. In other words the coverage rate $d\theta/dt$ does not depend on the terrace area. This is summarised in the following equations

$$\begin{aligned} \theta &\equiv \frac{\Delta A}{A} \\ \frac{d\Delta A}{dt} &\propto A \\ \frac{d\theta}{dt} = \frac{1}{A}\frac{d\Delta A}{dt} &= constant \end{aligned} \tag{3.2}$$

where ΔA is the total area of one specific covered area and hence $d\Delta A/dt$ is the growth rate of a single domain.
Domains grow in all directions until they touch each other. Further on only the gaps in 1^{st} layer are filled — the 2^{nd} layer starts not until the 1^{st} layer is about closed. Right before completion of the 1^{st} layer in the whole FoV, tiny domains as #4 (in the left plot of 3.7) show an increased coverage rate.

Having a look once more on the 0.3 ML–image in 3.5 with the superimposed **rotational domains**, one finds that neighboured nuclei lead to different rotational domains — even on the same terrace. Moreover in the domains outlined in red (later referred to as a and b) one finds that domains originating from the identical nucleus (but growing on adjacent terraces) have the same rotational orientation. That means, the rotational orientation of the nucleus determines the structure of all domains that start there.

Summary of findings on monolayer growth

The Ag(111) terraces are independent units for the growth of monolayer domains. Only on terraces larger than $\varnothing > 1\,\mu m$ several nuclei form at 313 K. Domains from independent nuclei have in general randomly chosen rotational structures. Domains on adjacent terraces have identical structure if they stem from the same nucleus. And finally overgrowth of monatomic steps is not observed.

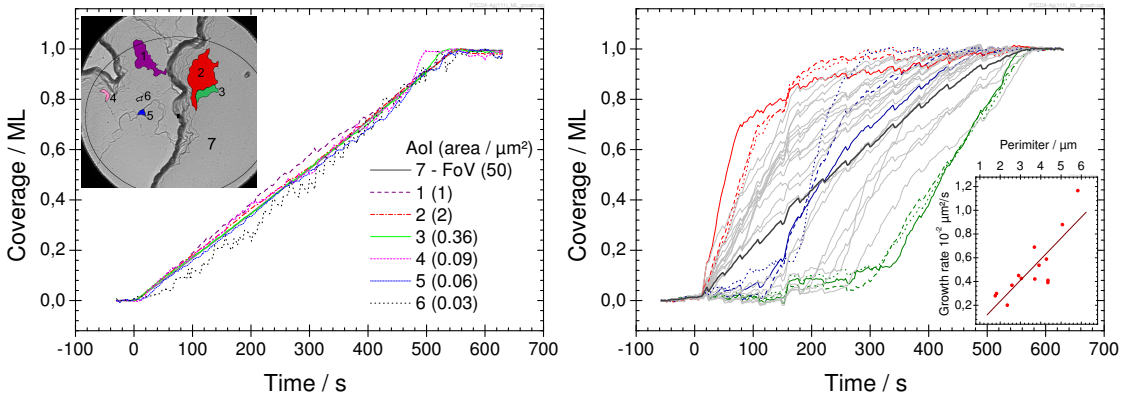

Figure 3.7: Change of the PTCDA coverage as a function of time (zero indicates the beginning of the layer) for the first and second layer.
On the left, the coverage of pure Ag(111) by the monolayer is shown. It was determined for the terraces (1–7) of different sizes (number in brackets; labels in the inset).
The evolution of coverage of monolayer–domains by the 2^{nd} layer is plotted on the right. Three growth regimes are identified and marked with red, blue and green (grey symbolises intermediate stages). The inset correlates the growth rate with the perimeter of the 1^{st} layer–domains.

3.3.2 2^{nd} layer– growth limitations, shape and kind

From an integrative point of view the 2^{nd} layer also grows in a layer–by–layer fashion, as already reported by others [16, 77]. But on the nano–scale the growth of the 2^{nd} layer differs to that of the first on some respects which are presented and discussed in the following.
The growth of 2^{nd} layer and its rotational domains are shown in figures 3.5 and 3.6, respectively. The data concerning the 2^{nd} layer are found in the second row. A general description of the figures and image–contrast is given in the previous section 3.3.1.

2^{nd} layer rotational domains

The second row of figure 3.6 shows the 2^{nd} layer in BF followed by the two variants of coloured images with rotational domain contrast. Keep in mind that only homogeneous, large domains can be taken into account; one has to be especially careful with the structural interpretation of the colours at boundaries and step bunches.
Already the BF–image shows some week contrast that might be due to interference at differently stacked layers or simply imperfect alignment of the microscope, i.e. non–normal incidence of the electron beam or non–centric position of the contrast aperture. The tiny bits of dark grey are the starting of the 3^{rd} layer. At first

glance the 2^{nd} layer–DF–images show basically the same domains as observed for the 1^{st} layer above. A boundary in the 1^{st} layer is also a boundary in the 2^{nd} layer. This is not true the other way round.
But the images appear less well sorted. This reflects the more complex situation in this case namely that some $_2$domains[3] share the same underlying $_1$domain (a domain in the 1^{st} layer). An example is domain#1 with the red outline. Yet, it seems that often a preferred 2^{nd} layer structure grows on a specific $_1$domain, e.g. the orange 1^{st} layer (#2 and others) is often covered by a green 2^{nd} layer. It is likely that both have the same orientation, but since the exact selection of spots in the LEED–pattern is not available, it cannot be assured. But this finding is not exclusive and one observes both, different $_2$domains on the same $_1$domain (e.g. #1) and vice versa (#1 and #b).
In summary three observations were made: (i) PTCDA in general grows in the known rotational domains (ii) $_1$domain–boundaries are preserved and (iii) a single $_1$domain can carry several $_2$domains. Alternatively the $_2$domain changes the structure of the underlying $_1$domain.

Nucleation of the 2^{nd} layer

First it has to be mentioned that the initially formed 2^{nd} layer is not stable, as observed when interrupting the deposition. As long as there are still gaps in the 1^{st} layer, the freshly formed 2^{nd} layer decays and fills up the gaps.
When the growth was continued, as presented in figure 3.5 (row 2), image of 1.1 ML shows that the $_2$domains have no preferential nucleation sites as e.g. steps, boundaries or specific rotational domains — i.e. domain #1, #a or #b. The nucleation density is with 42 nuclei/FoV much smaller than for the 1^{st} layer where 133 nuclei/FoV were found. Furthermore the nuclei are homogeneously spread across the FoV hence the nucleation density does not depend significantly on the surface roughness in contrast to the 1^{st} layer nucleation.

Three different growth regimes

The microscopic view on the coverage basically reveals three different growth regimes. The coverage $\theta(t)$ of differently sized underlying $_1$domains by 2^{nd} layer domains is plotted in the right of diagram 3.7. The black line corresponds to the average coverage in the whole FoV. The ripples in the curves with about 1 min period are analysis artifacts (due to low contrast in the 2^{nd} layer), the step around 2.5 min is due to rescaling.

[3] Abbreviation for (rotational) domains of the 2^{nd} layer molecular film, $_1$domains refer to the same in the monolayer.

The three regimes, marked with red, blue and green, differ in starting time and coverage rate. The slope of the black line (growth rate of the full FoV) starts to decline around 400 s when the 3^{rd} layer started to grow simultaneously.

1^{st} (red) regime: The growth in this regime (domains labelled with #1 in figures 3.5, 3.6) starts with no preference for the underlying crystallite size or orientation. This is also true for the regimes #2 and #3. In the growth series in fig. 3.5 one observes especially in this regime that the $_2$domains grow in a more dendritic/fractal way than the $_1$domains on the Ag–substrate. Even holes, well visible in the #1 labelled domains, are created when its perimeter closes at the boundaries of the underlying crystallite.
The inset in diagram 3.7 shows that the initial growth rate $d\delta A/dt$ is proportional to the perimeter of the underlying 1^{st} layer crystallite rather than dependent on its size.

2^{nd} (blue) regime: Domain #2 represents this type and is labelled in the 1.3 ML image of the growth series (fig. 3.5). These domains nucleate about 1.5 min or 0.2 ML after the 1^{st}–regime. At that time the perimeters of about half of the neighbouring domains are completed and hence only their central gaps are filled in the following. This clearly shows that molecules may diffuse across $_1$domain boundaries while an overgrowth with a $_2$domain across the same boundary is impossible.

3^{rd} (green) regime: When the $_2$domains nucleate (e.g., #3) typically their perimeter is already fully closed by other $_2$domains. Since the 3^{rd} layer has not yet started at a coverage around 1.7 ML this demonstrates once more the macroscopically gained image that downward diffusion is preferred and therefore layer–by–layer growth is observed. It is also a hint for extended molecular surface diffusion on the 2^{nd} layer.

Summary of findings on 2^{nd} layer growth

The microscopic picture showed large differences in the growth kinetics compared to the integral studies that resulted in simple layer–by–layer growth. The 2^{nd} layer nucleation density was about 1/3 compared to the 1^{st} layer on Ag(111). Also in contrast to the first layer the nucleation occurred pretty homogeneously and was at most weakly affected by the substrate morphology. The $_2$domains grew more dendritically than those of the 1^{st} layer. Three growth regimes were observed in terms of nucleation time and coverage rate that depends on the perimeters of

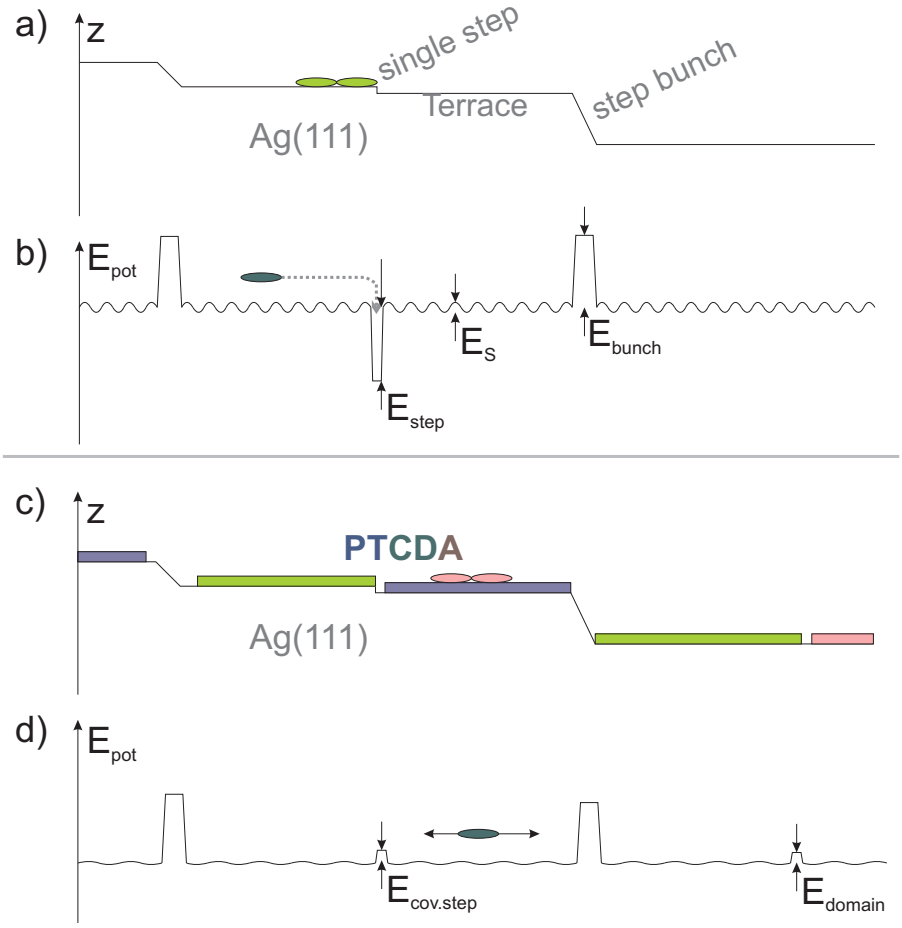

Figure 3.8: Schematics summarising the surface topography and potentials for the growth of the 1^{st} layer on Ag(111) (a) and b)) and of the 2^{nd} layer on 1 ML/Ag(111) (c) and d)). Different colours in the PTCDA–layers in c) symbolise different rotational domains.

the crystallites and their environment. 1^{st} layer crystallite boundaries persist as boundaries of the $_2$domains as well. There are preferred stacking sequences for succeeding rotational domains but also several structural contrasts are found on the identical $_1$domain.

3.3.3 Interpretation

The overall picture that allowed to explain all the described findings concerning the growth kinetics of the first two layers is summarised in the schematics of fig. 3.8. The surface topography and potentials are given for the growth of the monolayer on Ag(111) (a) and b)) and of the 2^{nd} layer on 1 ML/Ag(111) (c) and d)). Further details on morphological findings are summarised.

Morphology determined 1^{st} layer growth

The terrace size limit for multi–nuclei formation is attributed to T–dependant diffusion lengths. This was described earlier by our group [12]. Such behaviour is observed as well for 210 K and 270 K (see above 3.2) and expected for diffusion processes.
The terrace size–independent coverage rate $d\theta/dt$ (see also eqn. 3.2) and equal nucleation times lead to the conclusion that molecules do not interdiffuse between terraces and hence monatomic steps act as diffusion barriers. The temperature, that is required for molecules to overcome the barrier of monatomic steps E_{step} hence lies between 313 K and 340 K. For the latter Marchetto [17] stated, that mainly step bunches act as barriers. Since nucleation is preferentially observed at kinks and step–sites a drain–like behaviour is proposed. This is in contrast to facet–like step bunches where typically no nucleation is found.
The integral picture (e.g., [16, 77]) is confirmed as the linear rise in coverage demonstrates again the dominating downward diffusion of adsorbed molecules. It was shown for the monolayer that this average behaviour even holds for single terraces. Because steps are barriers in the 1^{st} layer the structure of adjacent domains is only by a chance of 1/6 identical. Only if they origin from identical nuclei they form one large rotational domain across steps.

2^{nd} layer — interplay of diffusion and growth limitations

In contrast to the growth of the monolayer, the second layer does show a much more complex picture than what is known from laterally averaging measurements.
First, the nucleation density in 2^{nd} layer is just 1/3 of that of the monolayer with corresponding average island areas. And second, the influence of the substrate morphology on the nucleation density or domain sizes is reduced. Hence the step barrier E_{step} know from the monolayer is absent or at least reduced. Taking into account that the nucleation sites are quite independent of the morphology it appears that the wetted steps act more as weak barriers than as drains.

Another issue is the shape of the 2^{nd} layer islands in the 1^{st} growth regime. It is found to be more dendritic than that of the monolayer islands. An audacious comparison relates this finding to the Mont–Carlo simulations of Ratsch et al. [78]. They resulted in the same, yet more pronounced, two island shapes as found, i.e. for PTCDA on Ag(111) and PTCDA on PTCDA/Ag(111). In figure 3.9 typical island shapes determined by the Monte–Carlo simulations (left) are compared to the findings in the PTCDA/Ag(111) system (right). The model prohibits desorption of atoms from the surface but allows aggregated atoms to detach from islands. The

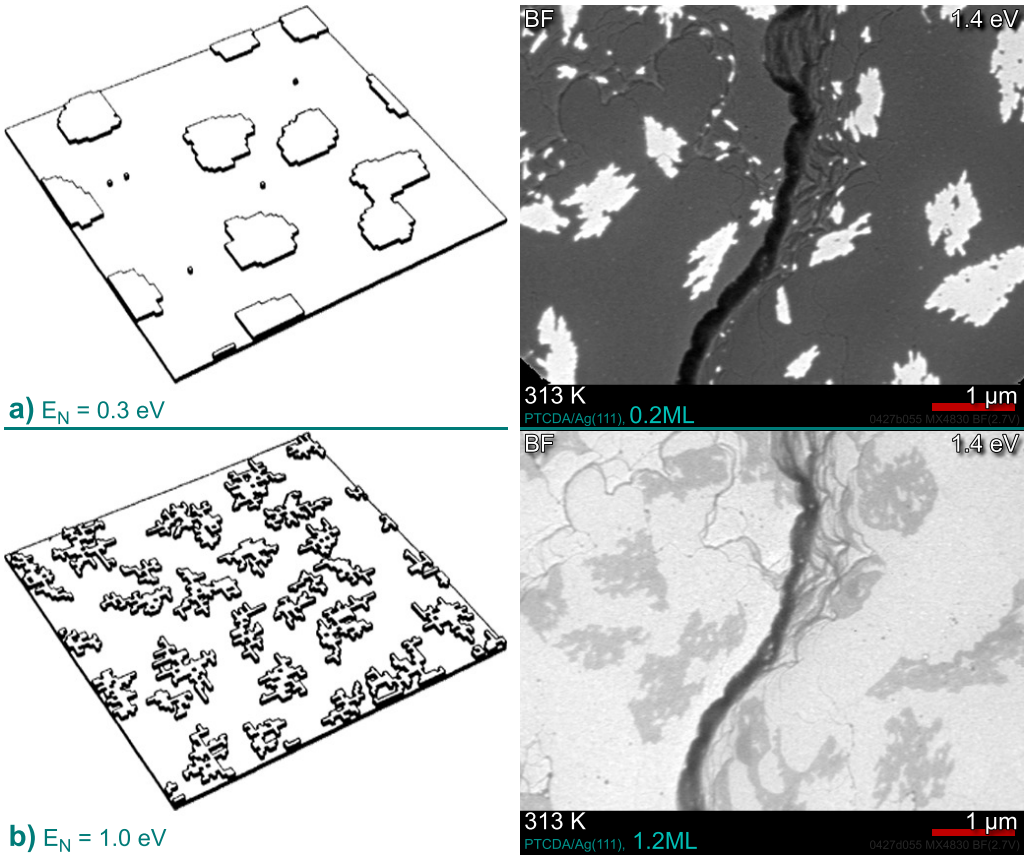

Figure 3.9: a) and b) show typical island morphologies at $\theta = 20\,\%$ for a $100x100$ section of a 400×400 lattice obtained by Monte–Carlo simulation where $T = 800\,\mathrm{K}$ and $E_S = 1.3\,\mathrm{eV}$ (figures depicted from Ratsch et al. [78]). On the right BF–images of PTCDA/Ag(111) at $\theta = 20\,\%$ for the $1st$ and 2^{nd} layer show a similar behaviour.

barrier E_N for diffusion along an island edge is identical to the detachment barrier from an island. The model is designed for diffusion of atoms on a surface with four–fold symmetry with $n = 0, 1, 2, 3, 4$ next neighbours.
For the simulation they formulate the hopping rate $k(T)$ of an atom to the next site as a function of the free atom migration rate $D(T)$ with the corrugation of the surface potential E_S

$$k(T) = D(T)e^{-\frac{nE_N}{k_BT}} \tag{3.3}$$

$$D(T) = \frac{2k_BT}{h}e^{-\frac{E_S}{k_BT}} \tag{3.4}$$

where T is the temperature and k_B the Boltzmann constant. For large values of the so–called pair bond energy E_N the growth is fractal, for smaller ones smooth.
Astonishingly, this simple model results already in similar island shapes, although the extension of molecules and related effects are not considered.

Taking the similarity in shape as reason to make use of this model for the investigated system PTCDA/Ag(111), the equations 3.3 can be rewritten and for the hopping rate follows

$$k(T) \propto e^{-\frac{1}{k_BT}E_N(n+\frac{E_S}{E_N})}. \tag{3.5}$$

From this equation the ratio between the energies E_S and E_N allows to draw conclusions for the present system, i.e. the stronger the interaction with the substrate E_S or the weaker the interaction with the neighbours E_N, the more fractal the growth (with all other parameters fixed). This model applies (within limits) to the symmetry of the investigated system since the quasi–rectangular shape of the unit cell of the PTCDA layers allows also for only four next neighbours.
Thus, the different shapes lead to two different interpretations: Either the pair bond energy E_N depends on the substrate or the shape difference of the islands indicates that the interaction with the surface E_S is lower on the PTCDA layer than on the Ag(111) surface. Since E_N results from the interaction of the PTCDA oxygen groups with the PTCDA hydrogen of the neighbours in the herringbone structure, it is expected to be the same for 1^{st} and 2^{nd} layer.
However, the stronger interaction between PTCDA and the Ag(111) surface (the interlayer distance d is smaller than in the α–modification [13, 62]) is expected. Hence it is concluded that the E_S of PTCDA on Ag(111) is higher than on the PTCDA–ML. This is legitimated since E_S strongly influences the nucleation density and PTCDA is found to be chemisorbed on Ag(111) by Rohlfing et al. [13].

Besides, it is astonishing, that a model developed for a very simple system as atoms on a surface with four–fold symmetry appears to describe reasonably well the growth

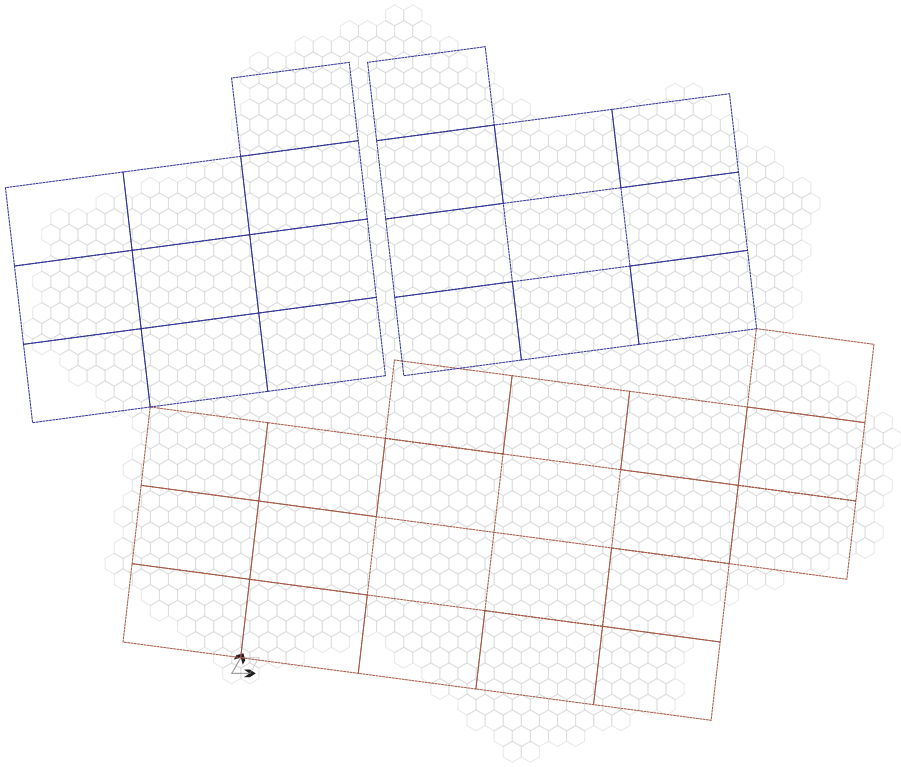

Figure 3.10: Schematic of the PTCDA/Ag(111) superstructure domain boundaries for translational domain boundary (blue) and boundary between two different rotational domains (blue/red) for the "best" fitting cases.

behaviour of the much more complex system. In general the shape of islands appears to depend on the ratio E_S/E_N, which is the ratio between the interaction with the substrate and the interaction with next neighbours.

On a new type of barrier

This in–plane barrier is apparent for the growth of 2^{nd} layer domains. It is the boundary between separate rotational domains in the 1^{st} layer. Different ways to form such boundaries between adjacent (rotational) domains are sketched in figure 3.10 for the best fitting cases — translation by a single Ag(111) lattice site (top, blue) and the horizontal boundary between two differently rotated domains. These boundaries cannot be overgrown by new $_2$domains but they hardly hinder the diffusion of molecules. For diffusion, the barrier seems to be rather small as concluded from the increased coverage rate at the perimeters of the underlying crystallites and because no major difference in nucleation density between areas with high and low monolayer domain density was found.
The high barrier for overgrowth by single $_2$domains is attributed to the misfit of the

crystalline structure. Usually the molecules get into an energetically more favourable state when attached to an existing layer than diffusing around. This is due to the interaction via the carboxyl groups to their neighbours and the coupling via the π–orbitals to the substrate. The pure interaction between neighboured molecules seems insufficient to clip molecules to the existing $_2$domain at positions where the interaction with the substrate is missing or at least reduced. Hence molecules keep diffusing until they find lattice sites on adjacent $_1$domains with higher interaction strengths.

This twofold description of the in–plane barrier is justified because (i) the $_2$domain growth rate is proportional to the perimeter of the underlying $_1$domain and (ii) a delayed nucleation of $_2$domains in the $2^{nd}(green)$ growth–regime exists. This delayed nucleation starts as soon as the perimeter is closed.
The described phenomena require a diffusion length which is larger than the average crystallite size and a low diffusion barrier between adjacent $_1$domains. Furthermore a different barrier for the overgrowth is necessary, as is introduced by translational or rotational lattice misfit of in–plane rotational domains.

Finally it is stated that there was no obvious asymmetry found for the nucleation and growth behaviour on different rotational domains besides a preferred stacking of rotational domains.

3.3.4 Conclusion

This detailed study of the growth of the first two layers of PTCDA/Ag(111) revealed the influence of substrate morphology and domain boundaries on the growth of the layers and enabled to develop a detailed model of the potential landscape (fig. 3.8). It was found that the molecular diffusion energy E_S is larger on Ag than on the PTCDA–ML. Once the Ag is covered by one layer of the organic molecules, steps are no longer diffusion barriers but step bunches still are. The formed inter–domain boundaries are no diffusion barriers as well.
These findings emphasise that the growth of the very first layer is crucial for high qualities of organic thin films. Domain sizes are constrained by monatomic steps up to a certain growth temperature and determined by the interplay of E_S and E_N. Succeeding layers are less homogeneous than the first one since originally formed domain boundaries cannot be overgrown.
In the following chapter it is demonstrated that an even more complex picture of the 2^{nd} layer has to be drawn exploring a phase that is to date unknown.

3.4 Second layer PTCDA ripple–phase

3.4.1 Several phases in the 2^{nd} layer

The second layer of PTCDA/Ag(111) is a very interesting sample, although so far just the monolayer [11] or thin films of several ten Å [79] were investigated. The second monolayer neither sees the strong influence of the substrate anymore nor encounters the pure intermolecular interaction within PTCDA bulk material.
Details on the growth of the "normal" phase, referred to as β–like and α phase (islands) were given in the previous chapter. It is stated that the 2^{nd} layer grows typically in the β phase within the present temperature range. Besides these differences in the growth mode of the first compared to the 2^{nd} layer several different 2^{nd} layer–contrasts were found. This implies that there are more possible phases in the 2^{nd} layer than the six known, three rotational (r_i) and the corresponding mirrored (m_i) domains [5]. The most prominent one is the so–called ripple phase (rp), which can be explained allowing for more rotational phases and is presented in this chapter.
First the temperature regime is discussed in which the rp was observed followed by an introduction of the new growth behaviour found for this phase. Finally the crystalline structure is investigated and a commensurate *super*^{2}structure[4] model is presented that describes the findings very well.

3.4.2 Temperature range

At several preparations in a temperature range between 243 and 319 K crystallites were found in the 2^{nd} layer that show a new phase with linearly alternating contrast. This is shown in figure 3.11.

Curved black lines are steps and step bunches, white areas are the 1^{st} layer or 3^{rd} layer (see QIC in sec. 2.2.3) while the darker ones are the three different 2^{nd} layer contrasts — the known, β–like phase (bright grey), the dark grey phase and the striped rp. With µ–LEED the bright grey phase is identified as simple rotational domain, which is described as β–like phase in literature. The following concentrates on the second layer contrasts.
These three different phases were found in the whole temperature range. It is noted that the two new (dark) phases are rarer than the normal phase. Especially the rp covers around 1 % of the overall surface area. However single rp–crystallites can cover large fractions of Ag(111) terraces and hence occupy about 10 % of the present FoV.

[4] *Super*^{2}structure refers to an additional 2^{nd} layer superstructure on top of the PTCDA/Ag(111) superstructure.

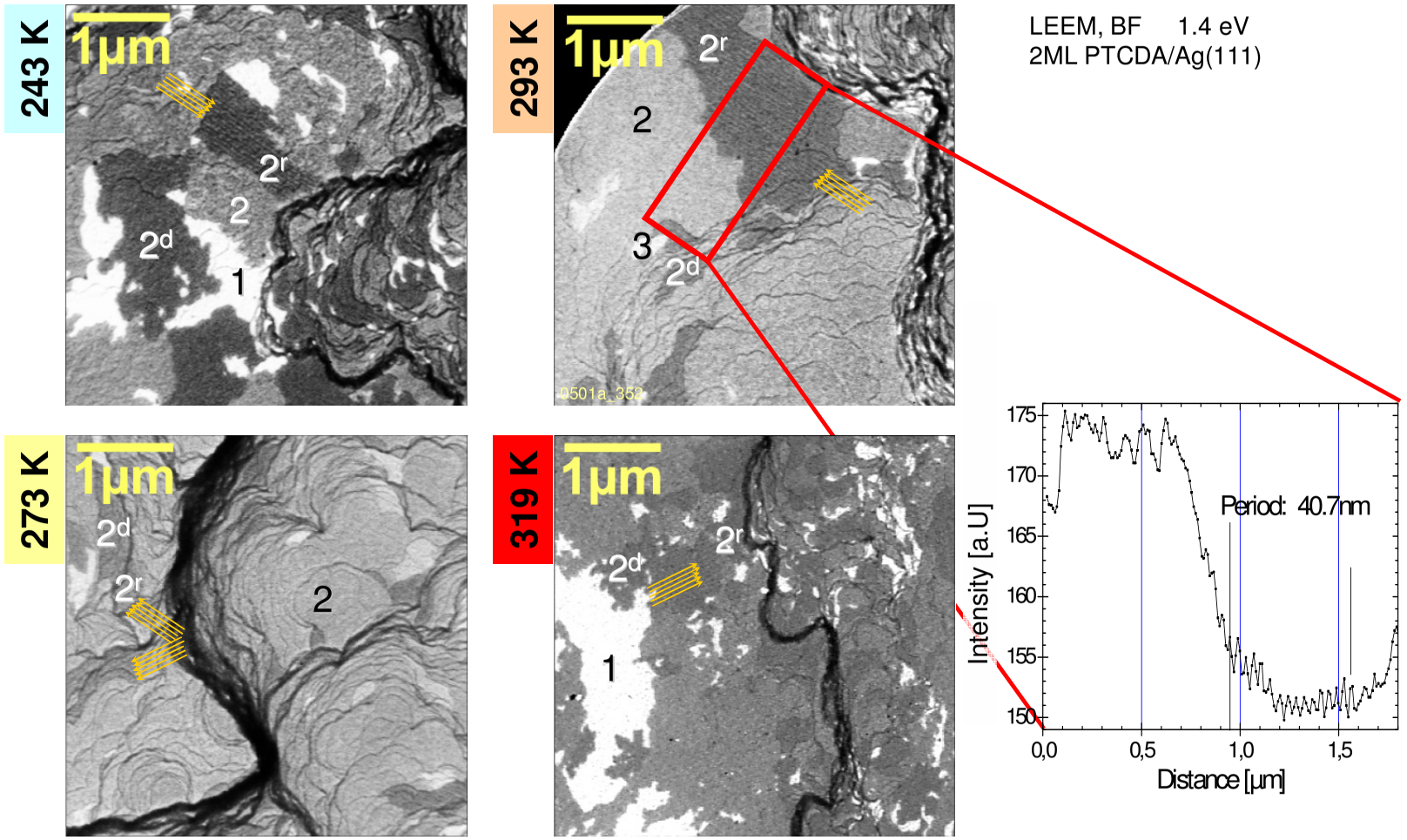

Figure 3.11: BF–images at 1.4 eV of the rp grown at temperatures between 243 and 319 K. A line scan across the ripples, averaged over the width of the red box (293 K–image), is displayed on the right. Orange arrows point along ripples in the different images to emphasise their orientation. Images are linearly min–max scaled. The different domains are labelled according to their thickness. Note that three variants of the second layer exist (i.e. 2, 2^d and 2^r).

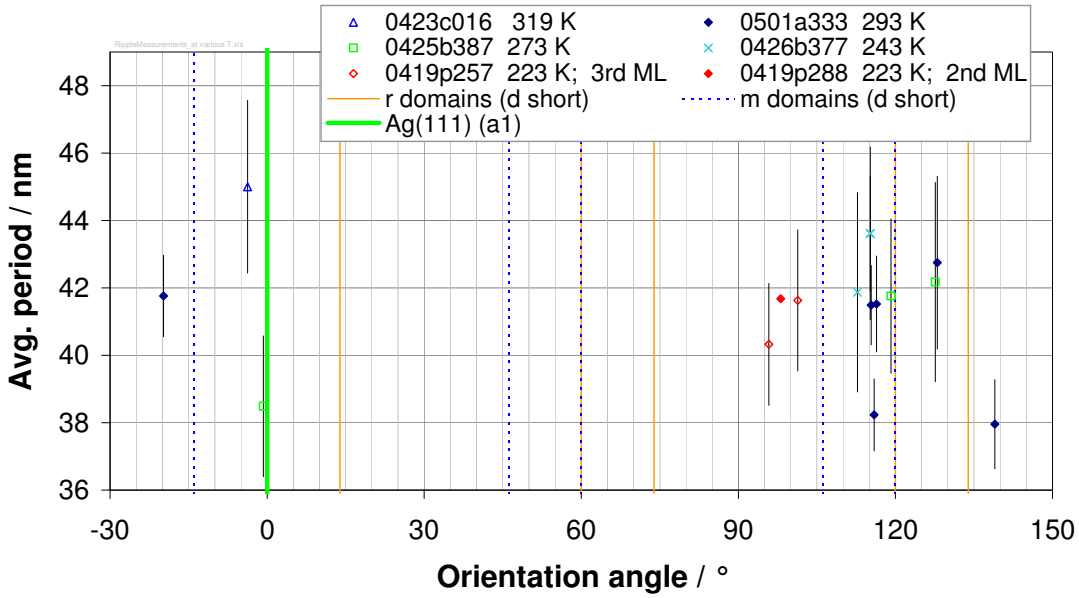

Figure 3.12: Orientations of the ripples and their periods recorded at different temperatures and preparations. The two sets of data are independent measures of the ripple orientations at the identical domains. The vertical lines represent the model predictions of the ripple directions for two stacked rotational domains.

Ripple periods were determined for a large variety of domains and were correlated to the growth and record temperatures and their orientation towards the image abscissa[5]. Within the accuracy of the measurements no correlation to any of these temperatures was found. The data of the periodicity are spread around 41.5(5) nm by several nm for all temperatures (see table 3.2).
The ripple periodicities are plotted in figure 3.12 as a function of the orientation. The green vertical line at angle zero marks the orientation of the Ag(111) a_1 (see also fig. 3.15) direction known from µ–LEED. The other vertical lines represent predictions from the model described below. The data stem from ripple domains that were obtained at samples grown at all indicated deposition temperatures.
No relation between orientation and period can be found. Further it was found that the ripples align preferentially along two symmetry axes of the Ag(111) crystal, the $[1\bar{1}0]$ and the $[10\bar{1}]$ direction (e.g., the large domains in images 243 and 293 K from figure 3.11). The count of only 14 domains or the low ripple contrast combined with asymmetric image resolution might explain the absence of rp–domains aligned along the $[01\bar{1}]$. But it could be an effect as well that is not yet understood.
The temperatures mentioned above are meant as temperatures during deposition of the PTCDA molecules. Furthermore it was found that the rp are stable up to at least 423 K during an annealing cycle. Annealing seems to improve the order of the

[5]The image abscissa is a reasonable reference, since for all experiments the identical substrate was used and kept in the manipulator.

structures.
Also differences were observed between the overgrowth of the rp–structures and, in a different case, the desorption of such layers. The 3^{rd} layer on top of a ripple phase (243 K) was observed to grow contrastless in one case. Whereas during desorption a 3^{rd} layer rp reveals another underlying rp structure with the same structure and periodicity (red diamonds in plot 3.12).

A detailed study of the growth process and the internal structure of the ripples grown at 293 K is exemplarily presented in the following sections. The findings, existence of the rp structure over a large temperature range, alignment with substrate lattice, and periodicity will be discussed in the model section.

3.4.3 Growth behaviour of the ripple phase

The growth of the ripple phase was observed at 293 K in addition to the growth of the common 2^{nd} layer phase presented in detail in section 3.3.2.

Linear growth along the ripples

In the BF snapshot series plotted in figure 3.13 the growth of both phases is shown. Again, the curved dark lines are steps and step bunches whereas the 1^{st} layer of PTCDA appears brighter than the Ag(111) substrate due to higher reflectivity at 1.4 eV. Further layers change contrast according to their thin film quantum interference. Here the 2^{nd} layer is darker (several grey scales) than the first and the third appears brighter again.
The red rectangles mark the identical AoI in the overview images on the left that is selected for the nominal coverage series from 0.1 to 1.9 ML. Image contrast is kept constant for all AoI snapshots. Labels describe the thickness of the PTCDA–layers (numbers) and the different 2^{nd} layer phases (1.9 ML): the β–like 2, the dark $2d$ and the ripple phase $2r$. A magnified version of image 1.9 ML can be found in figure 3.15 also allowing for better ripple resolution. $2p$ just highlights a crystallite that behaves cannibalistic and eats material for its own expansion from the adjacent, previously completed crystallite (see images 1.6 to 1.7 ML). This indicates once more the competitive growth behaviour of different 2^{nd} layer crystallites and hence reduced diffusion barriers and different formation energies.
The first series at the top of fig. 3.13 displays the growth of the underlying 1^{st} layer in the known manner on the clean Ag(111) substrate. Direct your attention to the large, single–terrace domains that are later (in image 1.9 ML) covered by the phases labelled 2 and $2r$. This single Ag(111) terrace is covered by two 1^{st} layer domains originating from two different nuclei. The boundary between these two monolayer domains persists later in the 2^{nd} layer as well.

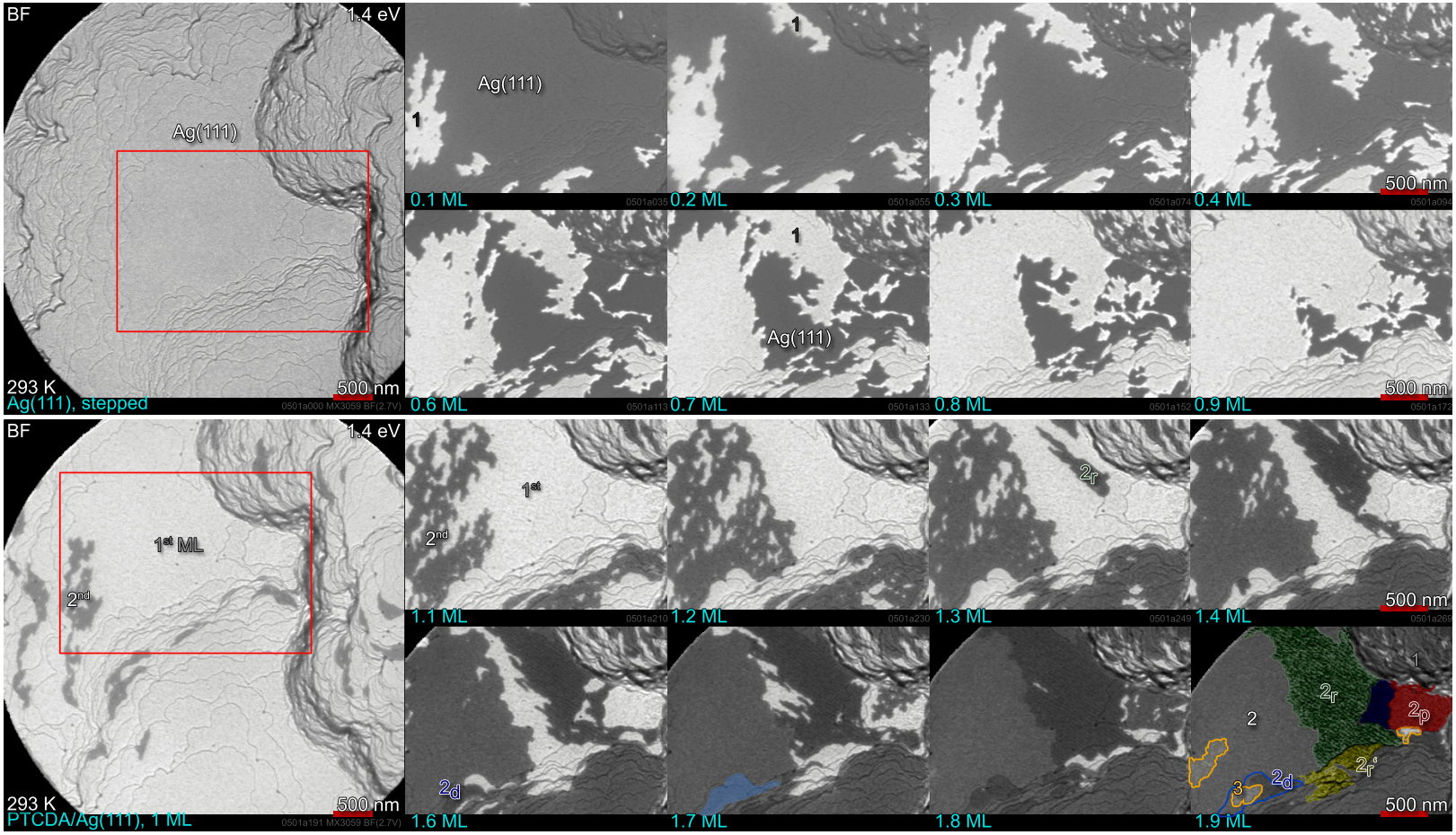

Figure 3.13: Snapshots from a BF image series acquired during growth of the 1^{st} layer (top) and 2^{nd} layer (bottom) of PTCDA/Ag(111) at 293 K. The two overview images on the left show the clean Ag(111) and the surface covered with the 1^{st} layer. A magnified and contrast–enhanced version of the 1.9 ML image can be found in figure 3.15.

In the second ML the 2–labelled domain nucleates first (growth regime #1(*red*) introduced in section 3.3.2) and grows in the earlier described dendritic way. First its perimeter closes at the border to the succeeding, adjacent $2r$ domain (regime #2(*green*)). Shortly after the perimeter of the 2–domain is closed the $2r$ domain starts to grow in a distinct elongated way from its nucleus at the bottom right kink along the [010] direction of the covered Ag(111) substrate. The substrate direction is known from comparison with the µ–LEED which is presented in figure 3.15. This is very uncommon and was not yet observed for the growth of standard phase in regime #2.
Domain $2p$ grows in the regime #3. A second rp is found in the $2r'$ domain that forms on a different terrace from a different nucleus but aligned with the ripple orientation of the $2r$ domain.

Overgrowth of 1^{st} by different 2^{nd} layer domains

As already presented for preparations at other temperatures it turns out that also in case of 293 K single 1^{st} layer domains are covered by several 2^{nd} layer domains. This is shown by the DF–images in figure 3.14. On the left the BF–images of the first (top) and 2^{nd} layer (bottom) are seen. Comparing the corresponding DF–images on the right it is clear that on single 1^{st} layer–domains several contrasts in the 2^{nd} layer exist. This is not to be expected if the PTCDA just grows in the standard β–phase stacking. From the standard model maybe a second contrast addressed to the α–stacking might be guessed. But the α–stacking is only reported for thin films [16] and PTCDA–islands and not for the 2^{nd} layer. Furthermore, as seen on the central (light–green) 1^{st} layer domain, there exist at least three different contrasts/domains in the 2^{nd} layer. This requires at least two new 2^{nd} layer phases besides the β–like phase.

Conclusion

It is remarkable that three different contrasts were observed in the 2^{nd} layer. This is not to be expected having a strained but commensurate growth in the β–phase in mind which is so far assumed for the thin film PTCDA growth. Moreover the structureless 2 and $2d$ type grew in a comparable, dentritic fashion while the $2r$ rp phase showed a preferentially one dimensional growth along the substrate symmetry axis [010]. These differences in growth behaviour and contrast were observed clearly at 243 and 293 K. Hence the dark $2d$ phase is not an unresolved rp phase but a self–contained third phase of still unknown structure. Such, it was possible to show that at least three different 2^{nd} layer phases exist over a wide range of temperatures.

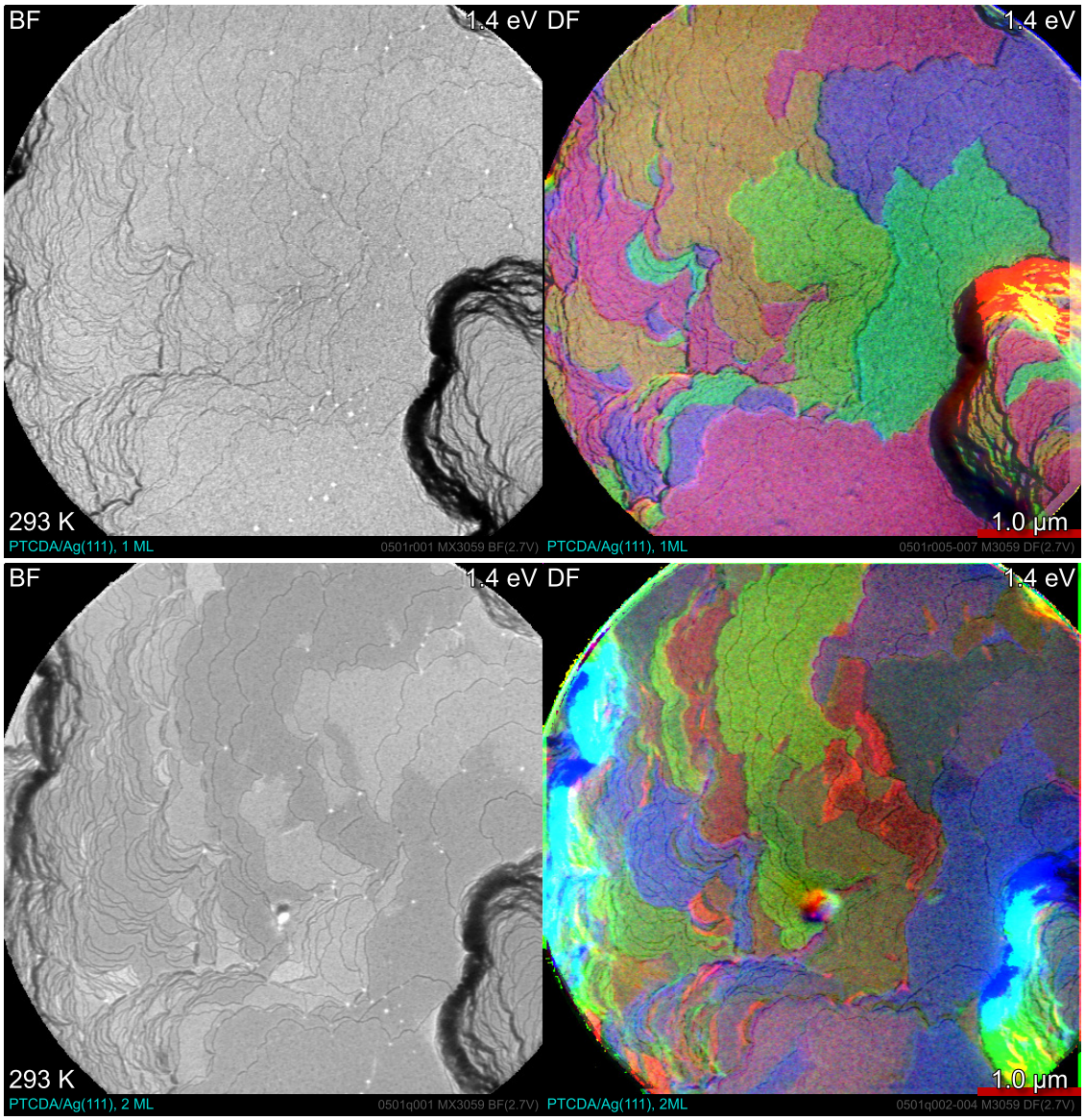

Figure 3.14: BF(left) compared to the corresponding DF image for the first(top) and 2^{nd} layer PTCDA after growth at 293 K and subsequent desorption.

This means further that the growth is already more complex in the 2^{nd} layer which might be explained by the additional quasi–rectangular symmetry of the underlying monolayer of PTCDA as shown in the following.

3.4.4 Commensurate ripple phase

With the help of in–situ µ–LEED measurements right at the rp and an adjacent common 2^{nd} layer domain, the molecular structure of the newly discovered rp was investigated. This was achieved although within the microscope images individual molecules cannot be resolved as with, e.g., a STM. On the other hand with STM a smooth long range periodicity of the order of 42 nm would be hard to discover if not strong changes in the layer interaction would be present. Especially if only 1 % of the surface is covered by the rp, one needs a tool that enables large area overview of the surface as, e.g., SMART to detect rare phases on purpose.

µ–LEED structure of adjacent crystallites

The µ–LEED images presented in figure 3.15 are another proof that the rp is not a detection artefact but a real and new PTCDA–phase. Unlike expected from the so–called universal curve (fig. 2.3) the penetration depth of electrons into PTCDA films is on the order of a few ML at kinetic energies of only several eV [17, 80]. Hence the µ–LEED pattern in figures 3.15 and 3.16 stem from structures in the topmost layers. This high surface sensitivity combined with the low energy allows to study non–destructively variations in the topmost layers.
The BF image 3.15 of the Ag(111) surface covered by 2 layers of PTCDA is depicted from the growth series in figure 3.13 with the earlier described domains. The two yellow and green circles mark the AoIs selected to derive the µ–LEED pattern from. The series of µ–LEED pattern are taken from the 2^r(top) and the standard 2 domain(bottom) at different kinetic energies each. The diameter of the circles indicates roughly the size of the Ewald sphere. Both LEED series were recorded within 30 s each, while it took not longer than 3 min to record both of them.
It is pretty obvious that the molecular structure within the domains is very different. In the bottom, green marked µ–LEED series one single rotational domain dominates the pattern and is identified as the m_2 domain (fig. 3.16) which grows in the β–stacked phase. Also few, weak contributions from other structures are visible that are attributed to the 2^d phase and the already started 3^{rd} layer which are within the selected AoI, too.
In contrary the pattern at the top, yellow µ–LEED series of fig. 3.15 from the rp is

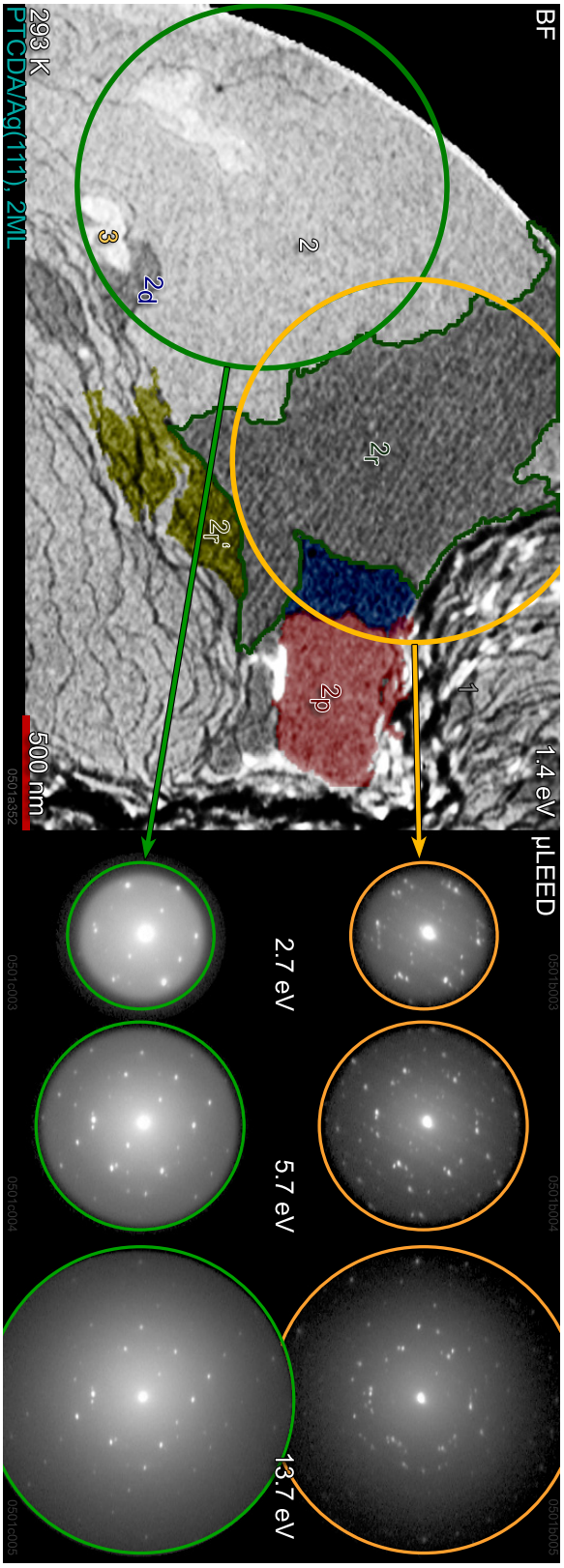

Figure 3.15: BF–image showing the different second layer phases and some third layers(labelled accordingly). The μ–LEED patterns on the right were taken at different energies from the circled areas in the LEEM image. The top row shows the μ–LEED of the ripple phase 2^r while the bottom row corresponds to a single rotational domain in the second ML.

very rich and contains many features that are discussed in detail in the following section.

LEED structure of the ripple phase

The structural composition of the µ–LEED pattern in figure 3.16 was analysed using the software *SpotPlotter* by Patrick Bayersdorfer [81] that allows to overlay LEED–reflexes calculated from basic lattice and super–structure parameters with the image to be decomposed.
Image a) shows the µ–LEED pattern of mainly one single domain (green selection in the image of figure 3.15) of the well known PTCDA herringbone structure as described above. The hardly visible modulation in the BG is due to the noise of the multi–channel plate. Intensities were nonlinearly scaled to visualise all present structures in the printout. The second pattern in image b) is the µ–LEED pattern of the rp (large, circled 2^r domain in figure 3.15). Most of the spots in both images can be explained by the standard rotational (r_1 to r_3) and the corresponding mirror (m_1 to m_3) domains that are described by [5]. Not all of them are within the selected AoIs. The selection of domains, that is necessary to describe the features apparent in the patterns, is found top–left of the corresponding image together with their superstructure–matrices. While the coloured super–structure unit cells in reciprocal space are given in the images the corresponding arrows next to the image are real space representatives with their orientation related to the a_1 direction of the primitive surface unit cell of the Ag(111) substrate (vectors are introduced in the real space sketch 3.1).
Most of the remaining spots, especially the intense ones in the spot–trains visible close to (00)–spot, can be explained by only one *super*^{2}structure[6]. It is called rp and represented by circles in green for the present and predicted spots. In the real space representation, the direction of its long periodicity is drawn.
Finally some spots remain, that are not yet described. They are easily found in the bottom–right half of image b) as the ones not marked. They cannot be allocated to the known structures or the rp. However they can be covered by an additional, yet unknown domain with similar dimension as the standard PTCDA unit cell just mirrored at its $(b_1 + b_2)$–axis.

Summary of findings

The µ–LEED pattern is dominated by the m_1–like phase while also quite intense contributions from the adjacent domain m_2 (large part on the left of the AoI) from

[6] *Super*^{2}structure refers to an additional 2^{nd} layer superstructure on top of the PTCDA/Ag(111) superstructure.

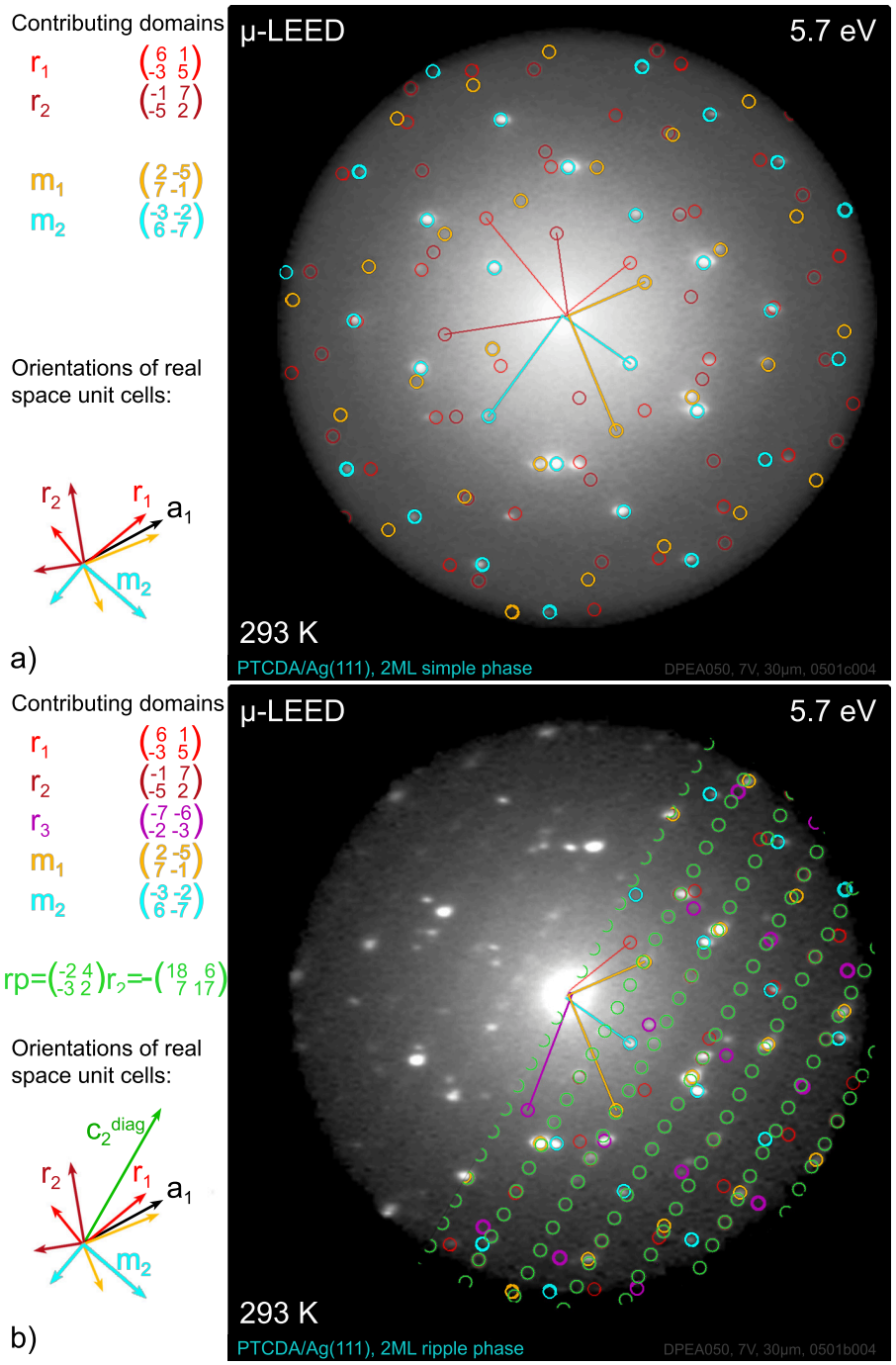

Figure 3.16: These μ–LEED patterns are picked from figure 3.15. Here, the intensities are nonlinearly scaled for optimum contrast. The found phases with their super–structure matrices are given at top left of each pattern. The arrows below indicate their real space unit cell. a_1 is a vector of the primitive surface unit cell of Ag(111). a) shows the domain consisting of the m_2 phase with some contributions from the adjacent areas. At b) the LEED pattern of the rp–domain is shown.

the β–like crystallite are visible. Rather intense spots are noticed correlated to the r_2 phase. Week contributions are found from the remaining rotational domains, that are dedicated to the other areas within the selection on top right of rp in figure 3.15. The dimensions determined from the µ–LEED–pattern and the real–space ripple analysis are summarised in table 3.2. The unit cell of the ripple phase, as derived from µ–LEED, has a very symmetric shape. The two diagonals (d_{11} and d_{12}) of the unit cell intersect under an angle of 89.9(20)°. Their length is $d_{11} = 11.8\,\text{nm}$ and $d_{12} = 3.2\,\text{nm}$. These dimensions are expected to be found in real space as well. However this it not observed. d_{12} is oriented along the ripples and below the resolution limit for this magnification. In the direction of d_{11} the real space period length found, varies between 38(5) nm and 45(5) nm. Both values do not agree with the reciprocal space data of d_{11} but are close to multiples of 3 and 4 , respectively. In the following section a rather simple model is presented that explains the majority of observations consistently.

3.4.5 Model to explain the ripple phase

A simple structural model was developed that explains consistently the ripple phase investigated and presented in the previous sections. It basically allows for two new PTCDA phases that are similar to the known herringbone structure but differ slightly in their unit cell dimensions and clearly in their orientation. Interference contrast in a wavy PTCDA carpet is proposed to build the bridge between the reciprocal– and real–space periods.

Superposition of different herringbone domains

The basic idea of the model is to superpose two different domains as suggested by the DF–images of the 2^{nd} layer. But unlike the domains of the monolayer, the stacked 2^{nd} layer domains are not compatible with the known rotational domains. They do not have equivalent dimensions or follow the $\beta(\alpha)$ stacking. In fact they are pretty similar in their dimensions but rotated in plane by about ±75° with respect to their 1^{st} layer–basis. Hence this leads to slightly strained PTCDA unit cells. The stacking model is illustrated schematically in fig. 3.17. Two variants (1: green/dashed, 2: rose/dotted) are shown, that lead to *super*^{2}structure unit cells of similar dimensions. In the sketch the m_1 domain (blue, $b'_{1,2}$) is chosen as the 1^{st} layer basis. It is constructed as commensurate to the Ag(111) surface according to Glöckler et al. [5] with the superstructure matrix (eqn. 3.1) of the monolayer.
The two superposed domains with angles $\beta_{1/2}$ in 3.17 a) are mirrored and rotated properly and sightly strained to form the commensurate *super*^{2}structure with the rhombus–like unit cells. The angle of rotation is only related to the Ag–substrate

Table 3.2: Findings for the ripple phase at different temperatures, comparing the data with the dimensions of the rotational domain r_1 on Ag(111) known from literature. At 293 K the unit cell data derived from the µ–LEED are presented. A labelled sketch of the data is given in 3.1. The error in the period of the rp, measured in real space, is ±5 nm for all measurements.

Substrate	**Modification**	**Data determined from µ–LEED**				**Ripple data from real space**			
	2^{nd} **layer**	**Unit cell vectors**		$\sphericalangle(a_1, c/d_{i1})$	$\sphericalangle(c/d_{i1}, c/d_{i2})$	**(long) Period**	**Unit cell Area**	**Molec.**	**T**
		$\overrightarrow{x_{i1}}$ [nm]	$\overrightarrow{x_{i2}}$ [nm]	δ_{i1} [°]	γ_i [°]	[nm]	[nm^2]	**[pcs.]**	[K]
Ag(111)	r_1[13]	1.896	1.261	6.4	89	none	2.39	2	
Ag/1ML	ripple (rp)					41.9-43.5			243
Ag/1ML	rp					38.5-42.2			273
Ag/1ML	rp_{diag} ($\overrightarrow{d_i}$)	3.2	11.8	30.2(20)	89.9(20)	38.2-41.5	18.8(1)	15.7	293
Ag/1ML	rp_c ($\overrightarrow{c_i}$)	6.1	6.1	316.0(20)	150.0(10)				293
Ag/1ML	rp					45(5)			319
Ag/1ML	rp					38-42.8			353
Ag/1ML	rp					40.3-41.7			403

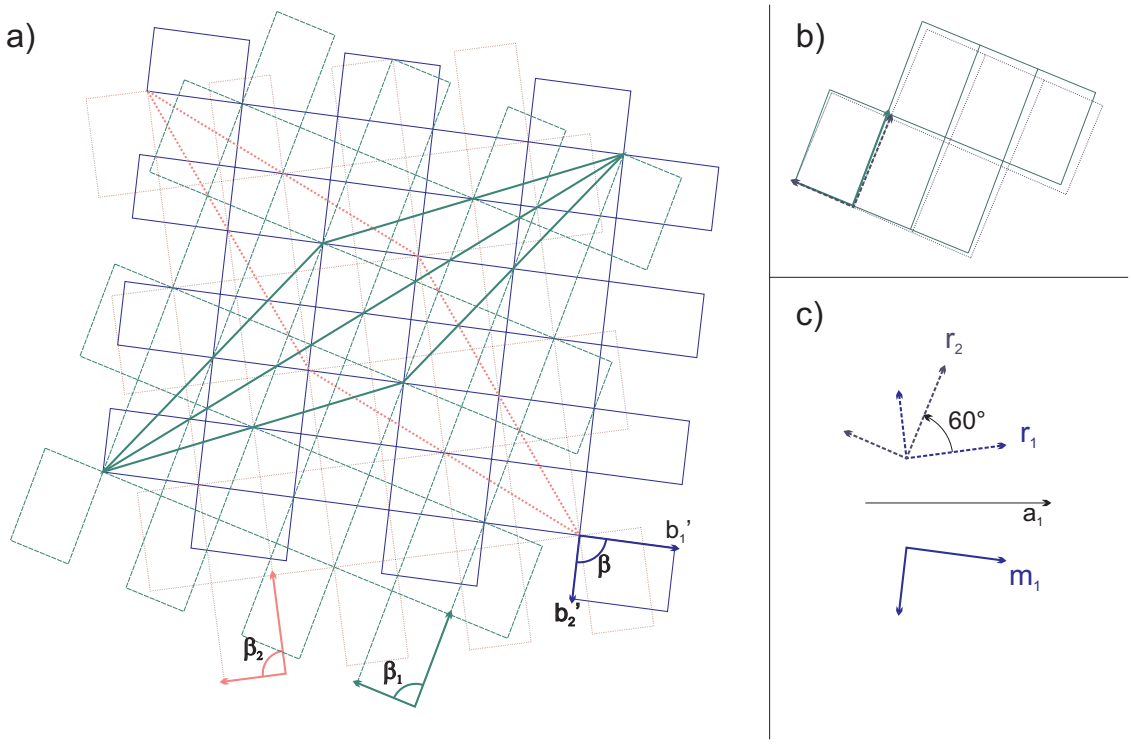

Figure 3.17: Model for the discovered ripple phase structure. a) shows the two possible (green/dashed & rose/dotted) stackings of rotational–like domains to generate the similar ripple phase unit cells when combined with the underlying, known m_1 1^{st} layer–mirror($\mathbf{b'}_{1,2}$) domain (blue/solid). b) compares the green(solid) structure with the known r_2 PTCDA/Ag(111) unit cell. c) illustrates the transformation of that underlying cell for the comparison in b).

via the underlying 1^{st} layer (m_1) domain. Due to the slight deviation of the commensurate monolayer PTCDA unit cell from the rectangular shape ($\beta' = 89°$), the described domains have no mirror symmetry. However, the dimensions of the resulting unit cells differ only slightly from each other as summarised in table 3.3. Moreover they are even more similar to the dimensions of the known β and α stacked bulk domains (see table 3.1).

Furthermore the green herringbone unit cell is oriented similarly to the rotational domain r_2. The differences are illustrated in b) while c) shows how r_2 is related to the base cell m_1. This is in contrast to the rose phase which is not similar to a known one.

Commensurate *super*^{2}structure and alignment with Ag(111)

The model introduced in the previous section can be summarised by the *super*^{2}–structure matrix representation.

Two different ripple phase structures. The matrix representations for the two different commensurate ripple phases of the 2^{nd} layer with respect to the 1^{st} layer PTCDA–phase are for phase rp_1 (green in 3.1)

$$\begin{pmatrix} -2 & 4 \\ -3 & 2 \end{pmatrix} \tag{3.6}$$

and for rp_2 (rose) the matrix

$$\begin{pmatrix} 2 & 4 \\ 3 & 2 \end{pmatrix} \tag{3.7}$$

that represent the *super*^{2}structure.

Alignment with the Ag–substrate. Thus it follows for rp_2 (eqn. 3.7) with the PTCDA/Ag(111) superstructure–matrix (eqn. 3.1) for r_1

$$\begin{pmatrix} 2 & 4 \\ 3 & 2 \end{pmatrix} \begin{pmatrix} 6 & 1 \\ -3 & 5 \end{pmatrix} = \begin{pmatrix} 0 & 22 \\ 12 & 13 \end{pmatrix} \tag{3.8}$$

that its primitive unit cell vector $\overrightarrow{c}_{21}$ is aligned with the Ag(111) lattice vector $a_2 \equiv [010]$. In case of rp_1 to the contrary not a primitive vector is aligned but the short diagonal of the rhombus $\overrightarrow{d}_{12}$. This is shown schematically in figure 3.1.
It is emphasised, that for the basis r_1 the vectors $\overrightarrow{c}_{21}$ and $\overrightarrow{d}_{12}$ are parallel to the

Table 3.3: Predictions derived from the model concerning the size and orientation of the $super^2$structure of PTCDA on Ag(111). The dimensions are given exemplarily for the basic domains r_2 and m_1 (mirrored along a_2) that result in similar orientations of the rp_1. rp_{PTCDA} indicate the strained herringbone–like 2^{nd} layer unit cell. A labelled sketch of the parameters is given in fig. 3.1.

Substrate	**Modification 2^{nd} layer**	**Real space: Unit cells** Unit cell vectors $\overrightarrow{x_{i1}}$ [nm]	$\overrightarrow{x_{i2}}$ [nm]	$\sphericalangle(a_1, c/d_{i1})$ δ_{i1} [°]	$\sphericalangle(c/d_{i1}, c/d_{i2})$ γ_i [°]	**Derived findings** Unit cell **Area** [nm^2]	**Molec.** [**pcs.**]	**Alignment**
Ag(111)	r_2 - basis	1.895	1.260	**67.6**	89.00	2.39	2 [5]	
Ag/1ML	rp_{PTCDA1}	1.941	1.232	**170.8**	88.3	2.39	2	$\sim\mathbf{m}_1$
Ag/1ML	rp_{PTCDA2}	1.957	1.221	**142.6**	90.0	2.39	2	
Ag/1ML	rp_{c1j}	6.25	6.18	**13.9**	29.6	19.12	16	
Ag/1ML	rp_{c2j}	6.34	6.26	**120.0**	28.7	19.12	16	$\mathbf{c}_{21} \parallel \mathbf{a}_3$
Ag/1ML	rp_{diag1j}	12.02	3.18	**28.6**	88.6	19.12	16	$\mathbf{d}_{12} \parallel \mathbf{a}_3$
Ag/1ML	rp_{diag2j}	12.22	3.13	**105.8**	88.1	19.12	16	
Ag(111)	m_1 - basis	1.895	1.260	-7.6	89.00	2.39	2 [5]	
Ag/1ML	rp_{PTCDA1}	1.941	1.232	69.3	88.3	2.39	2	$\sim\mathbf{r}_2$
Ag/1ML	rp_{PTCDA2}	1.957	1.221	97.4	90.0	2.39	2	
Ag/1ML	rp_{c1j}	6.25	6.18	46.1	29.6	19.12	16	
Ag/1ML	rp_{c2j}	6.34	6.26	120.0	28.7	19.12	16	$\mathbf{c}_{21} \parallel \mathbf{a}_3$
Ag/1ML	rp_{diag1j}	12.02	3.18	31.4	88.6	19.12	16	$\mathbf{d}_{12} \parallel \mathbf{a}_3$
Ag/1ML	rp_{diag2j}	12.22	3.13	134.2	88.1	19.12	16	

Ag substrate vector a_2. This is the same direction where the aromatic rings of one PTCDA molecule (A)[7] are nearly perfectly aligned with the Ag(111) atoms which is reported by Rohlfing et al. [13]. In case of rp_1 exactly this (A) molecule can find a counterpart in the corresponding new 2^{nd} layer phase (in case of rp_2, alignment with the (B) molecule may happen). But to investigate the molecular arrangement within the unit cell reliably, LEED–IV or STM data of the ripple phase would be necessary.

Predictions of the model

Plenty possible ripple phases. The model predicts two different possibilities for *super*^{2}structure domains on each basic (r_i, m_i) domain with very similar measures but with rotated d_i by about 100°. Therefore, a multitude of 12 possible ripple phases is expected as there are 6 known basic phases. These are presented schematically (not to scale) in figure 3.18 to illustrate the expected orientations. In figure 3.12, the derived orientations of the short diagonals $\overrightarrow{d}_{i2}$ with respect to the Ag(111) $\overrightarrow{a}_1$ are plotted as vertical lines for rotational (r_i, solid, orange) and mirror (m_i, dotted, blue) 1^{st} layer–domains. Also, the real–space data of the ripple period lengths and the corresponding orientation are charted.

Both periods might determine the ripple orientation. Since the diagonals d_{ij} are only close to normal to each other, the orientations of different domain constellations result in similar orientations. In the rp_1, based on the $\mathbf{r}_2$ phase, d_{11} forms an angle of 28.6° with respect to the a_1 direction while the normal on d_{12} includes 30.0°. For the phase with the same *super*^{2}structure matrix (eqn. 3.6) but based on $\mathbf{m}_1$, which results in similar orientations, the angle between a_1 and d_{11} is 31.4° and towards the normal on d_{12} it is again 30.0° (see also table 3.3). These three directions are candidates for the real space ripple orientation.
Due to the rotational symmetry of the 1^{st} layer, two more such bunches of orientation are expected plus a similar set for the rp_2 that is rotated by 102.8°. All these orientations are summarised in figure 3.12.

Connecting intermediate order with ripple period

The observed contrast variations with a periodicity spread around 42 nm might be explained by a height oscillation of the PTCDA carpet (see fig. 3.19). This change in height leads to the so–called (quantum) interference contrast as described in section 2.2.3 which results in contrast alterations with the corresponding period.

[7] A and B type molecules are introduced by Rohlfing [13] and shown in fig. 3.1.

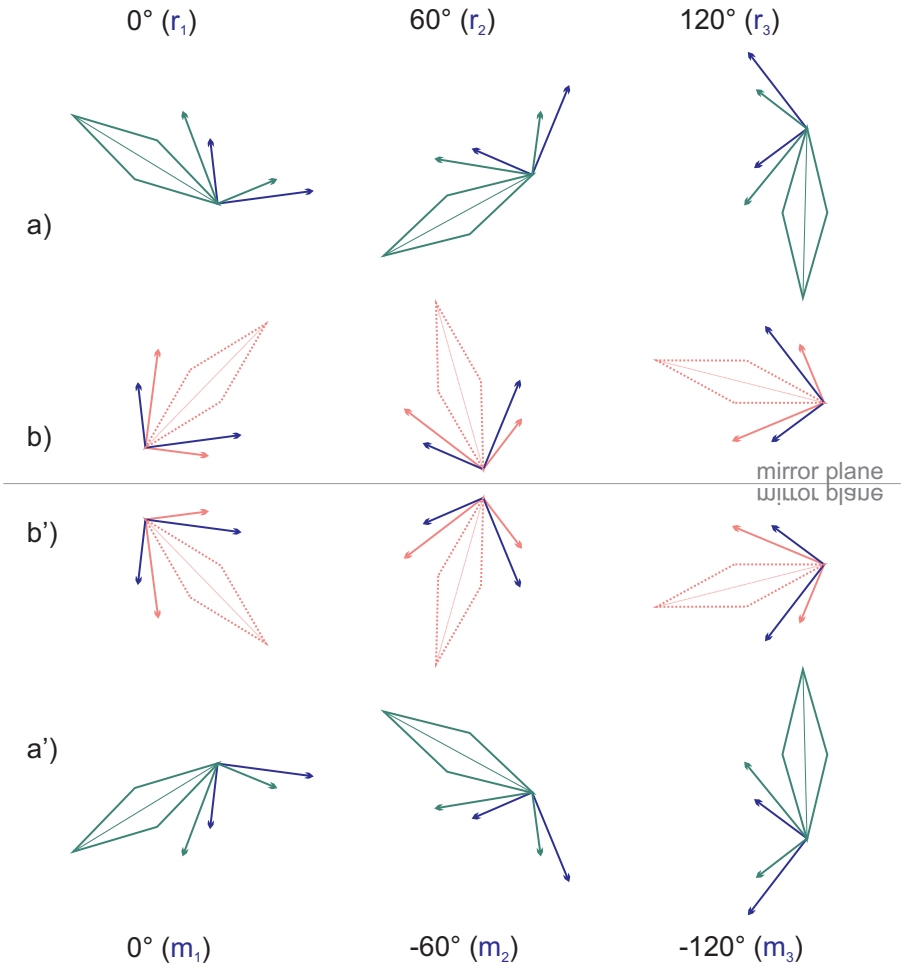

Figure 3.18: Illustration of the model predictions based on the underlying PTCDA/Ag(111) rotational domains. Two times six ripple phase domains are possible.

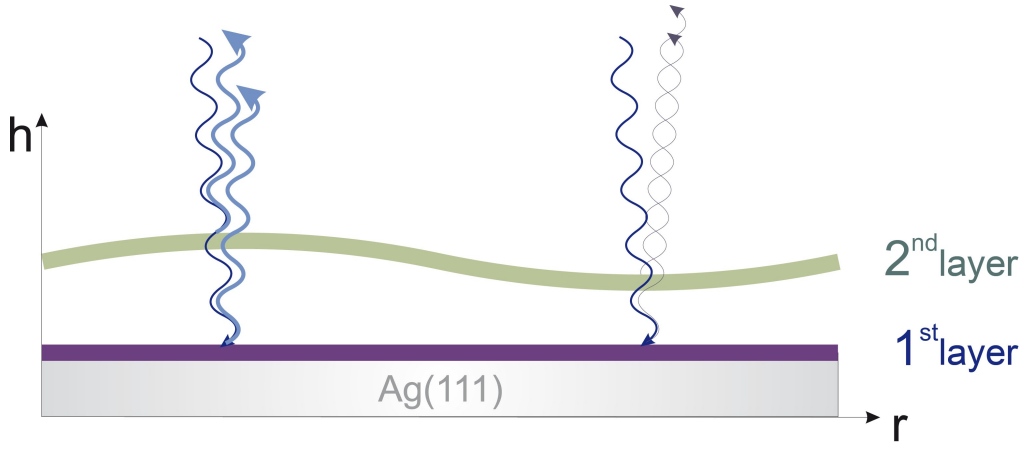

Figure 3.19: LEEM–image contrast model of the ripples. A height profile of the Ag(111) with first (flat, blue) and 2^{nd} layer of PTCDA is shown. Height oscillations for the ripple phase allow the electron beam to interfere differently at the peak and valley positions. Only the extremal case of constructive interference at the peak position is shown. Thus, the contrast could be tuned with the electron energy.

The period of the oscillations is suggested to be 3 and 4 times $d_{11}(d_{21})$ which results in either 36 or 48 nm period length. If the ripples do not only form in a single of these possibilities the observed period lengths between 38 and 45 nm can be explained as averages of ripples with 3 and 4 −-fold unit cell period.
LEEM–IV measurements would help to determine the height of variation of the ripples and verify the character of the contrast.

Summary

A new 2^{nd} layer PTCDA phase was observed in a wide temperature range around RT. It was characterised with BF–LEEM by its period and its real–space growth behaviour along the ripples. DF–LEEM shows, that in general there appear at least three different contrasts in the 2^{nd} layer on a single 1^{st} layer domain. The rp was investigated in–situ with µ–LEED that gives insight in medium range order of the phase. Period lengths and orientations were determined from these measurements. Finally a simple model is presented that allows to explain the findings. It just assumes new stacking together with slight strain of the rotational domains known from 1^{st} layer and bulk measurements. These findings lead to the following interpretation.

3.4.6 Interpretation

The data on the discovered rp presented in the first sections of this chapter can be well explained by the presented new stacking model, that introduces two further rotational domains besides the ones that Glöckler et al. [5] introduce for PTCDA/Ag(111). Besides the two α and β polymorphs found for bulk [58, 62, 63, 70], thin films [16, 79] and multilayered islands [12, 17] two further new polymorphs, rp_1 and rp_2, in the 2^{nd} layer are the consequence.
Within the nomenclature of the model the intensely investigated rp 2^r, shown in figure 3.15, is formed by a m_1–like domain on top of the standard r_2 phase. It is described by the *super*^{2}structure matrix (eqn. 3.6) of the polymorph rp_1.
Similarly large *super*^{2}structure domains are described for example for PTCDA and 3,4,9,10–perylene–tetracarboxylic acid diimide (PTCDI) on the Ag–Si(111)$\sqrt{3} \times \sqrt{3}R30°$ surface by Swarbrick et al. [82] and for tetracene on Ag(111) by Soubatch et al. [83]. While Swarbrick reports a kind of beat node of the lattices, as proposed by the model of this work as well, to describe the phenomenon, Soubatch reports on two alternating domains that form the new *super*^{2}structure where the 1^{st} layer and 2^{nd} layer intermix.

Discussion

These findings, m_1–like domain on top of r_2 in rp_1 polymorph, are corroborated by several independent measurements. (i)the stacking order is confirmed by the higher intensity of the µ–LEED–spots of the m_1–like domain compared to the also present r_2 domain. (ii) The growth along the ripples in the real–time investigation indicates a formation along the short diagonal d_{12} of the monoclinic *super*^{2}structure unit cell and hence a ripple period normal to d_{12} rather than along d_{11}.
Exactly this is confirmed (iii) by the orientation of the spot train in the µ–LEED of 30(2)° with respect to $\overrightarrow{a}_1$ and (iv) by the orientation (LEEM)along the ripples of 2^r (figure 3.15) in real–space of 119.7(25)°. Further (v) the large angular spread of the orientations of the investigated rp in LEEM is explained only with the help of the introduced model. Despite the large error bars for the orientations of up to 10° the spread would be too large otherwise. (vi) Supplemental to the model the three DF–LEEM contrasts on a single 1^{st} layer crystallite show that several polymorphs must be possible and that different rotational domains can grow on top of each other. This agrees with the coexistence of the $\alpha-$ and β–polymorph in PTCDA thin films on Ag(111) stated by Krause et al. [79].

Taking the molecular arrangement within the 2^{nd} layer into account the small difference of the strained rp unit cells to the known bulk and ML unit cells suggests

that such new rotational phases are likely to appear as well. Strain relaxation might be realised by the wavy structure of the PTCDA carpet. The interaction of the first with the second layer is considered with the alinement of one half of the molecules that forms the herringbone structure in the rp_1 and rp_2 with the (A) and (B)–type [13] molecules, respectively.
From the structural point of view the commensurate rp explains most of the unknown spots in the µ–LEED pattern and their relative intensities, if the other prominent contributions to the µ–LEED are related to the adjacent, known domain that is also partially selected.

The growth behaviour, especially the delayed start of the ripple domain 2^r, is explained in terms of competition driven growth found in section 3.3.2 on the growth of the normal polymorph β for the 2^{nd} layer [84]. But it might also point to a lower probability of these domains to form since they are strained with respect to the typical stacking and less well bound to the underlying domain. If the misfit influences the likelihood to appear, rp_1 is expected to be more common since it has a lower misfit to the β–phase than the rp_2 polymorph. This cannot be decided based on the available data, since the number of 13 ripple domains is too small for reliable statistics. Further the nucleation density of such rp–domains is required to determine the probability of formation. Despite the rather low correlation of these new polymorphs with the underlying 1^{st} layer it can be understood that they occur since their unit cells are closer to the relaxed β bulk polymorph than to the commensurate 1^{st} layer, which results in reduced strain.
The expected rather low correlation with the substrate also enables the wave–like carpet. This provides another mechanism for strain relaxation. Further it gives a hint for the preferred 1D growth direction that offers more relaxed well coordinated attachment sites.

No ripples oriented along 60°**.** The lack of ripples aligned with the 60° direction is quite surprising. This might be just coincidence due to the low number of domains. But it could be related to the vertical orientation towards the imaging system, hence aligned with the pixels of the charge coupled device (CCD) and therefore an artifact. But this is thought to be rather unlikely. Another alternative is a reduced horizontal resolution due to slightly astigmatic alignment, but this cannot be verified for the steps in the images because they are equally well resolved in all directions. It seems to be more reasonable that the symmetry of the preparation is somehow broken. Two options are the angle between evaporator and the surface, that is gracing of about 20°, or the stepped surface, that results from a slight miscut of less than 0.2°. Further one could think of strain in the Ag(111) crystal induced by the mounting to the sample holder that breaks the symmetry and hence makes

this orientation unfavourable. Because of the strong interaction of the 1^{st} layer with the substrate, as concluded from the commensurate growth and the small distance of only 0.29 nm [11, 66] between Ag(111) and PTCDA–molecules, its rotational domains would form as usual but the 2^{nd} layer might behave differently since the influence of the substrate is reduced. This is still an interesting question and subject to future studies.

All yet unexplained spots in the µ–LEED pattern can be explained as one further polymorph that might be formed from the m_1 domain mirrored along the $m_1[11] = b'_1 - b'_2$ direction. It appears similar to a standard rotational domain but turned by 75° towards the Ag(111) a_1 axis. It might be related to the dark phase 2^d that was observed in LEEM.
This dark phase might also have a similar molecular structure as the ripple phase but just grows flat lying instead of wave–like.
This shows that there are still plenty of questions remaining that should be addressed in future studies.

4

CdSe(Te)/ZnSe Quantum dots

So far, results of a detailed investigation were presented, that show in–situ and real–time the growth behaviour of the very first layers of the organic semiconductor PTCDA on the inorganic substrate Ag(111). In this second part again a semiconductor system was studied. But a very different and all inorganic material system was used. In this case the preparation procedure is reversed and hence less well defined than in the case of growing molecules. It is truly a very different approach to the formation of self–assembled, semiconductor nanostructures but the underlying mechanisms are similar and hence one has to pay tribute to the influence of the substrate. But also the structure and composition of the mediating cap plays a distinct role in the formation and alignment process.
For the CdSe/ZnSe quantum dots (QD) a stack of thin films of different composition is prepared first and the (trans–)formation of (self–)assembled nanostructures in a succeeding step was investigated. This approach shows that a large variety of pathways may lead to the formation of nanostructures. And with the following study it is demonstrated that an aberration corrected LEEM/PEEM–system is a great tool to investigate many different ways of such formation processes in detail, accompanied by detailed characterisation of the surface properties.

The CdSe/ZnSe quantum dot system. As already indicated, a large variety of different **approaches** of CdSe nano–particle formation exists. They might be divided into two branches of self–assembled structures: one kind bases on nano–particles that are fabricated, e.g., from solution and deposited, after the formation and selection is completed, onto a substrate for further studies [85, 86]. A second

Table 4.1: Collocation of some physical properties of the materials used for the QD sample system compared to the two common PTCDA substrates Ag and Au. The work function depends on the actual surface orientation while the lattice constant is given for the fcc (face centred cubic) unit cell.

Material	**Work function** [eV]	**Electron affinity** [eV]	**Heat of formation** [kcal/mol]	**Lattice constant** [Å]
Ag(111)	4.74 [40]			4.085 [69]
Au(111)	5.31 [40]			4.078 [91]
GaAs(001)	4.8 - 5.2 [92]			5.654 [93]
ZnSe		$3.51_{c(2\times2)}$ [94]		5.668 [94–96]
ZnTe		3.5 [94]		6.104 [93, 96]
CdSe	5.2 [54]	4.5 [94]	32.6 [97]	6.077 [94, 95]
CdTe	5.1 [98], 5.9 [99]	4.28 [94]	22.1 [97]	6.481 [94]
Se	5.9 [100, 101]			
Te	4.95 [101]			

type, which was studied within this work, forms strain induced – driven by the mismatch of lattice constants combined with adatom diffusion – at or close to the interface of a heterogeneous layer system.

The **deposition methods** range from evaporation of metals [7] and chemical vapour desposition (CVD) [87] via MBE [22, 88] to the careful preparation of strained epilayers by atomic layer epitaxy (ALE) [20]. A large variety of semiconductor materials, as Ge/Si (group IV), GaAs/(AlGa,In)As (III–V) [89, 90] and alloys of Cd and Zn (II) with Se and Te (VI), was used as well.

This work focusses on the **II–VI system** Cd(Se,Te)/(Cd,Zn)Se that more recently came into fashion. Properties of the involved materials are summarised in table 4.1. The reason for this development are on the one hand that methods became available, that allow to prepare thin films that are reasonably well, epitaxially grown and, on the other hand, that the optical properties of these materials make them attractive for device applications. The possibility to tune their large band gaps and lattice mismatch [102] in a rather wide range draws the attention to these materials as well. Quantum structures that base on these materials, promise various gaps (colours) combined with carrier confinement. This should enhance the efficiency of, e.g., LASERs and LEDs, especially in the high energetic range of the visible spectrum of light. Adopted device design also enables their use in photo detectors and solar cells.

The influence of structures and materials of the cap on the formation, the size distribution, the density and the structural quality and composition is of large interest. The detailed knowledge of the formation process allows to optimise the

process parameters and to tailor the properties of the device.
For industrial **applications** often a high homogeneity of these characteristics of the QDs are desired, as, e.g., for thin film solar cells on m^2–scale. Applications for QDs used as nano–photocathodes to produce hydrogen from water by sunlight [103], the change of the spectral response of photo resistors [104] or the enhancement of the quantum efficiency [6, 7] of thin film Si solar cells are discussed.
Strain relaxation is widely accepted as the driving force in QD formation for heterosystems. Besides the reduction of threshold power, which is attributed to the confinement of charge carriers by the dots, the relaxation of material increases the stability of the active region of the device [105]. Yet the question of the precise formation mechanism, e.g., the growth mode, is still under debate. However, indications for Stranski–Krastanov (SK) growth were already presented.
The preparation methods in case of the CdSe/ZnSe heterosystem differ further in the moment of QD–formation. The straight forward approach works without an additional preparation step and creates QDs directly in–situ during MBE at elevated temperature under Se–flux. Other preparations were suggested that introduce a two–step process. First, strained epilayers are deposited at reduced T onto the substrate and in a second step the QDs are formed by annealing. This second step again allows different approaches as in–situ annealing [88, 106, 107], (mostly under Se–flux) or in–situ desorption of an amorphous cap made from e.g α–Se [20, 108] or α–Te [18, 109–112].
These **two–step processes** are of special interest since they allow to control the size, density, and distribution of the formed QDs. Although it is known that subsequent capping (often done by ZnSe) of the QD layer may strongly alter the layer, in many studies the samples are capped after preparation of the dots (e.g [18, 113]). Other investigations are carried out in air. The most typical methods are (in–situ) AFM characterisation of the topography, cross–sectional TEM or PL measurements. Others use X–ray diffraction techniques to investigate the strain distribution within the dots [23, 114]. The sample preparation is typically monitored by RHEED.
But no study was found to date that addresses **in–situ and in real space** the formation process and the correlation of the QDs with the various features and properties of the substrate and the cap. In this work the formation and arrangement of Cd(Se,Te)/ZnSe QDs was investigated in–situ by time resolved LEEM supported by immediate, in–situ XPEEM, µ–LEED and µ–XPS studies of identical and nearby surface areas. These in–situ, real–time measurements were accompanied by on air AFM measurements.
In the following chapters the questions of the material distribution and arrangement and its change during the T–ramp were in the focus of the investigation. Quite some answers on, e.g., the composition and structures of the cap and its correlation with features of the QD–covered surface can be given. The decapping process was observed laterally resolved in–situ and in real–time for the first time.
Hence the use of SMART enabled a first, quite promising study of such a complex

system as the formation of realistic quantum dots from a stacked layer system. This is another step towards what Bauer [25] expected excitedly from aberration corrected LEEM/PEEM systems.
Not until the need for reasonably high resolution combined with extraordinary transmission is fulfilled, direct observations may be made. It is emphasised at this point, that the rise in transmission is likely more important than the enhanced resolution, both provided by the the aberration correction, since one can only make use of the resolution if it is possible to visualise the objects on reasonable time scales.

4.1 The MBE grown sample stack

The sample is a layered stack (see table 4.2) of II–VI semiconductors grown by conventional MBE in two interconnected RIBER Compact 21 (GaAs) and RIBER 32 (II–VI) [110, 111] chambers by Alexander Frey from the group of Prof. Karl Brunner, Experimentelle Physik III of Universität Würzburg. It was fabricated and packed in Würzburg and was shipped for in–situ decapping and investigations to the SMART in Berlin.

4.1.1 Stack composition

The carrier wafer is from silicon doped, epi-ready GaAs:Si(0 0 1) and a buffer of about 200 nm of GaAs:Si was epitaxially deposited to improve the homogeneity and smoothness of the surface.
On top of this III–V semiconductor the active II–VI layers of ZnSe and CdSe were grown successively, at temperatures of 573 K and 503 K, respectively. They were grown in a layered fashion with process parameters carefully determined in advance by monitoring RHEED oscillations. For homogeneity of the layers across the wafer it was rotated during growth.
35 of the 40 nm ZnSe substrate layer were iodine doped to enhance the conductivity of the sample to reduce charging and therefore to improve the quality of data from electron microscopic studies. The strained 3.5 layers of CdSe were covered at 300 K by a nominally 15 nm thick layer of amorphous α–Te to mediate CdSe/ZnSe nanostructure formation while being desorbed in situ [18, 110, 112].

Table 4.2: Stack composition of the 'cb' sample series according to the growth protocols of the MBE. From each wafer several fractions were used as samples. Accentuated are the investigated interfaces ZnSe/CdSe and CdSe/α-Te. The dopant concentration of the substrate buffer layers is about $5 \times 10^{18}\,\mathrm{cm}^{-3}$. In brackets the temperature during growth is stated.

Series	**cb3446**	**cb3466**	**cb3470**	**cb3494**
α-Se	1 µm	1 µm	1 µm (313 K)	1 µm (298 K)
α-Te	15 nm (300 K)	—	—	15 nm (298 K)
CdSe	3.5 ML (503 K)	3.5 ML(503 K)	5 ML (503 K)	3.5 ML (503 K)
ZnSe		5 nm (573 K)	5 nm (573 K)	
ZnSe:I	35 nm	95 nm	95 nm	35 nm
GaAs:Si		200 nm		

4.1.2 Transport precautions

For the transport from Würzburg to Berlin on top of the α–Te a thick layer of about 1 µm of α–Se was deposited in UHV. Then the samples were stored in several shells of N_2 atmosphere to prevent them from oxidation and carbon contamination during the long time scales of transport of several days up to months of storage, waiting to be used in a suitable beamtime.
In Berlin the samples were kept in N_2 atmosphere of a glove box. There they were mounted to the specific LEEM/PEEM sample cartridge. The in–air transfer from the glovebox to the UHV analysis chamber was done within seconds. During this time the surface was protected by the α–Se cap.

4.1.3 Contamination evaluation

These transport precautions have proven adequate as demonstrated in the following.

Homogeneity of the α–Se cap. First, as determined by AFM (see figure 4.1), the Se layer covers the whole surface without holes. The height varies within ± 0.45 nm around the average. This implies that the holes in the α–Te cap (see cp. 4.2) are filled well and the α–Se protection is homogeneous across the whole surface.

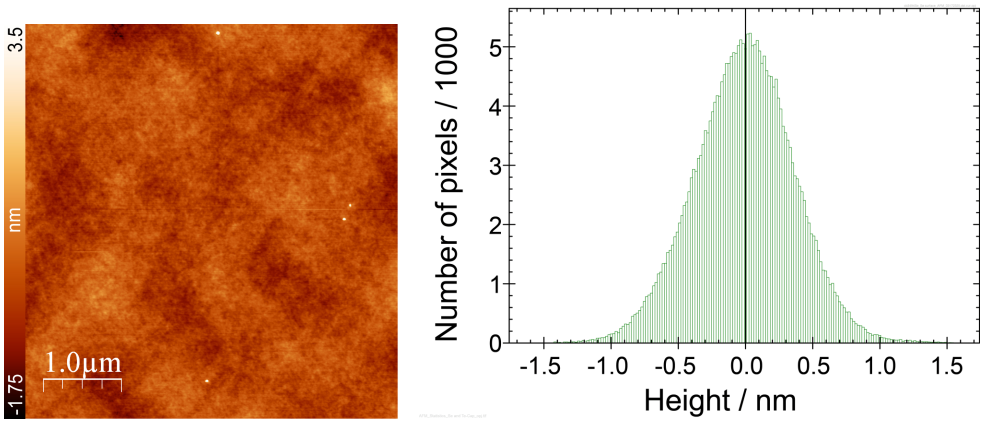

Figure 4.1: AFM image (left) shows the topography of the 1 µm protective cap from α–Se. A very smooth, closed surface with root mean square (RMS)=0.36 nm and 3.5 nm peak-peak distance. The average surface variation is given by the FWHM = 0.85 nm of the height histogram (left).

Elemental contamination

Secondly, not any oxygen contamination of the surface after removal of the α–Se protection was detected by the µ–XPS measurements shown in figure 4.2. This is a proof for a reasonably well protected surface during transport. The spectrum was taken with a photon energy of 650 eV in the spectroscopic mode.

Detail on overview spectra. The full range spectrum is composed from a series of about 13 eV wide sections of the whole spectrum. Each section represents the energy window on the screen that was recorded at once. The bias voltage was increased stepwise by 10 V for each succeeding spectrum. The colours in the spectral data illustrate the widths of the partial spectra. All single parts were intensity corrected by the identical flat field (FF) and offset values. For details on intensity correction see also section B.1.

Assignment of spectral features. XPS lines and Auger features of the contributing elements and the possible contaminations are labelled at the appropriate positions in the figure. The energies are taken from [43] if not otherwise stated.
Most prominent are the Te lines, especially the Te 3d doublet at 573.1 eV and the Te 4d around 40.5 eV. Also the Te MNN Auger features between 150 and 300 eV are strong. The step–like feature at 110 eV is, in accordance with [43], assigned to the Te 3p lines mixed with some contribution from Cd 4s.
Se shows at the Se 3d line (around 55.6 eV) two chemical species, the pure Se from the α–Se cap and the one bound in CdSe. Se 3s and Se 3p are visible and labelled

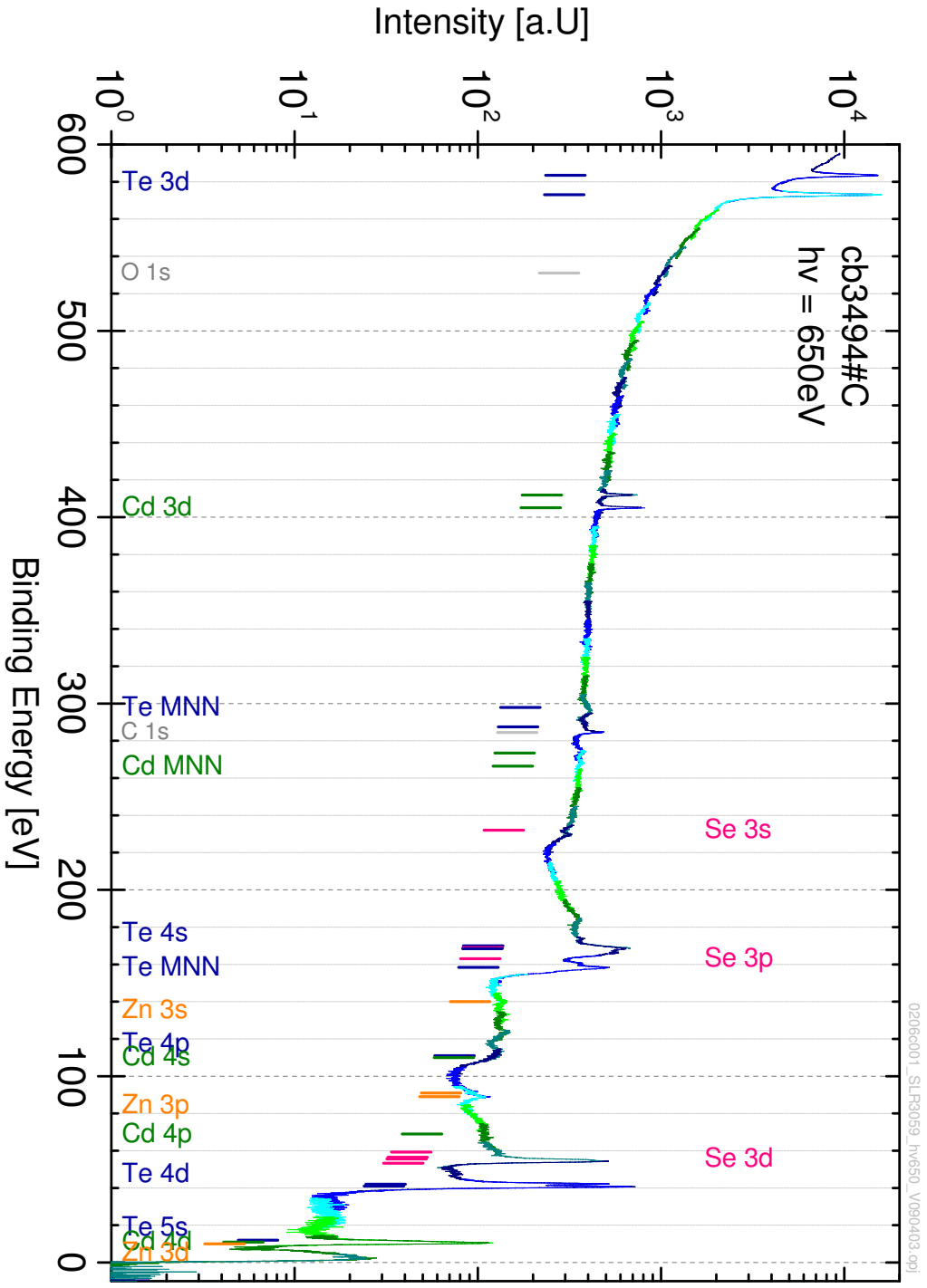

Figure 4.2: µ–XPS spectrum of the α–Te capped sample illuminated with $h\nu = 650\,\text{eV}$. Oxygen contamination can be excluded from the absence of the O 1s (∼533 eV) feature. Also no contribution to the Se 3d feature, which would lead to a large shift of about 3 to 4 eV, was observed. A small carbon contamination is seen at about 285 eV with the underlying Cd MNN auger feature.

as well.
Cadmium is clearly identified by the Cd $3d$ doublet at about 405.1 eV. Also weak contributions from the other Cd–lines (e.g. Cd $3p$ at 63.9 eV [115] and the Cd MNN around 270 eV are identified.
Zinc is the most deeply buried element but also Zn traces are found in the spectrum. The respective lines are marked in orange. The most prominent are the Zn $3p$ at 88.6 and Zn $3d$ at 10 eV which overlaps with the Cd $4d$ lines (11.7 and 10.7 eV [115]). But also the Zn $3s$ is found at 139.8 eV[116].
Some carbon is found by the C $1s$ at about 285 eV but at the position of O $1s$ at 531 eV no intensity was detected.

Result concerning the contamination issue. It was found that within the sensitivity limits contaminations of oxygen (e.g. O 1s at ∼531 eV) can be excluded. Also, neither oxidised Se nor Te were found. This would lead to ∼4 eV [43, 117] well separated and intense (large cross section, therefore high sensitivity) Se $3d$ and Te $4d$ features which are not observed.
Only some contamination by C is visible. Its inhomogeneous distribution is discussed in section B.3. It is probably adsorbed from the residual gas in the UHV either in the measurement chamber of the SMART after removal of the α–Se protective cap and/or while being fabricated at the MBE in Würzburg before the α–Se was deposited.

Summary on stoichiometry. The spectrum qualitatively represents the expected, very clean surface of the sample still covered with α–Te. Holes in the cap[1] allow Cd, Zn and Se from the underlying substrate to be visible as well. In case of Se a second contribution from the mostly desorbed α–Se is seen as well (see also figure 4.11).

4.1.4 α–Te desorption

The last step of sample preparation, the CdSe/ZnSe quantum dot formation mediated by the desorption of α–Te, was performed in–situ and in real–time while being observed enduringly. It is described and evaluated in section 4.3.

[1] For a description of the inhomogeneity of the α–Te cap see also the following section 4.2.

4.2 Inhomogeneous distribution and order of cap–Te

Since the Te cap is discussed [18] as mask for the formation and arrangement of the CdSe–QDs, it is important to know about the distribution, arrangement and order of the Te. Therefore this chapter addresses the question on the lateral distribution and structural phases of the participating elements. With the spectroscopic contrast in XPEEM layer thicknesses can be determined. The different film structures were analysed using LEEM in combination with µ–LEED. AFM measurements support these in–situ measurements with topographic information. The findings allow to draw a comprehensive picture of the Te cap, as a heterogenous, amorphous thin film with holes and embedded crystallites.

4.2.1 Structural investigation

To examine the structure the surface, covered with α–Te, LEEM and µ–LEED measurements were performed. The LEED pattern shows weakly the expected (001) surface with a (2x1) reconstruction of the underlying CdSe superimposed by a broad, diffuse BG attributed to amorphous Te (α–Te). This indicates a Se–reconstructed surface following the findings of Weigand et al. [118] for the ZnSe surface. The LEEM images reveal a rich variety of structures that are quite pronounced in the very low energy range between 0.5 and 2.5 eV.

In figure 4.3 a series of BF–LEEM images from this energy range and additionally an image at 8 eV are shown that were recorded at an elevated, stabilised temperature of 333 K. Intensities were linearly scaled to optimise contrast. The 1 eV image shows the FoV where the blue box marks the AoI presented in the other pictures.
At the bottom of the figure an intensity plot of the profiles taken along the red bars, averaged along the [110] direction is given.
Black arrows in all images indicate the identical positions of selected, specific surface features as tip, hole and line[2]. Depending on the kinetic energy they show more or less strong contrast.
The crystallographic directions were determined from the µ–LEED insets in figure 4.23 that were recorded after in–situ desorption of the α–Te cap. Since the sample was just translated in–situ in the µm–range between the two measurements the orientation did not change.

[2]Features are identified by their electron optical behaviour, XPEEM (sec. 4.2.2) and AFM (sec. 4.2.3).

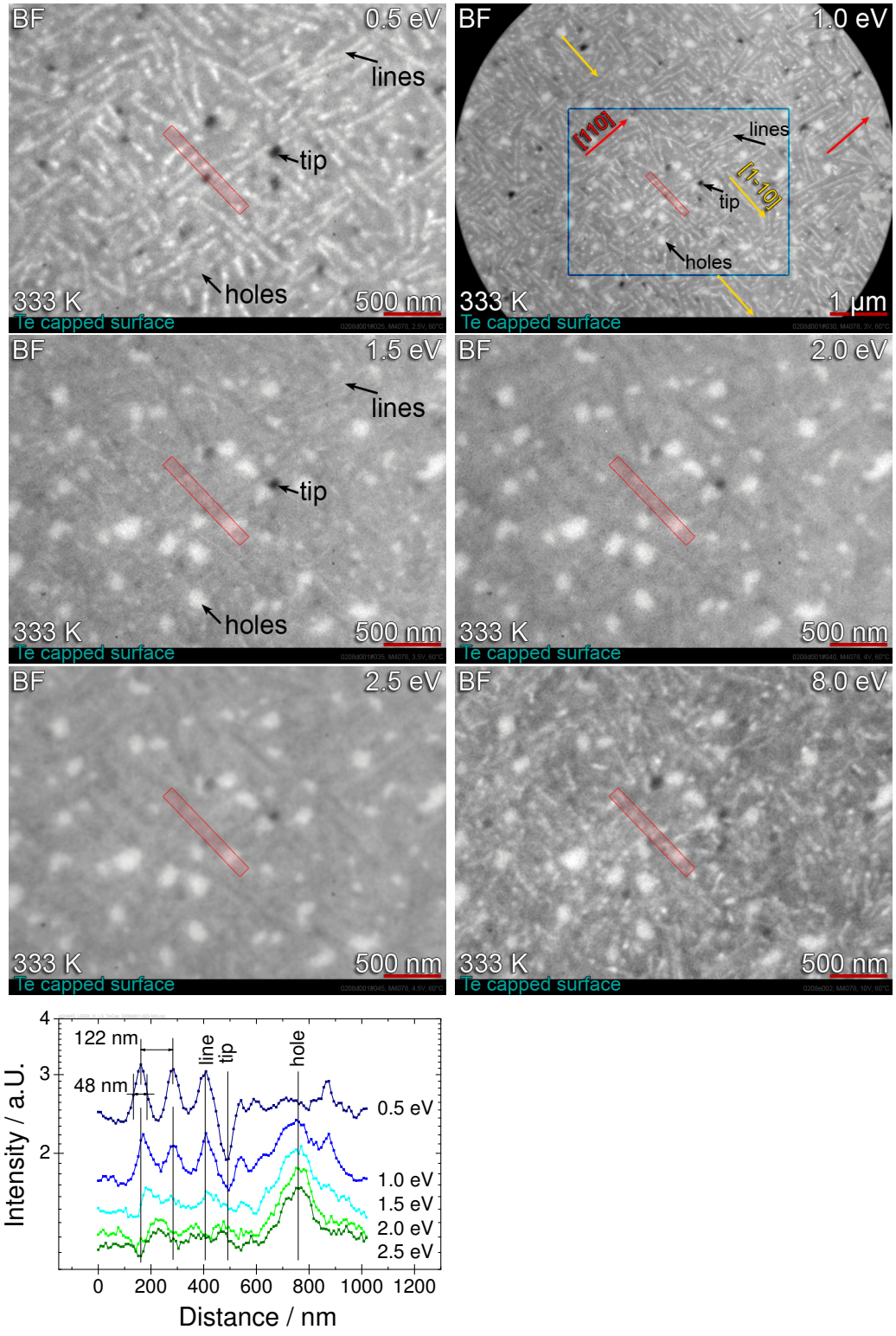

Figure 4.3: LEEM images (contrast optimised) of the α–Te cap at different electron energies E_{kin}. Line profiles (avg. across the [110] direction of the red rectangle) show changes in contrast correlated with the surface features, i.e. holes, lines and tips with respect to the BG.

Dimension and orientation of the features

The diameters of the **holes** range from several ten to a few hundred nm and cover about 10(3) % of the full surface area. This can be reasonably well determined since their contrast is MTF≈ 16 % in the 2.5 eV image.
Due to the lower contrast of $MTF < 9\,\%$ and the presumably faint and steep shape, the measurements of the dimensions of the **lines** are less reliable. The profiles cross some of the most pronounced lines. There the FWHM is determined as 48 nm whereas neighbours are separated by 122 nm. The lines are typically several hundred nm up to µm long and preferentially aligned along the [110] and [1$\bar{1}$0] direction of the substrate. Sporadically they are oriented in the [100] and [001] directions as well. These features cover about 20(10) % of the investigated FoV in the 0.5 eV image. This value is strongly influenced by the resolution which is rather uncertain for the α–Te cap.
No reliable diameter of the **tips** can be derived since it depends strongly on E_{kin} due to the distortion of the electrostatic immersion field. Also the extremely low depth of focus constrains the resolution of features on a surface whose topography ranges from 12 nm deep holes up to tips with about the same height above the average surface (seen in AFM fig. 4.16).

Lines and holes differ in atomic order

The intensity of lines and holes with respect to the BG changes drastically with E_{kin}. This indicates a crystalline order of the atoms at least within parts of these features. It is remarkable that the change in contrast is opposite which shows that the structures of these features are different. In case of the so–called lines even a reversal of contrast is observed leading to dark lines on the medium grey BG, e.g., in image 2.0 eV where the holes appear bright.
The faint, linear features in the 8 eV image are at different positions than the lines in image 0.5 eV. They are parallel to them an in their neighbourhood. This indicates a further type of structure. Their position coincides with the cracks or hole–chains identified during desorption in section 4.3.2. They may be present in the 2 to 2.5 eV images as well but just hardly visible due to the low contrast and imperfectly tracked focus[3].

[3] In this low energy range, the focus depends strongly on E_{kin} (see fig. B.2). Linear focus tracking, as used, hence limits the resolution.

Summary and conclusion

Several different structures were identified with BF–LEEM–I–V in the α–Te cap, namely holes, cracks or chains of tiny holes, tips, lines and the BG. Their dimensions were quantified and a distinct alignment of the lines with the crystal directions of the underlying CdSe was found.
Tips were identified by their electron optical behaviour at $E_{kin} \sim 0\,\text{eV}$ and by comparison with the AFM data presented later in section 4.2.3. Also the **holes** are clearly seen in the AFM images and confirmed as voids in the α–Te layer by XPEEM in the following section. The tiny features, especially present in the 8 eV image, are assigned to **cracks** or hole–chains due to their behaviour during desorption and in agreement with the AFM findings. Last, the **lines** are most likely **Te–crystallites** embedded into a matrix of amorphous Te. They must not be mixed up with cracks, that are undoubtedly found in their direct neighbourhood. The crystallinity is demonstrated by the contrast reversal with respect to the BG of the amorphous Te matrix when changing energy. They further show a different behaviour than holes and cracks. Their composition, mainly Te, is confirmed by their position right between holes and cracks, where the Te–signal is most intense (see section 4.2.2). Further a transition of the α–Te cap from an amorphous to a polycrystalline phase during desorption was found with RHEED by Mahapatra [18]. The clear alignment of the Te–crystallites with the substrate is a sign for the interaction between cap and CdSe–layer already in this early state of QD preparation.

4.2.2 Nano–spectroscopy of the α–Te cap

Two sets of spectroscopic image–stacks[4] from two samples, #C (cb3494#C) and #D (cb3494#D), are presented. The first was recorded with intensity optimised photon and kinetic energy. The photon energy was adjusted to the absorption cross section according to Yeh [46] summarised in table 4.3 and the flux of the beam line UE49PGMc (provided by BESSY–II [4]). Further care had to be taken not to have an Auger–feature within the energy range of interest. The kinetic energy was chosen as large as necessary to leave the high BG intensity of the secondary electrons behind, to gain good image contrast and yet as small as possible to keep an acceptable transmission $T \propto 1/E_{kin}$. This typically lead to quite surface sensitive measurements, since under these conditions E_{kin} is close to the minimum of the IMFP in the universal curve (fig. 2.3). Hence the following photon energies where chosen for the relevant elemental peaks

- Cd 3d, $h\nu = 470\,\text{eV}$ (figure 4.4)

[4] A detailed description of the information content of stack–figures is given in section B.4.2.

Table 4.3: XPS properties of the elements under consideration. For selected elements the experimental electron binding energies E_{bin} with the doublet splitting ΔE_{bin} are collected from references for the compounds (Cd,Zn)(Se,Te) and for the elements otherwise. The theoretical values of photoionisation cross sections σ and elemental binding energies are taken from Yeh et al. [46]. The lines of **major interest** are printed in bold face.

Z	**Line**	E_{bin} **(most intense)**			σ [46]		
		exp.	ΔE_{bin}	**theo.**	**at**		
		[43, 116, 119]	[43, 115, 116, 119]	[46]	140 eV	230 eV	470 eV
		[eV]	[eV]	[eV]	[Mbarn]	[Mbarn]	[Mbarn]
30	Zn 4s		—	8.4	0.038	0.018	0.006
52	Te 5p			8.6	0.064	0.040	0.018
6	C 2p			9.0	0.064	0.014	0.001
30	**Zn 3d**	10	0.1	10.1	**5.667**	2.474	0.461
48	**Cd 4d**	11	1.0	10.7	**0.324**	0.678	0.361
8	O 2p			14.2	0.498	0.122	0.014
34	Se 4s	14.7	—	14.6	0.095	0.048	0.017
52	Te 5s	12	—	17.1	0.073	0.037	0.013
6	C 2s		—	17.5	0.202	0.070	0.014
52	**Te 4d**	40.5	1.5	40.4	0.359	0.822	**0.561**
52	Te 4p	111		103.3	0.524	0.458	0.261
52	Te 4s	170	—	169.4	—	0.203	0.086
52	Te 3d	573.1	10.39	573	—	—	—
34	**Se 3d**	55.6	0.86	54.1	**6.651**	4.384	**1.028**
34	Se 3p	160.1	5.8	160.7	—	0.720	0.492
34	Se 3s	229.5	—	229.6	—	0.237	0.121
48	Cd 4p	69		63.9	0.446	0.388	0.204
48	Cd 4s	110	—	109.8	0.236	0.171	0.067
48	**Cd 3d**	405.1	6.74	405.2	—	—	**3.907**
30	**Zn 3p**	88.6	2.8	88.6	0.585	**0.762**	0.387
30	Zn 3s	140	—	139.8	0.302	0.223	0.099
6	C 1s	284.5	—	290.9	—	—	0.315
8	O 2s	23	—	23	0.337	0.143	0.034
8	O 1s	531.0	—	531	—	—	—

- Zn 3p, $h\nu = 230\,\text{eV}$ (figure 4.5)
- Se 3d, $h\nu = 140\,\text{eV}$ (figure 4.6)
- Cd 4d/Zn 3d (+VB), $h\nu = 140\,\text{eV}$ (figure 4.7)
- Te 3d, $h\nu = 650$ and $750\,\text{eV}$ line (figures 4.8 and 4.9)

in case of sample cb3494#C.
For sample cb3494#D a fixed photon energy $h\nu = 470\,\text{eV}$ was chosen for

- Cd 3d (figure 4.10)
- Se 3d (figure 4.11)
- Te 4d line (figure 4.12)

to allow for higher penetration depths and to enable quick and better alignment of image focus rather than changing the illumination and adjusting its focus.
For both samples the thickness of the Te–layer at the hole positions was determined as presented in section 4.2.2.
In the following the distribution of the elements and the resulting stacking and arrangement is discussed having in mind the interaction strength of electrons and photons with the matter they pass. Keep in mind that the large scale intensity variation, the increasing intensity from the image side to the centre, arises from the intensity profile of the illuminating X–ray beam.

Signal from the cap materials α–Te and α–Se

In figures 4.8 and 4.9 the Te $3d$ signal at $h\nu = 650$ and $750\,\text{eV}$ is shown for sample #C and in image 4.12 the Te $4d$ signal at $h\nu = 470\,\text{eV}$ for sample #D surface is presented. E_{kin} were about 80, 180 and 430 eV. All three images show that Te covers the surface widely but there are areas with lower signal intensity with diameters of typically a few hundred nm. These features were identified as the "holes" in α–Te cap. While in the X650 eV image the $Hole_1$–Cap–$Hole_2$ contrast is about 20 % it is 35 % in the X750 eV image. Moreover the Te spectrum in the profile taken from the X650 eV image at the cap position demonstrates that there is also Te at the bottom of the holes.
These findings clearly show that i) the cap–Te is not homogeneously distributed (i.e. the Te film has holes) and ii) there is a thin remainder of Te at the bottom of the holes. The energy dependance of the IMFP of electrons is used later (see sec. 4.2.2) to determine the thickness of the bottom Te layer.

Besides the Te signal also a quite strong Se signal was found, not just from within the holes but also from the cap. This is shown again for both samples in figures 4.6

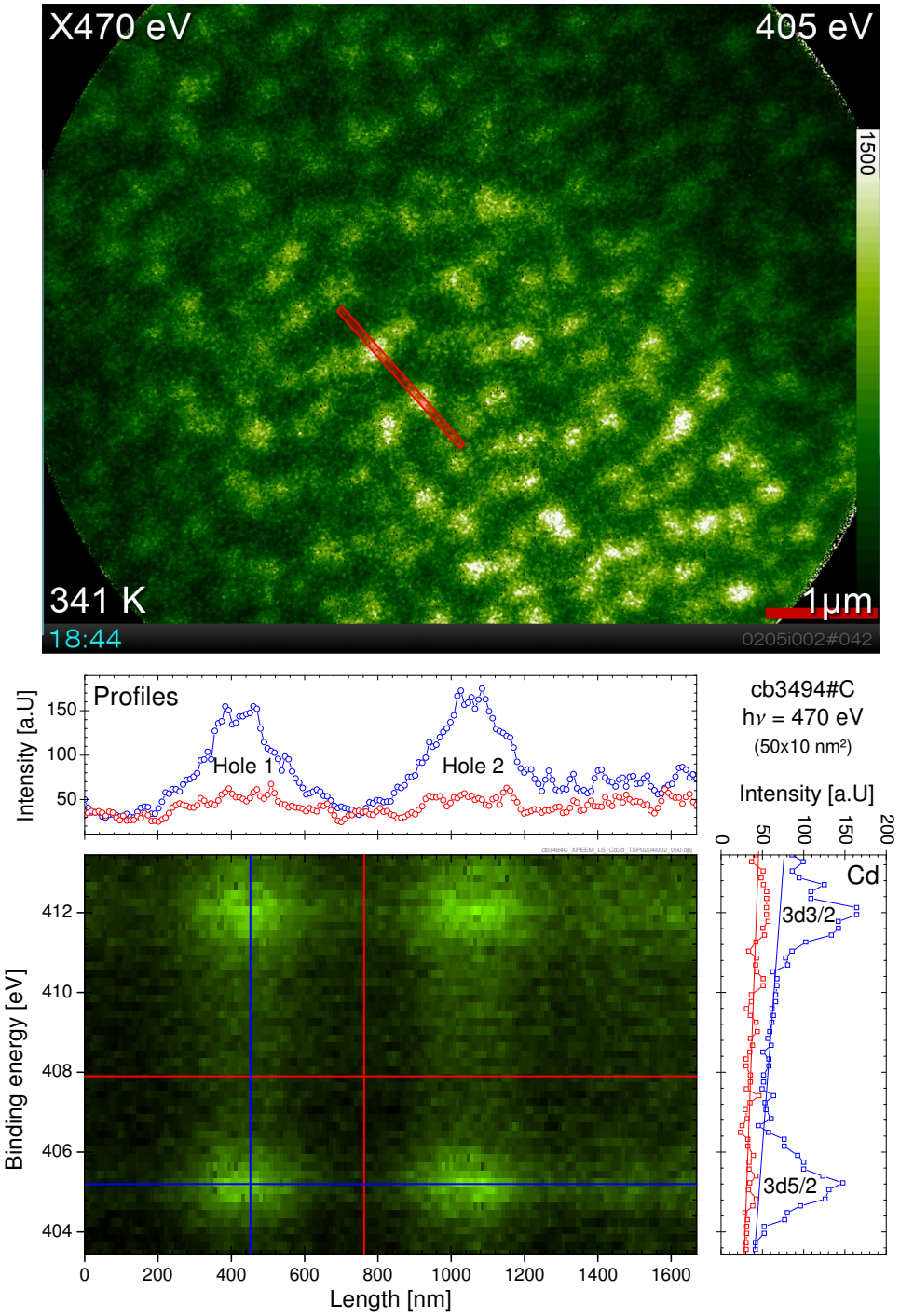

Figure 4.4: The top figure shows a 2D–plot of the α–Te capped surface with Cd $3d_{3/2}$ contrast. The photon energy was 470 eV, the electron binding energy E_{bin}=405 eV. A stack profile for the range of E_{bin} was taken along the red bar, averaged across its width. A length vs. E_{bin} plot is given in the lower figure. Profiles along the length and the energy axis were taken. They originate from the blue and red, vertical and horizontal lines.

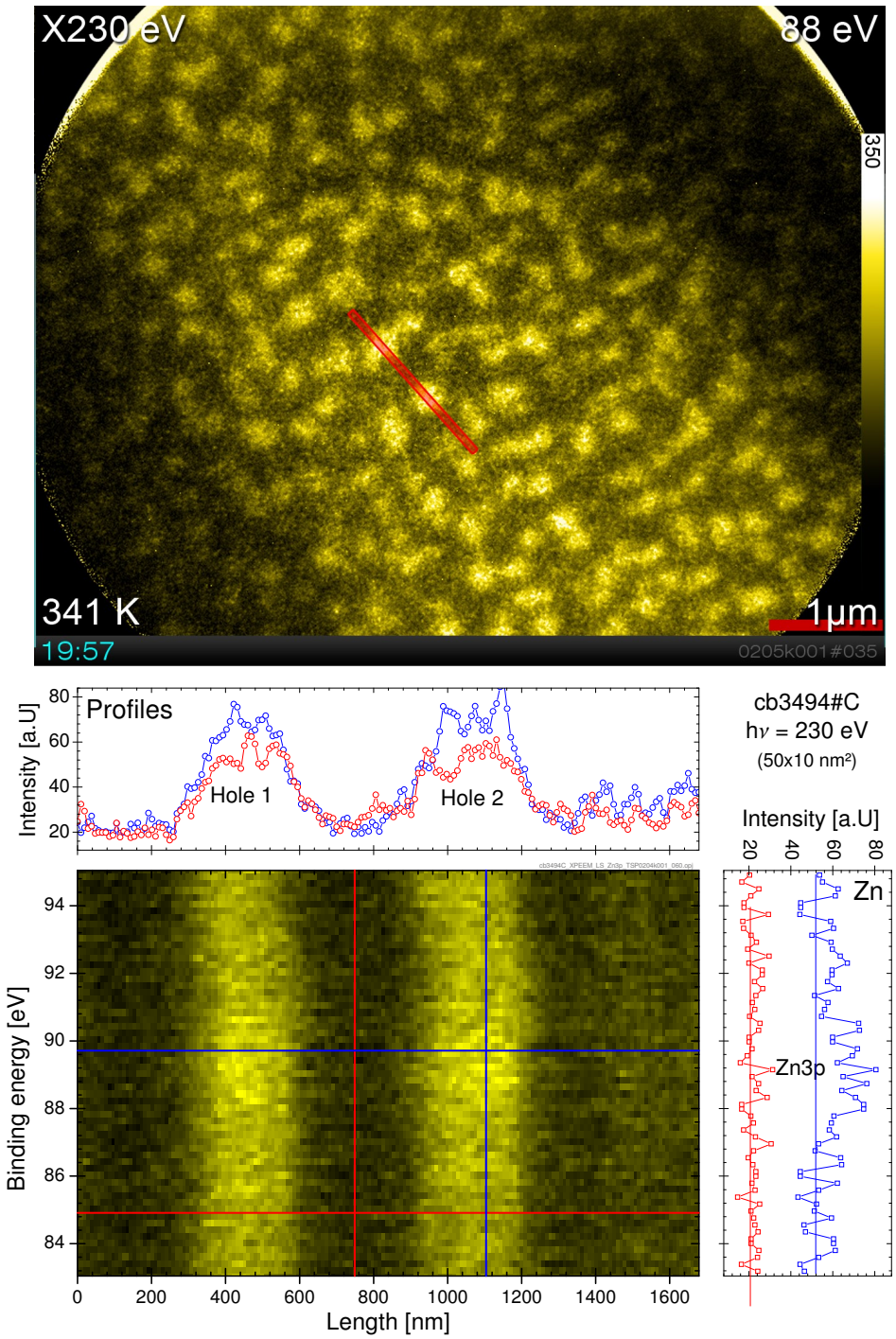

Figure 4.5: The top figure shows a 2D–plot of the α–Te capped surface in Zn $3p$ contrast. The photon energy was 230 eV, the electron binding energy 88 eV. Diagrams and profiles are derived analogue to fig. 4.4. The pronounced contrast at any energy position in the spectrum is due to the large intensity difference of XPS–BG between cap and substrate.

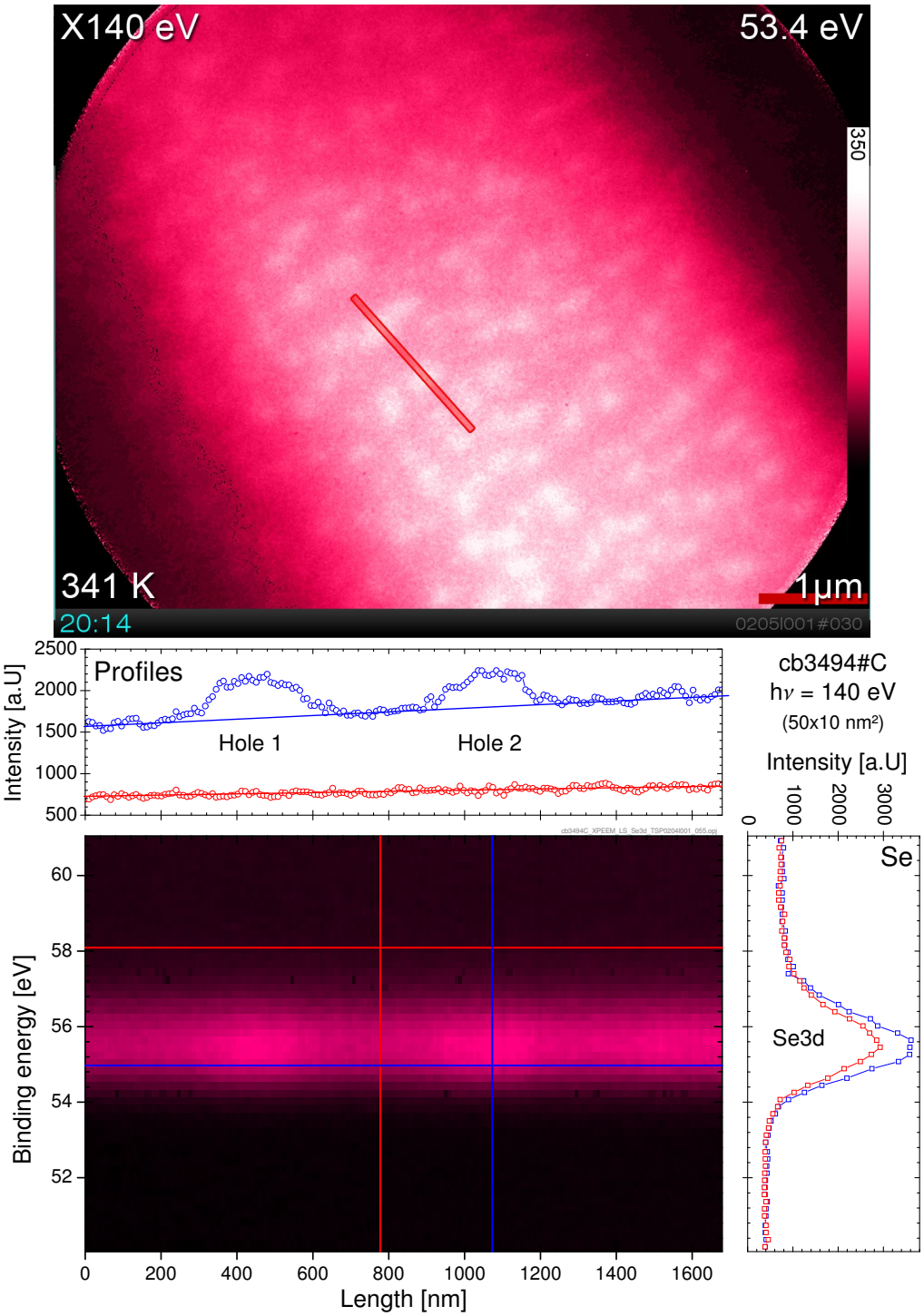

Figure 4.6: The figure shows an XY–plot of the α–Te capped surface at the Se 3*d* line. Diagrams and profiles are derived analogue to fig. 4.4. The photon energy was 140 eV, the electron binding energy 53.4 eV. Thus, the images were recorded with high surface sensitivity.

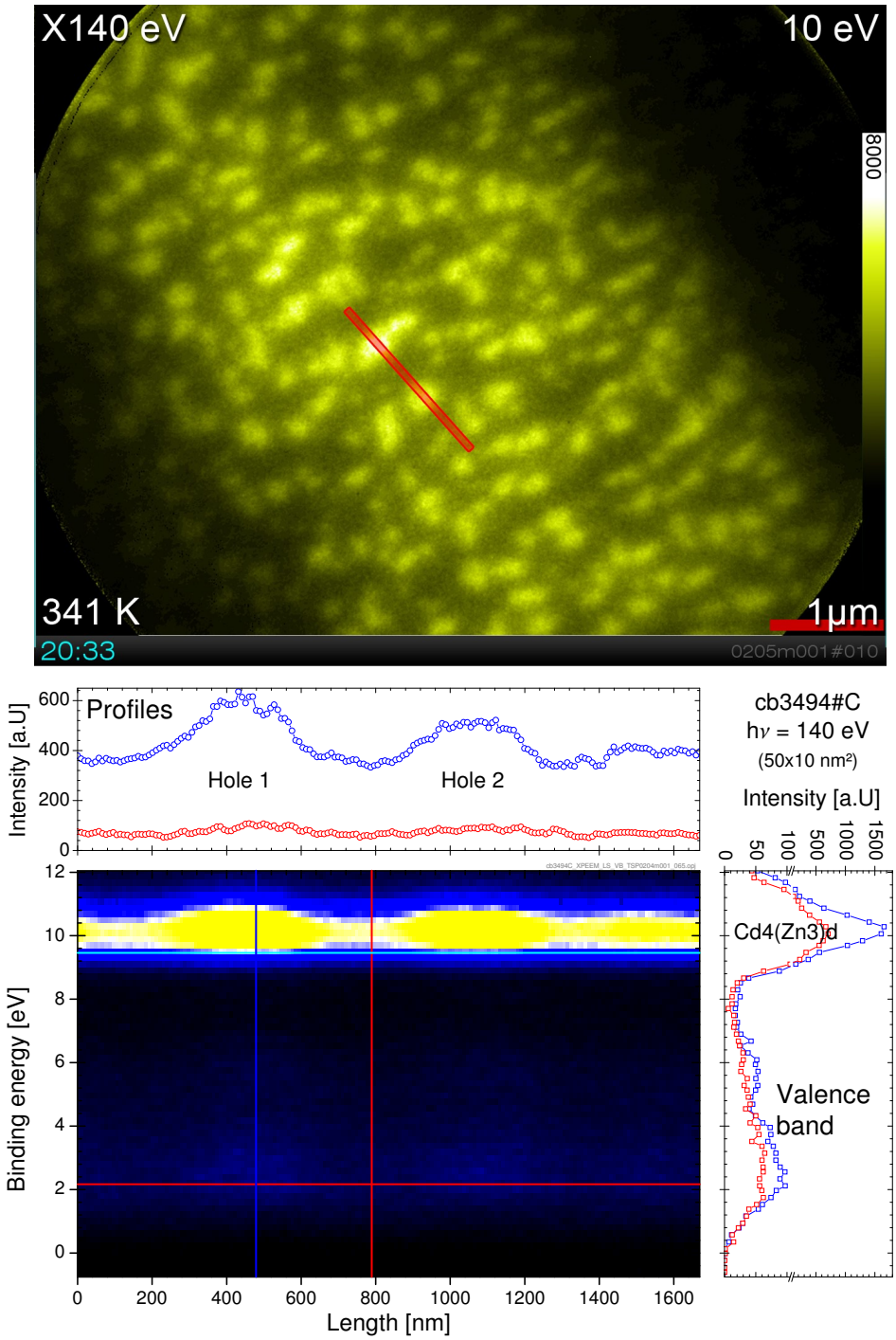

Figure 4.7: The top figure shows a 2D–plot of the α–Te capped surface with mixed Cd $4d$(Zn $3d$) contrast. The photon energy is 140 eV, the electron binding energy 10 eV. For further information see previous figures. Note the discontinuous intensity scale in the spectrum. Also, the contrast in the blue length profile is taken close to the Cd $4d$ (Zn $3d$) peak.

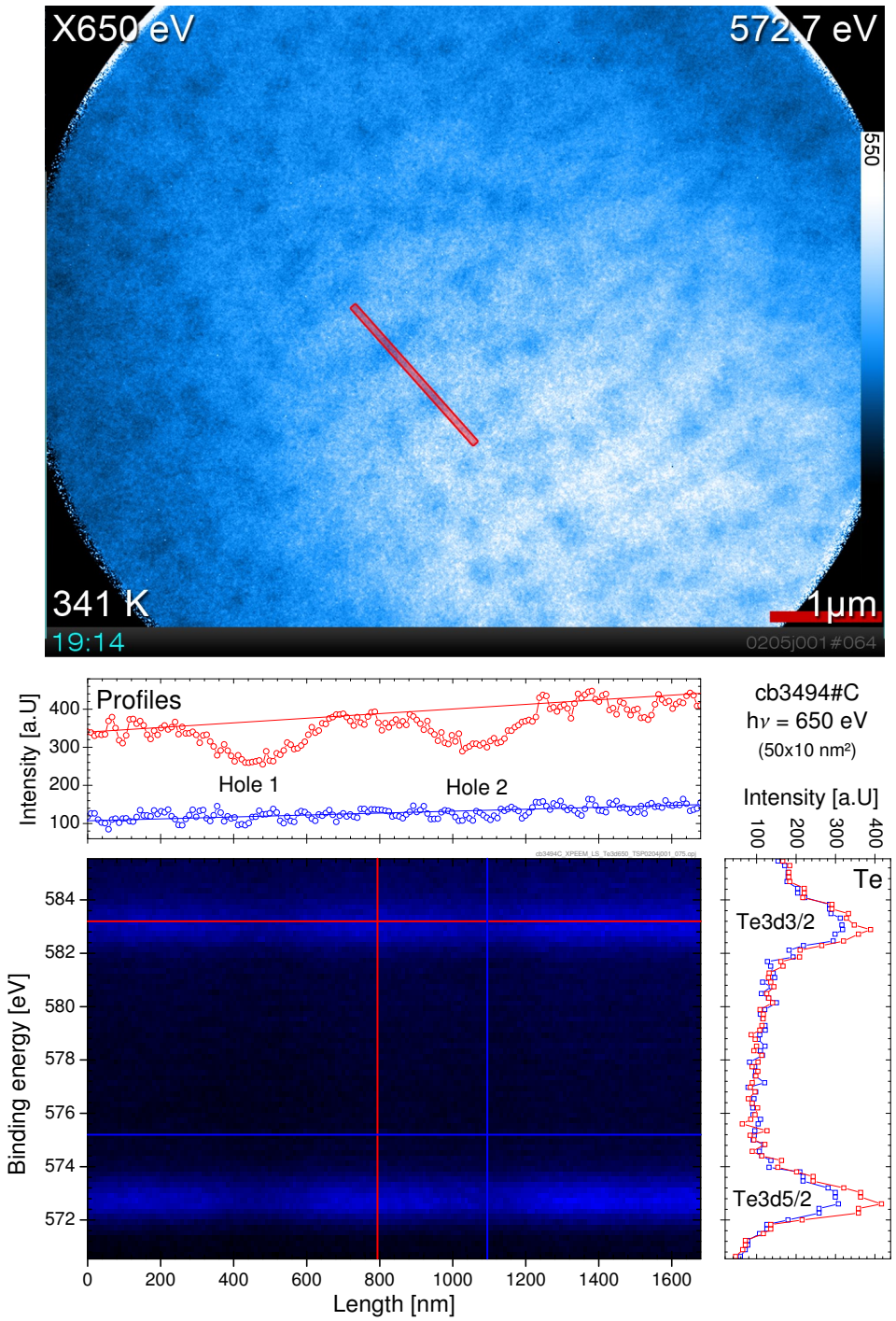

Figure 4.8: 2D–plot of the α–Te capped surface at the Te 3*d* line. The photon energy is 650 eV, the electron binding energy 572.7 eV. For further information see fig. 4.4. The chosen parameters make this experiment very surface sensitive. Thus, the contrast is low since the Te 3*d* doublet is seen in the holes as well.

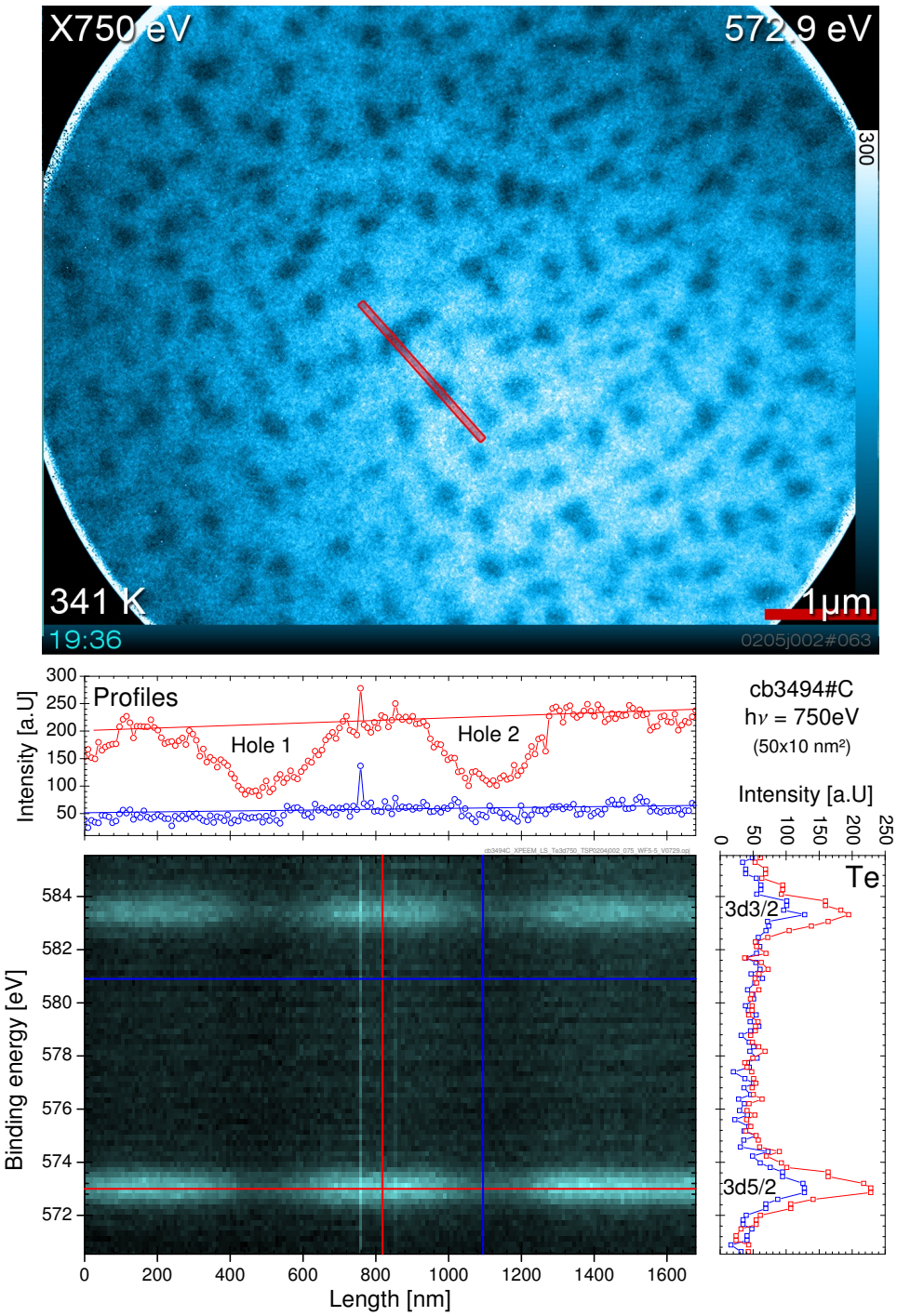

Figure 4.9: As in figure 4.8, the surface at the Te 3*d* line is shown, but the photon energy was elevated to 750 eV (electron binding energy as before). The higher E_{kin} of the photo emitted electrons makes this experiment less surface sensitive, hence holes show an enhanced contrast.

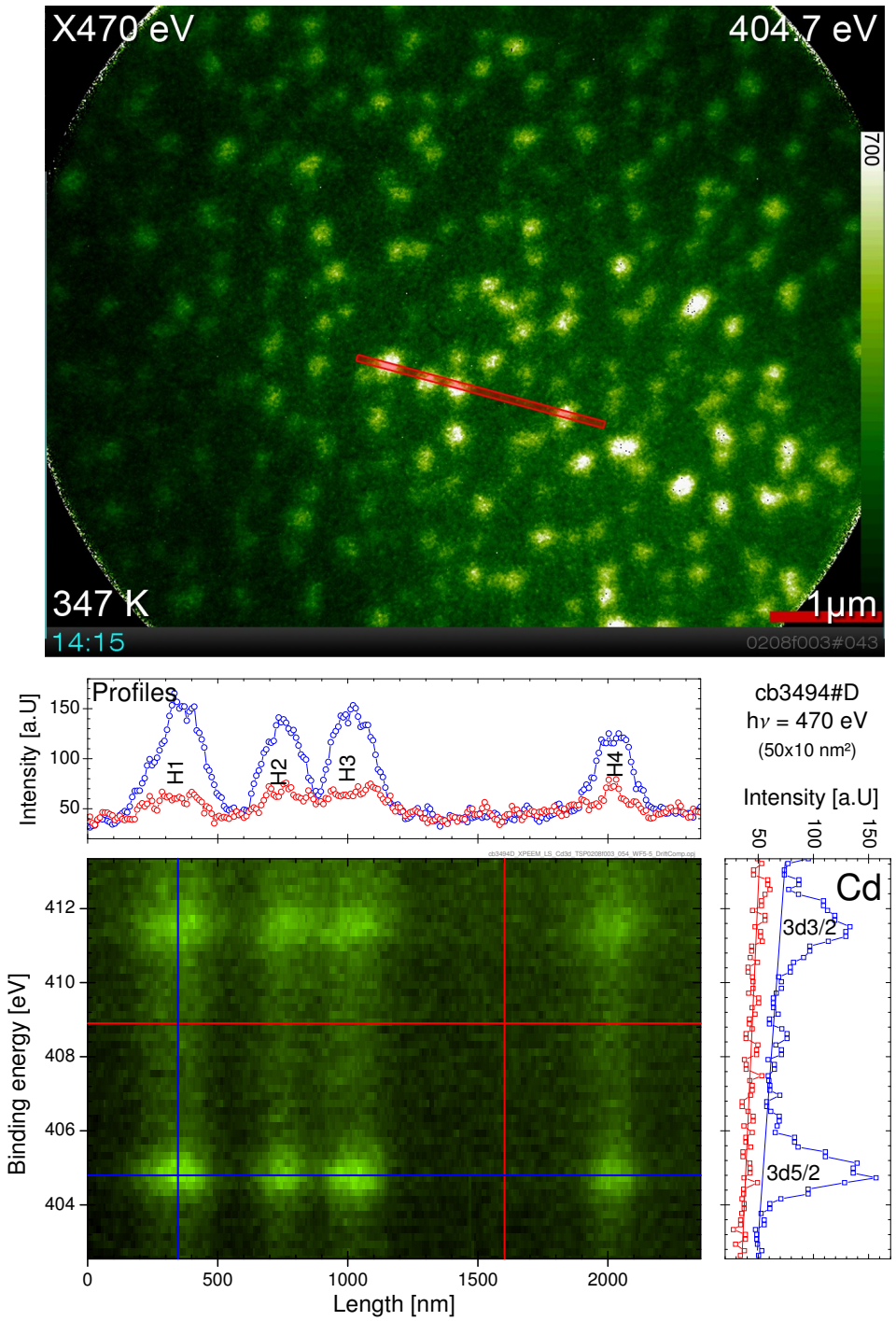

Figure 4.10: Second series of XPEEM stack figures showing the still capped surface of sample cb3494#D. Photon energy was kept constant at 470 eV. In this case the probed electron binding energy is Cd specific with 404.7 eV at the Cd 3*d* line. It compares well with sample cb3494#C (see fig. 4.4).

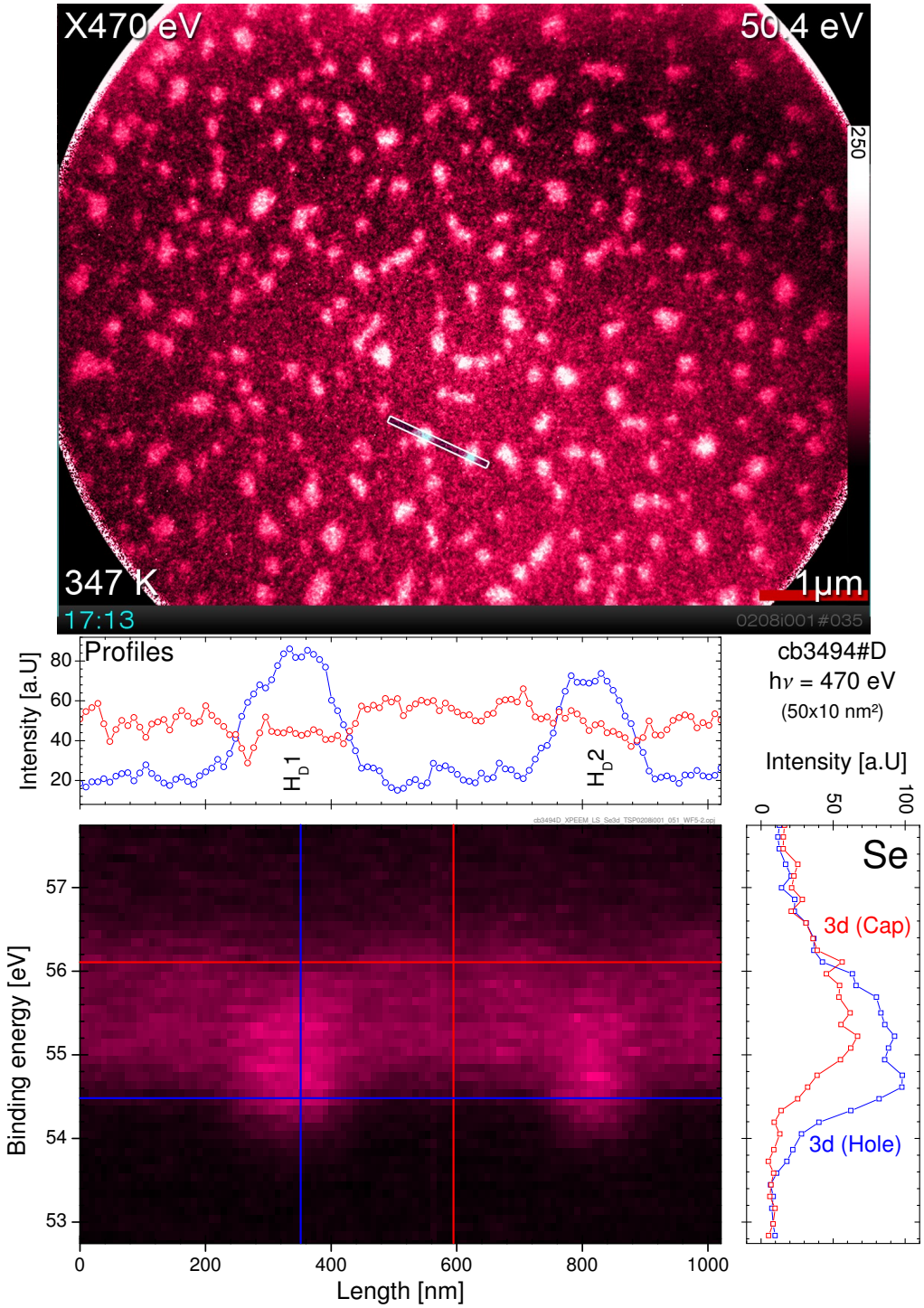

Figure 4.11: This figure is recorded with Se 3*d* contrast at $E_{bin} = 50.4\,\text{eV}$. Compared to the low E_{kin} case (fig. 4.6) the experiment is much more bulk sensitive and allows to catch some signal from selenium in (Cd,Zn)Se as well. The dip in the contrast profile at hole 1 is a hint for less α–Se in the holes than on the cap.

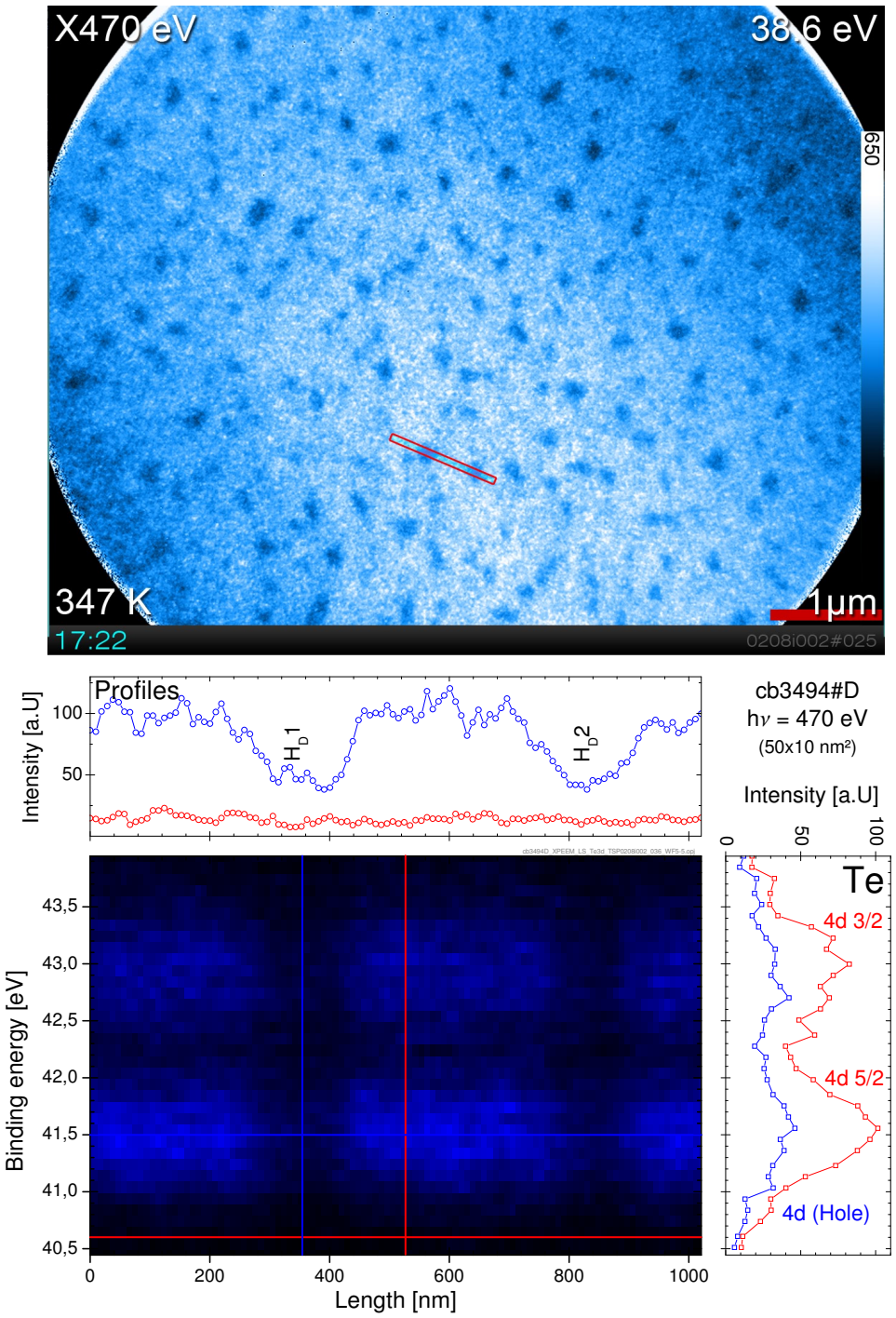

Figure 4.12: This figure is recorded at the E_{bin}=38.6 eV (Te 4*d* doublet). Clearly the cap–hole contrast is visible. The 4*d* features are separated by less than 1.5 eV. The overall intensity is low, because of the reduced transmission at $E_{kin} \sim 430$ eV.

and 4.11. The first stack of #C (fig. 4.6) is recorded with high surface sensitivity (IMFP≈ 2 ML, see fig. 2.3) at $E_{kin} \approx 90$ eV showing clearly Se 3*d* features at both, cap and hole positions. The signal intensity is higher at the hole position. This means that there is more α–Se within the holes than on the cap. It is noted that this causes reduced Te intensity at the positions of the so–called holes but an interpretation solely based on the α–Se capping is not supported by the sum of the findings.
The second stack with Se–contrast from sample #D (fig. 4.11) was taken at $E_{kin} \approx$ 420 eV (IMFP≈ 4 ML) hence including higher contributions to the signal from deeper layers. Again at cap as well as at hole positions the spectra show Se 3d features. But there is a difference at the hole position compared to the surrounding cap. The feature is broader in energy which results in enhanced contrast at $E_{bin} \sim 54.5$ eV, where the elemental signal nearly exclusively stems from the holes but none, besides XPS BG, from the cap. These spectra were analysed with the peak–fitting tool *fityk* [48]. The results of the stringent fit, that assumes two different Se species [43] — the pure α–Se type and Se in the (Cd,Zn)Se compound — are given in figure 4.13. This 2–species model explains well the experimental findings and fits to the expectations from the composition of the sample stack.

It is remarkable that the α–Te cap is such inhomogeneous and shows a rich variety of structures since the Te was deposited at low temperatures of 298 K to form an amorphous, hence featureless layer as confirmed by RHEED before capping with α–Se. The existence of holes implies atom mobility on the surface which typically allows for rearrangement and ordering of the deposits. It is up now not clear at which state of the growth process of the multi–layer film the holes are formed. They may have formed during deposition of the air protection α–Se film. But it is more likely that the rearrangement took place during the decapping of α–Se, due to the elevated temperatures, that was performed in the preparation chamber. To remove the α–Se the sample was annealed at $T_{max} < 363$ K which is sufficient to remove the α–Se cap within 1 min. This temperature is indeed much lower than the desorption temperature of the α–Te of 455 K (see also sec. 4.3) but might be sufficient to allow for (e.g., surfactant mediated) rearrangement of Te–atoms.
Further the question of the reason for the hole and crystallite formation arises. A similar effect, partial dewetting, was reported by Krause et al. [64] for the system PTCDA/Ag(111). The film grown at low T shows a smooth morphology with low crystalline order. This is explained by the missing thermal equilibrium during growth. During annealing the smooth film rearranges and dense crystallites form on top of some wetting layers. The tendency to form islands on wetting layers is observed as well during the growth of PTCDA at elevated temperatures in Stranski–Krastanov (SK) growth. This behaviour is explained by the lattice mismatch of the α– with respect to the underlying β–phase combined with the

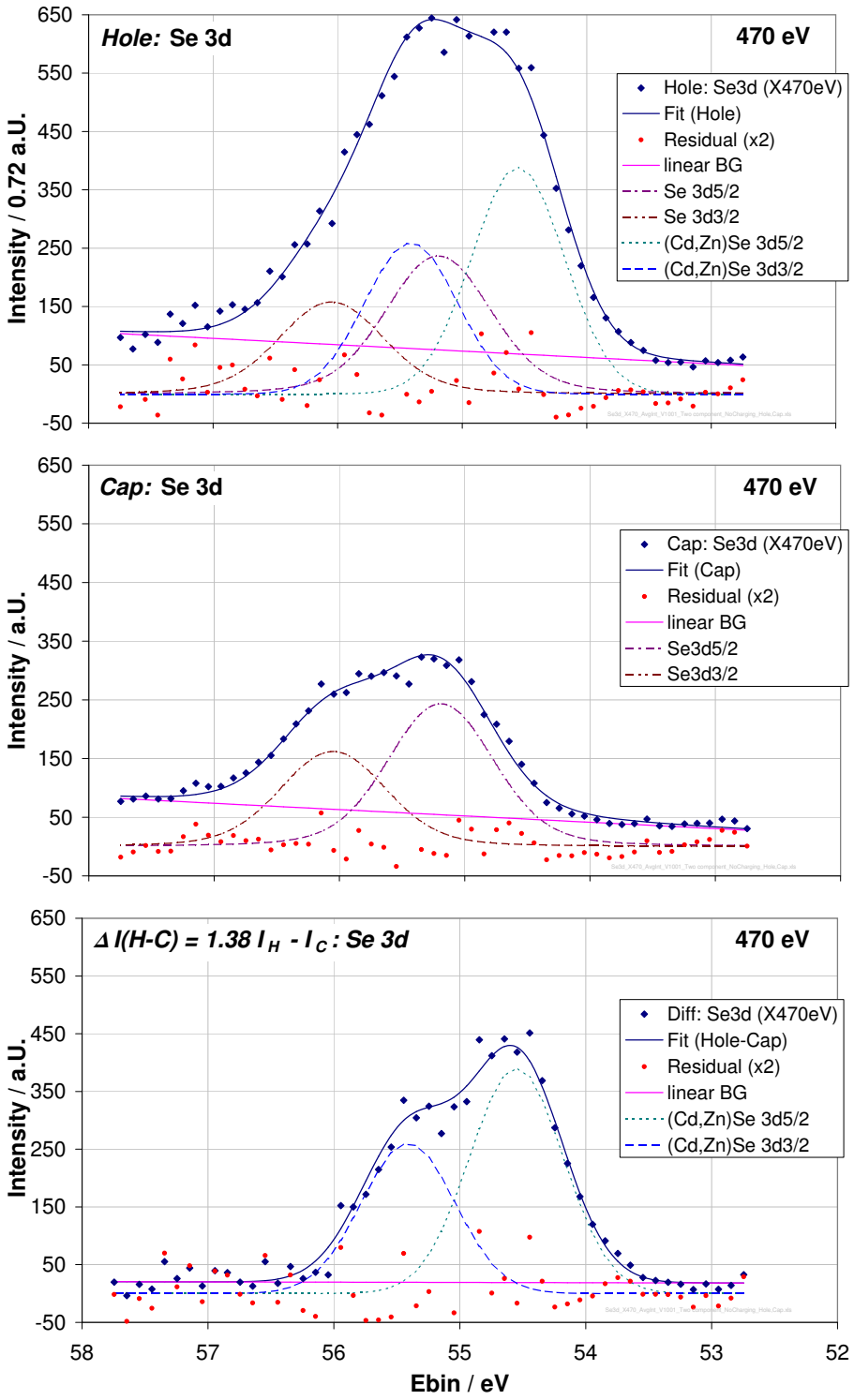

Figure 4.13: n–XPS showing the Se 3*d* features measured at hole and cap positions of the α–Te cap. Dots are data (blue) and the residuum (red) while solid and dashed lines are the fits of the total signal and its decomposition into α–Se and (Cd,Zn)Se species. The last spectrum shows the weighed difference between hole and cap position.

reduced influence of the substrate on layers succeeding the wetting layers. Hence, this argumentation offers an explanation for the behaviour of α–Te on strained CdSe.

Signal from the substrate: Cd and Zn

It was found, that Cd (figs. 4.4 and 4.10) and Zn (fig. 4.5) is mainly seen in the holes, as expected.
The hole contrast of the cap even between the Cd 3d lines at about 408 eV (and also next to the Zn 2p feature) is due to the difference in XPS background. This results from the additional photoionisation cross section of Cd at $E_{bin}(Cd\ 3d_{5/2}) \approx 405$ eV and the BG contribution from other lines at $h\nu = 470$ eV compared to the surrounding cap, mainly composed of Te with few strong lines within this energy range (see table 4.3).
Comparison of spectra from the hole– and cap–positions, shows hardly any peak intensity from these two elements at cap positions. This can be understood for the Cd signal in terms of the high surface sensitivity ($\lambda \approx 2$ ML see fig. 2.3) of electrons ($E_{kin} \approx 65$ eV) combined with its coverage by the α–Te and α–Se remainders and the low amount of only 3 ML although it has a high $\sigma = 3.9$ Mbarn [46]. Zn 3p on the other hand has a low $\sigma = 0.76$ Mbarn [46], is deeply buried and suffers from lower transmission since $T \propto \frac{1}{E_{kin}}$. This is directly seen if the two intensity scales are compared. This also results in the low S/N ratio.

This is different in the case of the Cd 4d (0.32 Mbarn) and Zn 3d (5.67 Mbarn) lines at E_{bin} ∼10 eV (fig. 4.7). $E_{kin} \sim 130$ eV results in about the doubled IMFP for the signal, the sensitivity for Zn ($\sigma \approx 5.7$ Mbarn at $h\nu = 140$ eV, see table 4.3) is enhanced and the XPS background is low. Hence the sensitivity (S/N) for the deeply buried substrate signal is good. Here also a strong signal from the CdSe/ZnSe under the α–Te cap is seen between the holes.
This supports the idea that although cracks are not resolved they went deep into the α–Te cap. In average (across a $10 \times 50\,nm^2$) with the surrounding thick cap this leads to the reduced (Cd,Zn)–signal at the cap position.
One might also think of a scenario with an enhanced IMFP due to different Te–phases (α–Te versus Te–crystallites), but the necessary dramatic change in IMFP is not expected. More likely is a contribution from other valence band features in this energy range as, e.g., Te 5p nominally at 8.6 eV with its low cross section of $\sigma = 0.064$ Mbarn (see table 4.3).

It is concluded, that in the stacking order of the layers there are no surprises. But the α–Te cap is still more structured than previously found from measurements at the Te 3d and Te 4d lines. Besides the large, deep holes it is likely that also chains of small holes or crack–like structures exist that penetrate deep into the surface. In

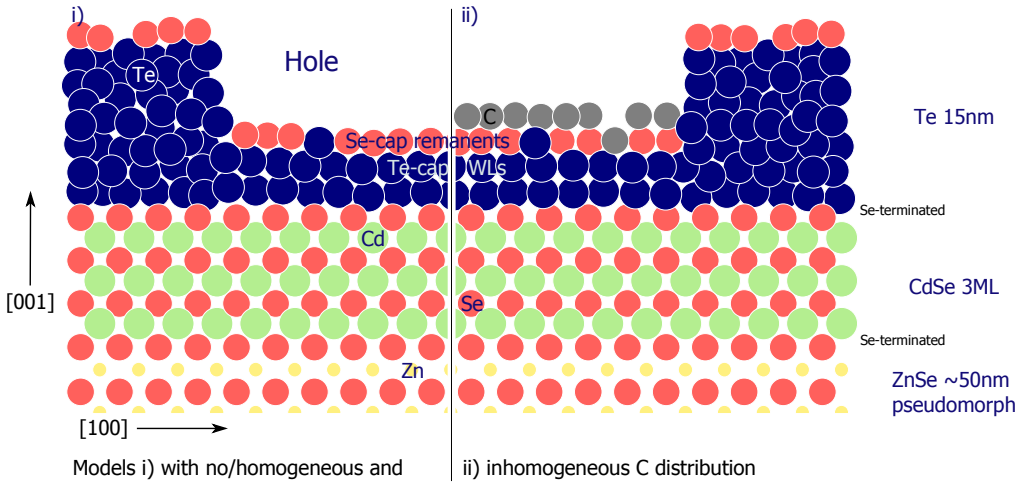

Figure 4.14: Model of the sample capped with α–Te. It was used as the basis for the thickness determination of the α–Te and Se remnants from the nano–spectroscopic data. The 15 nm thick α–Te covered i) just with heterogeneously distributed Se and ii) also with some carbon. Both variants were taken into account for two different model calculations.

any described scenario flat homogeneous CdSe and ZnSe layers were assumed on scales of several hundred nm. However the present results might also be explained by substrate material that has filled cracks from the bottom into the Te cap as, e.g., magma does in the earths crust or just by segregation into the amorphous material in between µ–crystallites.

2 Te layers present in the holes of the α–Te cap

The thickness of the Te at the bottom of the holes was determined with the help of the previously described XPEEM stacks. Spectra were acquired at two different samples from typical cap and hole positions. The intensities were analysed with the help of a peak fitting routine and the results were compared to a thin film model that allows to determine the thickness of the layers.

Introduction of the model. The easy approach to calculate the thickness from pure signal attenuation of the Se intensity from the (Cd,Zn)Se compound just by a heterogeneous α–Te cap failed. Hence a more complex model was derived from LEEM, XPEEM and AFM findings, RHEED measurements during MBE [120], and literature [118].
A schematics of the layer model for n–XPS thickness determination is shown in figure 4.14. The elemental distribution is known from XPEEM images as described above. AFM has shown that the holes penetrate deep into the surface (4.2.3) by about

12 nm. The lattice mismatch between ZnSe (5.67 Å [94, 95]) and CdSe (6.08 Å [94, 95]) is known from literature to be $1 - 5.67\,\text{Å}/6.08\,\text{Å} = 6.7\,\%$. However a growth mode is used that allows to deposit the material in a layer–by–layer fashion (e.g. [18]) with aligned but strained lattices. This was confirmed by in–situ RHEED monitoring during MBE of the stack system by Frey [120]. Further he found mixed c(2 × 2) and (2 × 1) surface reconstruction of the ZnSe and a (2 × 1) surface of the CdSe. According to Weigand et al. [118] the ZnSe–c(2 × 2) is Zn–terminated and the ZnSe(2 × 1) surface is Se–rich. It is assumed that this is correct as well for the similar, quasi–pseudomorphic compound CdSe.

Two variants of this model, that differ only in the distribution of carbon found in µ–XPS were investigated. They are shown in the schematics 4.14 where i) assumes no carbon and ii) takes one wetting C layer into account. Results for both are summarised in table 4.4 and allow to estimate any situation in between. Te and Se thicknesses were determined, whereas the Te at cap positions was approximated by an infinitely thick layer. This is an excellent assumption for a layer of 15 nm thickness. This assumption was also made for the Se bound in the (Cd,Zn)Se part of the sample.
It allows to determine first the Se thickness on the cap from the Te spectra, second the Se thickness within the holes from the comparison of the corresponding Se–spectra and such finally the thickness of the Te–layer within holes. The alternating elemental layers in the [001] surface of the compound materials CdSe and ZnSe were taken into account using equation 2.9.

Determination of the peak areas. Peak areas, to calculate the thickness of the layers, and line positions to check the model, were derived by peak fitting using the program *fityk* by Wojdyr [48].
The spectra used for the fits were averaged over all adjacent spectra (along the profile in the XPEEM figures), that have the same cap or rather hole characteristics. Thus, an intermixing of cap with hole contributions was prevented and statistics was improved.
The peaks were fitted with Voigt profiles. The BG was approximated by the synchronous fit of a straight line. Spectra from both, cap and hole positions, were simultaneously fitted with the identical set of parameters as (i) line width, (ii) E_{bin} of identical chemical species and (iii) doublet splitting. Further (iv) the intensity ratio of the doublets was fixed according to their multiplicity $2(J + 1)$.
In case of the Se 3*d* fit, presented in figure 4.13, only 8 out of 24 parameters were freely varied to fit two different spectra (cap, hole) at once with three different Se doublets (twice α–Se and once Se((Cd,Zn)Se)). Even one more spectrum, the last diagram in that figure 4.13, was simultaneously fitted. It was derived as the scaled intensity difference $\Delta I(H - C) = 1.38 I_H - I_C$ between hole (H) and cap (C)

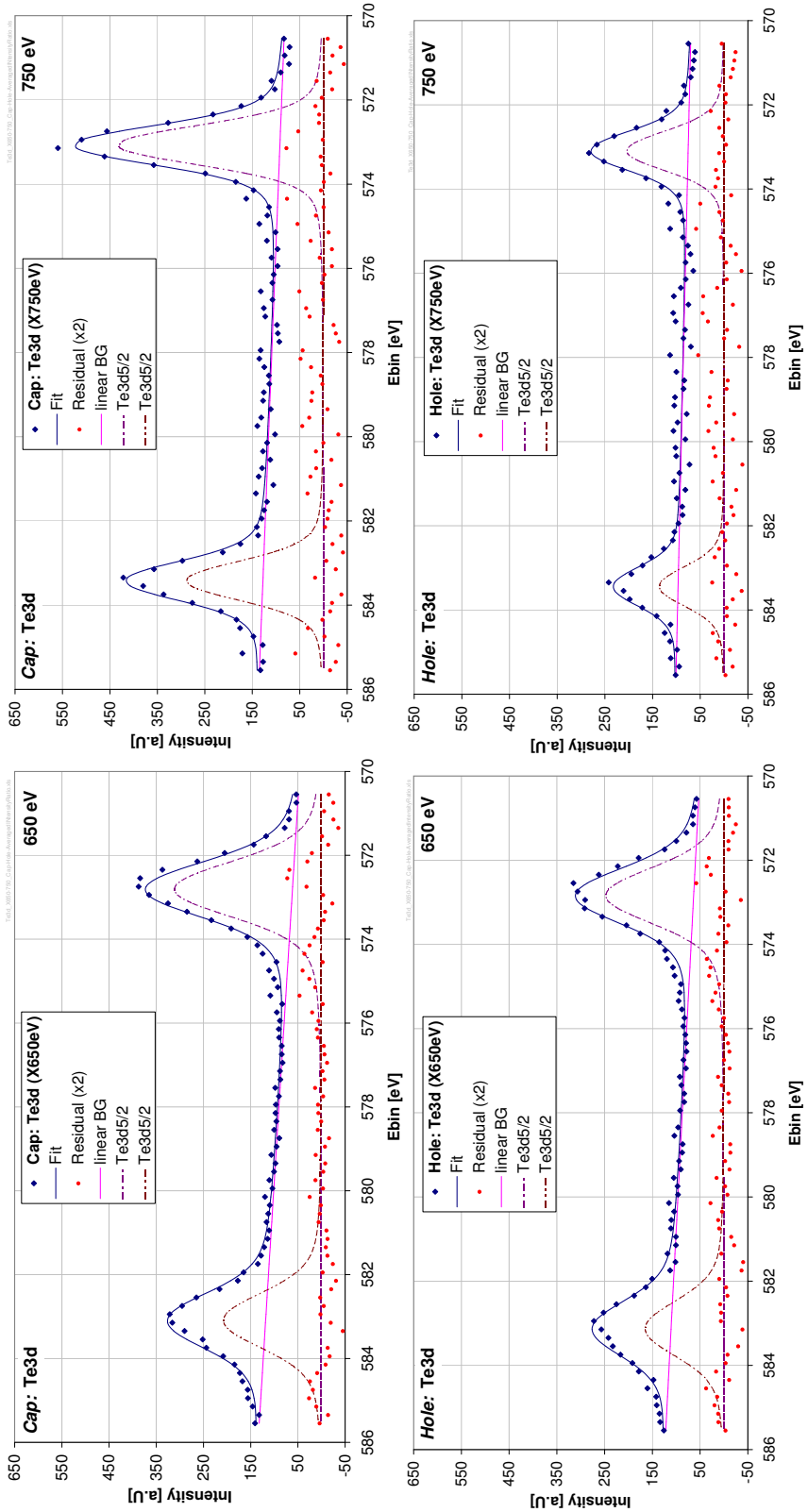

Figure 4.15: Spectra taken from the XPEEM stacks presented in figures 4.8 and 4.9 recorded at 650 and 750 eV, respectively. For each, a hole and a cap position were selected and spectra were extracted as averages across all similar pixel spectra. The Te 3*d* features were fitted using the tool *fityk* by Wojdyr [48].

intensities (I).
The resulting fits of the Te 3*d* features at two different $h\nu$ and for both positions are given in figure 4.15. The derived peak areas are summarised in table 4.4. These results were used in the following to determine thicknesses of the Se remnants and the Te layer in the holes.
The model of two different chemical Se species allows to fit the data reasonably well, and the E_{bin} of 55.2 eV and 54.6 eV correspond well to average literature [119] values of pure Se (55.2 eV) and (Zn,Cd)Se (54.7 eV).

Determination of thicknesses. Based on equations 2.6 together with 2.9, that relate the signal intensity to the thickness of a thin film measured in layers n, the thicknesses of the Te and Se layers were determined in two different ways. Commonly the parameters σ [46] and λ [80, 121–124] were taken from literature and the photon fluxes were taken from the beam line description [4]. The detection efficiency $D(\overrightarrow{r})$ was kept constant since the spectra were acquired with the identical detection setup[5] and the transmission was included by $T(E_{kin}) \propto E_{kin}^{-1}$.
For sample #C a change in photon energy $h\nu$ was used that leads to a change in the IMFP of the electrons and hence to a change in intensity. Thus, the ratio of intensities I_{X650eV}/I_{X750eV} allows to determine the number of layers n.
In case of sample #D the photon flux I_0 was measured at a cap area in case of Te and at the deep ((Cd,Zn)Se) signal in case of Se, since both can be approximated by an infinitely thick layers of known composition. Such intensities originating from cap and hole, for each element taken out of one single image, under identical conditions can be compared. This allowed to determine the number of layers of both, Se and Te separately. Solely the thickness of the carbon layer is left unknown and was therefore considered within two models with i) no C at all and ii) one wetting layer of carbon within the holes. This is justified by the low amount of carbon found in the µ–XPS spectra (see fig. 4.2). Its inhomogeneous distribution is given in section B.3. Only the difference in the carbon wetting is of interest, since a homogeneous layer attenuates both signals, from hole and cap, in the same way and is therefore already considered since the reference signal is intrinsic.

Results and interpretation. A detailed atomic layer model was used to derive a thickness between 1.8(15) and 3.2(15) layers of Te at the bottom of the holes in the cap. This range is due to two different models that estimate the C coverage by 0 and 1 ML, respectively.
For these calculations n–XPS[6] intensities were determined by stringent fits of the

[5] Inhomogeneous gain was corrected in advance by proper flat field normalisation (see also chap. B.1).
[6] n–XPS denotes XPS spectra from areas of nanometre size (selected in XPEEM stack images).

Table 4.4: Te thickness derived from laterally resolved XPS peak fitting of Se and Te data solely from the hole positions of sample cb3494#D using *fityk* [48]. Relative electron binding energies and peak areas were determined using stringent fits. Intensities were corrected in advance for transmission and inhomogeneous illumination. The first column indicates the energy $E_{h\nu}$ of ionising x–ray beam.

cb 3494 #D	**Description**	**Detail**	**Unit**	**Cap (Cp)**	**Hole (H)**	**Lit. [43] [119]**	**Cp/H**
X470	$E_{bin}(Se3d_{5/2})$	α–Se	[eV]	55.2	55.2	55.3(3)	
X470		Se((Cd,Zn)Se)	[eV]	54.6	54.6	54.7(3)	
X470	Doublet sp.	$\Delta E(Se3d)$	[eV]	0.86	0.86	0.86	
X470	Compound	$\Delta E(Se3d_{5/2})$	[eV]	0.64	0.64		
X470	Peak areas	α–Se	[a.U.]	470	330		1.42
X470		Se((Cd,Zn)Se)	[a.U.]	0	436		0
	Thickness	α–Se (w/o C)	[ML]	1.11	0.86(20)		
		α–Se (w/ C)	[ML]	0.86	0.86(20)		
X470	$E_{bin}(Te4d_{5/2})$	α–Te	[eV]	41.5	41.5	41	
X470	Doublet sp.	$\Delta E(Te3d)$	[eV]	1.42	1.42	1.5	
X470	Peak areas	α–Te	[a.U.]	785	328		2.39
	Thickness	α–Te (w/o C)	[ML]	∞	1.8(15)		
		α–Te (w/ C)	[ML]	∞	3.2(15)		

Table 4.5: Te thickness derived from laterally resolved XPS peak fitting of Se and Te data from cap compared to hole positions of sample cb3494#C using *fityk* [48]. Relative electron binding energies and peak areas were determined using stringent fits. Intensities were corrected in advance for transmission and inhomogeneous illumination. The first column indicates the energy $E_{h\nu}$ of the ionising x–ray beam.

cb 3494 #C	**Description**	**Detail**	**Unit**	**Cap (Cp)**	**Hole (H)**	**Lit. [43] [119]**	**Cp/H**
X140	$E_{bin}(Se3d_{5/2})$	α–Se	[eV]	55.3	55.3	55.3(3)	
X140	Doublet sp.	$\Delta E(Se3d)$	[eV]	0.86	0.86	0.86	
X140	Peak areas	α–Se	[a.U.]	4901	5876		0.83
X140	**Thickness**	α–Se	[ML]	1.3(7)	1.9(10)		
X650	$E_{bin}(Te3d_{5/2})$	α–Te(X650)	[eV]	572.8	572.8	573.1(4)	
X750		α–Te(X750)	[eV]	573.1	573.1	573.1(4)	
X650	Doublet sp.	$\Delta E(X650)$	[eV]	10.3	10.3	10.39	
X750		$\Delta E(X750)$	[eV]	10.4	10.4	10.39	
X650	Peak areas	α–Te(X650)	[a.U.]	599	476		1.26
X750		α–Te(X750)	[a.U.]	575	271		2.12
	Thickness	α–Te	[ML]	∞	2.2(15)		

peak areas and necessary parameters were investigated carefully. The fitting model in case of Se was tested with the literature values of its two species, pure Se and compound Se in (Cd,Zn)Se. Also the results of the other lines were compared to published results and are summarised in tables 4.4 and 4.5 together with the determined thicknesses of Se and Te.

Due to the inhomogeneous distribution of carbon it is expected that its amount in the holes is in between 0 and 1 ML and hence the Te layer is between the values that are given above as well. In terms of Te coverage the two different methods to determine the thickness agree well within the error bars.

The Se coverage is found neither to be constant nor to be homogeneous. The difference in thickness from sample #C to #D is explained by different desorption states, i.e. different heat quantities during decapping. Care was taken to desorb the Se as long as necessary but as short as possible to prevent early influences on the Te–cap. To hit the desired state is quite a challenge and cannot be perfectly reproduced without direct observation. Nevertheless no major differences in the Te cap were observed for any of these Se decappings. It turned out during the decapping step (see sec. 4.3) that it was stable up to at least 420 K.

This may explain for #C the thicker layer within the hole as well, since the α–Se surface was much smoother than the α–Te cap (see figures 4.1 and 4.16). Hence a thicker Se layer at this position is expected if the α–Te originally comes with holes.

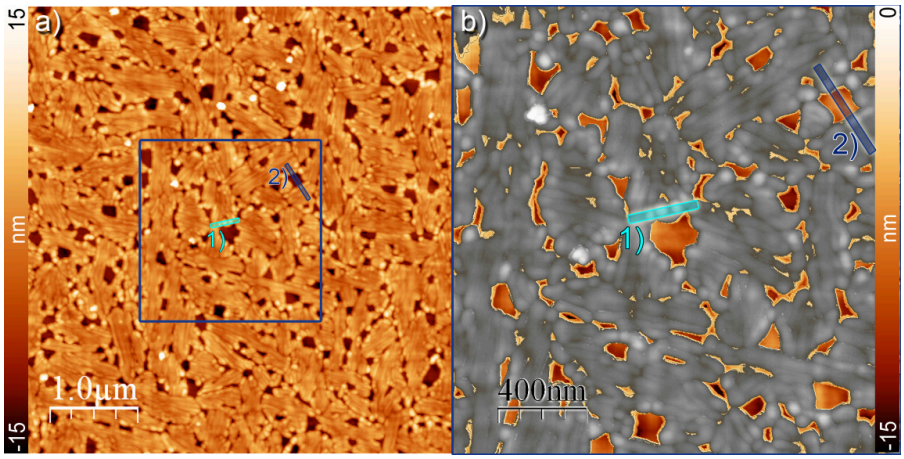

Figure 4.16: AFM images showing the topography of a nominally 15 nm thick α–Te capped surface. The cap layer is not fully closed. Image (a) gives an overview while (b) shows a magnified view where the holes are masked to highlight their height variations. Typical height profiles of the line–scans labelled (1) and (2) are shown in figure 4.17.

On the contrary the #D sample was largely decapped and just one homogeneous wetting layer of Se remained. The demand for homogeneity of Se again supports a model that leads to a Te–coverage within the holes above 2 layers.

4.2.3 Complementary AFM data reveal topography

The AFM images, shown in figures 4.16 and 4.17, were acquired in air at the sample cb3494#B directly after removal from UHV, where it was unsealed before.

Features found with AFM

Statistical analysis of the images given in fig. 4.16 reveals that holes larger than 0.001 µm^2 and deeper than 5 nm covered 10.9 % of the surface (fig. 4.17) with a density of $1.94 \times 10^9\,\mathrm{cm}^{-2}$. Their next neighbour distance was about 159 nm. Taking into account holes with a tenth of the upper area as well they covered together 11.4 % of the surface with $3.43 \times 10^9\,\mathrm{cm}^{-2}$ being 105 nm apart from each other. Holes ten times larger (0.01 µm^2) than the first covered only 4.6 % of the surface with a density of $2.7 \times 10^8\,\mathrm{cm}^{-2}$ and were separated by 380 nm.
Taking a look at the hills one finds structures larger than 400 nm^2, at least 4 nm high covering 6.1 % of the surface with a density of $3.16 \times 10^9\,\mathrm{cm}^{-2}$ and 94 nm apart. 5 nm high features cover 3.28 % as dense as $1.99 \times 10^9\,\mathrm{cm}^{-2}$ and 106 nm separated.

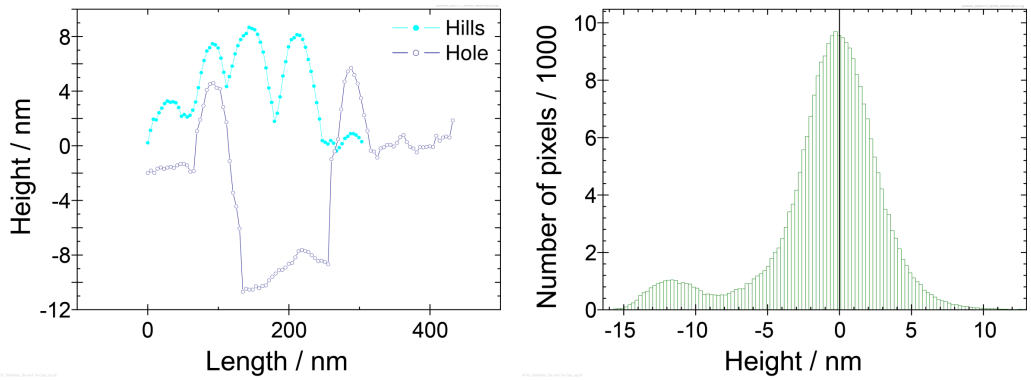

Figure 4.17: On the left two profiles marked as rectangles in figure 4.16 show the typical height and depth of hills (1) and holes (2), respectively. On the right the height distribution clearly shows the existence of two prominent levels with FWHM of about 6 nm correlated with the 'flat' surface and the holes.

Both, hills and holes have a typical areal density between 2 and $4 \times 10^9\,\mathrm{cm}^{-2}$. This is about one third of the QD density described by Mahapatra [18]. In case of the huge holes the factor is even 1/50.

Within single terraces, surrounded by holes and cracks, a linear ripple structure was found. It has a typical periodicity of about 50(10) nm. Its favoured orientation of $\pm 45(5)^\circ$ is along the long rang surface undulation(mounds). Such mounds were described by Mahapatra [18] and were assumed to be aligned along the $[1\bar{1}0]$ direction based on the work of Orme et al. [125] who studied large scale structures formed during GaAs(0 0 1) homoepitaxy. They find the mounds already present in the ZnSe layer and even (but less pronounced) in the GaAs buffer layer.

Summary

Clearly holes within the α–Te are visible in fig. 4.16. Their size corresponds to the structures found in LEEM and XPEEM. Furthermore the depth of the large ones ranges from about 12 to 15 nm. Together with the findings from Te XPEEM this shows, that the Te cap is still intact and not thinned out.
The plateaus seem to be constructed from bunches of needle like structures. At their ends pointing to holes, material is accumulated and forms peaky structures that tower up to about 10 nm above the average surface. Cracks or chains of tiny holes are found that deeply penetrate into the surface.

4.2.4 Conclusion

The α–Te cap has a rich variety of structures rather than being homogeneous and smooth which all applied methods as LEEM, XPEEM and AFM have shown. LEEM in combination with µ–LEED identifies Te crystallites within a α–Te matrix that are preferentially aligned with the [110] and [1$\bar{1}$0] directions of the [001] surface of the CdSe/ZnSe substrate. XPEEM measurements lead to a detailed model that allowed to determine the layer thicknesses of the remaining α–Se and α–Te at hole and cap positions. Thus, some two layers of Te were found at the bottom of the deep holes. And it was shown, that the α–Te and µ–crystalline Te are part of the thick Te cap. Although cracks stay unresolved in XPEEM, there is evidence that they deeply penetrate the Te cap as well. Complementary AFM images revealed the topography, justifying the designation of structures as tips, holes, cracks and the needle–like structures, identified as µ–crystallites by LEEM.

The richness of structures is quite surprising for a so called "amorphous" thin film. The presence of holes and crystallites requires at least some mobility and tendency to (re)arrange of the atoms that are deposited onto the surface. Therefore the question arises at which stage this (re)arrangement took place. In principle there are two possibilities: i) during the MBE deposition of the α–Te at 298 K or ii) during the removal of the α–Se protective cap at temperatures below 363 K. Since at neither process a detailed in–situ investigation took place, one has to consider several aspects.

First, the substrate temperature during Te deposition might be low but is already sufficient to allow for incomplete rearrangement of the atoms. This agrees with RHEED results of Mahapatra [18], who describes a faint ring structure attributed to a partially poly–crystalline Te phase which depends strongly on the substrate temperature. Assuming a coexistence of surface reconstructions that are Se– and Cd–rich, which was found, e.g., for the ZnSe–surface by Weigand et al. [118], a Cd–rich surface might hold the Te adatoms tighter than a Se–terminated due to the electronic structure of the resulting compounds. Hence one would expect the crystallites, with the high correlation with the substrate to form quasi–pseudomorphically at the Cd–rich surface reconstruction of the CdSe substrate. In between, at the Se–rich surface the atom mobility is higher and allows the Te to diffuse according to the substrate temperature over larger distances and hence accumulates preferably at the crystallite positions until they touch each other. This leaves behind holes and cracks depending on the total amount of Te deposited. It was stated by Schumacher [126], that the Te cap does not close until about 100 nm which is the reason for this large cap thickness in the investigations of Kumpf et al. [127].

Second, a sufficiently low substrate temperature during MBE–deposition might result in a perfectly amorphous α–Te cap. A change from the amorphous phase into

a poly–crystalline phase right before Te desorbs, was already found by Mahapatra as well and was observed via a "broken ring" structure of the in–situ RHEED measurements at the MBE supporting this investigation.
Krause et al. [64] investigated a totally different sample system, an "amorphous" thin film of PTCDA on Ag(111) with a similar thickness. The amorphous PTCDA film is deposited at 135 K and forms in an adjacent annealing phase a poly–crystalline structure with partial dewetting in between the crystallites already far below the desorption temperature. Although these two sample systems differ in many ways this might be a hint for a common principal behaviour.
The presence of the α–Se protective cap may assist this rearrangement of the Te as it might act as a surfactant that makes an amorphous phase of Te (e.g., at later hole positions) even less favourable than the µ–crystalline one. Surfactant mediated growth is typically used to enhance a pseudomorphic, hence layer–by–layer growth mode [33].
Either way, the alignment with the substrate is suspected to be influenced in the same way as described above. In fact it is expected that both cases are just the two extremes of the same process and the actual situation is somewhere in between.
A more detailed investigation of the CdSe surface during and after decapping is presented in the following section 4.3, where a corresponding linear structure was found, although no Te is left behind. Also the influence of the ZnSe/CdSe substrate on the structure of the cap is enlightened.

4.3 Cap and substrate structure influence QD formation

For QDs one major point of interest is the process of their formation. If this can be understood in more detail a more precise control of the their size distribution and areal density should become possible. While most of the resent studies are restricted to a two step investigation — first preparation of the QD sample followed by some kind of surface treatment for the ex–situ measurements in the second step — in the following the formation of the QDs was observed in real–time and in–situ with LEEM. To link the results with manifold previous studies the QDs were investigated ex–situ by accompanying AFM measurements as well.
The results of the real–time observation of the decapping are presented. The possibility to observe directly the formation process allows even to correlate the QD positions with the different surface structures on the cap, that were described in the previous chapter. Furthermore LEED was used to correlate the features with the crystallographic order of the CdSe/ZnSe(001) surface of the substrate.
Also the stoichiometry of the QDs and their surrounding is of large interest since, for example, a wetting layer is discussed as guide for carriers that inject charges into the active QDs in, e.g., LASERs. In this context first results of the spectro–

microscopic XPEEM investigation of the decapped surface are presented. They reveal a Cd distribution which is correlated with features in the previous α–Te cap.

4.3.1 Real–time observation of QD formation

The Te desorption process was observed live and in–situ. Therefore a BF–LEEM movie at $E_{kin} = 8\,\mathrm{eV}$ was recorded with an image every 2 s and an acquisition time of 1 s. Starting at a stabilised temperature of 419 K the temperature was ramped up with a rate of $1.7\,\mathrm{K\,s^{-1}}$ to nearly 550 K (fig. 4.20) to desorb the Te, uncovering the underlying CdSe surface with its quantum dots. The presence of QDs was confirmed directly afterwards with ex–situ AFM measurements as in figure 4.19.

A selection of images from this movie is given in figure 4.18. Note that the time scale is not linear and the T–ramp started at 0 s. From image 42 to 55 s all available images are presented that show the Te desorption and QD formation, which hence took place within less than 13 s (corresponding to 21 K). The other images show in a time lapse series the stability of the surface before and after desorption of the α–Te.
All images are equally scaled which shows the drastic increase of reflectivity during the desorption process. In general the black areas correspond to the Te cap material in its amorphous and microcrystalline phases. The (Te–wetted) CdSe appears in light–grey colours. A selection of holes is highlighted with red circles to illustrate the thermal drift and track the FoV. With the tips of the yellow triangles dark-grey dots are marked, e.g., in image 55 s, that move with the thermal expansion of the surface during ramping up. These features are QDs. A careful drift correction showed that the dark lines that dominate images 51 and 53 s can be correlated with micro–crystallites which are parallel and adjacent to the cracks. The cracks are seen as white lines for example in image −32 s. It is emphasised that both structures are close to each other but not at the same position.
Further the QDs are stable at temperatures up to at least 550 K, which is more than 70 K above the temperature where the Te vanished. Since the QDs move together with the other surface features across the detector, it is proven that the tiny structures on the surface are real and not a detection artifact or noise.
In the last two images above 75 s a dark band is seen in the lower left part. It marks the edge of the electron beam and is attributed to the deposition of carbon (see also section B.3). However, dots are found within the beam and further outside the carbon enriched areas. Hence they form independently of the electron beam. The uniform formation of the quantum dots is confirmed by AFM measurements at two

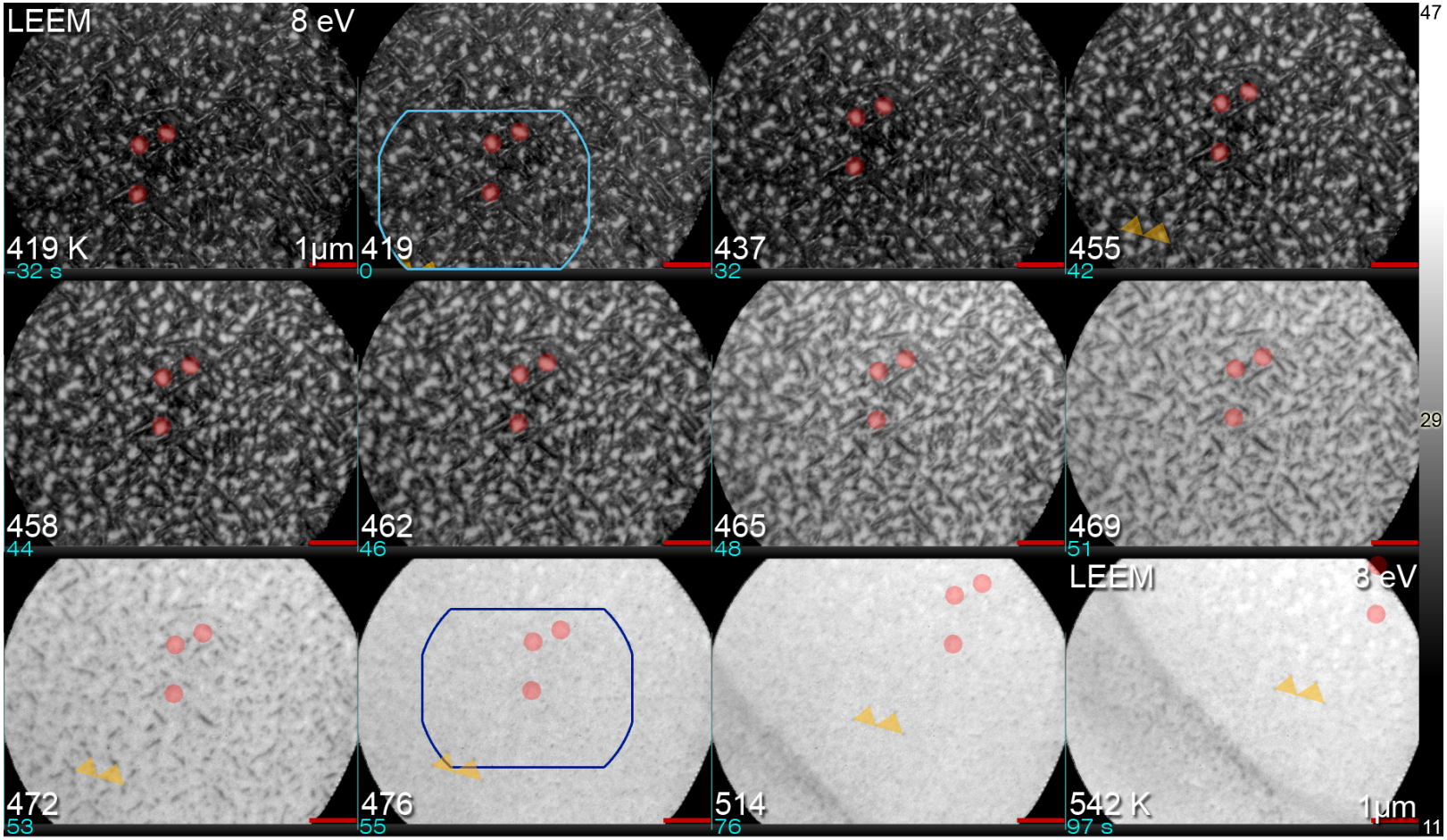

Figure 4.18: LEEM–BF ($E_{kin} = 8\,\text{eV}$) temperature series taken from the α–Te desorption movie. Images were recorded every 2 s with an acquisition time of 1 s. At 0 s the T–ramp (fig. 4.20) was started. α–Te cap regions appear black while holes and cracks show a higher reflectivity. The circular red marks (holes in Te cap) indicate identical features in all images that shift due to thermal expansion of the sample while heating. The tips of the triangular yellow marks highlight positions where QDs form on the CdSe surface.

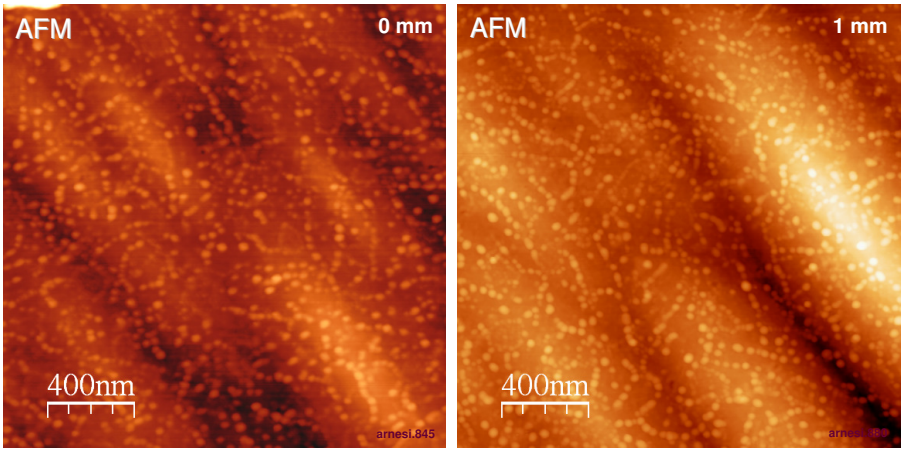

Figure 4.19: AFM images recorded at RT taken from two sample positions that are about 1 mm apart. Long range structures (waves) on the order of 1 µm are CdSe wetting layer undulations along the [110] direction of the ZnSe substrate [19, 128]. The dots with ~ 40 nm diameter are QDs.

randomly chosen surface areas (see fig. 4.19) that are about 1 mm apart (40 times the 25 µm diameter of the e–beam).

Comparison of temperature measurements. Targeted and actual temperatures are given in figure 4.20 together with the PID controlled heating power, showing the good linearity of the T–ramp. The T–scale was carefully calibrated with liquid N_2 and boiling water in advance. In blue the range is marked within which the cap vanished as observed in the real space image series from 44 to 55 s. With an uncritical delay of about 20 s the ramp rate of $1.7\,\mathrm{K\,s^{-1}}$ is excellently met. Hints were found, that a ramp rate well above $1\,\mathrm{K\,s^{-1}}$ is necessary to form QDs and not to desorb the CdSe layers as well. This was seen at least in case of a sample that was capped only by α–Se and without Se flux during decapping.
It appears not to be necessary to heat the sample up to 580 K to form QDs during decapping of α–Te. This is surprising since it was shown by Schallenberg et al. [129] that adatoms migrate on length scales below 10 nm in CdSe/ZnSe heteroepitaxy at 570 K. But these differences in temperature might result just from the different measurement geometries in the two setups. In the case of SMART the thermocouple was attached at to the front of the sample holder, next to the surface that was investigated. Further, the sample holder is quite small and hence follows easily the temperature changes (see also B.2). The MBE group in Würzburg [129] uses a carrier for 2 inch wafers (ours hold 0.5 inch samples), also heated from the rear side of the sample by radiation and electron bombardment, but with a higher mass and the thermocouple (TC) attached to the rear side. Therefore, especially during fast

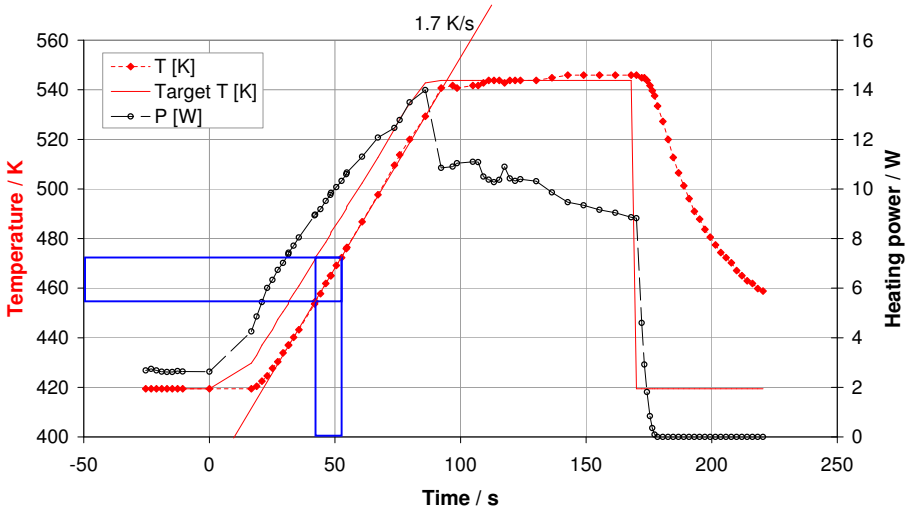

Figure 4.20: Heating power and temperature evolution to desorb the α–Te from the the surface of cb3494#D. At a ramp rate of $1.7\,\mathrm{K\,s^{-1}}$ the α–Te desorbs in the range marked by the blue rectangles as directly observed in figure 4.18. Temperature regulation was done using a *EUROTHERM* controller with calibrated T–scale and adjusted PID parameters.

ramping, their temperature measurement is probably higher than the actual surface temperature.

4.3.2 Dots form between holes and Te–crystallites

Having a closer look on the desorption process allows to locate the different features and to correlate them with respect to each other. Robin et al. [19] found for α–Se capped samples by TEM that the QDs form during desorption of the cap and not while the cap is deposited.

Identification and localisation of the features

Figure 4.21 shows details of the desorption process taken from the BF–LEEM movie shown in figure 4.18. (a) shows the α–Te cap with the holes as investigated in section 4.2. The following images are magnified and min/max scaled to optimise the contrast. They were recorded with the same contrast at $E_{kin} = 8\,\mathrm{eV}$. (b) is the last image where Te is still present (472 K, 53 sec) while (c) shows the quantum dots (476 K, 55 sec). From these three images, four different stages of decapping were extracted: (a) holes (orange contours) and cap layer (blue), (b) µ–crystallites (cyan) and (c) quantum dots (red). Selections of these features were overlayed to the original images, that were carefully drift compensated in advance. Thus (d) highlights

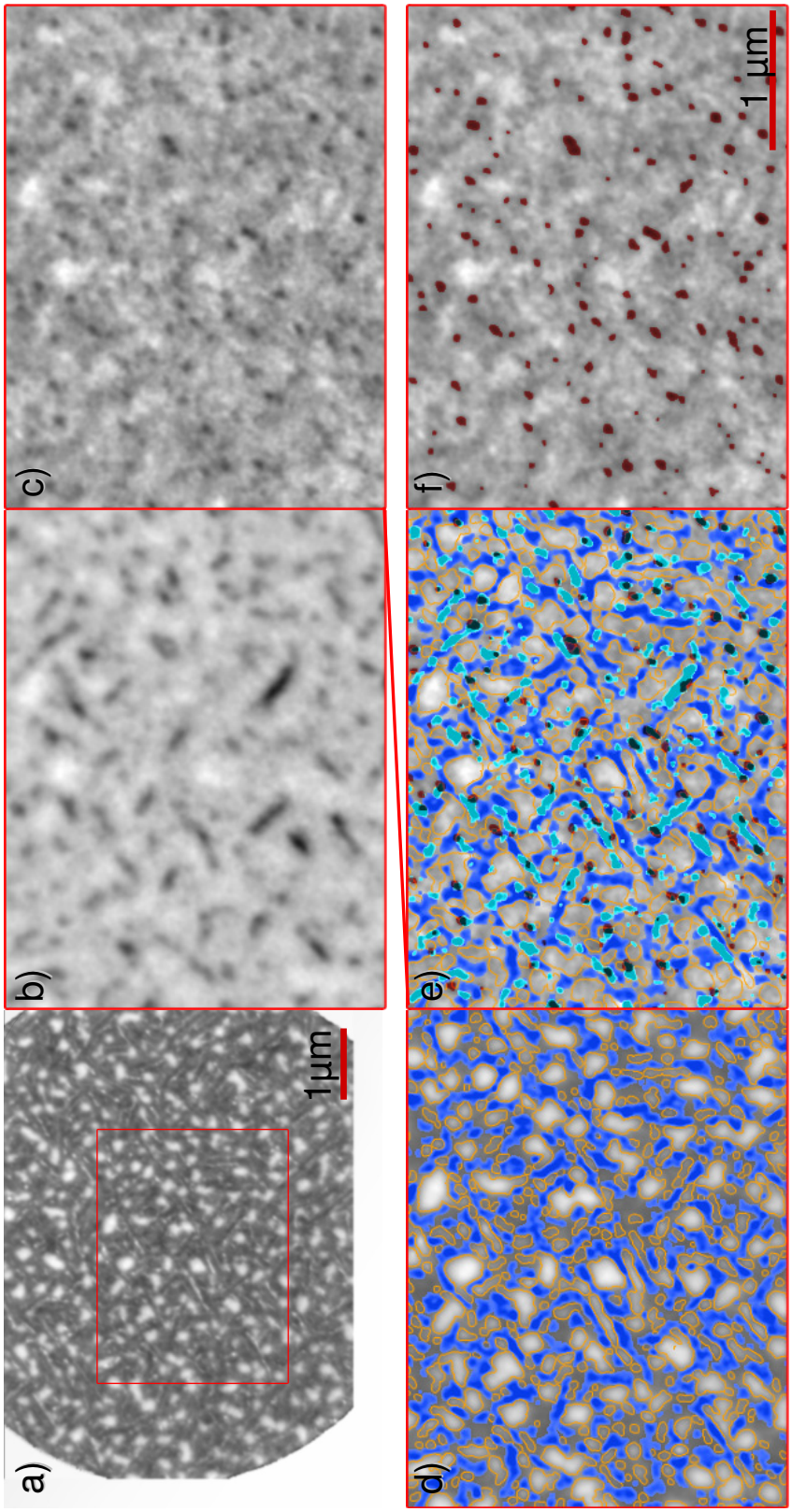

Figure 4.21: Te desorbs and QDs remain on the surface. Images (a) – (c) show the original min/max scaled LEEM images, recorded at 8eV. (a) shows an overview of the Te (dark) capped surface with holes (bright), (b) is the last image where still Te is on the surface and (c) shows the quantum dots. In (d) – (f) the features (Te — bluish, holes — yellow outline, QDs — red) are marked and superimposed on the original images (a), (c) and (c). Image (e) shows the superposition of all three stages of decapping.

holes and dark Te in the cap image (a), and (f) shows the pure selection of QDs on the decapped surface (c). In (e) all features are brought together and superimposed to the fully decapped surface shown in (c). Areas that lie in between the above described structures are attributed to transition stages, especially the amorphous Te matrix, in which the crystallites are embedded.
The elongated, dark features in (b) are called crystallites for the following reasons: they are clearly identified as elongated mounds by ex–situ AFM measurements, performed after interruption of the desorption process (cd3446#B). Furthermore, they are found at positions of the previously "darker" part of the cap, which was identified as crystallites in a previous section (4.2.1). Since they vanish from the surface during annealing, these observations imply that they are real parts of the cap and more precisely the remainders of the µ–crystallites. But not all features in (b) are crystallites. Some are QDs, as seen when the red QD–mask was overlayed on this image (e).

Correlation of dots with the rest

To correlate the QD positions with respect to the two main features, the holes and µ–crystallites, the distances between the centre of the dots and the edges of their nearest hole or crystallite were determined. A total of over 150 QDs was evaluated. The results and the distribution of dot sizes are shown in the histograms of figure 4.22.

The data are derived from the coloured markings in the images of figure 4.21. Histogram colours are chosen correspondingly. The "circular diameter" d is calculated from the area $A = \pi/4 \cdot d^2$ of the QDs assuming a circular shape of the dots. The QDs are found to have a typical diameter of about 50 nm and cover 3.9 % of the total surface area with a density of $1.4 \times 10^9\,\mathrm{cm}^{-2}$. Since some of them are close to each other and hence counted as a single large QD, the histogram overestimates especially the frequency of those. The measurements of the diameters have to be taken cautiously since the FWHM cannot be selected reliably due to the low contrast and the rather strong intensity variations of the surroundings, but they agree well with typical sizes also described by others [18] for QDs formed by this technique.

Findings and conclusion. It is clear that the QDs tend to form close to the edges of holes, favourably within 10 to 50 nm. This compares to an average dot distance of 0.29 µm. While the correlation with the edges of holes is obvious and marks a pretty rigid barrier (nearly no QD is found within the holes), the correlation with the edges of Te crystallites is weaker. The latter may be explained by the time in which the QDs form. There are already sole, stable dots visible, when remainders

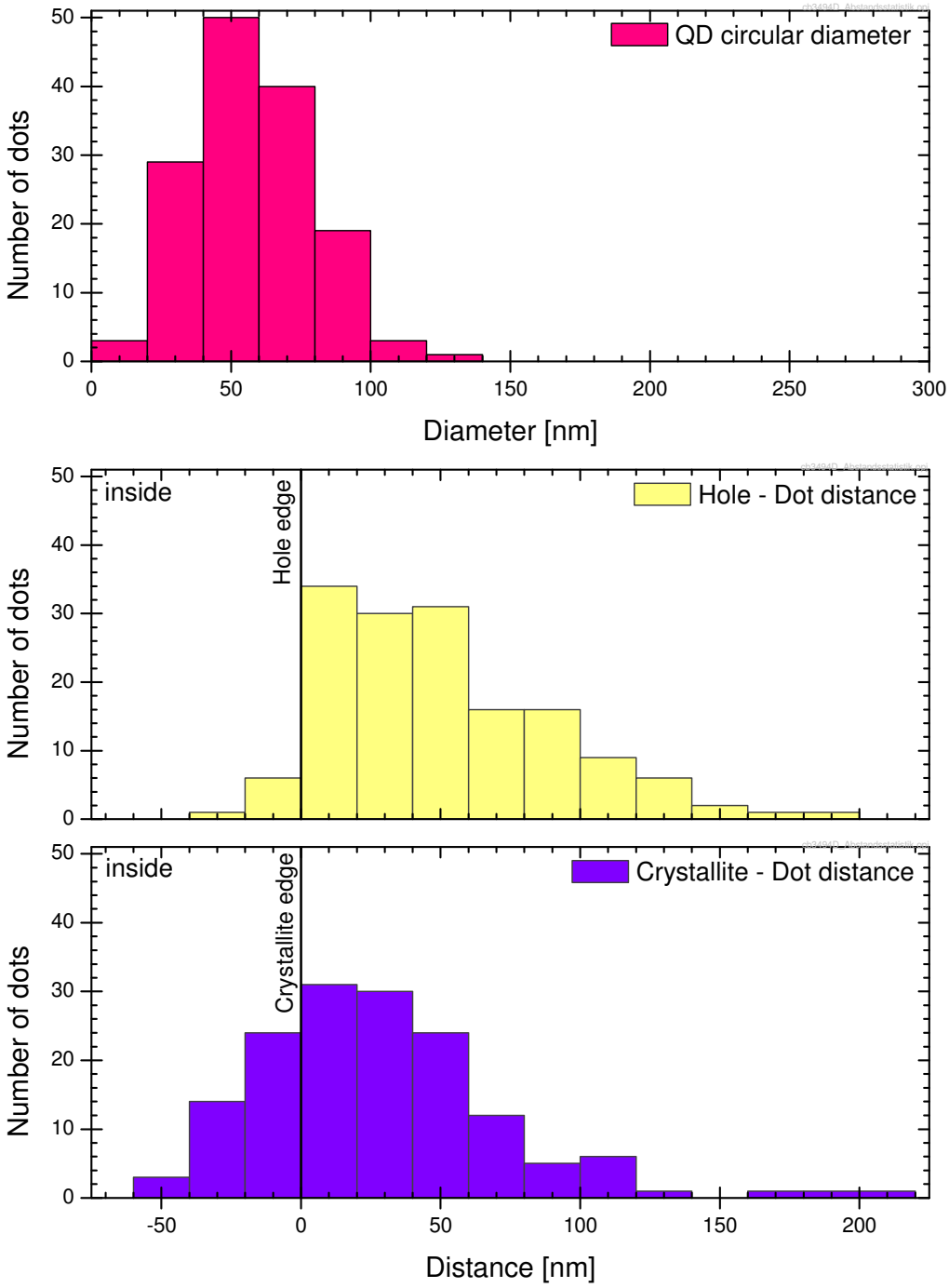

Figure 4.22: Histograms showing the distribution of 1) the diameters of the QDs (red), their positions with respect to 2) the edges of the holes (yellow) and 3) the edges of nearest crystallites (blue) in a late stage of Te cap desorption. These data were derived from figures 4.21 (a) to (c). Negative distances indicate that the dots were found within the corresponding structure.

of the cap are still present in the surrounding area, as already indicated earlier. Others are found even within the crystallite positions. Hence it is concluded that the vanishing cap leads to the formation of QDs during a long time of the desorption process. Therefore early grown QDs are found farther from the crystallite positions in the histogram than late grown QDs, while no QDs are found within the holes. This implies that the presence of the Te cap, at least in the close neighbourhood, is necessary for the nucleation of the QDs.

One can think of several mechanisms that induce the nucleation: (i) a CdTe cluster is incorporated in the dots, that acts as a stressor nuclei as used by Toropov et al. [130], (ii) additional strain at the edge of the Te enhances the accumulation of adjacent material via relaxation, or (iii) a kind of surfactant mediated "upclimb" of the adjacent CdSe is caused by a reduced diffusion barrier within the plane and in between layers. Surfactant mediation of the Te wetting layer might also increase the low migration length [129] of the CdSe adatoms that leads to the low density of the rather large QDs.
The heat of formation of CdSe (32.6 kcal/mol) is larger than that of CdTe (22.1 kcal/mol) [18, 97]. This makes the formation of the CdTe–compound less likely. However, the bulk lattice constant of CdTe (6.48 Å[94]) is much larger than that of CdSe (6.08 Å[94]). Compared to the bulk lattice constant of ZnSe (5.67 Å [96]) this would enhance the strain and may therefore induce the formation of QDs as suggested by Toropov [130]. Even if CdTe 2D–islands are formed just at a small fraction of the surface, these may act as nucleation centres for the QDs.
In this context especially the lateral Te distribution in QD layer is of major interest and should be addressed in future studies. It would be enlighting as well to stop once more the desorption process when still µ–crystallites are present, and to study then the Te distribution.
Unfortunately it was not possible to record in–situ and real–time an XPEEM movie, similar to the presented LEEM–series of figure 4.18. This was due to the thermal expansion of sample and sample holder along the microscope axis that lead to a change of the object distance. Hence the highly focussed X–ray beam, illuminating at gracing incidence of 20°, ran out of the FoV. This would have required an in–situ tracking, which needs a feed–back loop and a smooth position adjustment. A manual correction with optical feed–back lead to fuzzy images, due to the introduced vibrations. Alternatively this problem could be overcome by an on–axis illumination, similar to our e–beam illumination, that seems to become possible with the latest version of, e.g., *ELMITEC*s aberration corrected LEEM (AC–LEEM).

Summary

It was shown that holes and µ–crystallites influence the location of the quantum dot formation. QDs do not form at hole positions below the 2 wetting layers of Te. They are preferentially found at the boundaries of holes but are less strong correlated with the edges of the crystalline Te in the previous cap. This leads to the conclusion, that probably a Te–induced mechanism plays a role in the formation process that possibly enhances the local strain acting as a nucleation centre for relaxation by island formation. Furthermore, the Te wetting layer is suspected to act a surfactant that enhances the Cd(Se,Te) adatom mobility and consequently the diffusion lengths of adatoms.

4.3.3 Correlation of real space with LEED–structure

Once the Te is desorbed the in–situ combination of LEEM with LEED information allows to correlate the orientation especially of the elongated features with the structure of the ZnSe(001) surface. Differences in the structures of marks from former cap features were revealed. The findings are summarised in figure 4.23.

Description of the figures. Two BF–LEEM images of the identical, capless surface area composed from CdSe with QDs are presented in figure 4.23. They were recorded at kinetic energies of 2 and 15.5 eV. The sample was kept at 373 K to ensure stable conditions and prevent contaminations. The FoV is 8 µm. Basically three different features are visible: in the 2 eV image dark, round structures (hole stamps), bright linear features (crystallite stamps) and the layer in between. Intensities were independently linearly scaled for optimum contrast in both images. The intensity at 2 eV stems nearly solely from the (00) spot (the Ewald sphere has half the diameter as the 8 eV µ–LEED picture), since other spots are not yet included. Hence the contrast is dominated by variations of reflectivity and surface work function. Additional spots appear within the Ewald sphere at 8 eV that originate from the crystalline volume structure of the substrate. They also contribute to the image recorded at 15.5 eV, since the used 70 µm contrast aperture (CA) accepts all these angles. Therefore the contrast mechanisms of the two images are similar. Note that the penetration depth of 2 eV electrons is around 100 layers according to the universal curve (see fig. 2.3) while it drops below 6 layers at 10 eV.

At a microscopic AoI of less than half of the FoV, µ–LEED pattern were recorded just by switching modes. This was done in–situ and hence under identical conditions as for the microscopic images. These patterns are given in the blue framed inset in the 2 eV image. The intensity scale is optimised for presentation. They were

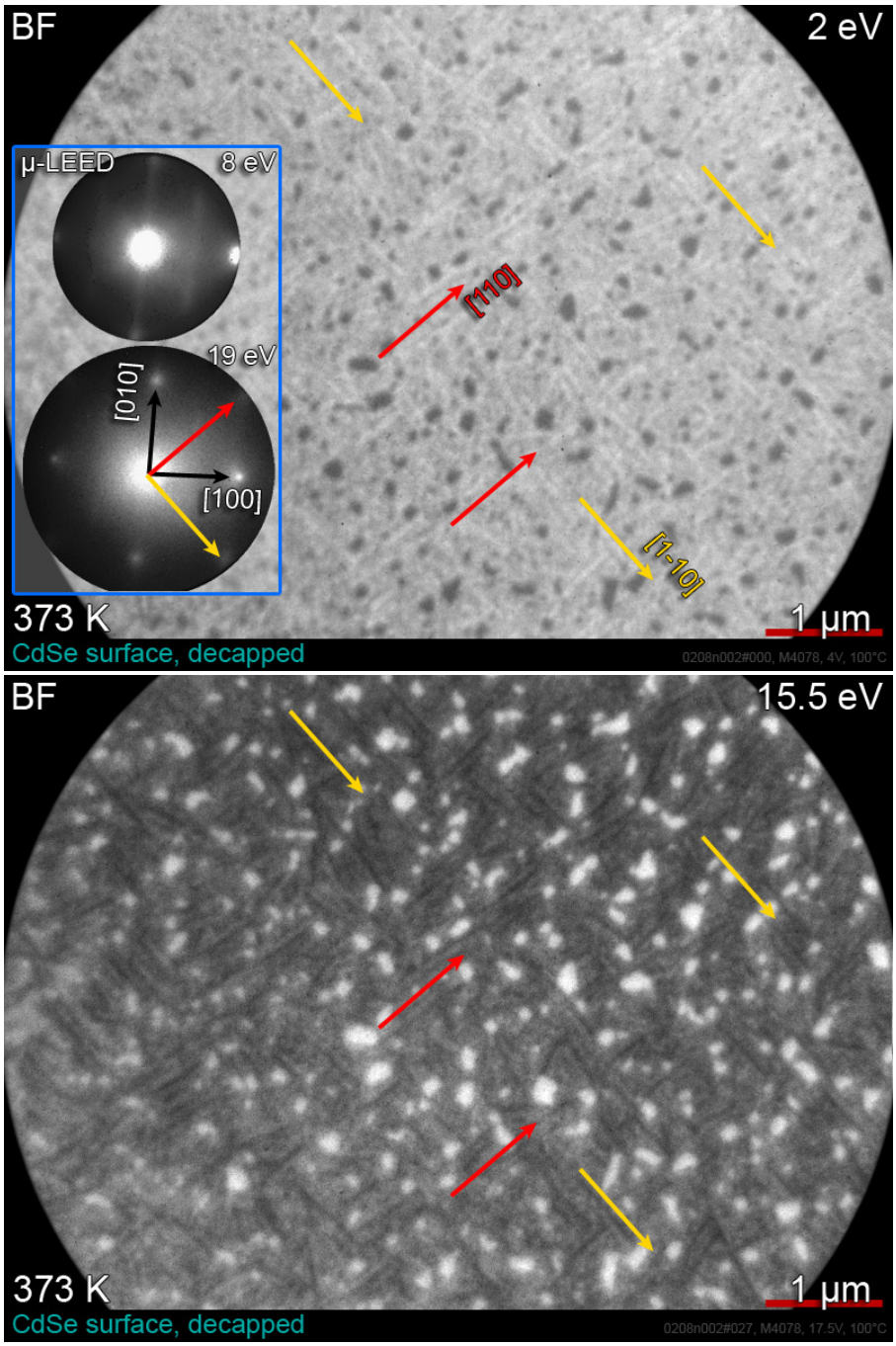

Figure 4.23: BF–LEEM images at two different energies of the decapped CdSe(Te) surface at 373 K. The insets in the top figure are μ–LEED records from about half the shown FoV at different E_{kin}. The surface structures show contrast reversal in LEEM, and the elongated structures are preferentially aligned with the {110}–directions.

recorded as labelled at kinetic energies of 8 and 19 eV. From the IMFP (fig. 2.3), penetration depths of about 8 and 2 layers, respectively, are expected. The diameter of the circles corresponds roughly to the diameter of the Ewald sphere. SMART has the speciality to project LEED spots at an identical detector position for all E_{kin}. This results in the fact, that at lower E_{kin} the structure specific spots cannot be observed anymore.
From the µ–LEED the crystallographic directions of the (001) surface are easily derived as indicated by the arrows in the 19 eV pattern. While the black arrows point along the lattice vectors [100] and [010], red ([110]) and yellow ([1$\bar{1}$0]) arrows point along the directions that are obviously preferred by the linear imprints in the LEEM images.

Findings. Although in general the {110} directions seem to provide the preferred orientation of the linear structures, that are likely to be the imprints of the µ–crystallites, some deviate largely from this direction and tend to be better aligned with the {100} directions.
The overall µ–LEED appears quite fuzzy which indicates that the long range order of the surface is rather imperfect, i.e. it is a "multi–level" rough surface [33]. The latter agrees well with the observation of low adatom mobility by Schallenberg et al. [129]. Nevertheless the substrate structure of the CdSe/ZnSe(001) surface is clearly visible. Further streaky c(2x2) and maybe (2x1) reconstructions are visible, especially at 8 eV, but at 19 eV as well. There are weak hints for facetting: faint extensions of the (00)–spot along the {110} directions (8 eV) and at the (10) and ($\bar{1}$0) spots that appeared to move by changing the energy. Hence they might result from incomplete facets or from a small, facetted fraction of the surface, or from both. Are they the faces of the QD pyramids or the prestage of the fully facetted ZnSe/CdSe interface? The contrasts for holes and lines compared to the BG are $MTF = -13$ and 3 % in the 2 eV and $MTF = 23$ and -7 % in the 15.5 eV images, respectively. Accordingly, the contrast is enhanced in the 15.5 eV image, recorded with high surface sensitivity. Besides the higher contrast for the more surface sensitive measure, both, disks (hole stamps) and lines, reverse contrast with respect to the surrounding — but inversely. The area in between shows in both cases an intermediate grey scale that basically scales just with the transmission of the microscope.

Conclusion. These areas have therefore different structures (e.g. surface reconstructions) and/or thin film thicknesses (QIC). The higher contrast for the more surface sensitive measurement implies that the origin of the contrast is close to the surface since both, crystallite and hole imprints, show the same tendency. The observation of mixed c(2x2) and (2x1) reconstructions in µ–LEED confirms the

presence of two different surface structures. They might be analogue to the similar ZnSe surface for which the (2x1) reconstruction is identified as Se–rich while the c(2x2) surface is found to be a Zn–rich phase [118, 131]. This is suggested by Robin et al. [19] for the CdSe(001) surface as well. The enhanced Cd signal at the positions of the holes, as described in the following section, might in this context point towards the c(2x2) reconstruction. Accordingly, a Se(Te)–rich(2x1) reconstruction is expected to be found at the positions of the lines.
These results show that the interaction of the Te cap with the CdSe/ZnSe MBE–grown surface leads to the formation of structures (µ–crystallites and holes) in the cap by rearrangement of the α–Te during T ramping. It is known from literature that the dominance of Se or Cd fluxes during the CdSe growth process leads to Se or Cd termination, hence (2x1) and c(2x2) reconstructions of the surface, respectively. The so formed Te structures strongly influence the formation and positioning of the QDs and hence act as a kind of retroactive template.
This kind of patterning was not observed yet when the CdSe was capped by α–Se. This might be explained by the lower sublimation temperature of approximately 350 K where the adatom mobility is still too low for a reorganisation on a scale of several hundred nm on the surface. Hence a higher density of smaller QDs is reported [18, 19, 88]. But in this case also the formation of µ–crystallites is missing. Moreover this gives rise to the aspect of surfactant mediation of the Te that might be of importance in this case.

4.3.4 First spectromicroscopic results of the CdSe/ZnSe QD surface

A brief presentation of results that were derived by µ–XPS measurements is followed by a first spectro–microscopic exploration of the CdSe(001) surface covered with QDs. The main results are the cadmium distribution, the presence of a CdSe–wetting layer and the quantification of the tellurium–remainder.

A spectroscopic overview

The spectroscopic mode, that makes use of the possibility to image the dispersive plane, was used to get a glance of the surface composition and to narrow the energy range of lines for the XPEEM studies presented in the following. Further it was useful for focussing since the available intensity is integrated and projected onto a small fraction of the detector allowing for reasonably low integration and hence adjustment times. However for tiny amounts of an element, that is well localised and therefore projected on a small fraction of the detector, the microscopy mode might be favourable.
The µ–XPS spectrum (not shown) shows strong Cd 3*d* and Se 3*d* features. Low

contrasts (not shown) in Cd 3*d* and Se 3*d* XPEEM images indicate a CdSe wetting layer (see also section 4.3.4 below). Thus, it is confirmed that the surface is widely composed of CdSe which is still present on top of the ZnSe substrate. The contaminations are low and heterogeneously distributed. The question whether a wetting layer is present or not is of special interest, as it is discussed as carrier guide, eventually necessary, e.g., to inject carriers to the QDs for localised, effective photoemission for example in LASERs. This role is discussed, e.g., by Sanguinetti et al. [90].
A comparison of the µ–XPS Te 4*d* intensities from the capped surface with the decapped surface was used to determine the remaining amount of Te. A total of 0.1 % of the original Te cap signal was found. This leads to a Te coverage of 0.6(3) % remaining near the CdSe surface. The model, on which this estimate bases, takes the cap topography (90 % thick, 10 % 2 layer–holes) and a fractional, one ML thick coverage by the remaining Te into account. It assumes that the Te stays at the surface. If intermixing took place the given amount is underestimated.

Hints for Cd accumulation at hole positions

In the following the very first laterally resolved spectroscopic information of the virgin CdSe surface with QDs is presented. The lateral resolution of the spectra derived from image stacks is equivalent to n–XPS from selected features. It allowed to demonstrate that Cd accumulates at the positions of the former holes.

Large area average. The spectra given in figure 4.24 were obtained from 0.06 µm^2 after appropriate flat field correction. Representative hole and cap positions (orange/solid and green/dashed boxes) were selected close to each other and with comparable illumination. For each energy the pixels from the marked areas in the inset images, were averaged for the resulting data point in the spectrum.
The insets show the lateral variation of intensity at two different binding energies, specific for Cd 4*d* (left, contrast enhanced image) and Zn 3*d* (linearly scaled intensity). The large scale, slight intensity variation results from the shape of the X–ray beam. The FoV of 8 µm is identical to the other XPEEM images shown earlier in this chapter.
Note the extraordinarily long acquisition time of 1239 s for the Cd image compared to the typical 10 s as used, e.g., for the Zn. This acquisition time, necessary for an acceptable S/N ratio, is owed to the reduced transmission at high kinetic energies and the low cross section of hardly half a Mbarn for both lines at a photon energy of 470 eV (see table 4.3).

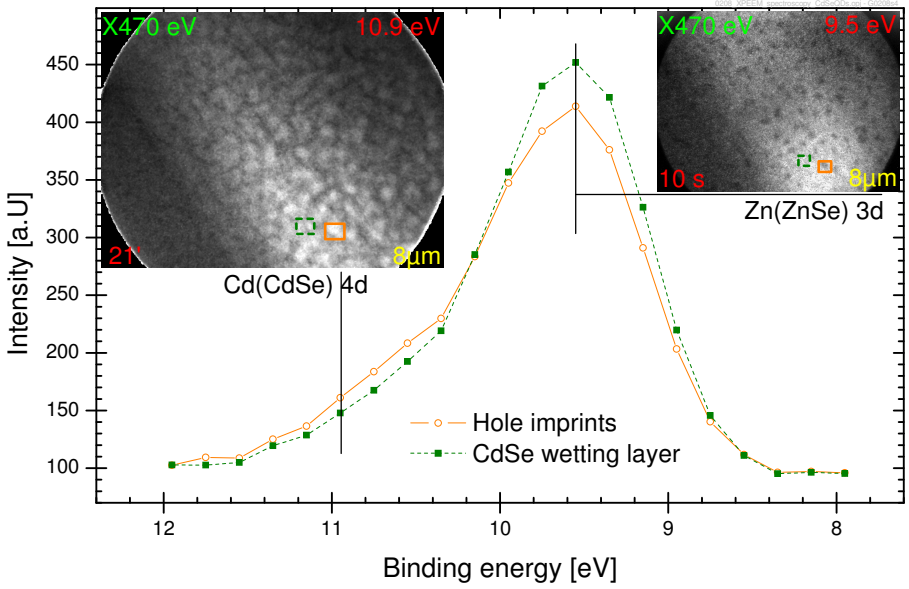

Figure 4.24: XPEEM–spectra from the signal averaged within the two marked AoI boxes. Contrast reversal is observed at $E_{bin} \sim 10\,\text{eV}$. The insets show the surface at the marked energies: on the left Cd 4*d* (CdSe)– and right the Zn 3*d* (ZnSe)–dominated contrast. Note the very different acquisition times for the images of 21 min in contrast to 10 s!

n–XPS with lateral information. Line profiles through hole imprints and the surrounding, that average across the line width of 300 nm were derived from the stack of XPEEM data at the Zn 3*d*/Cd 4*d* position near the valence band. They are presented in figure 4.25 in a 2D–plot. The image series was recorded at an illumination energy of $h\nu = 470\,\text{eV}$. Selected line scans along the spatial and the energy coordinate are above and right of the contour plot, respectively.

The spectra in figures 4.24 and 4.25 show the same tendency: The contrast reversal at about 10 eV. The reversed contrast at the Zn 3*d* compared to the Cd 4*d* is well seen in the profiles of figure 4.25, while its first occurrence at 10 eV is obvious as the intersection of the spectra from hole and cap positions. The main difference of the figures is the selected area used for the averages in the spectra. It is only 30×1 px in case of figure 4.25 and a roughly 20 times larger area for the spectrum in fig. 4.24 with $0.06\,\mu\text{m}^2(600\,\text{px})$. This justifies to use the small area average as well to derive information about the surface situation, despite the rather low S/N–ratio.

Why did it work at all? Only the vicinity of the two lines and the resulting contrast reversal enables these striking measurements. The sharpness in the Zn

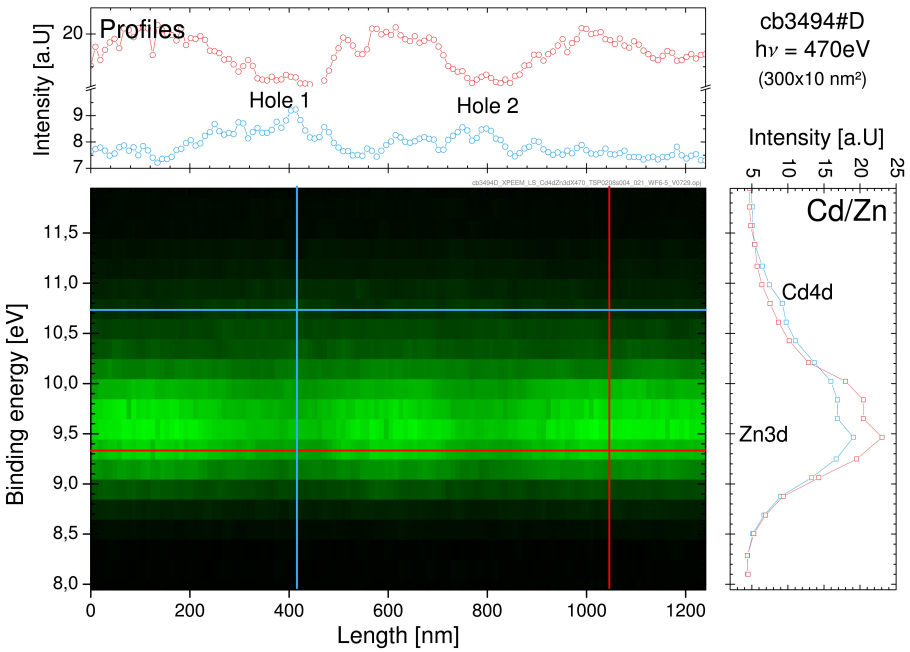

Figure 4.25: XPEEM–profiles across two former hole positions from a stack of images. The stack was recorded with $h\nu = 470\,\text{eV}$ at the energy of the Cd $4d$/Zn $3d$ lines. Despite the very week contrast especially for the Cd $4d$ signal, the observed contrast reversal is a good indication for the reliability of the results. It is visible in both, the profiles (top) and the spectra (right). Note the interrupted intensity scale in the profiles. Also, the smoother distribution of the Cd dominated signal can be seen compared the one of Zn, especially at the position of $hole_2$.

image combined with the rather high intensity (S/N–ratio) and the quite high contrast of the damping features in the Zn signal allowed for proper focussing. This is essential to reproduce very low contrasts as the one of the Cd feature, which would probably not have been found otherwise. The small energy separation between both lines and the large E_{kin} ensures proper focussing conditions within the whole energy range (see chap. B.1.1). Thus it became possible to image the weak Cd signal variations with extremely low intensity and hence signal–to–noise ratio.

Findings and discussion

The **contrast** of the profiles ($I(\vec{r})$) in figure 4.25 at the Zn energy (red) is 10(2) % while it is reversed and 6(3) % at the Cd line (blue). This is expressed by the intersection of the spectra $I(E)$ from the different positions and is directly seen in the image insets in the previous figure 4.24. It shows that the Zn signal drops at the positions of the holes while the Cd signal rises.

A Cd accumulation is emphasised if the carbon distribution is considered: A rough estimate from the Se 3*d* XPEEM image (not shown) suggests an attenuation by an additional C–layer of about 0.5 ML at the hole positions. It is assumed that CdSe/ZnSe stack is stoichiometric. Although the rather high penetration depth of about 3.5 ML[7] (3 layersin case of C 1*s* [80]) for $E_{kin} \sim 450$ eV electrons makes this probe less surface sensitive and hence reduces the influence of any carbon on the contrast, additional carbon reduces the anyway elevated Cd signal at the hole positions.

Dark lines in the Cd 4*d* image correlate with the position of the µ–crystallites in the former Te cap, found by LEEM. This is correlated via the linear structures in the 2 eV LEEM (fig. 4.23) of the bare CdSe surface. It is a further hint for enhanced CdSe adatom mobility mediated by Te. Remember at the micro–crystallite positions the Te left the surface last as discussed in section 4.3.2.

This gives rise to several possible interpretations: (i) a Cd segregation into the existing CdSe/ZnSe layers, occupying former Se sites and changing the stoichiometry. Segregation was reported as a mechanism for strain relaxation in the (In,Ga)As QD system by García et al. and Tillmann et al.[89, 132]. Or (ii) an additional CdSe layer at the hole positions that results from the low surface adatom mobility without surfactant that was reported by Schallenberg et al. [129]. Another effect (iii) on this result might origin from the c(2x2) in contrast to the (2x1) reconstructed surface, since the first is Cd terminated and the second is not [118, 133]. This leads

[7] Derived as an average of the IMFPs for Cd and Se in a CdSe crystal. The universal curve gives 4.5 ML.

to a significantly different signal of Cd in the nominally only 3.5 ML thick CdSe. This together with some carbon might be responsible for the attenuation of the Zn signal.

On resolution issues. The Zn image appears sharper than the Cd image. This visual impression from the insets in figure 4.24 is confirmed by the weak shape of the hole imprints in the profiles of figure 4.25.
Fuzziness might be attributed to two kinds of reasons: First the instrument may cause the blurring. Drift and instabilities may occur during the long acquisition time of 21 min and also trajectory displacement (or Börsch–effect[8]) in the BFP[9] of the objective lens caused by the pulsed X–ray beam[10]. However most of these effects should be observed already for an integration time of 10 s, as for the Zn 3*d* image, but they are less pronounced. A rather slow drift of about 1.5 nm/min was observed that smears out features by about 30 nm within the acquisition time of the Cd 3*d* image and has no noticeable influence within 10 s. Besides the low contrast and the poor S/N–ratio all these effects are suspected to hide the QDs themselves by fuzziness. Energetically the two lines are very close to each other, thus a difference in focus conditions is negligible (see fig B.2).

Second, the image is not blurred but a gradient in elemental distribution may cause the smooth intensity variation. For example, a segregation mechanism is expected to result in such smooth changes in the Cd concentration.
This gradient might explain the smooth edges of the hole imprints in the Cd–signal, while carbon and CdSe–adlayers at hole positions could be attributed to an additional attenuation of the Zn signal with a sharp rim. Another option is given by the arrangement of the QDs: they are found to form at the edges of the holes with separations of several diameters. Again with the immobile CdSe at hole positions this situation would also result in such contrasts.

Conclusion

Despite the discussion about fuzziness, there is more Cd signal at the hole positions than at the positions of the former Te µ–crystallites. Hence an accumulation of this element or its presence at the surface was found. To decide between both possibilities additional measurements are necessary as, e.g., DF–LEEM to determine the surface reconstruction or a change in depth sensitivity in XPEEM using different

[8] The Börsch–effect is also referred to as the energy spread, rather than the trajectory displacement, induced by approaching charged particles of initially identical energy [134].
[9] BFP – back focal plane.
[10] The duration of single pulses is only a few hundred ps [55] causing high density of photo emitted electrons within a single pulse.

photon energies. The lack of Cd at the former positions of the Te µ–crystallites might either point to Te as a surfactant or a different surface reconstruction. In the latter case the question remains, when this surface reconstruction has formed: (i) during CdSe MBE, (ii) when the α–Te was deposited or (ii) during the annealing step to remove the cap?
To resolve single QDs, shorter acquisition times and a better S/N–ratio are necessary. The potential here lies in a reduced photon energy of, e.g., $h\nu = 140\,\mathrm{eV}$. Also the planned exchange of the degenerate channel plate (ChPl) is a promising attempt. It will however stay challenging, since the contrast of the tiny CdSe QDs towards an extended CdSe wetting layer is necessarily low.

4.4 Summary and outlook

Summary. It was shown, that the transfer of the samples from the MBE in Würzburg to the SMART in Berlin was successful. Contaminations during the quick, on–air transport were avoided by the protective α–Se cap.
The α–Te cap, in its micromorph stage, was characterised in detail. Features were carefully assigned to different phases and cap thicknesses. The prominent orientation of the elongated µ–crystallites was correlated to the crystallographic directions of the CdSe substrate. Figure 4.26 summarises the features and their correlation with each other. The decapping process was observed in–situ and in real–time with LEEM. The appearance of QDs and their T stability was shown. They were identified as what is known from literature as 'type B' QDs [135], large dots with low areal density. Their average diameter is about 35 nm and a density of just $3.2 \times 10^9\,\mathrm{cm}^{-2}$ was found, which is confirmed by immediate, ex–situ AFM measurements. These densities are by more than two orders of magnitude lower than the density of 'faceted' islands ('type A' QDs) that form by MBE growth of strained CdSe at elevated temperatures.
Further, a cross–correlation of substrate surface and cap features was discovered. An arrangement of the QDs with respect to specific cap features was found. Hence it is concluded that the termination of the CdSe epi–layer influences the later arrangement of the QDs. This behaviour is thought to origin from different surface reconstructions.
It was shown that QDs typically form at the edges of holes or even at positions that were right below the thick α–Te cap, which indicates that the cap material is involved in the formation process, e.g. as a surfactant and/or a vapour barrier and/or a (stress/chemical) nucleation site. For example, Toporov et al. [130] used Te successfully to enhance the CdSe/ZnSe island formation and ascribed this effect to a stressor nuclei. Others deposit an additional Cd layer on top of an α–Se cap that is intended to act as barrier for the Se vapour, similar to the Se flux typically

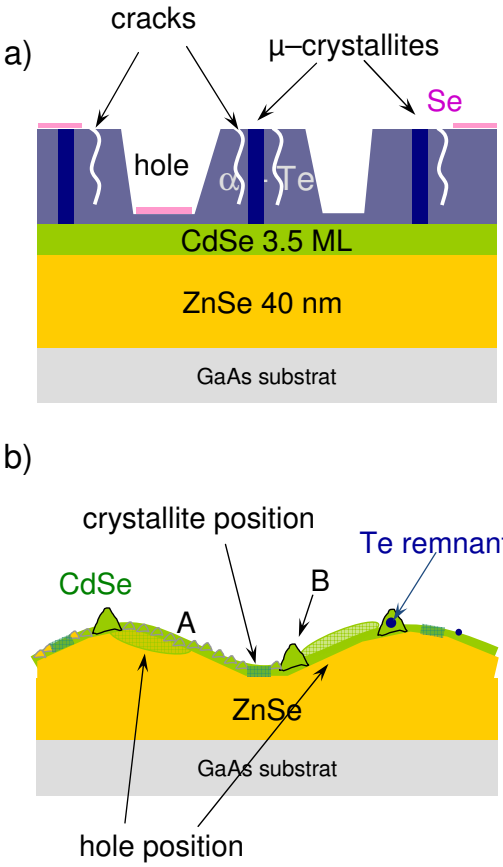

- α-Te (15 nm) capped surface on nominal 3.5 ML CdSe/ZnSe
- Se remnants from protective cap
- Holes and cracks
  - ~2 layers of Te at the bottom of the holes
  - How deep are the cracks?
- μ–crystallites in α-Te matrix

- Cd enrichment at hole positions:
  - Segregation or additional layer?
- Structural difference in hole and crystallite positions:
  - c(2x2) & (2x1)?
- Two types of QDs: A and B
  - Faceted interface and/or CdSe dots?
- < 0.1 ML of Te left:
  - Incorporated or at the surface?

Figure 4.26: The two steady state situations of the capped and uncapped CdSe/ZnSe sample are shown. The rich diversity of the surface features in both cases is summarised. Different possibilities for their interpretation are given.

applied during the annealing step.
Although it was not possible to determine the stoichiometry of single QDs, yet another very interesting finding was made: Cd accumulates at the positions of the holes in the former α–Te cap. This is attributed either to the c(2x2) reconstruction, which is Cd terminated, or to adlayers of CdSe that could not take advantage of enhanced adatom mobility by the Te cover or Cd segregation into the the ZnSe substrate.

Outlook. These results give directly rise to new questions for succeeding investigations. The still open question about the stoichiometry of the QDs, especially: Do the dots contain a little amount of the remaining 0.6(3) ML of Te or is it segregated into the (Cd,Zn)Se? To answer this question a combination of improved parameters is suggested: A recent study by Robin et al. [19, 128] claims, that most distinct islands are formed for 3 layers of strained CdSe on ZnSe by desorption of an α–Se cap. The window for QD formation is narrow between 2.5 and 3.5 layers [19]. Hence a sample with 3.0 layers of CdSe should be used.
Additionally the probe beam should be adjusted for higher surface sensitivity and improved S/N–ratio, e.g., for BESSY $E_{h\nu} = 140\,\mathrm{eV}$ at the Cd $4d$/Zn $3d$ position. As soon as the planned exchange of the multi channel plate was successful, an improved experiment would be possible. Further a temporal stretching of the pulsed X–ray beam could avoid the effect of trajectory displacement (or Börsch–effect[11]), which is expected to result in improved resolution. This will at least maximise the contrast and probably also enhances the resolution for tiny structures such as QDs.

Which option describes the Cd accumulation correctly? A segregation process or the surface termination? This question can probably be answered with additional DF–images combined with the above mentioned improvement of the Cd/Zn contrast. Additionally to the findings and the resulting open questions, first evidence was found (not shown) for further interesting discoveries: A low amount ($\sim 1\,\mathrm{ML}$) of CdSe (see also [18]) or a low desorption rate ($\sim 0.3\,\mathrm{K\,s^{-1}}$) of the ($\alpha$–Se) cap may lead to a fully facetted CdSe/ZnSe interface. Such a thin, probably strained layer seems to be sensitive to X–ray illumination as well. It was observed that the formation of quantum structures from strained epi–layers cannot just be induced by the rise of T but also by X–ray irradiation.

With the present investigation the first step was made. The capabilities of the spectro–microscope SMART were demonstrated. Already some very exciting findings could be presented. Structural phases of the heterogeneous Te cap were correlated to the

[11] The Börsch–effect is also referred to as the energy spread, rather than the trajectory displacement, induced by approaching charged particles of initially identical energy [134].

positions of QDs and other features that differ in structure and chemistry. Some further instrumental improvements together with an adjusted probe and optimised sample will allow more promising future experiments.

A

Acronyms

AC–LEEM	aberration corrected LEEM
AES	auger electron spectroscopy
AFM	atomic force microscopy
ALE	atomic layer epitaxy
AoI	area of interest
BESSY	Berliner Elektronenspeicherring-Gesellschaft für Synchrotronstrahlung m.b.H.
BF	bright field
BFP	back focal plane
BG	background
CA	contrast aperture
CCD	charge coupled device
cff	constant fixed focus
ChPl	channel plate
CVD	chemical vapour desposition
DF	dark field

EELS	electron energy loss spectroscopy
FA	field aperture
FF	flat field
FoV	field of view
FvM	Frank–van der Merwe
FWHM	full width at half maximum
Hg–PEEM	Hg–light PEEM
IMFP	inelastic mean free path
I–V	current–voltage
LASER	light amplification by stimulated emission of radiation
LED	light emitting diode
LEED	low energy electron diffraction
LEEM	low energy electron microscopy
MBE	molecular beam epitaxy
MCP	multi–channel–plate
MEM	mirror electron microscopy
ML	monolayer
MTF	modulation transfer function
NEXAFS	near–edge x–ray absorption fine structure
NTCDA	1,4,5,8–naphthalene–tetracarboxylic acid dianhydride
OLED	organic light emitting diode
OPV	organic photovoltaics
PED	photo–electron diffraction
PEAD	photo–electron angular distribution
PEEM	photoemission electron microscopy
PES	photoelectron spectroscopy
PGM	plane grating monochromator
PID	proportional – integral – differential

PL	photo luminescense
PTCDA	3,4,9,10–perylene–tetracarboxylic acid dianhydride
PTCDI	3,4,9,10–perylene–tetracarboxylic acid diimide
QD	quantum dot
QIC	quantum interference contrast
RGB	red, green, blue
RHEED	refelction high energy electron diffraction
RMS	root mean square
rp	ripple phase
RT	room temperature
SEM	scanning electron microsopy
SK	Stranski–Krastanov
SMART	spectro–microscope with aberration correction for resolution and transmission enhancement
SPALEED	spot–profile analysis LEED
SPELEEM	spectroscopic photo–emission and LEEM
SPLEEM	spin polarized LEEM
STM	scanning tunnelling microscopy
T	temperature
TC	thermocouple
TEEM	thermionic emission electron microscopy
TEM	transmission electron microscopy
UHV	ultra–high vacuum
UV	ultraviolet
UV–PEEM	ultraviolet PEEM
VB	valence band
VW	Vollmer–Weber
XMCD	x–ray magnetic circular dichroism

XMLD x–ray magnetic linear dichroism

XPEEM x–ray PEEM

XPS x–ray PES

XRD x–ray diffraction

B

Data acquisition, intensity and analysis

B.1 Intensity Calibration

The LEEM, XPEEM, LEED and XPS data were acquired in–situ with the multi–method spectro–microscope SMART, described in chapter 2.1. The shown AFM images were recorded on air with a digital instruments NanoScope IIIa Scanning Probe Microscope at BESSY II.
This section introduces details of the image acquisition system and discusses the intensity scale calibrations for the different techniques if applicable.

B.1.1 XPS intensity depends on objective focus

Focussing was found to have an unexpectedly huge influence on the intensity of the XPS–spectra (figure B.1).

This is due to the fact, that the brilliant synchrotron radiation is well focused down to about 9 µm FWHM which is in the region of the diameter of the sampled area. A small so–called field–aperture selects the AoI in the image plane (see figure B.3b). Therefore it is crucial that the image within this plane is kept focussed over the whole range of sampled kinetic energy. Otherwise the beam spot (as well as the surface structure) smears out (figure B.3a) and so the intensity that passes the aperture drops rapidly. The dependency of the focus on the chosen kinetic energy

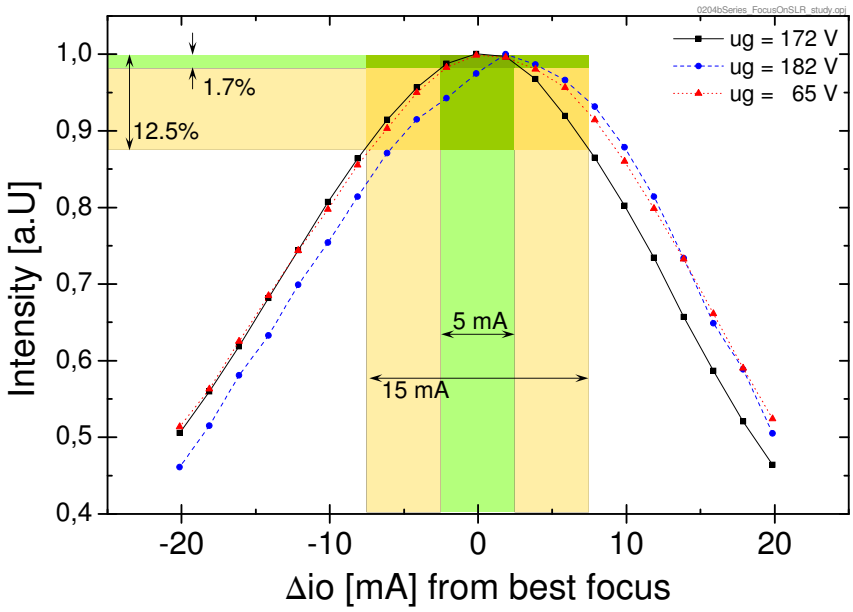

Figure B.1: Measured, normalised total intensity as a function of the objective lens current io with the in focus condition $io = 0$. Marked are the focus current ranges without tracking (yellow) and with optimised linear combination (green) of the focus to the bias voltage ug.

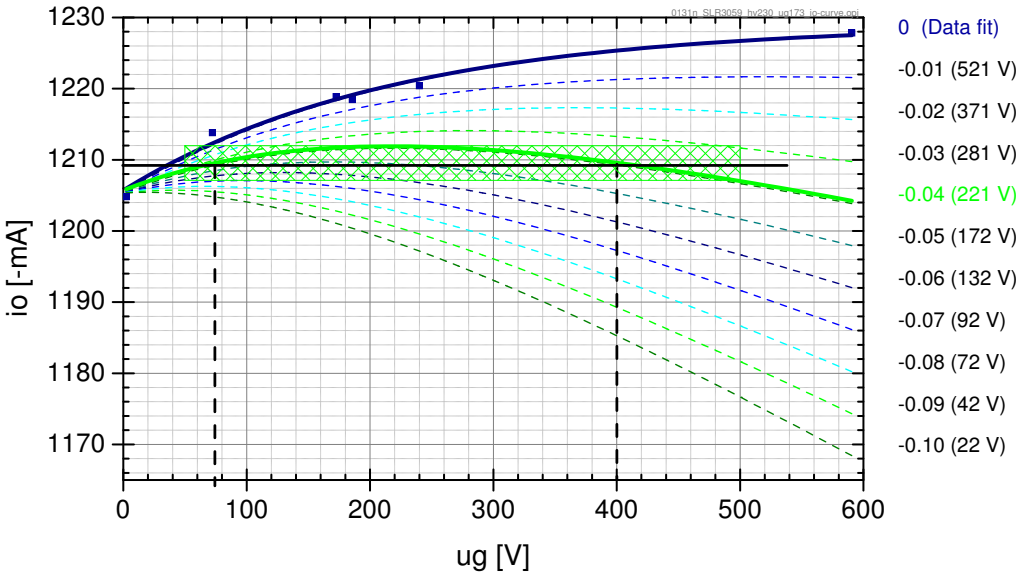

Figure B.2: Set of curves representing the objective current io as a function of the bias voltage ug for different combination settings. The numbers on the right are the slope m (and maximum position) of a linear contribution of ug to the effective io as $io = io_{set} + m \cdot ug \frac{mA}{V}$. The topmost solid curve is a 3^{rd} order polynomial fit to the data points. It serves as basis for the calculated curves below. The thick solid green curve has the optimum combination setting of -0.04 used for typical wide range µ–XPS measurements.

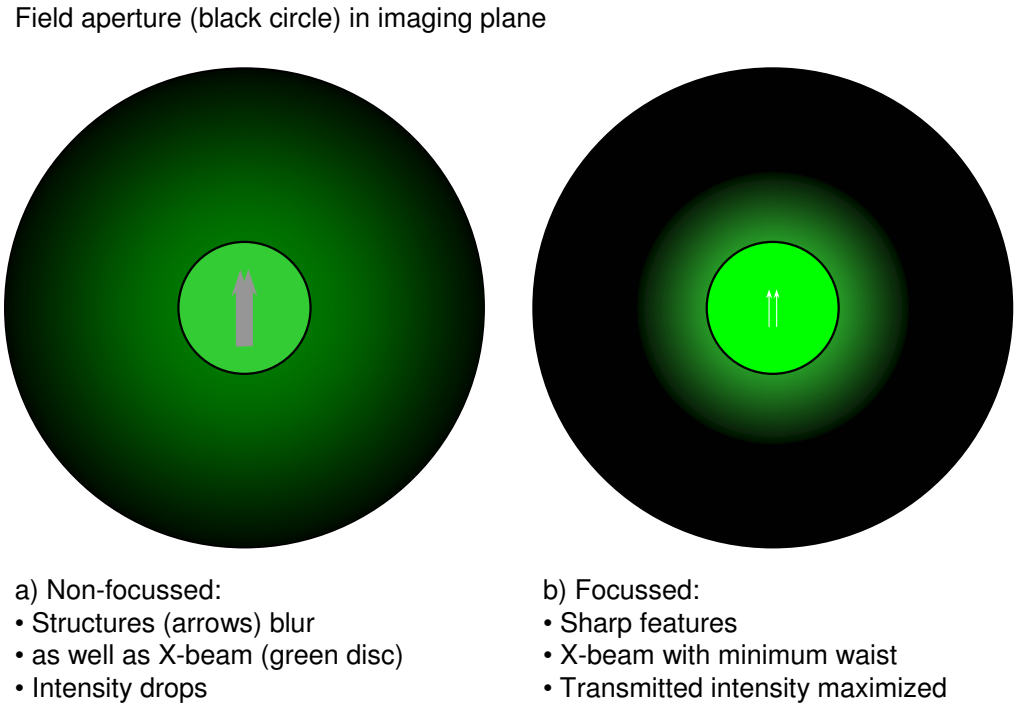

Figure B.3: In the field aperture (image) plane a) the defocussed and b) well focussed case is illustrated. Within the aperture (black circle) the selected AoI is shown. The green X–ray beam shows in the focussed case b) the gaussian beam profile and sharp features (arrows) on the surface. Intensity outside the black circle is blocked by the aperture.

is shown in figure B.2. It is not necessary to carry the focus along with it as long as the selected area is much larger than the spot of illumination. Alternatively if the spectral range is small enough the intensity does not vary significantly as well.

Vice versa this effect may be used to find roughly the proper focus conditions for XPEEM for an unknown system that is pre–aligned in LEEM at low kinetic energies if, e.g., e–beam damage might be a problem. This was demonstrated by a series of XPEEM images recorded after the intensity was maximised by focus adjustment in µ–XPS. This has the advantage that one can focus quite well even if the contrast or the overall intensity is very low and does not allow to screen the full focus range in necessary detail in the XPEEM mode on reasonable time scales. It is because the intensity from the full area of interest is collected to a small area on the detector and thus enhances the signal to noise (S/N) ratio. For example the intensity spread in XPEEM across an area with about 40 mm in diameter on the channel plate can be concentrated to an area as small as about 1 mm gaining a factor of 1600 in flux density and therefore in acquisition time.

B.1.2 Background removal for quantitative analysis

Appropriate BG removal is crucial for quantitative analysis, when spread across one image as it is the case especially for the XPS data. It is not necessary for stack analysis from the same image area, as long as it is not compared quantitatively to other AoI as desired in LEED/LEEM–IV.
Contributions to the BG are considered from three components of the data acquisition system: The microscope column, the MCP amplifier with the attached phosphor screen (ChPl) and the recording pco.1600 high performance CCD video camera. The different contributions to the recorded intensity I_{CCD} are

$$I_{CCD} = (I[x, y, t] + I_{stray}) \cdot Gain_{ChPl} + OFF_{CCD} \tag{B.1}$$

where $I[x, y, t]$ represents the signal one is interested in to measure, I_{stray} represents the intensity contribution by stray electrons within the microscope, $Gain_{ChPl}$ is the electron–photon conversion factor by the channel plate and OFF_{CCD} the intensity offset introduced by the camera. In general all these quantities depend on the image position (x, y).
The contributions from different parts can only be recorded together. Care was taken to record them as independently as possible. A description of the sources of this background is given and the induced error in intensity is estimated in the following paragraphs.

Image generation: SMART

From the microscope itself and its UHV components, as vibration–free ion pumps and electrostatic lenses, there might be scattered light and emitted electrons projected via side paths to the screen. This was observed to contribute to the signal from the so called burning lenses in the projection optics. Most likely this is caused by whisker–like tips that form on the highly negative electrodes. It was reduced carefully by plasma etching of the lens electrodes.
This was done by providing an air pressure of up to 10^{-4} mbar to the chamber of the burning lenses while applying 20 kV for several hours. The maximum operation voltage is 15 kV. This procedure typically reduces the interfering noise by several orders of magnitude and reduces it below the detection limit for data acquisition situations typical for the measurements of this work.
However, this kind of background returns with time of operation of the microscope and cannot be considered as permanent. It is approximated as a linear variation across the detector on top of the constant background of single images or image series acquired within several minutes.
For the XPS spectra it is fitted to the separate 13 eV wide spectra such, that there appears no jump to the adjacent ones.
In the case of imaging it is not crucial, since structure sizes are not influenced and laterally resolved XPEEM–stack Spectra are typically not affected. If fluctuations occur while recording an image stack the amplitudes are either within the noise or pretty obvious.

Intensity amplification: Channel plate and screen

Due inhomogeneities in manufacturing and to the naturally unbalanced exposition of the channel plate and the attached screen over the years of operation, the amplification factor has a lateral variation. To correct the detected intensities the images have to be divided by a recorded flat field (FF), representing this amplifier degeneration.
Good flat fields are achieved in LEEM at kinetic energies with low contrast, in a slightly defocused condition (or in perfect focus if only phase contrast at steps is observed) and when all the contrast enhancing apertures are removed. These settings are meant to reduce the contrast as far as possible. Zooming in and inducing vibrations to the sample while exposing the CCD for quite some time (several seconds) smears out eventually remaining features equally over the field of view (FoV). LEEM is used because of its high intensity and homogeneous illumination. The high intensity allows records with low amplification and therefore with a minimum channel plate noise. To minimise the influence of constant background, the acquisition time was set to use the capacity of the CCD as completely as possible, meaning close to the

full 72 dB dynamic range (digitalised with 14 bit). This leads to a relative error in the calibration of the intensity of less than 0.004.

Information recording: pco.1600 digital video camera

Possibly scattered visible light was shielded carefully from the optics of the camera. Its contribution is negligible for acquisition times up to at least 30 minutes.
To enable comprehensive noise analysis, also for signed electronic noise, the CCD is supposed to add up online 100 counts electronically. This is sufficient since the read out noise of the camera is below 21 electrons, equivalent to 10 cts. It was observed that this offset varies between 80 and 120 cts.
That is why for background subtraction it was taken from the dark, not illuminated, corners of the image, where the steel flange surrounding the embedded phosphor screen limits the FoV. In the case of XPS it is taken from the spectral part above the Fermi edge or the valence band.
Therefore the resulting error in intensity is considered to be less than 2 % in the worst case (signal intensity $\sim$ 50 cts). The uncertainty due to the CCD read out noise in a comparable scenario would be with 10 % dominating, but the XP–spectra are taken as a 101 pixel average. Also line scans average over several ten pixels and typically use a much higher fraction of the 14 bit (16384 grey scales) image intensity scale.

B.2 Scaling and accuracy

Due to the variety of applicable methods several scales and their accuracies had to be determined.

B.2.1 Time scale

The time was used directly for observation of changes in time (decapping, growth) and indirectly to assign the proper temperature to the images.
It was found in the case of the pco.1600 camera together with the frame grabber, that there is a deviation between desired (set) period between two images and the actually recorded images. Due to the hardware frame grabbing in average additional 0.106 s have to be added. As implied the resulting accuracy of these measurements is better than 10 ms.

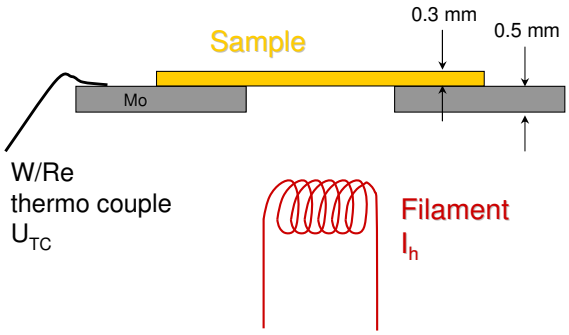

Figure B.4: Geometry for sample heating and T measurement implemented into the sample cartridge. Between the sample and the filament a voltage for electron bombardment can be applied.

B.2.2 Temperature measurement and scale

Temperatures were measured on top of the 0.5 mm strong Mo sample carrier, close to the sample surface (figure B.4). Within the cartridge a W–Re thermocouple as well as the filament are mounted and therefore transferred together with the sample into the UHV system. The contacts are made from W–Re as well.

The calibration of the thermocouple voltage was done carefully using the data for C–type TCs from Yates [136]. Temperatures displayed by the *EUROTHERM* T_{EURO} had to be adjusted by

$$T = 1.0366 \cdot T_{EURO} + 11.5\,K + 273.15\,K \tag{B.2}$$

due to calibration inaccuracies found by applying a constant voltage from a resistor decade to the whole detection setup.

Finally the temperatures are correlated to the images by their time–stamps. In case of fast T–ramps the clock of the pco.1600 camera was synchronised with the clock of a standard Fuji digital camera used to capture the process parameters. This was done with an accuracy of better than $\Delta t \sim 0.5\,s$ and results in a total temperature deviation of less than 1 K for ramps of 2 $K\,s^{-1}$.

B.2.3 Length scale — real space

The x–y–length scale on the sample was determined with the help of two mechano–photoelectric micrometre measuring sensors MT12B from Haidenhain [137] attached to the manipulator of the microscopy chamber. Distances were correlated by moving the sample stepwise by a distinct distance and recording images for each position. Within this magnification (mode M4078) the scale was determined and the following

Table B.1: Microscope operation modes and their corresponding magnifications M for imaging on screen, FoV and relative error when operating the camera with 2×2 binning. The present values apply for the measurements on quantum dot samples.

Mode	**M**/1	**FoV**/µm	**Error** [%]
MX 9650	2 200	18.20	3.6
M 6118	3 400	11.65	2.2
M 4078	5 100	7.80	2.2
M 3059	6 900	5.79	2.6
M 2039	10 400	3.86	2.5
M 1020	20 100	1.99	2.5

zooming allowed to calculate the distances also for higher and lower magnifications. A summary for the QD measurements is shown in table B.1.
In contrast, the resolution of the instrument is not determined by the scales. Mainly the alignment, the sample itself and the method influence the maximum resolving power.

B.3 Electron bombardment and C contamination

Typically carbon contamination is an issue in surface science since the aim is to observe well defined samples. But there are also residual gases in the microscopy chamber. The measurements were performed for hours which allows for C to stick to the surface although the total residual pressure is lower than 5×10^{-10} mbar. However, a sample preserving effect was observed that resulted from the collimated electron beam illuminating the surface. It was found that carbon was deposited mainly at the boundary of the electron beam. This results in a ring of carbon whereas at its centre the measurements were performed. The diameter of this ring was in order of 20 µm while the carbon ring was typically less than 0.3 µm wide (figure B.5). The area of interest was about 8 µm wide in the case of CdSe quantum dots and even less for the measurements of PTCDA on Ag(111).

This phenomenon can be explained (see figure B.6) assuming that residual gas molecules (1) are ionised by the intense e–beam (2) and then accelerated by the electric field (sample surface is at −15 kV with respect to the objective electrode) towards the sample (3) and deposited within a low penetration depth (parallel to surface into the beam) onto the sample surface (4). Due to the high electric field of $5\,\mathrm{kV\,mm^{-1}}$, only a small fraction of the residual gas ions can penetrate far

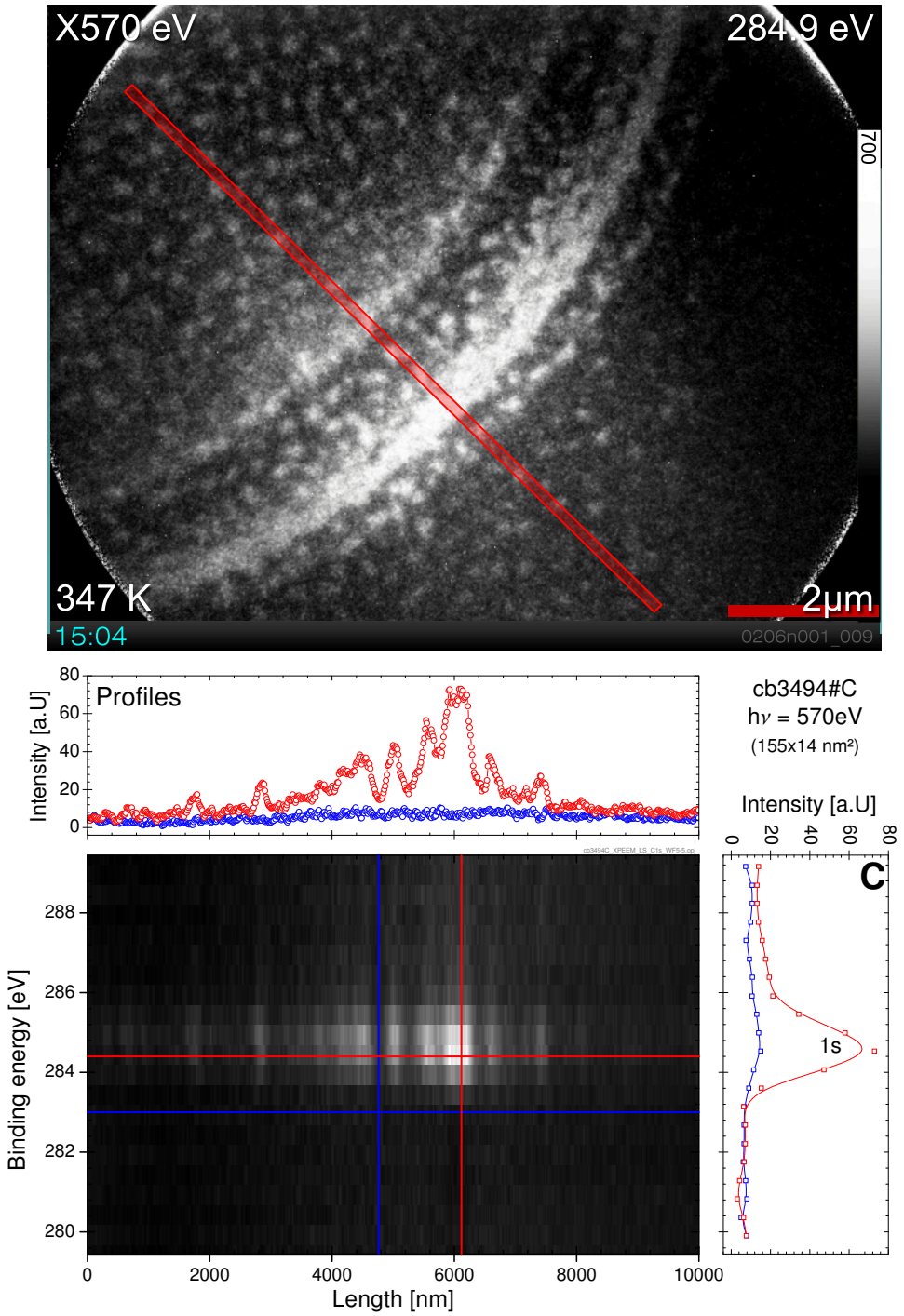

Figure B.5: The top figure shows a 2D–plot of the decapped CdSe surface. The photon energy is 570 eV the electron binding energy 285 eV at the *C* 1*s* line. A stack profile was taken along the red bar, averaged across its width, which is plotted in the lower figure. Along the length axis and the energy axis profiles were taken. The blue and red, vertical and horizontal lines mark the positions where the profiles were taken.

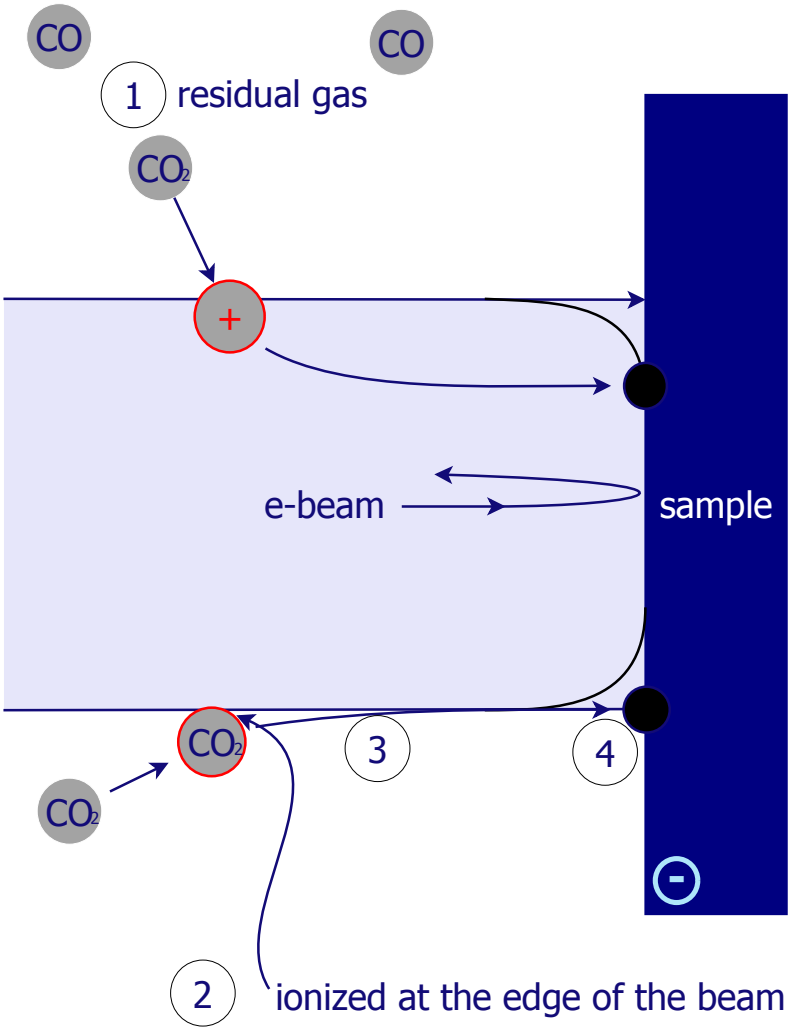

Figure B.6: Model for the C–deposition effect of the electron beam. See text for description.

enough into the beam to contaminate the area of interest. This leads to a quite low carbon entry into the sampled region. Nevertheless, the amount of carbon within the sampled area seems to be higher than in an area that was not investigated in advance.

B.4 Information content of images

B.4.1 Common information content

In general the images recorded with SMART provide more information than only the pure data. In the corners additional information on the recording conditions are given. Typically BF–LEEM images are in grey–scale, DF–images are red, green, blue (RGB)–coloured and XPEEM–figures are monochromatic. At top right the photon energy (preface X means X–rays) or the LEEM mode (BF or DF) is given. The top right corner presents the binding energy of the emitted (PEEM) or the kinetic energy of the reflected (LEEM, MEM) electrons. The bottom line contains the surface temperature during recording on the left and the length scale on the right with the red scale bar.
The cyan statement in the bottom line gives varying information, typically on the preparation stage or the time of recording.

B.4.2 How to read the XPEEM stack figures

XPEEM stack figures as 4.4 are derived from sequences of images recorded typically at different energies. They are divided in two parts:
On top a selected XPEEM image (colour coded according to table 4.2) of the sample surface is shown with chemical contrast at a selected binding energy. The smooth, large–scale intensity variation across the image originates from the size of the x–ray beam, which has a typical FWHM of ∼9 µm. The corners of the images contain – from top left to the bottom right – information on photon energy, binding energy, temperature and lateral scale. The time of acquisition is displayed below the temperature. Intensity was acquired for typically 10 sec per image leading to typical stack recording times of about 6 min. On the right of the image the vertical intensity scale contains the maximum counts after appropriate flat field (FF) and offset correction.

The lower part of the figure displays a line–scan along the red rectangle in the upper image averaged across its width of 50 nm. It was taken for a stack of images with different E_{bin} which is plotted along the vertical axis of the 2D–plot. For

both axes two line–scans were depicted at positions marked with a red and a blue line. On the right and on top of the $E_{bin}(\vec{r})$–plot the intensity is plotted as a function of the binding energy (spectrum) and the lateral coordinate (contrast) respectively. Intensities of single data points are collected from $10 \times 50\,\mathrm{nm}^2$ small areas and represent electron count rates. The intensity scales of the line–scans are normalised to 1 sec acquisition time and standard channel plate gain. This provides a comparable measure of the available electron flux.

Bibliography

[1] R. Fink, M. R. Weiss, E. Umbach, D. Preikszas, H. Rose, R. Spehr, P. Hartel, W. Engel, R. Degenhardt, R. Wichtendahl, et al. *SMART: a planned ultrahigh-resolution spectromicroscope for BESSY II.* J. Electron Spectrosc. Relat. Phenom. **84(1-3)** (1997), 231.

[2] T. Schmidt, H. Marchetto, P. L. Lévesque, U. Groh, F. C. Maier, D. Preikszas, P. Hartel, R. Spehr, G. Lilienkamp, W. Engel, et al. *Double aberration correction in a low–energy electron microscope.* Ultramicroscopy **110** (2010), 1358.

[3] I. Veeco. *diNanoScope Software 7.20 - Users Guide.* Veeco Instruments Inc., 7th edition, 2006/07.

[4] BESSY. *Two microfocus beamlines for high resolution photoelectron microscopy at UE49.* HZB, BESSY Intranet, 2005.

[5] K. Glöckler, C. Seidel, A. Soukopp, M. Sokolowski, E. Umbach, M. Bohringer, R. Berndt, and W. D. Schneider. *Highly ordered structures and submolecular scanning tunnelling microscopy contrast of PTCDA and DM-PBDCI monolayers on Ag(111) and Ag(110).* Surf. Sci. **405(1)** (1998), 1.

[6] E. Moulin, J. Sukmanowski, M. Schulte, A. Gordijn, F. Royer, and H. Stiebig. *Thin-film silicon solar cells with integrated silver nanoparticles.* Thin Solid Films **516(20)** (2008), 6813.

[7] E. Moulin, J. Sukmanowski, P. Luo, R. Carius, F. Royer, and H. Stiebig. *Improved light absorption in thin-film silicon solar cells by integration of silver nanoparticles.* J. Non-Cryst. Solids **354(19-25)** (2008), 2488.

[8] A. Schöll. *High-resolution investigation of the electronic structure of organic thin films.* Ph.D. thesis, Universität Würzburg, 2003.

[9] J. Stöhr, H. A. Padmore, S. Anders, T. Stammler, and M. R. Scheinfein. *Principles of X-Ray Magnetic Dichroism Spectromicroscopy.* Surf. Rev. Lett. **5(6)** (1998), 1297.

[10] M. Schneider, E. Umbach, and M. Sokolowski. *Growth-dependent optical properties of 3,4,9,10-perylenetetracarboxylicacid-dianhydride (PTCDA) films on Ag(1 1 1).* Chem. Phys. **325(1)** (2006), 185.

[11] A. Hauschild, K. Karki, B. C. C. Cowie, M. Rohlfing, F. S. Tautz, and M. Sokolowski. *Molecular Distortions and Chemical Bonding of a Large pi -Conjugated Molecule on a Metal Surface.* Phys. Rev. Lett. **94(3)** (2005), 036106.

[12] H. Marchetto, U. Groh, T. Schmidt, R. Fink, H.-J. Freund, and E. Umbach. *Influence of substrate morphology on organic layer growth: PTCDA on Ag(111).* Chem. Phys. **325(1)** (2006), 178.

[13] M. Rohlfing, R. Temirov, and F. S. Tautz. *Adsorption structure and scanning tunneling data of a prototype organic-inorganic interface: PTCDA on Ag(111).* Phys. Rev. B **76(11)** (2007), 115421.

[14] S. Schmitt. *Adsorbatinduzierte richtungsabhängige Facettierung und selbstorganisierte Domänen-Musterbildung auf vizinalen Ag(111)-Oberflächen.* Ph.D. thesis, Universität Würzburg, 2006.

[15] F. Pollinger. *Surface stress and large-scale self-organization at organic-metal interfaces.* Ph.D. thesis, Universität Würzburg, 2008.

[16] B. Krause. *Growth and Structure of the Organic Molecule PTCDA on Ag(111).* Ph.D. thesis, MPI für Metallforschung Stuttgart, 2002.

[17] H. Marchetto. *High-resolution spectro-microscopic investigations of organic thin film growth.* Ph.D. thesis, FHI Berlin, 2006.

[18] S. Mahapatra. *Formation and properties of epitaxial CdSe-ZnSe quantum dots.* Ph.D. thesis, Universität Würzburg, 2007.

[19] I.-C. Robin, T. Aichele, C. Bougerol, R. Andre, S. Tatarenko, E. Bellet-Amalric, B. V. Daele, and G. V. Tendeloo. *CdSe quantum dot formation: alternative paths to relaxation of a strained CdSe layer and influence of the capping conditions.* Nanotechnology **18(26)** (2007), 265701.

[20] T. Aichele, I.-C. Robin, C. Bougerol, R. André, S. Tatarenko, and G. Van Tendeloo. *CdSe quantum dot formation induced by amorphous Se.* Surf. Sci. **601(13)** (2007), 2664.

[21] Y. M. Niquet, C. Priester, C. Gourgon, and H. Mariette. *Inhomogeneous strain relaxation in etched quantum dots and wires: From strain distributions to piezoelectric fields and band-edge profiles.* Phys. Rev. B **57(23)** (1998), 14850.

[22] L. Borkovska, R. Beyer, O. Gudymenko, V. Kladko, N. Korsunska, T. Kryshtab, Y. Sadofyev, Y. Venger, and J. Weber. *Study of strain relaxation in CdSe/ZnSe nanostructures.* J. Cryst. Growth **275(1-2)** (2005), 2281.

[23] C. Kumpf, A. Stahl, I. Gierz, C. Schumacher, S. Mahapatra, F. Lochner, K. Brunner, G. Schmidt, L. W. Molenkamp, and E. Umbach. *Structure and relaxation effects in thin semiconducting films and quantum dots.* Phys. Status Solidi C **4(9)** (2007), 3150.

[24] C. Seidel, J. Poppensieker, and H. Fuchs. *Real-time monitoring of phase transitions of vacuum deposited organic films by molecular beam deposition LEED.* Surf. Sci. **408(1-3)** (1998), 223.

[25] E. Bauer. *Photoelectron spectromicroscopy: present and future.* J. Electr. Spectr. **114** (2001), 975.

[26] D. Preikszas. *Korrektur des Farb- und Öffnungsfehlers eines Niederspannungs-Elektronenmikroskops mit Hilfe eines Elektronenspiegels.* Ph.D. thesis, TU Darmstadt, 1995.

[27] D. Preikszas and H. Rose. *Correction properties of electron mirrors.* J. Electron Microsc. **46(1)** (1997), 1.

[28] T. Schmidt, S. Heun, J. Slezak, J. Diaz, K. C. Prince, G. Lilienkamp, and E. Bauer. *SPELEEM: Combining LEEM and Spectroscopic Imaging.* Surf. Rev. Lett. **5(6)** (1998), 1287.

[29] C. Davisson and L. H. Germer. *Diffraction of Electrons by a Crystal of Nickel.* Phys. Rev. **30(6)** (1927), 705.

[30] M. A. van Hove, W. H. Weinberg, and C.-M. Chan. *Low-Energy Electron Diffraction.* Springer Series in Surface Sciences 6. Springer, 1986.

[31] C. Stadler. *Strukturuntersuchungen organischer Monolagen auf Ag(111).* Ph.D. thesis, Universität Würzburg, 2009.

[32] U. Groh. *Spektromikroskopische Untersuchungen an organischen Nanostrukturen.* Ph.D. thesis, Universität Würzburg, 2006.

[33] M. Horn von Hoegen. *Growth of semiconductor layers studied by spot profile analysing low energy electron diffraction.* Z. Kristallogr. **214** (1999), 591.

[34] J. Pendry. *Multiple scattering theory of electron diffraction.* Surf. Sci. **299-300** (1994), 375.

[35] K.-M. Schindler. *Photoelektronenbeugung.* Chemie in unserer Zeit **30(1)** (1996), 32.

[36] R. Markowski, M. Piacentini, D. Debowska, M. Zimnal-Starnawska, F. Lama, N. Zema, and A. Kisiel. *Electronic structure of zincblende ZnSe: theory and experiment.* J. Phys.: Condens. Matter **6(17)** (1994), 3207.

[37] *Zinc selenide (ZnSe) band structure.* In O. Madelung, U. Rössler, and M. Schulz (editors), *Landolt-Börnstein - Group III Condensed Matter Numerical Data and Functional Relationships in Science and Technology*, volume 41B; II-VI and I-VII Compounds; Semimagnetic Compounds of *The Landolt-Börnstein Database*, chapter 2.1.27. SpringerMaterials, 2010.

[38] T. C. Chiang and F. J. Himpsel. *2.1.27 CdSe - Band structure and core levels of tetrahedrally-bonded semiconductors.* In A. Goldmann and E.-E. Koch (editors), *Landolt-Börnstein - Group III Condensed Matter Numerical Data and Functional Relationships in Science and Technology*, volume 23a of *The Landolt-Börnstein Database*, chapter 2.1.27. SpringerMaterials, 2010.

[39] T. Schmidt, U. Groh, R. Fink, and E. Umbach. *XPEEM with energy-filtering: Advantages and first results from the SMART project.* Surf. Rev. Lett. **9(1)** (2002), 223.

[40] S. Hüfner. *Photoelectron Spectroscopy.* Advanced Texts in Physics. Springer, third edition, 2003.

[41] M. P. Seah and D. Briggs. *Practial surface analysis*, volume 1. John Wiley & Sons Ltd, 1990.

[42] L. Weinhardt. *Elektronische und chemische Eigenschaften von Grenzflächen und Oberflächen in optimierten Cu(In,Ga)(S,Se)$_2$ Dünnschichtsolarzellen.* Ph.D. thesis, Universität Würzburg, 2005.

[43] J. F. Moulder, W. F. Stickle, P. E. Sobol, and K. D. Bomben. *Handbook of X-ray Spectroscopy A reference book of standard spectra for identification and interpretation of XPS data.* Perkin-Elmer Corporation - Physical Electronics Division, 1992.

[44] M. P. Seah. *Quantification of AES and XPS.* In D. Briggs and M. P. Seah (editors), *Practical Surface Analysis*, volume 1: Auger and X-ray Photoelectron Spectroscopy, chapter 5.3 XPS, 223. John Wiley and Sons Ltd., second edition, 1990.

[45] F. Erfurth, B. Hußmann, A. Schöll, F. Reinert, A. Grimm, I. Lauermann, M. Bär, T. Niesen, J. Palm, S. Visbeck, et al. *Chemical structure of the (Zn$_{1-x}$,Mg$_x$)O/CuIn(S,Se)$_2$ interface in thin film solar cells.* Appl. Phys. Lett. .

[46] J. J. Yeh and I. Lindau. *Atomic subshell photoionization cross sections and asymmetry parameters.* Atomic Data and Nuclear Data Tables **32(1)** (1985), 1.

[47] A. Jablonski. *Elastic scattering and quantification in AES and XPS.* Surf. Interface Anal. **14(11)** (1989), 659.

[48] M. Wojdyr. *fityk - a curve fitting and data analysis program*, 0th edition, 2010.

[49] G. Schmitt. *MTF–Analyse.* Schneider Kreuznach, Bad Kreuznach, 2003.

[50] E. Bauer. *Low-Energy-Electron Microscopy.* Rep. Prog. Phys. **57(9)** (1994), 895.

[51] M. S. Altmann, W. F. Chung, and C. H. Liu. *LEEM Phase Contrast.* Surf. Rev. Lett. **5(6)** (1998), 1129.

[52] M. S. Altman and W. F. Chung. *Step contrast in low energy electron microscopy.* Ultramicroscopy **74(4)** (1998), 237.

[53] J. Stöhr. *NEXAFS Spectroscopy*, volume 25 of *Springer Series in Surface Sciences.* Springer, 1992.

[54] I. A. Gryadil, N. I. Dovgoshei, V. M. Bentsa, D. V. Chepur, P. I. Otrokh, and T. I. Povkhan. *Synthesis, structure and certain properties of single-layer and multilayer single-crystal systems based on CdS-CdSe films.* Russian Physics Journal **13(8)** (1970), 1112.

[55] BESSY. *Betrieb des Beschleunigers – Betriebsmodi.* HZB, BESSY Intranet, 2010.

[56] I. Veeco. *diMultiMode V - SPM Instruction Manual.* Veeco Instruments Inc., 004th edition, 2006.

[57] G. Binnig, C. F. Quate, and C. Gerber. *Atomic Force Microscope.* Phys. Rev. Lett. **56(9)** (1986), 930.

[58] S. R. Forrest, M. L. Kaplan, and P. H. Schmidt. *Organic-on-inorganic semiconductor contact barrier diodes. I. Theory with applications to organic thin films and prototype devices.* J. Appl. Phys. **55(6)** (1984), 1492.

[59] Z. Shen, P. E. Burrows, V. Bulovic, S. R. Forrest, and M. E. Thompson. *Three-Color, Tunable, Organic Light-Emitting Devices.* Science **276(5321)** (1997), 2009.

[60] T. Oku, T. Noma, A. Suzuki, K. Kikuchi, and S. Kikuchi. *Fabrication and characterization of fullerene/porphyrin bulk heterojunction solar cells.* J. Phys. Chem. Solids .

[61] M. Fendrich. *Frequenzmodulierte Rasterkraftmikroskopie an organischen Molekülen.* Ph.D. thesis, Universität Duisburg-Essen, 2008.

[62] A. J. Lovinger, S. R. Forrest, M. L. Kaplan, P. H. Schmidt, and T. Venkatesan. *Structural and morphological investigation of the development of electrical conductivity in ion-irradiated thin films of an organic material.* J. Appl. Phys. **55(2)** (1984), 476.

[63] M. Möbus, N. Karl, and T. Kobayashi. *Structure of perylene-tetracarboxylic-dianhydride thin films on alkali halide crystal substrates.* J. Cryst. Growth **116(3-4)** (1992), 495.

[64] B. Krause, A. C. Dürr, F. Schreiber, H. Dosch, and O. H. Seeck. *Thermal stability and partial dewetting of crystalline organic thin films: 3,4,9,10-perylenetetracarboxylic dianhydride on Ag(111).* J. Chem. Phys. **119(6)** (2003), 3429.

[65] B. Krause, A. Dürr, F. Schreiber, H. Dosch, and O. Seeck. *Late growth stages and post-growth diffusion in organic epitaxy: PTCDA on Ag(111).* Surf. Sci. **572(2-3)** (2004), 385.

[66] S. Henze, O. Bauer, T.-L. Lee, M. Sokolowski, and F. Tautz. *Vertical bonding distances of PTCDA on Au(111) and Ag(111): Relation to the bonding type.* Surf. Sci. **601(6)** (2007), 1566.

[67] A. Kraft, R. Temirov, S. K. M. Henze, S. Soubatch, M. Rohlfing, and F. S. Tautz. *Lateral adsorption geometry and site-specific electronic structure of a large organic chemisorbate on a metal surface.* Phys. Rev. B **74(4)** (2006), 041402.

[68] F.-J. Meyer zu Heringdorf. *The application of low energy electron microscopy and photoemission electron microscopy to organic thin films.* J. Phys.: Condens. Matter **20(18)** (2008), 184007.

[69] L.-G. Liu and W. A. Bassett. *Compression of Ag and phase transformation of NaCl.* J. Appl. Phys. **44(4)** (1973), 1475.

[70] T. Ogawa, K. Kuwamoto, S. Isoda, T. Kobayashia, and N. Karl. *3,4:9,10-Perylenetetracarboxylic dianhydride (PTCDA) by electron crystallography.* Acta Crystallographica Section B **55(1)** (1999), 123.

[71] C. Seidel, C. Awater, X. D. Liu, R. Ellerbrake, and H. Fuchs. *A combined STM, LEED and molecular modelling study of PTCDA grown on Ag(110).* Surf. Sci. **371(1)** (1997), 123.

[72] L. Kilian, E. Umbach, and M. Sokolowski. *Molecular beam epitaxy of organic films investigated by high resolution low energy electron diffraction (SPA-LEED): 3,4,9,10-perylenetetracarboxylicacid-dianhydride (PTCDA) on Ag(111).* Surf. Sci. **573(3)** (2004), 359.

[73] E. Umbach, K. Glöckler, and M. Sokolowski. *Surface "architecture" with large organic molecules: interface order and epitaxy.* Surf. Sci. **402-404** (1998), 20.

[74] B. Krause, F. Schreiber, H. Dosch, A. Pimpinelli, and O. H. Seeck. *Temperature dependence of the 2D-3D transition in the growth of PTCDA on Ag(111): A real-time X-ray and kinetic Monte Carlo study.* Europhys. Lett. **65(3)** (2004), 372.

[75] L. Kilian. *Adsorption, Struktur und Morphologie hochgeordneter Adsorbatschichten.* Ph.D. thesis, Universität Würzburg, 2002.

[76] B. Krause, A. C. Dürr, K. Ritley, F. Schreiber, H. Dosch, and D. Smilgies. *Structure and growth morphology of an archetypal system for organic epitaxy: PTCDA on Ag(111).* Phys. Rev. B **66(23)** (2002), 235404.

[77] S. Kowarik, A. Gerlach, and F. Schreiber. *Organic molecular beam deposition: fundamentals, growth dynamics, and in situ studies.* J. Phys.: Condens. Matter **20(18)** (2008), 184005.

[78] C. Ratsch, A. Zangwill, P. Smilauer, and D. D. Vvedensky. *Saturation and scaling of epitaxial island densities.* Phys. Rev. Lett. **72(20)** (1994), 3194.

[79] B. Krause, A. C. Dürr, K. A. Ritley, F. Schreiber, H. Dosch, and D. Smilgies. *On the coexistence of different polymorphs in organic epitaxy: a and b phase of PTCDA on Ag(111).* Appl. Surf. Sci. **175-176** (2001), 332.

[80] T. Graber. *Streuung von Elektronen in organischen Festkörpern und Relevanz für Spektroskopische Methoden.* Ph.D. thesis, Universität Würzburg, 2010.

[81] P. Bayersdorfer. *Spot Plotter - Dieses Programm dient der Auswertung von SPA-LEED-Messungen in Form von Bilddateien.* Universtität Würzburg, EP II, first edition, 2008.

[82] J. C. Swarbrick, J. Ma, J. A. Theobald, N. S. Oxtoby, J. N. O'Shea, N. R. Champness, and P. H. Beton. *Square, Hexagonal, and Row Phases of PTCDA and PTCDI on Ag–Si(111)*$\sqrt{3} \times \sqrt{3}R°$. J. Phys. Chem. B **109(24)** (2005), 12167.

[83] S. Soubatch, C. Weiss, R. Temirov, and F. S. Tautz. *Site-Specific Polarization Screening in Organic Thin Films.* Phys. Rev. Lett. **102(17)** (2009), 177405.

[84] P. L. Lévesque, F. C. Maier, T. Schmidt, E. Umbach, and H.-J. Freund. *Initial stage growth study of PTCDA/Ag(111): direct correlation with atomic steps.* .

[85] F. Niederdraenk, K. Seufert, P. Luczak, S. K. Kulkarni, C. Chory, R. B. Neder, and C. Kumpf. *Structure of small II-VI semiconductor nanoparticles: A new approach based on powder diffraction.* Phys. Status Solidi C **4(9)** (2007), 3234.

[86] F. Niederdraenk. Ph.D. thesis, Universität Würzburg, 2009.

[87] F. M. Ross, R. M. Tromp, and M. C. Reuter. *Transition States Between Pyramids and Domes During Ge/Si Island Growth.* Science **286(5446)** (1999), 1931.

[88] M. Rabe, M. Lowisch, and F. Henneberger. *Self-assembled CdSe quantum dots Formation by thermally activated surface reorganization.* J. Cryst. Growth **184-185** (1998), 248.

[89] K. Tillmann, A. Thust, M. Lentzen, P. Swiatek, A. Förster, K. Urban, W. Laufs, D. Gerthsen, T. Remmele, and A. Rosenauer. *Determination of segregation, elastic strain and thin-foil relaxation in InxGa-1-x As islands on GaAs(001) by high resolution transmission electron microscopy.* Philos. Mag. Lett. **74(5)** (1996), 309.

[90] S. Sanguinetti, K. Watanabe, T. Tateno, M. Wakaki, N. Koguchi, T. Kuroda, F. Minami, and M. Gurioli. *Role of the wetting layer in the carrier relaxation in quantum dots.* Appl. Phys. Lett. **81(4)** (2002), 613.

[91] A. Maeland and T. B. Flanagan. *Lattice spacings of gold–palladium alloys.* Can. J. Phys. **42** (1964), 2364.

[92] J. Massies, P. Devoldere, and N. T. Linh. *Work function measurements on MBE GaAs(001) layers.* J. Vac. Sci. Technol. **16(5)** (1979), 1244.

[93] M. Lang, D. Schikora, T. Widmer, C. Giftge, A. Forstner, V. Holy, J. Humenberger, K. Lischka, G. Brunthaler, H. Sitter, et al. *Structural properties of perfect ZnTe epilayers on (001) GaAs substrates.* J. Cryst. Growth **138(1-4)** (1994), 81.

[94] S. Adachi. *II-VI Compound semiconductors*, volume 3 of *Handbook on physical properties of semiconductors.* Kluwer Academic Publishers, 2004.

[95] H. J. Lozykowski and V. K. Shastri. *Excitonic and Raman properties of ZnSe/$Zn_{1-x}Cd_xSe$ strained-layer quantum wells.* J. Appl. Phys. **69(5)** (1991), 3235.

[96] M. Yoneta, K. Nanami, M. Ohishi, K. Yoshino, and H. Saito. *The Structural and Optical Characterization of MBE-ZnSe Layer Grown on High-Quality VGF-ZnTe Substrate.* Phys. Status Solidi B **229(1)** (2002), 127.

[97] J. C. Phillips. *Bonds and Bands in Semiconductors.* Academic Press, New York, 1973.

[98] D. Kraft, U. Weiler, Y. Tomm, A. Thissen, A. Klein, and W. Jaegermann. *Alternative back contacts for CdTe solar cells: a photoemission study of the VSe2/CdTe and TiSe2/CdTe interface formation.* Thin Solid Films **431-432** (2003), 382.

[99] E. Janik and R. Triboulet. *Ohmic contacts to p-type cadmium telluride and cadmium mercury telluride.* J. Phys. D: Appl. Phys. **16(12)** (1983), 2333.

[100] L. Bergmann, C. Schaefer, and R. Kassing. *Lehrbuch der Experimentalphysik, Band 6: Festkörper.* 978-3-11-017485-4. Walter de Gruyter, second edition, 2005.

[101] Wikipedia. *Work function.* world wide web, 2010. From: CRC handbook on Chemistry and Physics, Version 2008, pp. 12.

[102] W. Faschinger, M. Ehinger, T. Schallenberg, and M. Korn. *High-efficiency p-i-n detectors for the visible spectral range based on ZnSTe–ZnTe superlattices.* Appl. Phys. Lett. **74(22)** (1999), 3404.

[103] T. Nann, S. Ibrahim, P.-M. Woi, S. Xu, J. Ziegler, and C. Pickett. *Water Splitting by Visible Light: A Nanophotocathode for Hydrogen Production13.* Angew. Chem., Int. Ed. **49(9)** (2010), 1574.

[104] J. Phillips, K. Kamath, and P. Bhattacharya. *Far-infrared photoconductivity in self-organized InAs quantum dots.* Appl. Phys. Lett. **72(16)** (1998), 2020.

[105] M. Klude, T. Passow, R. Kroger, and D. Hommel. *Electrically pumped lasing from CdSe quantum dots.* Electronics Letters **37** (2001), 1119.

[106] E. Kurtz, J. Shen, M. Schmidt, M. Grün, S. K. Hong, D. Litvinov, D. Gerthsen, T. Oka, T. Yao, and C. Klingshirn. *Formation and properties of self-organized II-VI quantum islands.* Thin Solid Films **367(1-2)** (2000), 68.

[107] D. Litvinov, A. Rosenauer, D. Gerthsen, P. Kratzert, M. Rabe, and F. Henneberger. *Influence of the growth procedure on the Cd distribution in CdSe/ZnSe heterostructures: Stranski–Krastanov versus two-dimensional islands.* Appl. Phys. Lett. **81(4)** (2002), 640.

[108] I.-C. Robin, R. André, H. Mariette, S. Tatarenko, L. Si Dang, J. Gérard, and E. Bellet-Amalric. *New method to induce 2D-3D transition of strained CdSe/ZnSe layers.* Physica E: Low-dimensional Systems and Nanostructures **26(1-4)** (2005), 119.

[109] S. Mahapatra, T. Kiessling, E. Margapoti, G. V. Astakhov, W. Ossau, L. Worschech, A. Forchel, and K. Brunner. *Formation mechanism and properties of CdSe quantum dots on ZnSe by low temperature epitaxy and in situ annealing.* Appl. Phys. Lett. **89(4)** (2006), 043102.

[110] S. Mahapatra, E. Margapoti, L. Worschech, A. Forchel, and K. Brunner. *Amorphous-Te-mediated self-organization of CdSe/ZnSe nanostructures.* J. Cryst. Growth **301** (2007), 293.

[111] S. Mahapatra, T. Kiessling, E. Margapoti, G. Astakhov, W. Ossau, L. Worschech, A. Forchel, and K. Brunner. *Layer-by-layer growth and island formation in CdSe/ZnSe heteroepitaxy.* J. Cryst. Growth **301** (2007), 310.

[112] S. Mahapatra, T. Kiessling, E. Margapoti, G. V. Astakhov, J. Renner, U. Bass, C. Bougerol, T. Schmidt, A. Bendounan, F. Schmitt, et al. *CdSe/ZnSe heteroepitaxy: Aspects of growth and self organization of nanostructures.* Phys. Status Solidi C **4(9)** (2007), 3129.

[113] N. Peranio, A. Rosenauer, D. Gerthsen, S. V. Sorokin, I. V. Sedova, and S. V. Ivanov. *Structural and chemical analysis of CdSe/ZnSe nanostructures by transmission electron microscopy.* Phys. Rev. B **61(23)** (2000), 16015.

[114] I. Gierz. *Strukturuntersuchungen an CdSe/ZnSe-Quantenpunkten und Zn(Cr)Se-Halbleiterschichtsystemen mit Hilfe von oberflächensensitiver Röntgenbeugung.* Master's thesis, Universität Würzburg, 2007.

[115] J. C. Fuggle and N. Mårtensson. *Core-Level Binding Energies in Metals.* J. Electron Spectrosc. Relat. Phenom. **21** (1980), 275.

[116] M. Cardona and L. Ley. *Photoemission in Solids I: General Principles with additional corrections.* Springer-Verlag, Berlin, 1978.

[117] H. Neumann, M. Mast, J. Enderlein, R. D. Tomlinson, and M. V. Yakushev. *XPS Analysis of Bridgman-grown $CuInTe_2$ and of its Native Oxide.* Cryst. Res. Technol. **31(1)** (1996), 75.

[118] W. Weigand, A. Müller, L. Kilian, T. Schallenberg, P. Bach, G. Schmidt, L. W. Molenkamp, O. Bunk, R. L. Johnson, C. Kumpf, et al. *Structural investigation of the ZnSe(001)-c(2 x 2) surface.* Phys. Rev. B **68(24)** (2003), 241314.

[119] Wagner. *NIST X-ray Photoelectron Spectroscopy Database, Version 3.5.* world wide web, 2007.

[120] A. Frey. *Wachstumsprotokolle, Proben cb3446, cb3494*, 2009.

[121] S. Tougard. *QUASES-IMFP-TPP2M, Inelastic electron mean free path calculated from the Tanuma, Powell and Penn TPP2M.* Quases-Tougaard Inc., 2002.

[122] S. Tanuma, C. J. Powell, and D. R. Penn. *Calculations of electron inelastic mean free paths (IMFPS). IV. Evaluation of calculated IMFPs and of the predictive IMFP formula TPP-2 for electron energies between 50 and 2000 eV.* Surf. Interface Anal. **20(1)** (1993), 77.

[123] E. M. Gullikson. *X-ray attenuation lengths Input parameters: 20° incidence; range 100-750 eV in steps of 2 eV (326 pts, linear).* world wide web, 2010.

[124] B. L. Henke, E. M. Gullikson, and J. C. Davis. *X-Ray Interactions: Photoabsorption, Scattering, Transmission, and Reflection at E = 50-30,000 eV, Z = 1-92.* Atomic Data and Nuclear Data Tables **54(2)** (1993), 181.

[125] C. Orme, M. D. Johnson, J. L. Sudijono, K. T. Leung, and B. G. Orr. *Large scale surface structure formed during GaAs (001) homoepitaxy.* Appl. Phys. Lett. **64(7)** (1994), 860.

[126] C. Schumacher. *"It is known that the Te–cap does not close until about 100 nm thickness.".* Personal communication, 2009.

[127] C. Kumpf, A. Müller, W. Weigand, E. Umbach, J. Wagner, V. Wagner, S. Gundel, L. Hansen, J. Geurts, O. Bunk, et al. *Analysis of structure and vibrational dynamics of the BeTe(001) surface using x-ray diffraction, Raman spectroscopy, and density functional theory.* Phys. Rev. B **68(3)** (2003), 035339.

[128] I.-C. Robin, R. Andre, C. Bougerol, T. Aichele, and S. Tatarenko. *Elastic and surface energies: Two key parameters for CdSe quantum dot formation.* Appl. Phys. Lett. **88(23)** (2006), 233103.

[129] T. Schallenberg, C. Schumacher, K. Brunner, and L. W. Molenkamp. *Selected area growth of II-VI nanostructures using shadow masks.* Phys. Status Solidi B **241(3)** (2004), 564.

[130] A. A. Toropov, I. V. Sedova, O. G. Lyublinskaya, S. V. Sorokin, A. A. Sitnikova, S. V. Ivanov, J. P. Bergman, B. Monemar, F. Donatini, and L. S. Dang. *Coexistence of type-I and type-II band lineups in Cd(Te,Se)/ZnSe quantum-dot structures.* Appl. Phys. Lett. **89(12)** (2006), 123110.

[131] W. Chen, A. Kahn, P. Soukissian, P. S. Mangat, J. Gaines, C. Ponzoni, and D. Olego. *ZnSe(100) surface: Atomic confgurations, composition and surface dipole.* Phys. Rev. B **49** (1994), 10790.

[132] J. M. Garcia, J. P. Silveira, and F. Briones. *Strain relaxation and segregation effects during self-assembled InAs quantum dots formation on GaAs(001).* Appl. Phys. Lett. **77(3)** (2000), 409.

[133] L. Zhu, K. L. Yao, Z. L. Liu, and Y. B. Li. *First-principles studies of the atomic reconstructions of CdSe (001) and (111) surfaces.* J. Phys.: Condens. Matter **21(9)** (2009), 095001.

[134] Y. Zou, Y. Cui, V. Yun, A. Valfells, R. A. Kishek, S. Bernal, I. Haber, M. Reiser, P. G. O'Shea, and J. G. Wang. *Compact high-resolution retarding field energy analyzer for space-charge-dominated electron beams.* Physical Review Special Topics Accelerators and Beams **5** (2002), 072801.

[135] T. Makino, R. Andre, J.-M. Gerard, R. Romestain, L. S. Dang, M. Bartels, K. Lischka, and D. Schikora. *Single quantum dot spectroscopy of CdSe/ZnSe grown on vicinal GaAs substrates.* Appl. Phys. Lett. **82(14)** (2003), 2227.

[136] V. S. Smentkowski and J. T. Yates. *Universal calibration of W5thermocouples in the temperature range 32–2588 K.* J. Vac. Sci. Technol., A **14(1)** (1996), 260.

[137] Haidenhain. *Inkrementale Messtaster.* Haidenhain, 2008.

List of Figures

List of Tables

Danksagung

Zu guter Letzt möchte ich mich bei all jenen bedanken, die mich auf ihre Weise unterstütz und so zum Gelingen dieser Arbeit beigetragen haben.

- Prof. E. Umbach für die vielseitige Themenstellung mit ihren zahlreichen Herausforderungen, die Unterstützung des SMART–Teams in schwierigen Zeiten und besonders für seine aufmunternde Verblüffung über manch unscheinbar anmutendes Ergebnis.
- Priv. Doz. J. Schäfer dafür, dass er sich begeistert die vorläufigen Ergebnisse angehört und schließlich unter Hochdruck das Zweitgutachten übernommen hat.
- Priv. Doz. R. Fink für seine Bereitschaft, als Prüfer zur Verfügung zu stehen.
- Prof. F. Reinert für die anhaltende Unterstützung trotz geänderter Umstände.
- Dr. Thomas Schmidt für die freundliche Aufnahme ins SMART–Team, die Vermittlung unzähliger Details über das SMART und dessen Geschichte, für viele andere Geschichtsgeschichten und die langwierigen, ausführlichen Korrekturen.
- Priv. Doz. C. Kumpf, Prof. K. Brunner und Priv. Doz C. Schumacher für die gute Zusammenarbeit bei der Suche nach geeigneten CdSe/ZnSe–Schichtsysteme für die Untersuchungen am SMART. Herrn Kumpf besonders auch dafür, dass er den Kontakt zur MBE–Gruppe in Würzburg vermittelt und geholfen hat, ihn über die Distanz am Leben zu erhalten.
- Dr. Pierre Lévesque, pour l'amabilité, mir in puncto Elektronenoptik Starthilfe zu leisten und für die Möglichkeit, über all die Fragen, die SMART so aufwarf, zu diskutieren. Et aussi pour ton amitié et le bon temps (et l'espoir d'explorer á "Käses" des produits de lait). Ferner für's Korrekturlesen des PTCDA–Kapitels.
- Unseren Ingenieuren vor Ort, Anton Rahm und besonders Marcel Springer, für ihre tatkräftige Unterstützung, wenn es zum Beispiel um (Um)Baumaßnahmen am Gerät von Kühlwasserregendächern bis zu Kamerastativen ging – von den vielen, völlig unscheinbaren und oft unsichtbaren Kleinigkeiten mit großer

Wirkung ganz zu schweigen. Marcel Springer besonders für die Crashkurse in Photoshop und viele Kameradiskussionen.

- Alexander Frey für die zahlreichen Proben, Informationen und Diskussionen zu Detailfragen rund um das MBE–Wachstum dünner Schichten.
- Meinen Mitstreitern der letzten Jahre Flo$\hbar$, Stefann, Schinki und Co., aber auch all den Kollegen der EPII (jetzt EPVII), die mich immer wieder herzlich bei Stippvisiten aufgenommen haben.
- Der Open Source Community und Flo$\hbar$ für den LaTeXSupport.

Ganz besonders möchte ich mich bei meiner Familie bedanken. Eva, vielen Dank, dass Du mich ertragen, immer wieder motiviert, mir zudem den Rücken von so manchen lebenserhaltenden Tätigkeiten freigehalten und für immer ausreichend Schokolade gesorgt hast. Christina, danke, dass Du mich an Deinen Erfahrungen beim Verfassen von umfangreichen Werken teilhaben ließt.
Meinen Eltern besonders dafür, dass ihr immer da seid! Es tut unglaublich gut zu wissen, dass ihr bedingungslos an mich glaubt und mir stets mit Rat und Tat zur Seite steht.
Ihr alle habt mich immer wieder motiviert weiter zu machen und mir den Rückhalt geboten, der mich in schwierigen Zeiten über Wasser gehalten hat. Vielen Dank!

Erklärung

Ich versichere hiermit an Eides statt, gemäß Paragraph 5, Abs. 2 Ziff. 2 und 5 der Promotionsordnung, dass ich die vorliegende Dissertation eigenständig, d.h. insbesondere selbstständig und ohne Hilfe eines kommerziellen Promotionsberaters angefertigt und keine anderen, als die angegebenen Quellen und Hilfsmittel benutzt habe. Die Dissertation lag bisher in keinem anderen Prüfungsfach vor.

Würzburg/Berlin, im Oktober 2010

Florian C. Maier